



**FACULTY  
OF MATHEMATICS  
AND PHYSICS**  
Charles University

## **DOCTORAL THESIS**

Jiří Kuchařík

**Charge transport in semiconductor nanostructures investigated  
by time-resolved multi-terahertz spectroscopy**

Institute of Physics of the Czech Academy of Sciences

Supervisor of the doctoral thesis: Mgr. Hynek Němec, Ph.D.

Study programme: Physics

Specialization: Quantum Optics and Optoelectronics

Prague 2019



I declare that I carried out this doctoral thesis independently, and only with the cited sources, literature and other professional sources.

I understand that my work relates to the rights and obligations under the Act No. 121/2000 Coll., the Copyright Act, as amended, in particular the fact that the Charles University has the right to conclude a license agreement on the use of this work as a school work pursuant to Section 60 paragraph 1 of the Copyright Act.

In..... date.....

Jiří Kuchařík





I would like to express my gratitude to my supervisor, Mgr. Hynek Němec, Ph.D., for his precise guidance, patience and critical comments which helped to substantially improve this manuscript. I would like to thank the members of the THz group—doc. RNDr. Petr Kužel, Ph.D., Ing. Christelle Kadlec, Dr., Mgr. Filip Kadlec, Dr. and Vladimir Puskarev, MSc.—for creating a friendly and supporting working environment. I am grateful to a former colleague Volodymyr Skoromets, Ph.D. for his help with the experiments. I would like to thank Dr. Ing. Jan M. Macák from University of Pardubice for providing the TiO<sub>2</sub> nanotubes samples. I also thank RNDr. Ivan Rychetský, CSc. for providing the results of effective medium calculations for TiO<sub>2</sub> nanotubes and to doc. RNDr. Tomáš Ostatnický, Ph.D. for providing the quantum-mechanical calculations which allowed a deeper understanding of parts of this thesis.



Title: Charge transport in semiconductor nanostructures investigated by time-resolved multi-terahertz spectroscopy

Author: Jiří Kuchařík

Department / Institute: Institute of Physics of the Czech Academy of Sciences

Supervisor of the doctoral thesis: Mgr. Hynek Němec, Ph.D., Institute of Physics of the Czech Academy of Sciences

Abstract: Terahertz conductivity spectra contain information on charge transport mechanisms and charge confinement on nanometer distances. In this thesis, we make a substantial progress in understanding of terahertz conductivity in several regimes. First, we theoretically investigate linear terahertz conductivity of confined electron gas: while the spectra of degenerate electron gas exhibit geometrical resonances, the response in non-degenerate case smears into a single broad resonance due to the wide distribution of charge velocities. Then, we theoretically and experimentally analyze various TiO<sub>2</sub> nanotube layers: their linear charge transport properties strongly depend on the fabrication process, which influences the internal structure of the nanotube walls. In the main part of the thesis, we develop a framework for evaluation of the nonlinear terahertz response of semiconductor nanostructures based on microscopic Monte-Carlo calculations. The nonlinear regime is highly non-perturbative even in moderate fields as illustrated by efficient high harmonics generation. We investigate measurable nonlinear signals for various semiconductor nanostructures; metallic nanoslits filled with nanoelements are the most promising for the experimental observation of terahertz nonlinearities. These nonlinearities per unit charge are stronger than those in doped graphene which has been considered to be one of the most nonlinear terahertz materials.

Keywords: time-domain terahertz spectroscopy, semiconductor nanostructures, terahertz conductivity, Monte-Carlo calculations, nonlinear terahertz response



# Contents

<b>Introduction</b>	<b>1</b>
<b>1. Response to electromagnetic terahertz radiation</b>	<b>4</b>
1.1 Linear response .....	4
1.2 Nonlinear response .....	4
<b>2. Monte-Carlo calculations of conductivity</b>	<b>11</b>
2.1 Linear response: Monte-Carlo calculations based on Kubo formalism .....	11
2.2 Non-perturbative Monte-Carlo calculations in the presence of the electric field .....	12
<b>3. Wave propagation in linear media</b>	<b>14</b>
3.1 Linear effective medium theories .....	15
3.1.1 Bergman spectral representation and VBD model .....	15
3.1.2 Maxwell-Garnett effective medium theory .....	16
3.1.3 Brick-wall model .....	17
3.1.4 Distribution of local electric fields in inhomogeneous structures .....	19
3.2 Solution of the wave equation in inhomogeneous photoexcited media .....	20
3.2.1 Percolated term .....	23
3.2.2 Non-percolated term .....	25
<b>4. Wave propagation in nonlinear media</b>	<b>28</b>
4.1 Homogeneous thin films .....	28
4.2 Heterogeneous thin films – monochromatic electric fields .....	34
4.3 Heterogeneous thin films – broadband THz pulses .....	37
4.4 Conclusions .....	40
<b>5. Linear THz conductivity of confined electron gas</b>	<b>42</b>
5.1 Non-degenerate electron gas .....	43
5.2 Degenerate electron gas confined in infinitely deep rectangular well .....	45
5.2.1 Semi-classical calculations .....	45
5.2.2 Quantum-mechanical calculations .....	51
5.3 Coupling between geometrical and plasmonic resonances .....	54
5.4 Degenerate electron gas confined in further model 2D nanostructures .....	59
5.5 Conclusions .....	62
<b>6. Nonlinear THz conductivity of 1D confined electron gas</b>	<b>64</b>
6.1 Non-degenerate electron gas .....	64
6.1.1 Linear response .....	65
6.1.2 Nonlinear response – high harmonics generation .....	66
6.1.3 Qualitative properties of harmonic mobility spectra .....	66
6.1.4 Analogy with an anharmonic oscillator .....	70
6.2 Degenerate electron gas .....	72
6.3 Conclusions .....	78

<b>7. Nonlinear THz response of semiconductor nanostructures</b>	<b>79</b>
7.1 Theoretical assessment of nonlinear THz signal .....	81
7.2 Nanostructures of GaAs .....	86
7.2.1 Linear response.....	88
7.2.2 Nonlinear response under broadband THz and multi-THz pulses .....	88
7.2.3 Nonlinear response under narrowband pulses generated by free electron laser .....	103
7.3 ZnO nanoparticles and CdS nanocrystals .....	108
7.4 The most promising structure – metallic nanoslits filled with GaAs nanobars .....	113
7.4.1 Linear response.....	114
7.4.2 Nonlinear response .....	116
7.5 Discussion of strength of nonlinearities.....	118
7.6 Conclusions .....	123
<b>8. THz spectroscopy of TiO<sub>2</sub> nanotubes</b>	<b>126</b>
8.1 Studied samples .....	126
8.1.1 Sample preparation .....	126
8.1.2 Morphological characteristics .....	128
8.2 Time-domain THz spectroscopy .....	129
8.3 Theoretical calculations of the THz response .....	130
8.3.1 Microscopic properties of TiO <sub>2</sub> nanotube walls .....	131
8.3.2 Effective properties of the TiO <sub>2</sub> nanotube layer.....	133
8.3.3 THz wave propagation in the nanotube layer.....	134
8.4 Experimental results and discussion .....	135
8.4.1 Steady-state effective permittivity and percolation of samples.....	135
8.4.2 THz photoconductivity spectra and dynamics.....	137
8.5 Conclusions .....	144
<b>Conclusions</b>	<b>145</b>
<b>Appendices</b>	<b>149</b>
A. Transient transmission of an inhomogeneous sample with background conductivity.....	149
B. Derivation of mobility of classical anharmonic oscillator .....	153
C. Nonlinear response of 1D confined degenerate electron gas .....	159
D. Nonlinear response of GaAs nanobars under broadband THz pulses.....	161
E. Nonlinear response of GaAs nanowires under broadband THz pulses.....	162
<b>References</b>	<b>163</b>
<b>List of publications</b>	<b>170</b>
<b>List of symbols</b>	<b>171</b>
A. Latin symbols.....	171
B. Greek symbols .....	177

## Introduction

Charge transport is a fundamental process required for the operation of electronic and photovoltaic devices. Many of the novel electronic high-tech components are based on nanostructured semiconductors. For example, the electrodes in Grätzel-type solar cells are made of percolated networks of metal oxide nanoparticles [1]. In such inhomogeneous systems, however, the charge transport occurs on various time- and length-scales and it is strongly influenced, e.g., by nanoparticle boundaries or by the nature of the contacts between nanoparticles [2]. High demand on more efficient devices with completely new functionalities thus requires not only advances in the field of material fabrication, but also a development of theoretical models and experimental techniques, which bring the most complete information on the charge transport processes in semiconductor nanostructures.

The application potential of semiconductor nanostructures is closely related to the charge transport which includes also processes on the scales of several tens of nanometers. It has been shown, that the pertinent information on nanoscale charge transport is encoded in the terahertz (THz) spectral range (the frequencies from  $\sim 0.1$  THz to  $\sim 3$  THz) [2]. The measurements of THz (photo)conductivity spectra are thus highly desired. For this task, a suitable technique is the time-domain THz spectroscopy [3]-[5]. This non-contact method is based on pulsed THz radiation and usually employs phase-sensitive detection, i.e. it allows one to obtain both the real and imaginary part of complex conductivity spectra from a single measurement. Additionally, one can combine it with a synchronized optical photoexcitation. This modified method is then usually referred to as optical pump-THz probe spectroscopy.

Traditionally, the (optical pump-THz probe) time-domain THz spectroscopy utilizes broadband THz pulses generated by optical rectification in a nonlinear crystal or by a photoconductive switch. Fields generated in this way have amplitudes typically of at most a few kV/cm (e.g.  $\sim 5$  kV/cm in our lab). In such a case, the THz response of most materials is still linear. In recent years, however, there has been a huge development in the area of table-top high-field THz sources, e.g. tilted-wavefront optical rectification in  $\text{LiNbO}_3$  (traditional THz range) [6]-[8] or generation from air-based plasma (the multi-THz range, i.e. the frequencies up to  $\sim 30$  THz) [9]-[13]. These sources can generate pulses with peak amplitudes up to 1 MV/cm [14]. There are also large-scale facilities such as free electron lasers producing narrowband pulses with high mean power [15]-[17]. It has been shown that such strong fields lead to nonlinear response of conductive carriers in bulk materials [18]-[24]. However, this field is very recent and the bulk THz nonlinearities are still not completely understood. It is then not surprising that there are almost no reports on THz nonlinearities in nanostructured systems [25],[26]. While the mechanisms of bulk nonlinearities should still be present in nanostructures, we also expect a completely new class of nonlinearities to emerge in isolated nanoobjects where the long-range charge transport is suppressed by potential barriers (i.e. charge confinement). These barriers create a strongly anharmonic binding potential and we thus anticipate a strong nonlinear response for high electric fields. These nonlinearities would then influence the THz and multi-THz conductivity of the nanostructures. The proper understanding of these effects could then facilitate development of new devices

including THz and multi-THz mixers or harmonic generators. The ongoing miniaturization of electronic devices also leads to higher electric field intensities inside the components; understanding of the charge transport in strong electric fields is thus important in this respect, too.

In the first part of this thesis, we introduce theoretical background required for the evaluation of both linear and nonlinear THz response of nanostructured systems. While the linear response is well described in the literature ([2] and references therein), the considered nonlinearities are completely unexplored and we thus have to entirely develop the corresponding theoretical framework. Chapter 1 introduces the phenomenological description of both the linear and nonlinear THz conductivity. For frequency mixing induced by broadband THz pulses, this is not straightforward due to multiple nonlinear interactions between different spectral components. In Chapter 2, we describe Monte-Carlo calculations of the conductivity. These include the well-known calculations based on Kubo formalism [27] and also the newly developed non-perturbative approach applicable in the presence of strong and arbitrarily shaped electric field. We then review the topic of linear response of inhomogeneous media in Chapter 3. This includes an overview of linear effective medium theories relevant for our work and also a solution of linear wave equation in a photoconductive medium, which provides a link to signals measurable in the experiments. In Chapter 4, we then describe our treatment of nonlinear response of inhomogeneous media and we also solve the nonlinear wave equation to provide formulae for measurable nonlinear signals.

In the second part, we use the above theoretical approaches to analyze both the linear and nonlinear conductivity of charges confined in semiconductor nanostructures. In Chapter 5, we investigated the linear response of an electron gas confined in various model structures. We show that the conductivity spectra of non-degenerate electron gases can exhibit characteristic resonances linked to (quasi-)periodic trajectories. In isolated structures, these resonances couple with the plasmonic resonance and the character of this coupling depends on the dimensionality. In Chapter 6, we examine the nonlinear THz conductivity of electron gas confined in a 1D potential well. Namely, we demonstrate that the charge confinement in semiconductor nanostructures can lead to a highly efficient high harmonics generation. Chapter 7 then contains the most important results of this thesis. Here, we evaluate the measurable nonlinear signals for several model semiconductor nanostructures. We show that the strongest nonlinear signals are predicted for structures where the semiconductor nanostructure is surrounded by metallic environment concentrating the THz electric field. We also argue why the traditional THz range is more perspective for the observation of nonlinearities than the multi-THz one.

Chapter 8 then presents experimental results of the thesis. We studied a linear THz response of  $\text{TiO}_2$  nanotubes which are very promising for photovoltaic applications. We show that the THz photoconductivity of the nanotubes strongly depends on the fabrication process. Monte-Carlo calculations of the conductivity then reveal a strong influence of the internal structure of nanotube walls in some of the samples.



Originally, the thesis was intended to be focused on the multi-THz spectroscopy of semiconductor nanostructures. The existing setup in our lab delivers pulses with peak amplitudes of  $\sim 120$  kV/cm, which was thought to be intense enough to induce nonlinear response of confined carriers. Our extensive calculations, however, revealed that these nonlinearities in realistic nanostructures are weaker than those in the THz range. The thesis then focuses mainly on the theoretical analysis of the nonlinearities induced by various high-field THz and multi-THz sources in several model semiconductor nanostructures.

# 1. Response to electromagnetic terahertz radiation

## 1.1 Linear response

Terahertz (THz) radiation strongly interacts with free charges in the matter. This interaction gives rise to an electric current, which in a linear material has the form of a convolution respecting the causality principle

$$j(t) = \int_0^{\infty} E(t - \tau) \sigma(\tau) d\tau, \quad (1.1)$$

where  $E(t - \tau)$  is the applied time-varying THz electric field and  $\sigma(\tau)$  is the linear conductivity of the material in the time-domain. Fourier transform allows us to express the current in the frequency-domain as a simple product

$$j(\omega) = \sigma(\omega) E(\omega), \quad (1.2)$$

where  $\omega$  is the angular frequency and the conductivity spectrum  $\sigma(\omega)$  is generally complex.

In systems with a single dominant type of charge carriers, the charge transport properties are assessed by the mobility of carriers  $\mu(\omega)$ , which can be viewed as the conductivity of a single unit charge

$$\mu(\omega) = \frac{\sigma(\omega)}{e_0 N}, \quad (1.3)$$

where  $e_0$  is the elementary charge and  $N$  is the concentration of carriers. While the conductivity describes the electric current induced by the unit electric field (1.2), the mobility describes the induced drift velocity  $v(\omega)$  of charges:

$$v(\omega) = \mu(\omega) E(\omega). \quad (1.4)$$

## 1.2 Nonlinear response

The electric current density  $j$  is expected to show nonlinear behavior for sufficiently strong electric fields  $E(t)$ . Here, we introduce a phenomenological description of this nonlinear response. The most straightforward approach is the adaptation of the perturbation theory used in nonlinear optics [28]. We thus expand the components of the electric current density  $j_i$  ( $i \in \{x, y, z\}$ ) into a series of individual nonlinear orders ( $\alpha$ ) proportional to the  $\alpha$ -th power of the electric field

$$j_i(t) = \sum_{\alpha=1}^{\infty} j_i^{(\alpha)}(t). \quad (1.5)$$

The lowest order nonlinear currents  $j^{(\alpha)}(t)$  are introduced as

$$j_i^{(1)}(t) = \sum_j \int_0^\infty E_j(t - \tau_1) \sigma_{ij}^{(1)}(\tau_1) d\tau_1 \quad (1.6.1)$$

$$j_i^{(2)}(t) = \sum_j \sum_k \int_0^\infty \int_0^\infty E_j(t - \tau_1) E_k(t - \tau_2) \sigma_{ijk}^{(2)}(\tau_1, \tau_2) d\tau_1 d\tau_2 \quad (1.6.2)$$

$$j_i^{(3)}(t) = \sum_j \sum_k \sum_l \int_0^\infty \int_0^\infty \int_0^\infty E_j(t - \tau_1) E_k(t - \tau_2) E_l(t - \tau_3) \sigma_{ijkl}^{(3)}(\tau_1, \tau_2, \tau_3) d\tau_1 d\tau_2 d\tau_3, \quad (1.6.3)$$

where  $\sigma^{(\alpha)}(\tau_1, \tau_2, \dots, \tau_\alpha)$  is the  $\alpha$ -th order nonlinear conductivity in the time-domain and the functional form reflects the causality principle. In the general case, the nonlinear conductivities are  $(\alpha+1)$ -rank tensors  $\sigma_{ij\dots kl}^{(\alpha)}$ , where  $i, j, \dots, k, l \in \{x, y, z\}$ . In this thesis, we will assume linearly polarized electric field and study the response in the direction of its polarization. In such case, the response is fully described just by the appropriate diagonal components  $\sigma_{ii\dots ii}^{(\alpha)}$ . In the rest of the text, we will drop the indices for simplicity.

As an example, we treat in detail the third-order nonlinearity as other orders can be treated in a similar way. Using the spectral representation of  $E$ , we get

$$j^{(3)}(t) = \int_{-\infty}^\infty \int_{-\infty}^\infty \int_{-\infty}^\infty E(\omega_1) E(\omega_2) E(\omega_3) \sigma^{(3)}(\omega_1, \omega_2, \omega_3) e^{-i(\omega_1 + \omega_2 + \omega_3)t} d\omega_1 d\omega_2 d\omega_3, \quad (1.7)$$

where  $\sigma^{(\alpha)}(\omega_1, \omega_2, \dots, \omega_\alpha)$  is generally complex. Transformation into the frequency-domain is straightforward and leads to

$$j^{(3)}(\omega) = \int_{-\infty}^\infty \int_{-\infty}^\infty E(\omega - \omega_2 - \omega_3) E(\omega_2) E(\omega_3) \sigma^{(3)}(\omega - \omega_2 - \omega_3, \omega_2, \omega_3) d\omega_2 d\omega_3. \quad (1.8)$$

We will now assume monochromatic field  $E(t) = E_0 \cos(\omega_0 t)$ , which is a sum of delta functions in the frequency-domain

$$E(\omega) = \frac{1}{2} E_0 [\delta(\omega - \omega_0) + \delta(\omega + \omega_0)]. \quad (1.9)$$

The substitution into (1.8) then yields

$$\begin{aligned} j^{(3)}(\omega) = & \frac{1}{8} E_0^3 \{ \delta(\omega - 3\omega_0) \sigma^{(3)}(\omega - 2\omega_0, \omega_0, \omega_0) + \delta(\omega + 3\omega_0) \sigma^{(3)}(\omega + 2\omega_0, -\omega_0, -\omega_0) + \\ & + \delta(\omega - \omega_0) [\sigma^{(3)}(\omega - 2\omega_0, \omega_0, \omega_0) + \sigma^{(3)}(\omega, -\omega_0, \omega_0) + \sigma^{(3)}(\omega, \omega_0, -\omega_0)] + \\ & + \delta(\omega + \omega_0) [\sigma^{(3)}(\omega + 2\omega_0, -\omega_0, -\omega_0) + \sigma^{(3)}(\omega, -\omega_0, \omega_0) + \sigma^{(3)}(\omega, \omega_0, -\omega_0)] \}. \end{aligned} \quad (1.10)$$

The third-order nonlinear current density  $j^{(3)}$  contains terms oscillating at two different frequencies – the fundamental one ( $\omega_0$ ) and its third harmonic ( $3\omega_0$ ). The underlying nonlinear process is thus a general four-wave mixing resulting in the frequency  $\omega = \pm \omega_0 \pm \omega_0 \pm \omega_0$ .

The eight individual coefficients  $\sigma^{(3)}$  encoding the material properties are not independent due to the symmetry reasons [28]. Firstly, the electric fields and currents are real quantities, therefore their positive and negative frequency components are complex conjugates:  $\sigma^{(3)}(\mp\omega_0, \mp\omega_0, \mp\omega_0) = \sigma^{(3)*}(\pm\omega_0, \pm\omega_0, \pm\omega_0)$ . This reduces the number of independent coefficients to four. Moreover, the intrinsic permutation symmetry applies, which allows us to freely interchange the frequencies in the considered diagonal components of the conductivity tensor:  $\sigma^{(3)}(-\omega_0, \omega_0, \omega_0) = \sigma^{(3)}(\omega_0, -\omega_0, \omega_0) = \sigma^{(3)}(\omega_0, \omega_0, -\omega_0)$ . This leaves us with just two independent coefficients:  $\sigma^{(3)}(\omega_0, \omega_0, \omega_0)$  and  $\sigma^{(3)}(-\omega_0, \omega_0, \omega_0)$ , which are responsible for the third-harmonics generation and the intensity-dependent refractive index, respectively. In the time-domain, the third-order nonlinear current  $j^{(3)}(t)$  can be thus equivalently written as

$$j^{(3)}(t) = \frac{1}{4} E_0^3 \text{Re}\{\sigma^{(3)}(\omega_0, \omega_0, \omega_0) e^{-i3\omega_0 t}\} + \frac{3}{4} E_0^3 \text{Re}\{\sigma^{(3)}(-\omega_0, \omega_0, \omega_0) e^{-i\omega_0 t}\}. \quad (1.11)$$

Note that the  $\alpha$ -th order nonlinear current  $j^{(\alpha)}(t)$  generally has components oscillating not only at  $\alpha$ -th harmonic frequency  $\alpha\omega_0$  but also at lower harmonic frequencies. It is useful to represent the total current (including nonlinear components of all orders) as a spectral decomposition into individual harmonic orders [ $m$ ]

$$j(t) = \text{Re}\left\{\sum_{m=0}^{\infty} j^{[m]}(m\omega_0) e^{-im\omega_0 t}\right\}, \quad (1.12)$$

where the  $m$ -th order harmonic current amplitude  $j^{[m]}(m\omega_0)$  is generally complex. We emphasize the difference between the nonlinear ( $\alpha$ ) and the harmonic [ $m$ ] orders. The nonlinear orders are directly associated with the  $\alpha$ -th power of the electric field  $E^\alpha$ , and as pointed above, generally contain more spectral components oscillating at various harmonic frequencies. On the other hand, the harmonic orders [ $m$ ] contain only one spectral component at the frequency  $m\omega_0$  while their relation to the electric field is more complex.

The spectral decomposition (1.12) is not commonly used in nonlinear optics where an intense laser light interacts with the matter. Since the distance between the resulting harmonic frequencies is higher than the widths of the corresponding spectral lines, the individual harmonic processes do not overlap in the frequency domain. Furthermore, the phase-matching condition ensures that one nonlinear process is typically much stronger than the others. In the nonlinear optics, it is thus usually sufficient to consider the single dominant nonlinear interaction and to neglect the others (e.g., optical rectification is ignored when second-harmonic generation is examined). In the THz range, however, the situation is different. THz spectroscopy commonly employs broadband pulses for which the central frequency and the spectral width are comparable to each other. Different harmonics of different parts of the input spectra may then produce the same resulting frequency. Furthermore, we typically focus on thin samples, where the phase-matching condition is insignificant.

The signal at a given frequency is then a result of nonlinear processes of various orders. Later, we will demonstrate that the nonlinear THz response is extremely strong and the perturbative expansion into the powers of  $E^a$  makes no longer sense. In such situation, we have to inevitably use the spectral decomposition (1.12).

We introduced two different representations of the nonlinear current – the perturbative description in the terms of powers of the electric field (1.5) and the spectral decomposition into the distinct harmonic components (1.12). Now, we investigate the relation between these two approaches. We will first illustrate the formalism for nonlinearities up to the third order. In the nonlinear order representation, the net electric current density  $j(t)$  then consists of the contributions from the first- to the third-order

$$\begin{aligned} j(t) = & E_0 \operatorname{Re}\{\sigma^{(1)}(\omega_0)e^{-i\omega_0 t}\} + \\ & + \frac{1}{2} E_0^2 \operatorname{Re}\{\sigma^{(2)}(\omega_0, \omega_0)e^{-i2\omega_0 t}\} + \frac{1}{2} E_0^2 \operatorname{Re}\{\sigma^{(2)}(-\omega_0, \omega_0)e^{-i0\omega_0 t}\} + \\ & + \frac{1}{4} E_0^3 \operatorname{Re}\{\sigma^{(3)}(\omega_0, \omega_0, \omega_0)e^{-i3\omega_0 t}\} + \frac{3}{4} E_0^3 \operatorname{Re}\{\sigma^{(3)}(-\omega_0, \omega_0, \omega_0)e^{-i\omega_0 t}\} \end{aligned} \quad (1.13)$$

In the harmonic order representation, the current consists of the components oscillating at the harmonic frequencies from  $0\omega_0$  to  $3\omega_0$

$$j(t) = \operatorname{Re}\{j^{[0]}(0) + j^{[1]}(\omega_0)e^{-i\omega_0 t} + j^{[2]}(2\omega_0)e^{-i2\omega_0 t} + j^{[3]}(3\omega_0)e^{-i3\omega_0 t}\}. \quad (1.14)$$

The comparison between (1.13) and (1.14) directly yields

$$j^{[0]}(0) = \frac{1}{2} \sigma^{(2)}(-\omega_0, \omega_0) E_0^2 \quad (1.15.1)$$

$$j^{[1]}(\omega_0) = \sigma^{(1)}(\omega_0) E_0 + \frac{3}{4} \sigma^{(3)}(-\omega_0, \omega_0, \omega_0) E_0^3 \quad (1.15.2)$$

$$j^{[2]}(2\omega_0) = \frac{1}{2} \sigma^{(2)}(\omega_0, \omega_0) E_0^2 \quad (1.15.3)$$

$$j^{[3]}(3\omega_0) = \frac{1}{4} \sigma^{(3)}(\omega_0, \omega_0, \omega_0) E_0^3 \quad (1.15.4)$$

Relations (1.15) summarize the equivalence of both descriptions for nonlinearities up to the third order and up to the third harmonic order. This scheme can be straightforwardly generalized to an arbitrary order and the harmonic current  $j^{[m]}(m\omega_0)$  thus generally reads

$$j^{[m]}(m\omega_0) = \sum_{\alpha=m}^{\infty} C_{m,\alpha} \sigma^{(\alpha)} E_0^\alpha, \quad (1.16)$$

$C_{m,\alpha}$	$\sigma^{(1)}E^1$	$\sigma^{(2)}E^2$	$\sigma^{(3)}E^3$	$\sigma^{(4)}E^4$	$\sigma^{(5)}E^5$	...	$\sigma^{(\alpha=2\beta)}E^{2\beta}$	$\sigma^{(\alpha=2\beta+1)}E^{2\beta+1}$
$j^{[0]}(0\omega_0)$		$\frac{1}{2}$ (-,+)		$\frac{3}{8}$ (-, -, +, +)			$\frac{1}{2^{2\beta}} \binom{2\beta}{\beta}$	
$j^{[1]}(1\omega_0)$	1 (+)		$\frac{3}{4}$ (-, +, +)		$\frac{10}{16}$ (-, -, +, +, +)			$\frac{1}{4^\beta} \binom{2\beta+1}{\beta}$
$j^{[2]}(2\omega_0)$		$\frac{1}{2}$ (+, +)		$\frac{4}{8}$ (-, +, +, +)			$\frac{1}{2^{2\beta-1}} \binom{2\beta}{\beta-1}$	
$j^{[3]}(3\omega_0)$			$\frac{1}{4}$ (+, +, +)		$\frac{5}{16}$ (-, +, +, +, +)			$\frac{1}{4^\beta} \binom{2\beta+1}{\beta-1}$
$j^{[4]}(4\omega_0)$				$\frac{1}{8}$ (+, +, +, +)			$\frac{1}{2^{2\beta-1}} \binom{2\beta}{\beta-2}$	
$j^{[5]}(5\omega_0)$					$\frac{1}{16}$ (+, +, +, +, +)			$\frac{1}{4^\beta} \binom{2\beta+1}{\beta-2}$
$\vdots$						$\ddots$		
$j^{[m=2n]}(2n\omega_0)$							$\frac{1}{2^{2\beta-1}} \binom{2\beta}{\beta-n}$	
$j^{[m=2n+1]}((2n+1)\omega_0)$								$\frac{1}{4^\beta} \binom{2\beta+1}{\beta-n}$

Tab. 1.1. Table of coefficients  $C_{m,\alpha}$  from the relation (1.16) between the harmonic amplitudes  $j^{[m]}(m\omega_0)$  and the nonlinear diagonal conductivities  $\sigma^{(\alpha)}$ . While constructing the equations for harmonic currents, the frequency dependence of  $\sigma^{(\alpha)}$  has to be carefully considered – the brackets below the coefficients schematically represent the signs of the frequency parameters, e.g.  $(-, +, +)$  represents the process  $-\omega_0 + \omega_0 + \omega_0 \rightarrow \omega_0$ . Obviously, it makes sense to consider only harmonic orders  $m \leq \alpha$ . Blank spaces represent zero values of  $C_{m,\alpha}$ .

where the conductivities  $\sigma^{(\alpha)}$  are functions of appropriate frequencies (determined by the index  $m$ ) and  $C_{m,\alpha}$  are positive fractions. The coefficients  $C_{m,\alpha}$  can be derived from the trigonometric power series and are summarized in Tab. 1.1.

We now describe the extraction of nonlinear conductivities  $\sigma^{(\alpha)}$  from the known harmonic current densities  $j^{[m]}(m\omega_0)$ . Since the odd- and even-order nonlinearities are described by mutually independent sets of equations ((1.16) and (Tab. 1.1)), we can treat each parity separately. As an example, we analyze a system with odd nonlinearities up to the fifth order. Then, we need to consider harmonic current densities  $j_k^{[m]}(m\omega_0)$  for three different amplitudes of the electric field  $E_{0,k}$  ( $k = 1, 2, 3$ ). The set of equations connecting  $j_k^{[m]}(m\omega_0)$  and  $\sigma^{(\omega)}$  directly follows from (1.16) and reads

$$j_k^{[1]}(\omega_0) = \sigma^{(1)}(\omega_0)E_{0,k}(\omega_0) + \frac{3}{4}\sigma^{(3)}(-\omega_0, \omega_0, \omega_0)E_{0,k}^3(\omega_0) + \frac{10}{16}\sigma^{(5)}(-\omega_0, -\omega_0, \omega_0, \omega_0, \omega_0)E_{0,k}^5(\omega_0) \quad (1.17.1)$$

$$j_k^{[3]}(3\omega_0) = \frac{1}{4}\sigma^{(3)}(\omega_0, \omega_0, \omega_0)E_{0,k}^3(\omega_0) + \frac{5}{16}\sigma^{(5)}(-\omega_0, \omega_0, \omega_0, \omega_0, \omega_0)E_{0,k}^5(\omega_0) \quad (1.17.2)$$

$$j_k^{[5]}(5\omega_0) = \frac{1}{16}\sigma^{(5)}(\omega_0, \omega_0, \omega_0, \omega_0, \omega_0)E_{0,k}^5(\omega_0). \quad (1.17.3)$$

Each of the above rows represents a set of linear equations and the nonlinear conductivities  $\sigma^{(a)}$  are then easily found as their solution. In our case, the equation (1.17.2) represents the set of two equations for two variables  $\sigma^{(3)}(\omega_0, \omega_0, \omega_0)$  and  $\sigma^{(5)}(-\omega_0, \omega_0, \omega_0, \omega_0, \omega_0)$

$$\begin{pmatrix} \frac{1}{4}E_{0,1}^3(\omega_0) & \frac{5}{16}E_{0,1}^5(\omega_0) \\ \frac{1}{4}E_{0,2}^3(\omega_0) & \frac{5}{16}E_{0,2}^5(\omega_0) \end{pmatrix} \begin{pmatrix} \sigma^{(3)}(\omega_0, \omega_0, \omega_0) \\ \sigma^{(5)}(-\omega_0, \omega_0, \omega_0, \omega_0, \omega_0) \end{pmatrix} = \begin{pmatrix} j_1^{[3]}(3\omega_0) \\ j_2^{[3]}(3\omega_0) \end{pmatrix} \quad (1.18)$$

and the equation (1.17.1) leads to a set of three equations for three nonlinear conductivities  $\sigma^{(1)}(\omega_0)$ ,  $\sigma^{(3)}(-\omega_0, \omega_0, \omega_0)$  and  $\sigma^{(5)}(-\omega_0, \omega_0, \omega_0, \omega_0, \omega_0)$

$$\begin{pmatrix} E_{0,1}(\omega_0) & \frac{3}{4}E_{0,1}^3(\omega_0) & \frac{10}{16}E_{0,1}^5(\omega_0) \\ E_{0,2}(\omega_0) & \frac{3}{4}E_{0,2}^3(\omega_0) & \frac{10}{16}E_{0,2}^5(\omega_0) \\ E_{0,3}(\omega_0) & \frac{3}{4}E_{0,3}^3(\omega_0) & \frac{10}{16}E_{0,3}^5(\omega_0) \end{pmatrix} \begin{pmatrix} \sigma^{(1)}(\omega_0) \\ \sigma^{(3)}(-\omega_0, \omega_0, \omega_0) \\ \sigma^{(5)}(-\omega_0, -\omega_0, \omega_0, \omega_0, \omega_0) \end{pmatrix} = \begin{pmatrix} j_1^{[1]}(\omega_0) \\ j_2^{[1]}(\omega_0) \\ j_3^{[1]}(\omega_0) \end{pmatrix}. \quad (1.19)$$

Equation (1.17.3) is then specific as it directly yields the the fifth-order conductivity  $\sigma^{(5)}(\omega_0, \omega_0, \omega_0, \omega_0, \omega_0)$ .

The sets of equations (1.18) and (1.19) have to be treated carefully since the system can easily become ill-conditioned. This is due to the necessity to consider electric fields from a rather narrow interval of amplitudes to avoid the presence of higher-harmonics. If these sets of equations were ill-conditioned, the solution would then extremely depend on the noise and systematic errors in the experiments or theoretical calculations<sup>1</sup>. We also note that this issue becomes more important with increasing highest order of nonlinearity.

---

<sup>1</sup> The electric current density will be later calculated by a Monte-Carlo approach which inevitably provides noisy results. We thus have to be aware of the discussed issue.

The above approach can be easily generalized to a system with nonlinearities up to the  $m$ -th order. The extraction of all nonlinear conductivities then requires the knowledge of  $j^{[m]}(m\omega_0)$  for  $m$  different values of  $E_0$  and solving the  $m$  systems of sets of equations analogous to (1.18) and (1.19). This framework also applies for the even-order nonlinearities, since they obey equations similar to (1.17).

In the weakly nonlinear case where only a few lowest nonlinearities exist, the described approach provides a way to calculate the nonlinear conductivities  $\sigma^{(\alpha)}$  from the harmonic current densities  $j^{[m]}(m\omega_0)$  spectra known for several values of the electric field, and thus the direct assessment of the material properties. In a strongly nonlinear case where many nonlinear orders exist, however, it is more convenient to interpret the results in the spectral representation of harmonic orders (instead of introducing photoconductivities  $\sigma^{(\alpha)}$ ) as it captures the nature of both the nonlinear and spectral properties.

In the linear regime, we introduced the mobility of carriers  $\mu(\omega)$  (1.3) for the assessment of charge transport properties. Here, we analogically define nonlinear mobilities  $\mu^{(\alpha)}(\omega_1, \omega_2, \dots, \omega_\alpha)$  as

$$\mu^{(\alpha)}(\omega_1, \omega_2, \dots, \omega_\alpha) = \frac{\sigma^{(\alpha)}(\omega_1, \omega_2, \dots, \omega_\alpha)}{e_0 N}, \quad (1.20)$$

which do not depend on the carrier density  $N$  and are subject to the same symmetry considerations as  $\sigma^{(\alpha)}$ . The equations derived in this section remain valid for the nonlinear mobility  $\mu^{(\alpha)}$  as can be shown by the substitutions  $j(t) \rightarrow v(t)$  and  $\sigma^{(\alpha)} \rightarrow \mu^{(\alpha)}$ , where  $v(t)$  is the drift velocity of carriers.



## 2. Monte-Carlo calculations of conductivity

Monte-Carlo calculations are the main theoretical tool for the determination of conductivity of semiconductor nanostructures [27],[29]. Here, we first recall an approach based on Kubo formalism (Section 2.1) which is convenient for the calculations of linear conductivity [27]. In this method, the thermal motion of carriers is simulated and the response is calculated from thermal fluctuations in equilibrium without an applied driving field. This approach, however, cannot be extended to the case of nonlinear response under strong electric fields as the linear Kubo formalism is no longer valid. In Section 2.2, we thus develop non-perturbative Monte-Carlo calculations of a nonlinear THz conductivity which are based on the monitoring of the charge velocity which arises as a response to an input time-varying electric field. Such an approach has been recently applied also for the calculation of the linear response [29]. A drawback is that the spectra calculated by non-perturbative approach typically exhibit higher noise than those obtained by Kubo formalism.

### 2.1 Linear response: Monte-Carlo calculations based on Kubo formalism

The basis for the calculations of *linear* conductivity is the Kubo formula for the mobility tensor [30],[31]

$$\mu_{jk}(\omega) = e_0 \frac{\int_0^\infty dt e^{i\omega t} \sum_{\alpha} \left( -\frac{\partial F}{\partial E} \right)_{E=E_{\alpha}} v_j(\alpha, 0) v_k(\alpha, t)}{\sum_{\alpha} F(E_{\alpha})}, \quad (2.1)$$

where  $e_0$  is the elementary charge,  $F$  is the statistical distribution function and the summation takes place over all states  $\alpha$ , and  $v_j(\alpha, t)$  are the time-dependent components of thermal carrier velocity in the state  $\alpha$ . In the simulations, however, we consider just trajectories of selected states. We account for this by introducing initial state probabilities  $p_j$  which follow the distribution  $(-\partial F/\partial E)$ . The Kubo formula (2.1) is then transformed to

$$\mu_{jk}(\omega) = e_0 \int_0^\infty dt e^{i\omega t} \sum_j p_j v_j(0) v_j(t, v_j) \underbrace{\frac{\sum_{\alpha} \left( -\frac{\partial F}{\partial E} \right)_{E=E_{\alpha}}}{\sum_{\alpha} F(E_{\alpha})}}_{\mathfrak{R}}, \quad (2.2)$$

The normalization factor  $\mathfrak{R}$  can be simplified to

$$\mathfrak{R} = \frac{1}{\int F(E) G(E) dE}, \quad (2.3)$$

where  $G(E)$  is a density of states. For Maxwell-Boltzmann statistics,  $\mathfrak{R}$  is always  $1/k_B T$  ( $k_B$  is Boltzmann constant and  $T$  is temperature). For Fermi-Dirac statistics with Fermi energy  $E_F$

and a  $D$ -dimensional space,  $\Re = D/(2E_F)$  when  $k_B T \ll E_F$ . Equation (2.2) can be written in a more compact form as [27]

$$\mu_{jk}(f) = e_0 \Re \int_0^\infty \langle v_j(0) v_k(t) \rangle e^{2\pi i f t} dt, \quad (2.4)$$

where  $\langle v_j(0) v_k(t) \rangle$  is the velocity autocorrelation function and the averaging takes place over the ensemble of carriers.

In this work, we use the calculations which were originally introduced in [27]. In these, we consider a thermal classical motion of non-interacting charges confined to a nanoobject. During their movement, the carriers undergo random scattering with a mean scattering time  $\tau_s$ , which represents the scattering in the bulk material. Each of these events causes randomization of the charge velocity according to the selected distribution (e.g. Maxwell-Boltzmann or Fermi-Dirac statistics). We have several choices for describing the interaction of charges with nanoobject boundaries. In this work, we assume that the carriers are either randomly backscattered or reflected elastically and specularly (only one of these regimes is always assumed in particular calculations). In this way, the trajectory and the time evolution of velocity the  $\vec{v}(t)$  is simulated for each carrier in the ensemble. The charge mobility spectrum is then calculated using the Kubo formula (2.4).

## 2.2 Non-perturbative Monte-Carlo calculations in the presence of the electric field

We assume, that the motion of carriers is classical and it obeys the Newton's equations

$$\frac{d\vec{r}(t)}{dt} = \vec{v}(t) \quad \frac{d\vec{v}(t)}{dt} = -\frac{e_0}{m} \vec{E}(t) - \frac{1}{m} \nabla V(\vec{r}), \quad (2.5)$$

where  $\vec{r} = (x, y, z)$  is the charge position,  $\vec{v} = (v_x, v_y, v_z)$  is the charge velocity,  $\vec{E}(t) = [E_x(t), 0, 0]$  is spatially homogeneous local time-varying electric field linearly polarized in the  $x$ -direction,  $V(\vec{r})$  is the local potential,  $e_0$  is elementary charge,  $m$  is carrier effective mass and  $t$  is time. The velocity directly yields the electric current density  $\vec{j}(t) = N e_0 \vec{v}(t)$  ( $N$  is the concentration of carriers), which can be expanded into the nonlinear (1.5) and harmonic (1.12) series. This allows the calculation of harmonic  $\sigma^{[m]}$  and nonlinear  $\sigma^{(a)}$  conductivities and the corresponding mobilities  $\mu^{[m]}$  and  $\mu^{(a)}$ , respectively, which are introduced in Section 1.2.

Here, we focus on an ensemble of non-interacting carriers enclosed in an infinitely deep potential well. At the start of the simulation, the carrier position and velocity is randomly generated with respect to the statistical distribution and the local potential  $V(\vec{r})$ . The carriers then move classically inside the well according to the Eq. (2.5). During their movement, the carriers undergo random isotropic scattering with mean time  $\tau_s$ , which corresponds to the scattering in the bulk material. As a result of this event, no velocity component is conserved and the carriers acquire a random new velocity according to the equilibrium statistical

distribution (i.e. not affected by the electric field). This is a considerable simplification as we do not account for the influence of the electric field on the statistical distribution. Individual scattering events are independent. When the carriers reach the well boundary, they are reflected elastically and specularly (although other interactions can be implemented as well [27]).

For each carrier in the ensemble, its trajectory and time evolution of the velocity  $v(t)$  is recorded. In the end, we calculate statistical average over the ensemble and we obtain mean carrier trajectory and time evolution of mean (drift) velocity  $\langle v(t) \rangle$ , and thus the mean (drift) electric current  $\langle j(t) \rangle$ . In equilibrium (without the electric field), only thermal motion is present and the drift current  $\langle j(t) \rangle$  vanishes.

The drift electric current  $\langle j(t) \rangle$  constitutes the main output of this non-perturbative approach. In particular, a response to an arbitrary temporal profile of the electric field can be calculated. For monochromatic electric field (1.9), analysis similar to the one presented in Section 1.2 is possible as the calculated stationary current density directly represents a single spectral component from (1.12). In this case, the conductive properties are further assessed by the nonlinear mobilities of carriers  $\mu^{(w)}(\omega)$  (1.20). This entire approach is in contrast with the Kubo formalism-based calculations, where the carrier thermal velocity (i.e. without the electric field) autocorrelation function is tracked, and the mobility spectrum is then obtained using the formula (2.1).

### 3. Wave propagation in linear media

Semiconductor nanostructures are inherently inhomogeneous systems with potentially complicated morphologies. This has fundamental implications for THz spectroscopy as the incident THz electric field  $E_{\text{inc}}$  creates a complex spatial distribution of local electric fields inside the nanostructure. Any measured data then contain information on both the local conductivity and the structure morphology and it is necessary to carefully disentangle them. For nanoparticles of subwavelength sizes, there are two views of this problem. Here, we focus on the description based on effective medium theory. The other way is to consider charge separation inside the nanostructures and describe the response in terms of localized plasmonic resonances [32],[33].

In the effective medium approach, we replace the spatial distribution of local electric fields by a single effective value  $E_{\text{eff}}$  which is a volume average of the local electric field (Fig. 3.1). The dielectric sample properties are then characterized by an effective permittivity  $\epsilon_{\text{eff}}$  (or an effective photoconductivity  $\Delta\sigma_{\text{eff}}$  in the photoexcited case). This approach is valid for characteristic nanoparticle dimensions much smaller than the wavelength of the radiation, which is safely satisfied in the THz range. In this section, we first provide an overview of selected linear effective medium theories for two-component systems and we also discuss the spatial distribution of the local electric fields (Section 3.1). Then, we recall the solution of the wave equation from [34] which allows to link the measured THz spectra with microscopic dielectric properties of the nanostructures and also with their morphology (Section 3.2). Later in Section 4, we generalize some of these results to the case of nonlinear response.

We note that the results shown here do not depend on a particular mechanism of conductivity. Later in Section 5, we illustrate how the effective medium theory affects the response linked to a particular model of the conductivity.

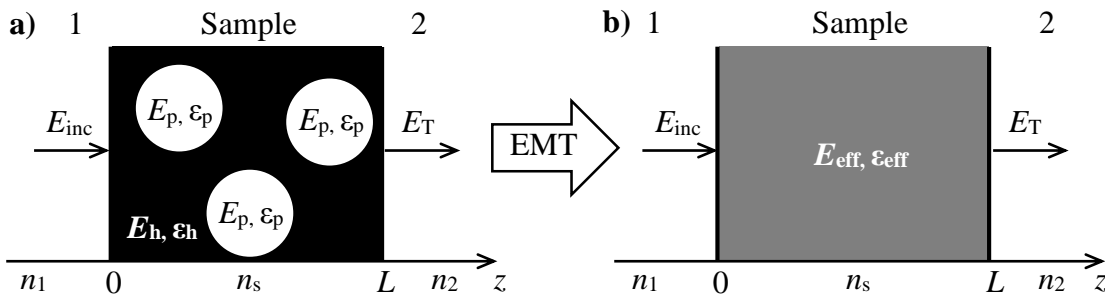


Fig. 3.1. The scheme of electric fields and permittivities in an inhomogeneous sample. The incident electric field  $E_{\text{inc}}$  creates a complex distribution of electric fields across the structure (a). It is necessary to distinguish the mean electric field  $E_p$  inside the photoconductive parts and the mean electric field inside the matrix  $E_h$ . Using an appropriate effective medium theory (EMT), this spatial distribution is replaced with a single effective field  $E_{\text{eff}}$  and the structure is treated as a homogeneous material with effective permittivity  $\epsilon_{\text{eff}}$  (b).  $E_T$  is the field transmitted through the sample in equilibrium,  $\epsilon_p$  and  $\epsilon_h$  are the permittivities of the inclusions and the matrix, respectively.

### 3.1 Linear effective medium theories

#### 3.1.1 Bergman spectral representation and VBD model

In this part, we consider general two-component systems of arbitrary morphologies (e.g. any component may or may not be percolated). The effective properties are then the most generally described using the Bergman spectral representation [35]. Within this framework, the effective permittivity of non-photoexcited structure can be written as [36]

$$\varepsilon_{\text{eff}} = V_h \varepsilon_h + V_p \varepsilon_p + \int_0^1 \frac{v(L) \varepsilon_h \varepsilon_p}{(1-L) \varepsilon_p + L \varepsilon_h} dL, \quad (3.1)$$

where  $\varepsilon_p$  and  $\varepsilon_h$  are the permittivities of the constituents,  $V_h$  and  $V_p$  are their percolation strengths in the direction of the probing field,  $v(L)$  is a spectral function and  $L$  is a depolarization factor. The integral in (3.1) represents the contribution of non-percolated clusters. Each such cluster is characterized with a depolarization factor  $L$  and its influence on the effective response is weighted by the spectral function  $v(L)$ .

We now consider that the p-component is formed by a photoconductive material (while the h-component remains insulating). Upon photoexcitation, the permittivity  $\varepsilon_p$  changes to

$$\varepsilon_p \rightarrow \varepsilon_p + i \frac{\Delta \sigma_p}{\varepsilon_0 \omega}, \quad (3.2.1)$$

where  $\Delta \sigma_p$  is the photoconductivity of the p-component. The effective permittivity thus changes to

$$\varepsilon_{\text{eff}} \rightarrow \varepsilon_{\text{eff}} + i \frac{\Delta \sigma_{\text{eff}}}{\varepsilon_0 \omega}, \quad (3.2.2)$$

where  $\Delta \sigma_{\text{eff}}$  is the effective photoconductivity of the entire structure.

For a known structure morphology, we can unambiguously determine the spectral function  $v(L)$  and the percolation strengths  $V_p$  and  $V_h$  using e.g. finite-element numerical calculations [37] (analytic solutions are known only for a few specific systems [38]-[41]). For photoexcited systems, a significant simplification is possible. In Ref. [37], it was shown for a large variety of structures that a single depolarization factor  $L_0$  often dominates in the spectral function, i.e.  $v(L) = v_0 \delta(L - L_0)$ . The effective photoconductivity  $\Delta \sigma_{\text{eff}}$  then reads [37]

$$\Delta \sigma_{\text{eff}} = V \Delta \sigma_p + \frac{B \Delta \sigma_p}{1 + i D \frac{\Delta \sigma_p}{\omega \varepsilon_0}}, \quad (3.3)$$

where we denote  $V = V_p$  and the coefficients  $B$  and  $D$  read

$$B = \frac{v_0 L_0 \varepsilon_h^2}{[(1 - L_0)\varepsilon_p + L_0 \varepsilon_h]^2} \quad (3.4.1)$$

$$D = \frac{1 - L_0}{(1 - L_0)\varepsilon_p + L_0 \varepsilon_h}. \quad (3.4.2)$$

Equation (3.3) constitutes the foundation of the VBD model which describes the effective response of two-component systems with various levels of percolation [37]. Structure morphology is fully represented by three coefficients  $V$ ,  $B$  and  $D$  (which are real constants for non-dispersive real  $\varepsilon_p$  and  $\varepsilon_h$ ). The coefficients  $V$  and  $B$  represent the weights of percolated and non-percolated parts, respectively, and  $D$  is directly linked to the dominant depolarization factor. In non-percolated structures,  $V = 0$ . In percolated systems, however,  $V$  is non-zero and usually is much higher than the  $B$  coefficient (see e.g. Tab. 8.2).

We now briefly discuss the dependence of  $\Delta\sigma_{\text{eff}}$  on the carrier concentration  $N$  (as  $\Delta\sigma_p = Ne_0\mu$  according to (1.3)) in non-percolated systems (i.e.  $V = 0$ ). For low enough  $N$ , the  $D$ -term in the denominator of (3.3) can be neglected (typically,  $D \sim 10^{-2}$  [34],[42]) and thus  $\Delta\sigma_{\text{eff}} \approx B\Delta\sigma_p$ . The effective photoconductivity  $\Delta\sigma_{\text{eff}}$  is then directly proportional to the local photoconductivity  $\Delta\sigma_p$  and the proportionality constant is determined just by the sample morphology. In the limit of high  $N$ , the  $D$ -term becomes dominant and  $\Delta\sigma_{\text{eff}}$  no longer depends on  $\Delta\sigma_p$ . Instead, it becomes purely imaginary and directly proportional to the frequency. In the intermediate regime,  $\Delta\sigma_{\text{eff}}$  depends on  $\Delta\sigma_p$  (and thus on  $N$ ) in a more complicated way. We demonstrate this for  $\Delta\sigma_p$  with resonant behavior in Sections 5.2.2 and 7.2.1 (Fig. 7.5): a plasmonic resonance emerges in  $\Delta\sigma_{\text{eff}}$  and blueshifts with increasing  $N$  [32],[33].

The VBD model describes two-component systems of quite various morphologies where one component is photoconductive. However, the determination of the morphologic parameters  $V$ ,  $B$  and  $D$  requires to employ a time-consuming finite-element calculations [37]. For certain systems, it is then more practical to apply less general effective medium theories. In the following sections, we consider two such approaches – the Maxwell-Garnett theory (Section 3.1.2) and the brick-wall model (Section 3.1.3).

### 3.1.2 Maxwell-Garnett effective medium theory

Maxwell-Garnett effective medium theory [43]-[45] is rather simple but at the same time one of the most used homogenization approaches. It correctly describes systems formed by non-percolated inclusions which are sparsely dispersed in a matrix (i.e. low volume filling factor  $s$  is required). The effective permittivity  $\varepsilon_{\text{eff}}$  of the nanostructure then satisfies

$$\frac{\varepsilon_{\text{eff}} - \varepsilon_h}{\varepsilon_{\text{eff}} + K\varepsilon_h} = s \frac{\varepsilon_p - \varepsilon_h}{\varepsilon_p + K\varepsilon_h}, \quad (3.5)$$

where  $\varepsilon_p$  and  $\varepsilon_h$  are the permittivities of the inclusions and the matrix, respectively,  $K$  is the factor related to the shape of the inclusions ( $K = 2$  for spheres,  $K = 1$  for long cylinders with

axis perpendicular to the electric field) and  $s$  is their volume filling factor. From the above relation, it stems

$$\varepsilon_{\text{eff}} = \varepsilon_h \frac{(1 + sK)\varepsilon_p + K(1 - s)\varepsilon_h}{(1 - s)\varepsilon_p + (s + K)\varepsilon_h}. \quad (3.6)$$

In the photoexcited case (i.e. photoconductivity of inclusions  $\Delta\sigma_p \neq 0$ ), substitution of (3.2) into the above relations yields the effective photoconductivity  $\Delta\sigma_{\text{eff}}$

$$\Delta\sigma_{\text{eff}} = \frac{s(1 + K)^2 \varepsilon_h^2}{[(1 - s)\varepsilon_p + (s + K)\varepsilon_h]} \frac{\Delta\sigma_p}{\left[ (1 - s) \left( \varepsilon_p + i \frac{\Delta\sigma_p}{\omega \varepsilon_0} \right) + (s + K)\varepsilon_h \right]}. \quad (3.7)$$

The above relation is a specific case of the VBD model (3.3) for  $V = 0$ . Indeed, the Maxwell-Garnett theory is a special case of the Bergman spectral representation (spectral function dominated by a single peak at  $L = (1 - s)/3$  for spherical inclusions) [39]. The above relation thus also describes the build-up and blueshift of the plasmonic resonance with increasing  $\Delta\sigma_p$ .

### 3.1.3 Brick-wall model

We consider a geometry from Fig. 3.2(a) where a periodic structure consists of alternating photoconductive (permittivity  $\varepsilon_p$  in the ground state, permittivity  $\varepsilon_p + i\Delta\sigma_p/(\omega\varepsilon_0)$  upon photoexcitation) and nonconductive (permittivity  $\varepsilon_h$ ) blocks with widths  $d_h$  and  $d_p$  ( $d_h, d_p \ll \lambda$ , where  $\lambda$  is the wavelength of the THz field). The incident electric field  $E_{\text{inc}}$  is polarized perpendicularly to the block boundaries. In the quasi-static approximation, we describe the structure by an equivalent electric circuit formed by two capacitors with capacitances  $C_p$  and  $C_h$  connected in series (Fig. 3.2(b)) [46]. These capacitors are linked to the photoconductive and nonconductive blocks. This serial connection can be then replaced with a single capacitor with capacitance  $C$  which satisfies

$$\frac{1}{C} = \frac{1}{C_h} + \frac{1}{C_p}. \quad (3.8)$$

From the above relation, we then straightforwardly find the effective permittivity of the structure (without photoexcitation)

$$\varepsilon_{\text{eff}} = \frac{d_p + d_h}{\frac{d_p}{\varepsilon_p} + \frac{d_h}{\varepsilon_h}}. \quad (3.9)$$

In the photoexcited case ( $\Delta\sigma_p \neq 0$ ), the above relation remains valid if we apply the substitutions (3.2). The effective photoconductivity of the entire structure then reads

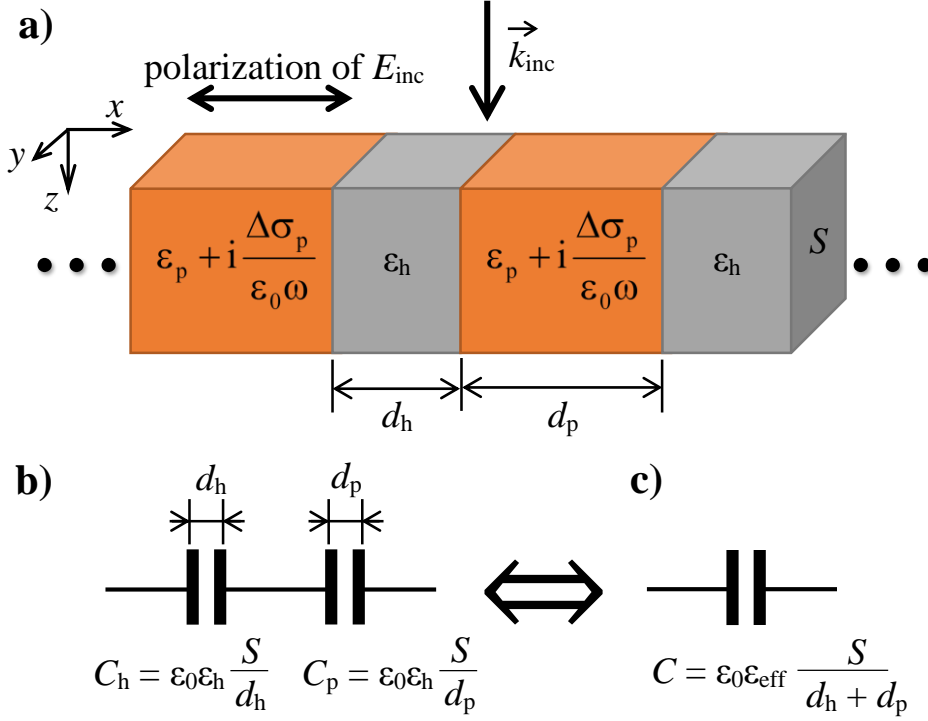


Fig. 3.2. Scheme of the geometry considered for the brick-wall model of effective medium (a). The sample is formed by periodically alternating photoconducting (orange; photoconductivity  $\Delta\sigma_p$ ) and nonconductive (gray) blocks with equilibrium permittivities  $\epsilon_p$  and  $\epsilon_h$ , respectively. The incident electric field  $E_{inc}$  is linearly polarized in the  $x$ -direction. In the considered geometry, the structure is equivalent to an electric circuit consisting of two capacitors (with capacitances  $C_p$  and  $C_h$ ) connected in series (b). The connected capacitors can be then replaced a single capacitor with capacitance  $C$  which is linked to the effective response of the structure (c).

$$\Delta\sigma_{eff} = \frac{(d_p + d_h)d_p\epsilon_h^2}{[d_h\epsilon_p + d_p\epsilon_h]} \left[ \frac{\Delta\sigma_p}{d_h \left( \epsilon_p + i \frac{\Delta\sigma_p}{\omega\epsilon_0} \right) + d_p\epsilon_h} \right]. \quad (3.10)$$

Comparison with (3.3) reveals that the above brick-wall model is also described within the VBD framework (for  $V = 0$ ) from Section 3.1.1. Therefore, similar qualitative behavior is expected (e.g. the build-up and blueshift of the plasmonic resonance with increasing  $\Delta\sigma_p$ ). If we introduce the filling factor of the photoconductive material  $s = d_p/(d_p + d_h)$ , we can rewrite (3.10) as

$$\Delta\sigma_{eff} = \frac{s\epsilon_h^2}{[(1-s)\epsilon_p + s\epsilon_h]} \left[ \frac{\Delta\sigma_p}{(1-s) \left( \epsilon_p + i \frac{\Delta\sigma_p}{\omega\epsilon_0} \right) + s\epsilon_h} \right], \quad (3.11)$$



which is formally equivalent to the formula (3.7) for  $K = 0$ . For this reason, we will further formally describe the brick-wall model within the Maxwell-Garnett effective medium approach (for shape factor  $K = 0$  and arbitrary filling factor  $s$ ).

### 3.1.4 Distribution of local electric fields in inhomogeneous structures

Here, we discuss the distribution of electric fields in inhomogeneous structures. While this is not required for the analysis of the linear THz photoconductivity of nanostructures, we will use it later to describe the nonlinear systems (Section 4) where the response is field-dependent. For the sake of simplicity, we focus just on two-component systems with geometries described within the Maxwell-Garnett effective medium theory or the brick-wall model.

In the first step, we discuss the distribution of electric fields in the sample in equilibrium. Here, it is necessary to distinguish the electric field  $E_h$  in the insulating matrix and the electric field  $E_p$  inside the photoconductive parts (Fig. 3.1(a)). In the effective medium theory, we replace this spatial distribution with a single effective field  $E_{\text{eff}}$  which is a volume average of the local electric field (Fig. 3.1(b)). In the linear case,  $E_p$  is directly proportional to  $E_{\text{eff}}$

$$E_p(\omega) = Q E_{\text{eff}}(\omega), \quad (3.12)$$

where we introduced the proportionality term  $Q$  called the equilibrium field-enhancement factor. For Maxwell-Garnett theory,  $Q$  reads

$$Q = \frac{(1+K)\epsilon_h}{(1-s)\epsilon_p + (s+K)\epsilon_h}. \quad (3.13)$$

For  $K = 0$ , the above relation yields the field-enhancement factor for the brick-wall model (as we discussed in Section 3.1.3).

In the photoexcited case, the local field  $E_p$  remains directly proportional to the effective field  $E_{\text{eff}}$  according to (3.12) but the proportionality term changes to  $Q_{\text{exc}}$ . Substitution of (3.2.1) into the field enhancement factor  $Q$  (3.13) then yields

$$Q_{\text{exc}} = \frac{(1+K)\epsilon_h}{(1-s)\left(\epsilon_p + i \frac{\Delta\sigma_p}{\epsilon_0\omega}\right) + (s+K)\epsilon_h} \quad (3.14)$$

In terms of the field-enhancement factors (3.13) and (3.14), we can rewrite the effective photoconductivity  $\Delta\sigma_{\text{eff}}$  as

$$\Delta\sigma_{\text{eff}} = s Q Q_{\text{exc}} \Delta\sigma_p. \quad (3.15)$$

### 3.2 Solution of the wave equation in inhomogeneous photoexcited media

In this part, we describe propagation of THz electric fields through a heterogeneous sample with effective response described by the VBD model (3.3) (which comprises also the Maxwell-Garnett theory and the brick-wall model). Since raw experimental results directly reflect just the effective response, our aim is to find the relations which provide link with the microscopic properties (i.e. local photoconductivity  $\Delta\sigma_p$  and morphology). Our description is motivated by the optical pump-THz probe experiments which allow to measure low differential signal between the photoexcited and the equilibrium states of the sample. These experiments offer higher sensitivity than the steady-state measurements [47]. We assume, that there are no free charges in the equilibrium state which is satisfied for most undoped semiconductors. In such case, the carriers are generated solely by the photoexcitation. Here, we focus just on the linear response and summarize the thorough analysis from Ref. [34]. In appendix A, we provide description for a sample with non-zero conductivity in the equilibrium state. In Section 4, we then generalize some of these results to the case of weak nonlinearities.

We consider the waves irradiating and leaving a parallel-plane slab (Fig. 3.3). With respect to the optical pump-THz probe experiments, we decompose the THz electric field in the sample as

$$E = E_s + \Delta E, \quad (3.16)$$

where  $E_s$  is the field propagating through the sample in the equilibrium and  $\Delta E$  is the transient field induced in the photoexcited sample. The incident wave  $E_{\text{inc}}$  produces interferences inside the slab; the equilibrium field  $E_s$  can be then written as a superposition of forward- and back-propagating waves

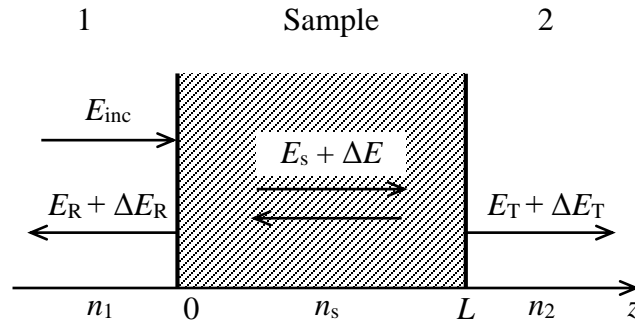


Fig. 3.3. The scheme of the electric fields a photoexcited sample.  $E_{\text{inc}}$  is the incident electric field while  $E_R$ ,  $E_T$  and  $E_s$  are reflected from, transmitted through and in the sample in equilibrium state (i.e. without photoexcitation).  $E_{\text{inc}}$  and  $E_s$  are linked by the Fresnel coefficient  $t_1$  (3.19).  $\Delta E$  is the transient field in the photoexcited sample.  $\Delta E_R$  and  $\Delta E_T$  are the transient fields leaving the sample input and output surface, respectively. All electric fields are linearly polarized.

$$E_s(z) = E_{\text{inc}} t_1 a [\exp(ikz) + r_2 \exp(-ik(z - 2L))], \quad (3.17)$$

where  $k = k_{\text{vac}} n_s$  is the wave vector in the sample ( $k_{\text{vac}}$  is the wave vector in the vacuum),  $z$  is the spatial coordinate perpendicular to the sample surface,  $L$  is the sample thickness and the coefficient  $a$  (which describes multiple internal reflections of the THz wave in the sample) reads

$$a = [1 - r_1 r_2 \exp(2ikL)]^{-1}. \quad (3.18)$$

The coefficients  $r_j$  and  $t_j$  in the above equations are the reflection and transmission Fresnel coefficients at the input ( $j=1$ ) and output ( $j=2$ ) sample surfaces

$$\begin{aligned} r_1 &= \frac{n_s - n_1}{n_s + n_1} & t_1 &= \frac{2n_1}{n_s + n_1} \\ r_2 &= \frac{n_s - n_2}{n_s + n_2} & t_2 &= \frac{2n_s}{n_s + n_2} \end{aligned}, \quad (3.19)$$

where  $n_j$  are the refractive indexes of superstrate ( $j=1$ ) or substrate ( $j=2$ ) and  $n_s$  is the refractive index of the sample.

The transient field  $\Delta E$  obeys a wave equation

$$\frac{d^2 \Delta E(z)}{dz^2} + k^2 \Delta E(z) = -ik_{\text{vac}} Z_0 \underbrace{\Delta \sigma_{\text{eff}}(\omega, z) E(z)}_{j(z)}, \quad (3.20)$$

where  $k_{\text{vac}}$  is the wave vector in the vacuum,  $Z_0$  is the vacuum impedance,  $\Delta \sigma_{\text{eff}}(\omega, z)$  is the effective photoconductivity and  $j(z)$  is the photo-induced electric current density. In the limit of small signal (i.e.  $\Delta E \ll E_s$ , which is usually satisfied in experiments with nanostructures),  $E \approx E_s$  and (3.20) thus becomes linear differential equation with constant coefficients and a right-hand side term. Its general solution then can be written as

$$\Delta E(z) = \gamma \exp(ikz) + \delta \exp(-ikz) + G(z), \quad (3.21)$$

where  $\gamma$  and  $\delta$  are the coefficients of the solution of homogeneous equation and  $G(z)$  is a particular solution of (3.20). The corresponding magnetic field then stems from Maxwell's equations and reads

$$\Delta H = \frac{i}{\mu_0 \omega} \frac{d \Delta E(z)}{dz}. \quad (3.22)$$

We now wish to find the equilibrium  $E_T$  and transient  $\Delta E_T$  fields which leave the output sample surface and are thus detectable in experiments (Fig. 3.3). Using the Fresnel coefficients (3.19) and summing up the interferences, we find

$$E_T(\omega) = t_1 t_2 a \exp(ikL) E_{\text{inc}}. \quad (3.23)$$

Regarding the transient field  $\Delta E_T$ , we have to consider the appropriate boundary conditions – i.e. the continuity of transient electric  $\Delta E$  and magnetic fields  $\Delta H$  on sample surfaces. These conditions then yield the following set of equations [48]

$$\begin{aligned} \underline{z} = 0: & \quad \Delta E(0) = \Delta E_R \\ \underline{z} = L: & \quad \Delta E(L) = \Delta E_T \\ i \frac{d\Delta E(z)}{dz} \Big|_{z=0} &= -k_{\text{vac}} n_1 \Delta E_R \quad i \frac{d\Delta E(z)}{dz} \Big|_{z=L} = -k_{\text{vac}} n_1 \Delta E_T, \end{aligned} \quad (3.24)$$

where  $\Delta E_R$  is the field leaving the input sample surface (this field would be measured in experiments utilizing a reflection geometry). Solution of the above set of equations for a given depth-profile of conductivity then gives the sought transient field  $\Delta E_T$ .

In the experiments, we have to consider also the wave propagation behind the sample and the detector response which distort the measured signal. In the frequency-domain, the detected signals thus read [49]

$$S_T(\omega) = \mathcal{D}(\omega) \mathcal{P}(\omega) E_T(\omega) \quad \Delta S_T(\omega) = \mathcal{D}(\omega) \mathcal{P}(\omega) \Delta E_T(\omega), \quad (3.25)$$

where  $\mathcal{P}(\omega)$  is the response functions describing the propagation behind the sample (i.e. in the free space or through the focusing optics [50], [51]) and  $\mathcal{D}(\omega)$  describes the detector response [52], [53] (Fig. 4.2). The most common output of optical pump-THz probe experiments is the transient transmission  $\Delta T/T$  which is the ratio of measured transient  $\Delta S_T$  and equilibrium  $S_T$  signal

$$\frac{\Delta T}{T} = \frac{\Delta S_T(\omega)}{S_T(\omega)} = \frac{\Delta E_T(\omega)}{E_T(\omega)}. \quad (3.26)$$

It is the characteristics of the linear response that this approach eliminates the influence of instrumental functions and  $\Delta T/T$  thus directly describes the sample properties [49]. In Ref. [34], a normalized transient transmission  $\Delta T_{\text{norm}}$  was defined

$$\Delta T_{\text{norm}}(\omega) = -\frac{(n_1 + n_2)}{Z_0} \frac{1}{e_0 \phi} \frac{\Delta E_T(\omega)}{E_T(\omega)}, \quad (3.27)$$

where  $\phi$  is the photoexcitation fluence (in photons per unit area). In a bulk material,  $\Delta T_{\text{norm}}$  is equal to the quantum yield-mobility product [34],[37]

$$\Delta T_{\text{norm}}(\omega) = \xi \mu(\omega), \quad (3.28)$$

where the quantum yield of mobile carriers  $\xi$  captures that not all photoexcited carriers necessarily contribute to the conductivity [42],[54].

In inhomogeneous systems,  $\Delta \sigma_{\text{eff}}$  follows the VBD model (3.3) where the local photoconductivity  $\Delta \sigma_p(\omega, z)$  is directly proportional to the concentration  $N(z)$  of mobile carriers in the photoexcited parts and to their mobility  $\mu(\omega)$  according to (1.3). For linear absorption, the depth profile of  $N$  follows the Lambert-Beer's law  $N(z) = \phi \alpha_p \exp(-\alpha_{\text{eff}} z)$ . Because of the

sample inhomogeneity, we have to carefully distinguish between the local absorption coefficient  $\alpha_p$  (which describes absorption just in the photoconductive material) and the effective absorption coefficient  $\alpha_{\text{eff}}$  (which describes the pump attenuation in the nanostructured sample and we can find using suitable effective medium theory). The depth profile of local photoconductivity  $\Delta\sigma_p(\omega, z)$  thus reads

$$\Delta\sigma_p(\omega, z) = \Delta\sigma_p(\omega) \exp(-\alpha_{\text{eff}} z) = \phi \alpha_p e_0 \xi \mu(\omega) \exp(-\alpha_{\text{eff}} z), \quad (3.29)$$

where  $\Delta\sigma_p(\omega)$  is the local photoconductivity close to the sample surface. We note that we neglect a possible dependence of the charge mobility  $\mu(\omega)$  on  $N$  (which may appear e.g. due to interactions between carriers for higher  $N$  [55]).

For  $\Delta\sigma_{\text{eff}}$  following the VBD model (3.3), the source term in the wave equation (3.20) consists of two additive terms which separately describe the contributions from the percolated and non-percolated parts. The linearity of the wave equation (3.20) then allows us to treat both terms separately. A detailed solution for the percolated case  $\Delta T_{\text{norm}}^P$  (i.e. the source term consisting just of the  $V$ -term from (3.3)) is described in [48]. The solution for non-percolated case  $\Delta T_{\text{norm}}^N$  (i.e. only the  $B$ -term is considered in (3.3)) was discussed in [56]. Here, we provide just a summary of these results from Ref. [34]. If a structure consists of both the percolated and non-percolated parts, the resulting solution is then  $\Delta T_{\text{norm}} = \Delta T_{\text{norm}}^P + \Delta T_{\text{norm}}^N$ .

### 3.2.1 Percolated term

Substitution of the  $V$ -term from (3.3) into the wave equation (3.20) in the small signal limit transforms the wave equation into

$$\frac{d^2 \Delta E(z)}{dz^2} + k^2 \Delta E(z) = -ik_{\text{vac}} Z_0 V \Delta\sigma_p \exp(-\alpha_{\text{eff}} z) E_s(z), \quad (3.30)$$

where  $E_s(z)$  is given by (3.17). The solution of the above equation with boundary conditions from Fig. 3.3 then leads to the following expression for  $\Delta T_{\text{norm}}^P$  [34]

$$\begin{aligned} \Delta T_{\text{norm}}^P = & \frac{n_1 + n_2}{2n_s} aV \frac{\alpha_p}{\alpha_{\text{eff}}} \xi \mu \times \left[ (1 + r_1 r_2 \exp(2ikL))(1 - \exp(-\alpha_{\text{eff}} L)) + \right. \\ & \left. + r_1 \frac{1 - \exp(2ikL) \exp(-\alpha_{\text{eff}} L)}{1 - 2ik/\alpha_{\text{eff}}} + r_2 \frac{\exp(2ikL) - \exp(-\alpha_{\text{eff}} L)}{1 + 2ik/\alpha_{\text{eff}}} \right]. \end{aligned} \quad (3.31)$$

$\Delta T_{\text{norm}}^P$  thus does not depend on the photoexcitation fluence  $\phi$  (i.e. on the concentration of photoexcited mobile carriers) in systems with percolation.

We now examine the simplifications of (3.31) which can be applied for real samples [34]. In practice, usually  $k \ll \alpha_{\text{eff}}$  (i.e. optical absorption occurs on a shorter length scale than the THz wavelength). Otherwise, there would be almost no absorption in a sample with realistic thickness and thus no measurable signal due to photoexcitation. In the limit of a thin sample (i.e.  $kL \ll 1$ )  $\exp(ikL) \rightarrow 1$  and (3.31) thus simplifies to

$$\Delta T_{\text{nom}}^{\text{P}} = V \frac{\alpha_{\text{p}}}{\alpha_{\text{eff}}} \xi \mu [1 - \exp(-\alpha_{\text{eff}} L)]. \quad (3.32)$$

In the case of strong optical absorption ( $\alpha_{\text{eff}} L \gg 1$ ), the entire excitation power is absorbed in the sample ( $\exp(-\alpha_{\text{eff}} L) \rightarrow 0$ ) and thus

$$\Delta T_{\text{nom}}^{\text{P}} = V \frac{\alpha_{\text{p}}}{\alpha_{\text{eff}}} \xi \mu. \quad (3.33)$$

For a weakly absorbing sample ( $\alpha_{\text{eff}} L \ll 1$ ), the Taylor expansion leads to

$$\Delta T_{\text{nom}}^{\text{P}} = V L \alpha_{\text{p}} \xi \mu. \quad (3.34)$$

For thick enough samples ( $kL \gg 1$ ), there is no temporal overlap between the pulse directly passing through the sample and the echoes originating from multiple internal reflections. In such case, we apply the so-called temporal windowing – we consider just the directly transmitted pulse in the data analysis and discard the signal due to echoes [58]. In the discussed theory, this means to neglect all terms containing the propagator  $\exp(2ikL)$  representing internal reflections in the sample.  $\Delta T_{\text{nom}}^{\text{P}}$  given by (3.31) then simplifies to

$$\Delta T_{\text{nom}}^{\text{P}} = \frac{n_1 + n_2}{2n_{\text{s}}} V \frac{\alpha_{\text{p}}}{\alpha_{\text{eff}}} \xi \mu \times \left[ 1 - \exp(-\alpha_{\text{eff}} L) + \frac{r_1}{1 - 2ik/\alpha_{\text{eff}}} - \frac{r_2 \exp(-\alpha_{\text{eff}} L)}{1 + 2ik/\alpha_{\text{eff}}} \right]. \quad (3.35)$$

For weak optical absorption ( $\alpha_{\text{eff}} \ll k$ ), the above equation further simplifies to

$$\Delta T_{\text{nom}}^{\text{P}} = \frac{n_1 + n_2}{2n_{\text{s}}} V \frac{\alpha_{\text{p}}}{\alpha_{\text{eff}}} \xi \mu \times [1 - \exp(-\alpha_{\text{eff}} L)]. \quad (3.36)$$

In the case of strong absorption ( $\alpha_{\text{eff}} \gg k$ ), the simplified relation reads

$$\Delta T_{\text{nom}}^{\text{P}} = \frac{n_1 + n_2}{2n_{\text{s}}} V \frac{\alpha_{\text{p}}}{\alpha_{\text{eff}}} \xi \mu. \quad (3.37)$$

For percolated structures, the normalized transient transmission  $\Delta T_{\text{nom}}^{\text{P}}$  is thus always directly proportional to the mobility of carriers  $\mu(\omega)$ . In the limits of strong and weak absorption, the proportionality factor is rather simple as it depends only on the disperion of the refractive indices. Outside these limits, the measured spectrum is strongly modulated by a complicated envelope function which contains information e.g. on the Fabry-Pérot interferences inside a thick enough sample (the  $\alpha$ -term and the term in the square brackets in (3.31)). In such case, a careful analysis is required to distinguish the corresponding resonances from those of microscopic origin (compare e.g. Fabry-Pérot [42] and excitonic [57] resonances in layers of percolated TiO<sub>2</sub> nanotubes, Section 8.4.2).

### 3.2.2 Non-percolated term

Substitution of the  $B$ -term from (3.3) into the wave equation (3.20) in the small signal limit leads to

$$\frac{d^2 \Delta E(z)}{dz^2} + k^2 \Delta E(z) = -ik_{\text{vac}} Z_0 B \frac{\Delta \sigma_p \exp(-\alpha_{\text{eff}} z)}{1 + iD \frac{\Delta \sigma_p \exp(-\alpha_{\text{eff}} z)}{\omega \epsilon_0}} E_s(z), \quad (3.38)$$

The above equation was solved analytically in [56] and its solution was found to be in terms of principal value of complex logarithm  $\text{Ln}$  and Gaussian hypergeometric function  ${}_2F_1$  [59] which is a function of four complex arguments. For convenience, we introduce the following notation

$$F(\kappa, Y) = \frac{{}_2F_1(1, \kappa, 1 + \kappa; -Y)}{\kappa}. \quad (3.39)$$

The normalized transient transmission  $\Delta T_{\text{norm}}^N$  can be then written as [34]

$$\begin{aligned} \Delta T_{\text{norm}}^N = & \frac{n_1 + n_2}{2n_s} aB \frac{\alpha_p}{\alpha_{\text{eff}}} \xi \mu \times \left[ (1 + r_1 r_2 \exp(2ikL)) \frac{\text{Ln}(1 + Y_0) - \text{Ln}(1 + Y(L))}{Y_0} + \right. \\ & + r_1 \{ F(1 - 2ik/\alpha_{\text{eff}}, Y_0) - \exp(2ikL) \exp(-\alpha_{\text{eff}} L) F(1 - 2ik/\alpha_{\text{eff}}, Y(L)) \} +, \\ & \left. + r_2 \{ F(1 + 2ik/\alpha_{\text{eff}}, Y_0) \exp(2ikL) - \exp(-\alpha_{\text{eff}} L) F(1 + 2ik/\alpha_{\text{eff}}, Y(L)) \} \right] \end{aligned} \quad (3.40)$$

where

$$Y(z) = Y_0 \exp(-\alpha_{\text{eff}} z) = i \underbrace{\frac{D}{\omega \epsilon_0} e_0 \alpha_p \phi \xi \mu}_{Y_0} \exp(-\alpha_{\text{eff}} z). \quad (3.41)$$

General relation (3.40) simplifies significantly for low photoexcitation fluences  $\phi$ . In the limit  $\phi \rightarrow 0$ ,  $Y_0$  also approaches 0 according to (3.41). In such case, both  $\text{Ln}(1 + Y_0)/Y_0$  and  ${}_2F_1$  are approximately 1 and (3.40) then takes form of the general formula for percolated samples (3.31) (we just replace morphology coefficient  $V$  with  $B$ ). For a weak photoexcitation, the non-percolated samples thus behave in same way as percolated structures – i.e.  $\Delta T_{\text{norm}}$  does not depend on  $\phi$  and is directly proportional to the yield-mobility product  $\xi \mu(\omega)$ . This also provides a recipe to distinguish both cases experimentally as non-percolated structures exhibit very different behavior for stronger photoexcitations.

We now examine the practically important case  $k \ll \alpha_{\text{eff}}$ . If this condition is satisfied, the hypergeometric function (3.39) simplifies considerably

$$F(\kappa \rightarrow 1, Y) \rightarrow \frac{\text{Ln}(1 + Y)}{Y}. \quad (3.42)$$

The normalized transient transmission  $\Delta T_{\text{norm}}^N$  given by (3.40) then reduces to [34]

$$\Delta T_{\text{nom}}^{\text{N}} = \frac{n_1 + n_2}{2n_s} aB \frac{\alpha_p}{\alpha_{\text{eff}}} \xi_{\mu} \times \left[ \frac{\text{Ln}(1 + Y_0)}{Y_0} (1 + r_1)(1 + r_2 \exp(2ikL)) - \frac{\text{Ln}(1 + Y(L))}{Y_0} (1 + r_1 \exp(2ikL))(1 + r_2) \right]. \quad (3.43)$$

In the limit of a thin sample ( $kL \ll 1$ ), the above equation further simplifies to

$$\Delta T_{\text{nom}}^{\text{N}} = B \frac{\alpha_p}{\alpha_{\text{eff}}} \xi_{\mu} \frac{\text{Ln}(1 + Y_0) - \text{Ln}(1 + Y(L))}{Y_0}. \quad (3.44)$$

For strongly absorbing sample ( $\alpha_{\text{eff}}L \gg 1$ ,  $Y(L) \ll 1$ ), we obtain

$$\Delta T_{\text{nom}}^{\text{N}} = B \frac{\alpha_p}{\alpha_{\text{eff}}} \xi_{\mu} \frac{\text{Ln}(1 + Y_0)}{Y_0}. \quad (3.45)$$

In a case of weak absorption ( $kL \ll \alpha_{\text{eff}}L \ll 1$ ),  $\Delta T_{\text{nom}}$  reads

$$\Delta T_{\text{nom}}^{\text{N}} = B \frac{\alpha_p L}{1 + Y_0} \xi_{\mu} = B \frac{L}{1 + i \frac{D}{\omega \epsilon_0} \Delta \sigma_p} \frac{\Delta \sigma_p}{e_0 \phi}. \quad (3.46)$$

In the limit of weak absorption ( $kL \ll \alpha_{\text{eff}}L \ll 1$ ), we later investigate the nonlinear response of semiconductor nanostructures (Sections 4 and 7). For this reason, we now provide also the corresponding relation for the transient transmission  $\Delta T/T$  (which is directly measured in optical pump-THz probe experiments). In a general case,  $\Delta T/T$  is linked to the effective transient sheet conductivity  $\Delta \Sigma_{\text{eff}}$  as [37]

$$\frac{\Delta T}{T} = - \frac{Z_0}{(n_1 + n_2)} \Delta \Sigma_{\text{eff}}, \quad (3.47)$$

where  $\Delta \Sigma_{\text{eff}}$  is generally the integral of effective photoconductivity over the sample thickness

$$\Delta \Sigma_{\text{eff}} = \int_0^L \Delta \sigma_{\text{eff}}(z) dz. \quad (3.48)$$

For the considered weak absorption, we can neglect the depth-profile of  $\Delta \sigma_{\text{eff}}$  and thus

$$\frac{\Delta T}{T} = - \frac{Z_0}{n_1 + n_2} L \Delta \sigma_{\text{eff}}. \quad (3.49)$$

The transient transmission  $\Delta T/T$  is thus directly proportional to the effective photoconductivity  $\Delta \sigma_{\text{eff}}$  of the sample.

We note that (3.49) is valid just in the limit of a small signal. Above this limit, the transient transmission follows the Tinkham formula [114],[115]



$$\frac{\Delta T}{T} = \frac{1}{1 + \frac{Z_0}{n_1 + n_2} \Delta \sigma_{\text{eff}} L} - 1, \quad (3.50)$$

which ensures that the transient signal  $\Delta T$  cannot be larger than the reference  $T$ . It is obvious that for small values of the transient sheet conductivity  $\Delta \sigma_{\text{eff}} L$ , (3.50) yields the same results as (3.49).

## 4. Wave propagation in nonlinear media

In Section 3, we described the linear THz response of two-component semiconductor nanostructures of arbitrary morphology. Namely, we linked the charge mobility in photoconducting constituents with transient transmission measurable in optical pump-THz probe experiments. Here, we generalize some of these results to the case of nonlinear THz response: for simplicity, we describe just the limit of a thin weakly absorbing sample. At the local level, we assess the nonlinearities by the non-perturbative MonteCarlo calculations with electric field  $E$  which yield a functional of the mean electric current density  $j[E]$ . The main aim of this section is then to establish the relation between the nonlinear response characterized by  $j[E]$  and the transient fields or transmittances measurable in experiments. As previously, we will assume that there are no free charge carriers in the equilibrium state and they are generated solely by the photoexcitation (this is satisfied for most undoped semiconductors).

We first study the propagation of fields through a thin homogeneous photoconductive film in the presence of the nonlinear electric current density  $j[E]$  (Section 4.1). We namely solve the nonlinear wave equation in the limit of a weak signal and link  $j[E]$  with the signals measurable in experiments. In Section 4.2, we then develop a treatment of two-component inhomogeneous nanostructures exhibiting nonlinear response. This task is more complicated than in the linear case as the nonlinear response is field-dependent and it is thus necessary to carefully consider the distribution of local fields across the nanostructures. In particular, we expand upon the existing nonlinear effective medium theories [60]-[64] to derive a relation between the effective and local nonlinear photoconductivities (we consider only simple geometries which can be described by the Maxwell-Garnett theory or by the brick-wall model). Synthesis of these results with the solution of the nonlinear wave equation from Section 4.1 then allows us to provide formulae linking the local nonlinear photoconductivities with transient signals measurable in experiments. Finally, we derive an important general relation between the effective and local nonlinear electric current density (Section 4.3). This allows us to directly link the results of non-perturbative Monte-Carlo calculations with transient fields measurable in experiments which is of fundamental importance for our study of nonlinear THz response of semiconductor nanostructures in Section 7.

### 4.1 Homogeneous thin films

We start our investigation with a homogeneous photoconductive slab (Fig. 4.1). The THz electric field  $E$  inside the slab obeys the wave equation

$$\frac{\partial^2 E}{\partial z^2} - \mu_0 \epsilon_0 \epsilon \frac{\partial^2 E}{\partial t^2} = \mu_0 \frac{\partial j}{\partial t}, \quad (4.1)$$

where  $z$  is the spatial coordinate perpendicular to the slab surface,  $\epsilon$  is the linear permittivity of the slab without photoexcitation,  $\epsilon_0$  and  $\mu_0$  are the permittivity and the permeability of the vacuum, respectively, and  $j$  is the electric current density of free charges and has both linear and nonlinear contributions. It is generally a functional of the electric field ( $j[E]$ ). As in Section 3 (Eq. (3.16)), we express the THz electric field inside the slab as

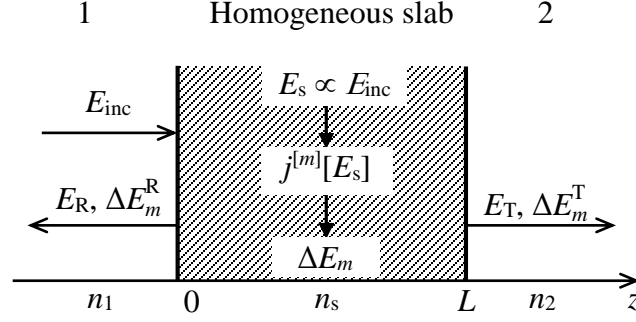


Fig. 4.1. The scheme of the fields and currents in a photoexcited homogeneous slab. The THz electric field  $E_s$  propagating through the slab in the equilibrium gives rise to the harmonic electric currents  $j^{[m]}[E_s]$  in the photoexcited sample. These currents generate transient nonlinear electric fields  $\Delta E_m$ , which then transform into transient fields  $\Delta E_m^R$  and  $\Delta E_m^T$  surging at sample surfaces and radiating into surrounding media 1 and 2, respectively.  $E_{\text{inc}}$  is the incident electric field, which transforms into the field  $E_s$  inside the slab.  $E_R$  and  $E_T$  are the fields reflected from and transmitted through the sample in the equilibrium, respectively. All electric fields are linearly polarized.

$$E = E_s + \Delta E, \quad (4.2)$$

where  $E_s$  is the field propagating through the slab in the equilibrium, and  $\Delta E$  is the transient field induced in the photoexcited slab. These fields give rise to electric current density  $j_{\text{exc}}[E_s + \Delta E]$  in the photoexcited slab. The wave equations for the field propagating in a non-excited sample and for the transient field thus take the form

$$\frac{\partial^2 E_s}{\partial z^2} - \mu_0 \epsilon_0 \epsilon \frac{\partial^2 E_s}{\partial t^2} = 0 \quad (4.3.1)$$

$$\frac{\partial^2 \Delta E}{\partial z^2} - \mu_0 \epsilon_0 \epsilon \frac{\partial^2 \Delta E}{\partial t^2} = \mu_0 \frac{\partial j_{\text{exc}}[E_s + \Delta E]}{\partial t}. \quad (4.3.2)$$

Here, we focus on the limit of weak signals ( $\Delta E \ll E_s$ ), which can be easily satisfied in the experiments by using a weak photoexcitation. In this limit, we can consider that the transient field is too weak to affect the nonlinearities, i.e.  $j_{\text{exc}}[E_s + \Delta E] = j_{\text{exc}}[E_s]$ . This assumption neglects the depletion of the transient field due to the frequency mixing. The absorption of the fields in the sample remains encoded in the imaginary part of the refractive index.

The limit of the weak nonlinear signal linearizes (4.3.2) and for a monochromatic field  $E_s(t) = E_{s,0} \cos(\omega_0 t)$ , it is possible to split the right-hand side into separate harmonic components

$$j_{\text{exc}}[E_s] = \text{Re} \left\{ \sum_{m=1}^{\infty} j^{[m]}(E_s) e^{im\omega_0 t} \right\}. \quad (4.4)$$

The harmonic current densities  $j^{[m]}(E_s)$  give rise to transient fields  $\Delta E_m$ , which oscillate at harmonic frequencies  $m\omega_0$ . The net transient electric field in the slab is then a superposition of all harmonic orders

$$\Delta E = \sum_{m=1}^{\infty} \Delta E_m(m\omega_0). \quad (4.5)$$

Since we neglect the depletion of the electric field  $E_s$  due to the frequency mixing, the following set of independent wave equations for individual harmonic orders stems directly from (4.3.2)

$$\frac{d^2 \Delta E_m}{dz^2} + k_m^2 \Delta E_m = -imk_{\text{vac}} Z_0 j^{[m]}(E_s), \quad (4.6)$$

where  $k_m = mk_{\text{vac}}n(m\omega_0)$  are the wave vectors of transient fields in the slab and  $Z_0$  is the vacuum impedance. Equations (4.6) describe the propagation of transient electric fields  $\Delta E_m$  generated by the harmonic currents  $j^{[m]}(E_s)$  – this is represented by the source terms on their right-hand sides. For  $m = 1$ , this equation describes the linear response (3.20), which is solved in Section 3.2. Here, we develop the solution for transient fields oscillating at higher harmonic frequencies.

The harmonic transient fields inside the sample can be simply expressed as

$$\Delta E_m(z) = \gamma_m \exp(ik_m z) + \delta_m \exp(-ik_m z) - im \underbrace{\frac{k_{\text{vac}}}{k_m^2} Z_0 j^{[m]}(E_s)}_{S_m}, \quad (4.7)$$

$$\Delta H_m = \frac{i}{\mu_0 m \omega_0} \frac{\partial \Delta E_m(z)}{\partial z}. \quad (4.8)$$

where  $\gamma_m$  and  $\delta_m$  are the coefficients of the solution of homogeneous equation and the term  $S_m$  is a particular solution of the equation (4.6). The first and second term of (4.7) represent the waves propagating through the sample forwards and backwards, respectively. The transient electric fields  $\Delta E_m^R$  and  $\Delta E_m^T$  leaving the rear and front sample surfaces, respectively, can be found by applying the appropriate boundary conditions – the continuity of transient electric  $\Delta E_m$  and magnetic  $\Delta H_m$  fields must be satisfied on the sample surfaces. There are no waves coming towards the sample and thus the amplitudes of the waves transmitted and reflected (in and from a non-magnetic material) given by (4.8) simplify to

$$\Delta H_m^R = -n_1(m\omega_0) \Delta E_m^R \quad \Delta H_m^T = n_2(m\omega_0) \Delta E_m^T, \quad (4.9)$$

where  $n_1$  and  $n_2$  are the refraction indexes of the media 1 and 2 surrounding the sample, respectively, at the frequency of the transient wave  $\Delta E_m$ .

From now on, we will be focusing solely on the thin-film limit ( $L \rightarrow 0$ ). We thus work in the limit  $kL \ll \alpha_{\text{eff}}L \ll 1$  from Section 3.2, where  $\alpha_{\text{eff}}$  is the effective optical absorption

coefficient (introduced in (3.29)). Substitution of (4.7)-(4.9) into the field continuity condition yields the following set of equations

$$\begin{aligned} \underline{z=0}: \quad & \gamma_m + \delta_m + S_m = \Delta E_m^R \\ & n_s(m\omega_0)(\gamma_m - \delta_m) = -n_1(m\omega_0)\Delta E_m^R \\ \underline{z=L}: \quad & \gamma_m + \delta_m + S_m = \Delta E_m^T \\ & n_s(m\omega_0)(\gamma_m - \delta_m) = n_2(m\omega_0)\Delta E_m^T, \end{aligned} \quad (4.10)$$

where  $n_s$  is the THz refraction index of the sample. The solution of (4.10) is

$$\Delta E_m^T(m\omega_0) = \Delta E_m^R(m\omega_0) = -\frac{Z_0}{n_1(m\omega_0) + n_2(m\omega_0)} Lj^{[m]}(E_s) \quad (4.11)$$

This relation forms the basic link between the transient fields  $\Delta E_m^R$  and  $\Delta E_m^T$  leaving the homogeneous slab (and thus in principle accessible in the experiments) and the microscopic nonlinear current densities  $j^{[m]}(E_s)$ , which are determined by the non-perturbative Monte-Carlo calculations.

In the transmission geometry, the direct experimental output in the linear regime is the transient transmission  $\Delta T/T$  (3.26). Here, we introduce analogical quantities  $\Delta E_m^T/E_T$  for homogeneous systems with the described nonlinear behavior. For known incident THz electric field  $E_{\text{inc}}$ , the reflected  $E_R$  and transmitted  $E_T$  fields and the field  $E_s$  inside the slab (Fig. 4.1) are found by matching boundary conditions analogous to the ones used above. In the thin-sample limit, we find

$$E_R(\omega_0) = \frac{n_1(\omega_0) - n_2(\omega_0)}{n_1(\omega_0) + n_2(\omega_0)} E_{\text{inc}}(\omega_0) \quad (4.12.1)$$

$$E_s(\omega_0) = \frac{2n_1(\omega_0)}{n_1(\omega_0) + n_2(\omega_0)} E_{\text{inc}}(\omega_0) \quad (4.12.2)$$

$$E_T = \frac{2n_1(\omega_0)}{n_1(\omega_0) + n_2(\omega_0)} E_{\text{inc}}(\omega_0), \quad (4.12.3)$$

i.e. Fresnel equations for an interface between media 1 and 2 (separated by an infinitely thin sample layer). After substituting (1.16) into (4.11) and using (4.12), we get (for the lowest three harmonics)

$$\begin{aligned}
\frac{\Delta E_1^T(\omega_0)}{E_T(\omega_0)} = & -\frac{Z_0}{n_1(\omega_0) + n_2(\omega_0)} L \times \\
& \times \left[ \Delta\sigma^{(1)}(\omega_0) + \frac{3n_1^2(\omega_0)}{[n_1(\omega_0) + n_2(\omega_0)]^2} \Delta\sigma^{(3)}(-\omega_0, \omega_0, \omega_0) E_{\text{inc}}^2(\omega_0) + \right. \\
& + \frac{10n_1^4(\omega_0)}{[n_1(\omega_0) + n_2(\omega_0)]^4} \Delta\sigma^{(5)}(-\omega_0, -\omega_0, \omega_0\omega_0, \omega_0) E_{\text{inc}}^4(\omega_0) + \\
& \left. + \dots + \binom{2\beta+1}{\beta} \frac{n_1^{2\beta}(\omega_0)}{[n_1(\omega_0) + n_2(\omega_0)]^{2\beta}} \Delta\sigma^{(2\beta+1)}(\dots) E_{\text{inc}}^{2\beta}(\omega_0) + \dots \right]
\end{aligned} \tag{4.13.1}$$

$$\begin{aligned}
\frac{\Delta E_2^T(2\omega_0)}{E_T(2\omega_0)} = & -\frac{Z_0}{n_1(2\omega_0) + n_2(2\omega_0)} L \left[ \frac{n_1(\omega_0)}{n_1(\omega_0) + n_2(\omega_0)} \Delta\sigma^{(2)}(\omega_0, \omega_0) E_{\text{inc}}(\omega_0) + \right. \\
& + \frac{4n_1^3(\omega_0)}{[n_1(\omega_0) + n_2(\omega_0)]^3} \Delta\sigma^{(4)}(-\omega_0, \omega_0, \omega_0\omega_0) E_{\text{inc}}^3(\omega_0) + \\
& \left. + \dots + \binom{2\beta}{\beta-1} \frac{n_1^{2\beta-1}(\omega_0)}{[n_1(\omega_0) + n_2(\omega_0)]^{2\beta-1}} \Delta\sigma^{(2\beta)}(\dots) E_{\text{inc}}^{2\beta-1}(\omega_0) + \dots \right]
\end{aligned} \tag{4.13.2}$$

$$\begin{aligned}
\frac{\Delta E_3^T(3\omega_0)}{E_T(3\omega_0)} = & -\frac{Z_0}{n_1(3\omega_0) + n_2(3\omega_0)} L \times \\
& \left[ \frac{n_1^2(\omega_0)}{[n_1(\omega_0) + n_2(\omega_0)]^2} \Delta\sigma^{(3)}(\omega_0, \omega_0, \omega_0) E_{\text{inc}}^2(\omega_0) + \right. \\
& + \frac{5n_1^4(\omega_0)}{[n_1(\omega_0) + n_2(\omega_0)]^4} \Delta\sigma^{(5)}(-\omega_0, \omega_0\omega_0, \omega_0, \omega_0) E_{\text{inc}}^4(\omega_0) + \\
& \left. + \dots + \binom{2\beta+1}{\beta-1} \frac{n_1^{2\beta}(\omega_0)}{[n_1(\omega_0) + n_2(\omega_0)]^{2\beta}} \Delta\sigma^{(2\beta+1)}(\dots) E_{\text{inc}}^{2\beta}(\omega_0) + \dots \right]
\end{aligned} , \tag{4.13.3}$$

where  $\beta$  is a natural number. The above equations are valid for waves just leaving the output surface of the sample.

In experiments, it is necessary to consider also the influence of the beam propagation behind the sample and the detector response, which may distort the measured signal. These are accounted for by the instrumental functions  $\mathcal{P}(\omega)$  and  $\mathcal{D}(\omega)$  introduced in Eq. (3.25). Here, we have to consider a different frequency dependence of the fields  $E_T$  and  $\Delta E_m^T$ . In the frequency-domain, the detected signals  $S_T$  and  $\Delta S_m^T$  thus read (Fig. 4.2) [49]

$$S_T(\omega_0) = \mathcal{D}(\omega_0) \mathcal{P}(\omega_0) E_T(\omega_0) \quad \Delta S_m^T(m\omega_0) = \mathcal{D}(m\omega_0) \mathcal{P}(m\omega_0) E_m^T(m\omega_0). \tag{4.14}$$

In the linear regime, the response functions are evaluated at identical frequencies and the linear transient transmission  $\Delta T/T$  thus directly describes the sample properties. In the nonlinear

regime, the response functions do not have the same frequency argument, therefore their elimination is not entirely possible. The substitution of (4.14) into (4.13) yields

$$\frac{\Delta S_1^T(\omega_0)}{S_T(\omega_0)} = \frac{\Delta E_1^T(\omega_0)}{E_T(\omega_0)} \quad (4.15.1)$$

$$\frac{\Delta S_2^T(2\omega_0)}{S_T(\omega_0)} = \frac{\mathcal{D}(\omega_0)\mathcal{P}(\omega_0)}{\mathcal{D}(2\omega_0)\mathcal{P}(2\omega_0)} \frac{\Delta E_2^T(2\omega_0)}{E_T(\omega_0)} \quad (4.15.2)$$

$$\frac{\Delta S_3^T(3\omega_0)}{S_T(\omega_0)} = \frac{\mathcal{D}(\omega_0)\mathcal{P}(\omega_0)}{\mathcal{D}(3\omega_0)\mathcal{P}(3\omega_0)} \frac{\Delta E_3^T(3\omega_0)}{E_T(\omega_0)}. \quad (4.15.3)$$

Regarding the first-order response,  $\mathcal{P}(\omega)$  and  $\mathcal{D}(\omega)$  are evaluated at the same frequency for both  $S_T$  and  $\Delta S_1^T$ , therefore they cancel out and  $\Delta S_1^T/S_T$  contains information just on the sample properties. For the response of higher orders, however, the appropriate instrumental functions do not cancel each other out due to different frequency dependence and remain present in the form of the fraction  $\mathcal{P}(\omega_0)\mathcal{D}(\omega_0)/\mathcal{P}(m\omega_0)\mathcal{D}(m\omega_0)$ . The corresponding transmission spectra are thus inevitably deformed and contain information not only on the sample properties, but also on the propagation of the transient THz waveform behind the sample and the detector response. We emphasize that relations (4.15) can be applied only when both the fundamental frequency  $\omega_0$  and its higher harmonic frequency  $m\omega_0$  lie within the spectral bandwidth of the used detector. Outside this bandwidth, the detector response function  $\mathcal{D}(\omega)$  decreases sharply to

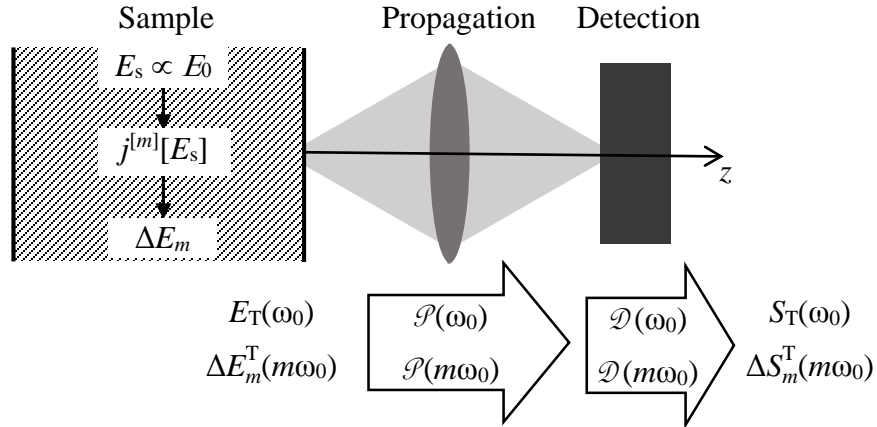


Fig. 4.2. The scheme of detection of the fields transmitted through or emitted from the sample.  $E_T(\omega_0)$  and  $\Delta E_m^T(m\omega_0)$  are the field values at the output sample surface. Beyond the sample, the fields are propagating through the free space and focusing optics which is described by the propagation function  $\mathcal{P}(\omega)$ . The electric field then reaches the detector with a response function  $\mathcal{D}(\omega)$  which causes a further difference between the incident and measured fields. We thus do not detect the field  $E_T(\omega_0)$  and  $\Delta E_m^T(m\omega_0)$  but the signals  $S_T(\omega_0)$  and  $\Delta S_m^T(m\omega_0)$  defined by (4.14).

zero and no signal is detected. We note that (4.15) reduces to the form of (3.49) in the regime of linear response.

Extraction of transport parameters from the nonlinear transmission spectra thus requires the knowledge of instrumental functions  $\mathcal{P}(\omega)$  and  $\mathcal{D}(\omega)$ . For a spatial Gaussian profile of the THz beam and common electro-optic detection, these functions were derived in [50]-[52]. Evaluation of the instrumental response was needed e.g. in [65] where mixing of frequencies occurred.

## 4.2 Heterogeneous thin films – monochromatic electric fields

Relations (4.11) and (4.15) were derived for a homogeneous photoconductive sample and a spatially uniform local electric field  $E_s$ , and thus spatially uniform local electric current density  $j(E_s)$ . Real nanostructures, however, are inherently inhomogeneous with potentially complicated morphologies. The incident electric field  $E_{\text{inc}}$  thus creates a complex spatial distribution of local electric fields inside the nanostructure. The individual photoconductive constituents become electrically polarized and the local electric field  $E$  inside the structure thus becomes spatially inhomogeneous. Since individual photoconductive parts may exhibit different shapes, sizes and surrounding environment, the local electric field  $E$  can be different in distinct structures. While this is not a problem for linear response (Section 3), it constitutes a challenging issue in nonlinear systems where the response is field-dependent. The task may be further complicated by inhomogeneous profile of carrier concentration induced by the photoexcitation and possibly by the transient fields emitted from surrounding photoconductive parts. The effective transient field transmitted through the entire nanostructure is thus expected to be different from the homogeneous one given by (4.11).

This problem can be in principle addressed by a suitable nonlinear effective medium theory. Here, we expand upon the existing theories describing the nonlinear response of inhomogeneous systems [60]-[64]. Since the development of a general approach directly applicable to our case is clearly beyond the scope of this work, we will consider the simplest situation – a two-component system consisting of non-percolated weakly nonlinear inclusions in a matrix with linear behavior. Furthermore, we focus on the geometries which are described by the Maxwell-Garnett effective medium theory or by the brick-wall model (Section 3.1).

First, we recall our discussion (Section 3.1.4) of the spatial distribution of local electric fields in the sample. There, we argued that the local field  $E_p$  in the photoconductive inclusions is directly proportional to the effective electric field  $E_{\text{eff}}$  (3.12). The knowledge of the local field  $E_p$  is then essential as it drives the nonlinear response. For experimental reasons, we wish to link the local field  $E_p$  with the electric field  $E_{\text{inc}}$  incident on the sample. Since the effective electric field  $E_{\text{eff}}$  in the inhomogeneous sample is equivalent to the field  $E_s$  inside the homogeneous slab from the previous section, combining (4.12.2) and (3.12) leads to

$$E_p(\omega_0) = \frac{2n_1(\omega_0)}{n_1(\omega_0) + n_2(\omega_0)} Q(\omega_0) E_{\text{inc}}(\omega_0), \quad (4.16)$$



which constitutes the relation between the fields  $E_{\text{inc}}$  and  $E_p$  inside the inclusions without photoexcitation (the field-enhancement  $Q(\omega_0)$  is given by (3.13)). The above relation remains valid also for the photoexcited sample, if we replace the  $Q(\omega_0)$  with  $Q_{\text{exc}}(\omega_0, \Delta\sigma_p^{(1)})$  given by (3.14)<sup>1</sup>. We emphasize that the argument  $(\omega_0, \Delta\sigma_p^{(1)})$  denotes that the linear photoconductivity  $\Delta\sigma_p^{(1)}$  is a function of frequency  $\omega_0$ , too.

Now, we turn to the effective photoconductivity of the studied system. The first-order effective photoconductivity  $\Delta\sigma_{\text{eff}}^{(1)}(\omega_0)$  (3.15) is described within the framework of the linear theories (Section 3.1). To reflect the notation used in this section, we rewrite (3.15) as

$$\Delta\sigma_{\text{eff}}^{(1)}(\omega_0) = sQ(\omega_0)Q_{\text{exc}}(\omega_0, \Delta\sigma_p^{(1)})\Delta\sigma_p^{(1)}(\omega_0). \quad (4.17)$$

For higher-order transient conductivities, we generalize the results derived in [61]-[63] for nonlinear susceptibility in the limit of a weak nonlinearity. In these works, it was shown that the effective and microscopic nonlinear response are directly proportional to each other and the proportionality constant is given by the local-field correction factor. In our case, the nonlinearity is driven by the field  $E_p$  and the correction factor thus equals the field-enhancement factor (3.14). The condition of the weak nonlinearity means that we neglect the frequency mixing between individual nonlinear orders. Finally, we consider that there is no conductivity without photoexcitation. Under these assumptions, inspection of results from the cited works<sup>2</sup> allows us to provide the sought relation between the effective nonlinear photoconductivity and the nonlinear photoconductivity of inclusions

$$\Delta\sigma_{\text{eff}}^{(\alpha)}(\omega_1, \omega_2, \dots, \omega_\alpha) = sQ_{\text{exc}}\left(\sum_{j=1}^{\alpha} \omega_j, \Delta\sigma_p^{(1)}\right) \prod_{j=1}^{\alpha} Q_{\text{exc}}(\omega_j, \Delta\sigma_p^{(1)}) \Delta\sigma_p^{(\alpha)}(\omega_1, \omega_2, \dots, \omega_\alpha) \quad (4.18)$$

The field-enhancement factors at the fundamental frequencies  $\omega_j$  appear  $\alpha$ -times in (4.18) ( $\alpha \geq 2$  is the order of the nonlinearity, i.e. power of the electric field), while the additional factor at the resulting frequency of the nonlinearity  $\sum_{j=1}^{\alpha} \omega_j$  appears since the material also responds linearly to the field generated by the nonlinearity [61]. In the dilute limit ( $s \ll 1$ ), our results reduce to the ones from [62] and [63].

We now assess the nonlinear transient transmission for the investigated weakly nonlinear system. The equations (4.13) and (4.15) derived for the homogeneous slab remain valid if we replace the slab parameters with the effective parameters of the studied structure. The substitution of (4.18) into (4.15) then yields

---

<sup>1</sup> In Section 3, we denoted the linear photoconductivity by  $\Delta\sigma_p$ . Here, we denote it by  $\Delta\sigma_p^{(1)}$  to emphasize the difference between the linear and the nonlinear response.

<sup>2</sup> This concerns namely the Eq. (5.15) in [61], Eqs. (30) and (33) in [62] and Eqs. (35) and (38) in [63].

$$\begin{aligned}
\frac{\Delta S_1^T(\omega_0)}{S_T(\omega_0)} = & -\frac{Z_0}{n_1(\omega_0) + n_2(\omega_0)} Ls Q_{\text{exc}}(\omega_0, \Delta\sigma_p^{(1)}) \times \left\{ Q(\omega_0) \Delta\sigma_p^{(1)}(\omega_0) + \right. \\
& + \frac{3n_1^2(\omega_0)}{[n_1(\omega_0) + n_2(\omega_0)]^2} Q_{\text{exc}}(\omega_0, \Delta\sigma_p^{(1)}) |Q_{\text{exc}}(\omega_0, \Delta\sigma_p^{(1)})|^2 \Delta\sigma_p^{(3)}(-\omega_0, \omega_0, \omega_0) |E_{\text{inc}}(\omega_0)|^2 + \\
& + \frac{10n_1^4(\omega_0)}{[n_1(\omega_0) + n_2(\omega_0)]^4} Q_{\text{exc}}(\omega_0, \Delta\sigma_p^{(1)}) |Q_{\text{exc}}(\omega_0, \Delta\sigma_p^{(1)})|^4 \Delta\sigma_p^{(5)}(-\omega_0, -\omega_0, \omega_0, \omega_0, \omega_0) |E_{\text{inc}}(\omega_0)|^4 + \\
& \left. + \dots + \binom{2\beta+1}{\beta} \frac{n_1^{2\beta}(\omega_0)}{[n_1(\omega_0) + n_2(\omega_0)]^{2\beta}} Q_{\text{exc}}(\omega_0, \Delta\sigma_p^{(1)}) |Q_{\text{exc}}(\omega_0, \Delta\sigma_p^{(1)})|^{2\beta} \Delta\sigma_p^{(2\beta+1)}(\dots) |E_{\text{inc}}(\omega_0)|^{2\beta} + \dots \right\}
\end{aligned} \tag{4.19.1}$$

$$\begin{aligned}
\frac{\Delta S_2^T(2\omega_0)}{S_T(2\omega_0)} = & -\frac{Z_0}{n_1(2\omega_0) + n_2(2\omega_0)} \frac{\mathcal{D}(\omega_0)\mathcal{P}(\omega_0)}{\mathcal{D}(2\omega_0)\mathcal{P}(2\omega_0)} Ls Q_{\text{exc}}(2\omega_0, \Delta\sigma_p^{(1)}) Q_{\text{exc}}^2(\omega_0, \Delta\sigma_p^{(1)}) \times \\
& \times \left\{ \frac{n_1(\omega_0)}{[n_1(\omega_0) + n_2(\omega_0)]} \Delta\sigma_p^{(2)}(\omega_0, \omega_0) E_{\text{inc}}(\omega_0) + \right. \\
& + \frac{4n_1^3(\omega_0)}{[n_1(\omega_0) + n_2(\omega_0)]^3} |Q_{\text{exc}}(\omega_0, \Delta\sigma_p^{(1)})|^2 \Delta\sigma_p^{(4)}(-\omega_0, \omega_0, \omega_0, \omega_0) E_{\text{inc}}(\omega_0) |E_{\text{inc}}(\omega_0)|^2 + \\
& \left. + \dots + \binom{2\beta}{\beta-1} \frac{n_1^{2\beta-1}(\omega_0)}{[n_1(\omega_0) + n_2(\omega_0)]^{2\beta-1}} |Q_{\text{exc}}(\omega_0, \Delta\sigma_p^{(1)})|^{2\beta-2} \Delta\sigma_p^{(2\beta)}(\dots) E_{\text{inc}}^{\beta-1}(\omega_0) |E_{\text{inc}}(\omega_0)|^\beta + \dots \right\}
\end{aligned} \tag{4.19.2}$$

$$\begin{aligned}
\frac{\Delta S_3^T(3\omega_0)}{S_T(3\omega_0)} = & -\frac{Z_0}{n_1(3\omega_0) + n_2(3\omega_0)} \frac{\mathcal{D}(\omega_0)\mathcal{P}(\omega_0)}{\mathcal{D}(3\omega_0)\mathcal{P}(3\omega_0)} Ls \times \\
& \times Q_{\text{exc}}(3\omega_0, \Delta\sigma_p^{(1)}) Q_{\text{exc}}^3(\omega_0, \Delta\sigma_p^{(1)}) \times \\
& \times \left\{ \frac{n_1^2(\omega_0)}{[n_1(\omega_0) + n_2(\omega_0)]^2} \Delta\sigma_p^{(3)}(\omega_0, \omega_0, \omega_0) E_{\text{inc}}^2(\omega_0) + \right. \\
& + \frac{5n_1^4(\omega_0)}{[n_1(\omega_0) + n_2(\omega_0)]^4} |Q_{\text{exc}}(\omega_0, \Delta\sigma_p^{(1)})|^2 \Delta\sigma_p^{(5)}(-\omega_0, \omega_0, \omega_0, \omega_0, \omega_0) E_{\text{inc}}^2(\omega_0) |E_{\text{inc}}(\omega_0)|^2 + \\
& \left. + \dots + \binom{2\beta+1}{\beta-1} \frac{n_1^{2\beta}(\omega_0)}{[n_1(\omega_0) + n_2(\omega_0)]^{2\beta}} |Q_{\text{exc}}(\omega_0, \Delta\sigma_p^{(1)})|^{2\beta-2} \Delta\sigma_p^{(2\beta+1)}(\dots) E_{\text{inc}}^\beta(\omega_0) |E_{\text{inc}}(\omega_0)|^\beta + \dots \right\}
\end{aligned} \tag{4.19.3}$$

Relations (4.19) constitute the main result of this section. They link the macroscopic signals  $\Delta S_m^T$  and  $S_T$  measured in the experiments with the transient conductivities  $\Delta\sigma_p^{(w)}$  of the photoconductive parts, therefore they enable estimation of the amplitudes of the measured signals. We emphasize, that the above relations were derived in the limit of optically thin

sample with weak photoexcitation (i.e. the limit  $kL \ll \alpha_{\text{eff}}L \ll 1$  from Section 3.2). For the linear response, formulae (4.19) reduce to (3.49).

### 4.3 Heterogeneous thin films – broadband THz pulses

Until now, we have assumed monochromatic electric fields. Here, we expand our theory to broadband THz pulses  $E_{\text{inc}}(\omega)$ . In such case, it is necessary to consider the frequency mixing between individual spectral components of the pulse. The net electric current density inside the photoconductive constituents  $j_p(\omega)$  then consists of the linear contribution  $j_p^{(1)}(\omega)$  and the contribution  $j_p^{\text{NL}}(\omega)$  of all nonlinear processes with the resulting frequency  $\omega$

$$j_p(\omega) = j_p^{(1)}(\omega) + j_p^{\text{NL}}(\omega). \quad (4.20)$$

These two contributions read

$$j_p^{(1)}(\omega) = \Delta\sigma_p^{(1)}(\omega)E_p(\omega). \quad (4.21.1)$$

$$\begin{aligned} j_p^{\text{NL}}(\omega) &= j_p^{(2)}(\omega) + j_p^{(3)}(\omega) + \dots = \\ &= \sum_{\omega_1 + \omega_2 = \omega} \frac{1}{2!} \Delta\sigma_p^{(2)}(\omega_1, \omega_2) E_p(\omega_1) E_p(\omega_2) + \\ &+ \sum_{\omega_1 + \omega_2 + \omega_3 = \omega} \frac{1}{3!} \Delta\sigma_p^{(3)}(\omega_1, \omega_2, \omega_3) E_p(\omega_1) E_p(\omega_2) E_p(\omega_3) + \dots \end{aligned} \quad (4.21.2)$$

where the sums in (4.21.2) take place over all wave mixings yielding frequency  $\omega$  and  $1/(\alpha!)$  is a degeneracy factor. Analogous relations hold also for the effective current densities  $j_{\text{eff}}(\omega)$ ,  $j_{\text{eff}}^{(1)}(\omega)$  and  $j_{\text{eff}}^{\text{NL}}(\omega)$ .

Using (4.17), (4.21.1) and (3.12) the effective linear current density  $j_{\text{eff}}^{(1)}(\omega)$  can be written as

$$j_{\text{eff}}^{(1)}(\omega) = sQ(\omega)j_p^{(1)}(\omega), \quad (4.22)$$

and it is thus proportional to the microscopic linear current density  $j_p^{(1)}(\omega)$ . Regarding the effective nonlinear current density  $j_{\text{eff}}^{\text{NL}}(\omega)$ , we will, for the sake of simplicity, consider the second-order nonlinearities. Higher orders can be treated in an analogous way. From (4.21.2), the effective second-order current density  $j_{\text{eff}}^{(2)}(\omega)$  reads

$$j_{\text{eff}}^{(2)}(\omega) = \sum_{\omega_1 + \omega_2 = \omega} \frac{1}{2} \Delta\sigma_{\text{eff}}^{(2)}(\omega_1, \omega_2) E_{\text{eff}}(\omega_1) E_{\text{eff}}(\omega_2). \quad (4.23)$$

Substitution of (4.18) and (3.12) into the above relation leads to

$$j_{\text{eff}}^{(2)}(\omega) = s \sum_{\omega_1 + \omega_2 = \omega} \left\{ \frac{1}{2} Q_{\text{exc}}(\underbrace{\omega_1 + \omega_2}_{\omega}, \Delta\sigma_p^{(1)}) Q_{\text{exc}}(\omega_1, \Delta\sigma_p^{(1)}) Q_{\text{exc}}(\omega_2, \Delta\sigma_p^{(1)}) \times \right. \\ \left. \times \Delta\sigma_p^{(2)}(\omega_1, \omega_2) \frac{E_p(\omega_1)}{Q_{\text{exc}}(\omega_1, \Delta\sigma_p^{(1)})} \frac{E_p(\omega_2)}{Q_{\text{exc}}(\omega_2, \Delta\sigma_p^{(1)})} \right\} \quad (4.24)$$

Since  $\omega_1 + \omega_2 = \omega$ , we can factor  $Q_{\text{exc}}(\omega_1 + \omega_2, \Delta\sigma_p^{(1)})$  out of the sum and comparison with (4.21.2) yields

$$j_{\text{eff}}^{(2)}(\omega) = s Q_{\text{exc}}(\omega, \Delta\sigma_p^{(1)}) j_p^{(2)}(\omega), \quad (4.25)$$

where  $j_p^{(2)}(\omega)$  is the microscopic second-order current density. Identical relation holds for all other orders. The effective nonlinear current density is then directly proportional to the nonlinear current density in the inclusions

$$j_{\text{eff}}^{\text{NL}}(\omega) = s Q_{\text{exc}}(\omega, \Delta\sigma_p^{(1)}) j_p^{\text{NL}}(\omega). \quad (4.26)$$

The net effective current density  $j_{\text{eff}}$  is then the sum of the linear (first-order) effective current density (4.22) and the nonlinear current density (4.26)

$$j_{\text{eff}}(\omega) = j_{\text{eff}}^{(1)}(\omega) + j_{\text{eff}}^{\text{NL}}(\omega) = s [Q(\omega) j_p^{(1)}(\omega) + Q_{\text{exc}}(\omega, \Delta\sigma_p^{(1)}) j_p^{\text{NL}}(\omega)]. \quad (4.27)$$

This derived relation constitutes a non-trivial result which links the effective electric current density with the linear and non-linear components of electric current density in the photoconductive parts.

We now turn to the discussion of the transient transmission  $\Delta E^T/E_T$ . Since we consider nonlinear processes with the same resulting frequency  $\omega$ , the generalization of (4.11) yields the total transient field  $\Delta E^T(\omega) = \Delta E^{(1)}(\omega) + \Delta E^{\text{NL}}(\omega)$ , where  $\Delta E^{(1)}(\omega)$  is the linear component and  $\Delta E^{\text{NL}}(\omega)$  is the component due to the nonlinearities. These transients are generated by the pertinent current densities and read

$$\Delta E^T(\omega) = \Delta E^{(1)}(\omega) + \Delta E^{\text{NL}}(\omega) = -\frac{Z_0}{n_1(\omega) + n_2(\omega)} L [j_{\text{eff}}^{(1)}(\omega) + j_{\text{eff}}^{\text{NL}}(\omega)] \quad (4.28.1)$$

The above equation is valid for waves just leaving the output surface of the sample.

The pertinent transient transmissions then follow straightforwardly from the above relations by using (4.12) and making substitutions for effective current densities

$$\frac{\Delta E^T(\omega)}{E_T(\omega)} = -\frac{Z_0}{n_1(\omega) + n_2(\omega)} L s Q_{\text{exc}}(\omega) \frac{[Q(\omega) j_p^{(1)}(\omega) + Q_{\text{exc}}(\omega) j_p^{\text{NL}}(\omega)]}{E_p(\omega)} \quad (4.29.1)$$

$$\frac{\Delta E^{(1)}(\omega)}{E_T(\omega)} = -\frac{Z_0}{n_1(\omega) + n_2(\omega)} Ls Q(\omega) Q_{\text{exc}}(\omega, \Delta\sigma_p^{(1)}) \frac{j_p^{(1)}(\omega)}{E_p(\omega)} \quad (4.29.2)$$

$$\frac{\Delta E^{\text{NL}}(\omega)}{E_T(\omega)} = -\frac{Z_0}{n_1(\omega) + n_2(\omega)} Ls Q_{\text{exc}}^2(\omega) \frac{j_p^{\text{NL}}(\omega)}{E_p(\omega)}. \quad (4.29.3)$$

In the above equations, we express the transient transmissions as functions of the electric current density  $j_p(\omega)$  and the electric field  $E_p$  inside the photoconductive constituents. This is convenient for our non-perturbative Monte-Carlo calculations (Section 2.2) where we evaluate  $j_p(\omega)$  as a functional of  $E_p$ . The formulae (4.29) thus allow us to directly transform the calculated spectra into predicted measurable signals. While (4.29.1) describes the signal arising from the net current density  $j_p$ , (4.29.2) and (4.29.3) are the partial signals due to the linear and the nonlinear conductivity, respectively.

For experiments, it is more convenient to link the transient transmission  $\Delta E^T/E_T$  with the response function of a single carrier. For the linear contribution, it stems from the equations (1.2) and (1.3) that the electric current density  $j_p^{(1)}(\omega)$  is proportional to the linear mobility of carriers  $\mu^{(1)}(\omega)$ :  $j_p^{(1)}(\omega) = Ne_0\mu^{(1)}(\omega)E_p(\omega)$ . Regarding the nonlinear contribution, we introduce the net nonlinear mobility  $\mu^{\text{NL}}(\omega)$  in an analogous way:  $j_p^{\text{NL}}(\omega) = Ne_0\mu^{\text{NL}}(\omega)E_p(\omega)$ . We emphasize that while the linear mobility  $\mu^{(1)}(\omega)$  does not depend on the electric field from the definition, the nonlinear mobility  $\mu^{\text{NL}}(\omega)$  is a functional of the driving electric field. Substitution for the electric current densities in (4.29) then yields

$$\begin{aligned} \frac{\Delta E^T(\omega)}{E_T(\omega)} &= \frac{\Delta E^{(1)}(\omega)}{E_T(\omega)} + \frac{\Delta E^{\text{NL}}(\omega)}{E_T(\omega)} = \\ &= -\frac{Z_0}{n_1(\omega) + n_2(\omega)} Ls Q_{\text{exc}}(\omega) Ne_0 [Q(\omega)\mu^{(1)}(\omega) + Q_{\text{exc}}(\omega)\mu^{\text{NL}}(\omega)] \end{aligned} \quad (4.30)$$

For monochromatic fields, we discussed the difference between the fields emitted directly from the sample and the detected fields (4.14). Here, the transient fields  $\Delta E^T(\omega)$  and the reference wave  $E_T(\omega)$  depend on frequency in the same way. The instrumental functions thus cancel each other out and the same relations (4.29) and (4.30) thus hold also for the detected signals  $\Delta S^T(\omega)/S_T(\omega)$ .

The developed theory provides a way to determine theoretically the measurable signal for broadband THz pulse of arbitrary shape. In the first step, we employ the non-perturbative Monte-Carlo calculations which yield the net electric current density  $j_p$  (4.20). Then, if we know the linear conductivity spectrum  $\Delta\sigma_p^{(1)}$ , we can calculate the linear current density  $j_p^{(1)}(\omega)$  using (4.21.1). The nonlinear current density is then easily retrieved as  $j_p^{\text{NL}}(\omega) = j_p(\omega) - j_p^{(1)}(\omega)$ . This allows the calculation of the effective current density  $j_{\text{eff}}$  (4.27) and the related signal  $\Delta E^T/E_T$  (4.29.1).

A significant simplification is achieved in the limit of low photoexcitation (i.e.  $|\Delta\sigma_p^{(1)}| \ll |\epsilon_p \epsilon_0 \omega_0|$  in (3.14)). We can then replace  $Q_{\text{exc}}(\omega, \Delta\sigma_p^{(1)})$  with  $Q(\omega)$  in the effective electric current density  $j_{\text{eff}}(\omega)$  (4.27) which is then directly proportional to the electric current density  $j_p(\omega)$  in the photoconductive parts

$$j_{\text{eff}}(\omega) = sQ(\omega)j_p(\omega). \quad (4.31)$$

The total transient transmission  $\Delta E^T/E_T$  (4.29.1) is then also directly proportional to the local current density  $j_p$

$$\frac{\Delta E^T(\omega)}{E_T(\omega)} = -\frac{Z_0}{n_1(\omega_0) + n_2(\omega_0)} LsQ^2(\omega) \frac{j_p(\omega)}{E_p(\omega)}. \quad (4.32)$$

We now express this result in terms of the response function of a single carrier. In analogy to linear equations (1.2) and (1.3), we thus introduce a generalized mobility of carriers  $\mu_{\text{gen}}(\omega) = j_p(\omega)/[Ne_0E_p(\omega)]$  which is directly proportional to the electric current density<sup>1</sup>. The mobility  $\mu_{\text{gen}}(\omega)$  contains contributions from both the linear and the nonlinear responses and is thus a functional of the driving electric field. The pertinent substitution in (4.32) then yields

$$\frac{\Delta E^T(\omega)}{E_T(\omega)} = -\frac{Z_0}{n_1(\omega_0) + n_2(\omega_0)} LsQ^2(\omega) Ne_0\mu_{\text{gen}}(\omega). \quad (4.33)$$

## 4.4 Conclusions

We analytically solved the nonlinear wave equation for a thin *homogeneous* slab. This allowed us to express the measurable nonlinear transient transmission signal as a function of nonlinear photoconductivities  $\Delta\sigma_p^{(a)}$  (4.15). Unlike in the linear case, new spectral components emerge, therefore the nonlinear transient transmission signals depend on the instrumental response functions describing the propagation of THz waves behind the sample and the detector response.

We further developed a framework for the treatment of *inhomogeneous* nonlinear media. Here, it is important to realize and account for the difference between the electric field incident on the sample and the local fields in the constituents of inhomogeneous structure (4.16). The principal derived relation is then (4.18) which links the nonlinear effective photoconductivity  $\Delta\sigma_{\text{eff}}^{(\alpha)}$  and the local photoconductivities  $\Delta\sigma_p^{(a)}$ . This homogenizes the problem and thus allows us to substitute the effective photoconductivity into the solution for the thin homogeneous slab. As a result, we can express the measurable nonlinear transient transmission directly as a function of the local photoconductivities (4.19).

A major simplification is achieved if we consider the total nonlinear response (i.e. we disregard the decomposition into the nonlinear photoconductivities  $\Delta\sigma^{(a)}$ ): the effective

---

<sup>1</sup> In the general case (4.30), a definition of a single generalized charge mobility  $\mu_{\text{gen}}$  is not straightforward as the depolarization fields influence the linear and the nonlinear responses in a different way.

nonlinear electric current density is then directly proportional to the local one (4.26). Since the nonlinearity can generate new spectral components, we have to distinguish the measurable signals within and above the incident pulse bandwidth. Within the incident pulse bandwidth, we can define nonlinear transient transmission (4.30) which does not depend on the instrumental response behind the sample and detector response functions. Outside the bandwidth of pulses transmitted through an unphotoexcited sample, the main output is the transient wave which is distorted by the instrumental response functions (no reference measurement is possible)<sup>1</sup>. The formulae (4.29) then form a basis for our study of nonlinear response of semiconductor nanostructures in Section 7.

For a quantitative analysis of real experiments, it is essential to determine the shape and the amplitude of the THz electric pulse incident on the structure. We point out, however, that the real pulse shape would be necessarily different from the detected one due to the detector response function  $\mathcal{D}(\omega)$  and possibly also due to the reshaping due to propagation. A careful deconvolution of the detector response measured in the place of a sample would be required to retrieve the real THz electric field [49].

---

<sup>1</sup> In practice, the detector bandwidth would have to be considerably wider than the bandwidth of the THz emitter. For example, emitters based on ZnTe deliver broadband pulses with frequencies from  $\sim 0.1$  THz to  $\sim 2.5$  THz while a GaP electro-optic sensor allows detection of frequencies up to  $\sim 6$  THz [66].

## 5. Linear THz conductivity of confined electron gas

In Section 3, we described how to link the microscopic linear conductivity with the effective response of nanostructured systems and the corresponding measurable quantities. Here, we discuss the fundamental aspects of linear THz conductivity of a confined electron gas. We focus just on the band-like transport (we do not consider other mechanisms such as hopping [67]). The nonlinear THz conductivity of confined charges is covered in Section 6.

In most bulk semiconductors, the linear THz (photo)conductivity  $\sigma$  of conduction-band electrons is well described by the Drude model [5],[68],[69] which assumes a ballistic motion of charges interrupted by scattering events randomizing the carrier velocity

$$\sigma(\omega) = \frac{Ne_0^2\tau_s}{m} \frac{1}{1-i\omega\tau_s} \equiv \frac{\sigma_{dc}}{1-i\omega\tau_s}, \quad (5.1)$$

where  $N$  is the concentration of carriers,  $m$  is the carrier effective mass,  $\tau_s$  is the bulk scattering time and  $\sigma_{dc}$  is the dc conductivity. Examples of Drude spectra are shown in Fig. 5.1. In nanostructured systems (i.e. for confined carriers), however, linear THz conductivity spectra generally differ from the Drude model due to the presence of confining potential. For example, no steady electric current can flow through an isolated object and thus the dc conductivity  $\sigma_{dc} = 0$  which inevitably affects also the rest of THz spectrum. On a semi-classical level, this problem can be generally treated by the Monte-Carlo calculations from Section 2. However, these are often time-consuming and development of simpler models is thus desired.

The linear THz conductivity spectrum of confined non-degenerate electron gas exhibits a single very broad resonance [29],[70]-[82]. We will review theoretical approaches for this well-documented case in Section 5.1. Then, we introduce our model describing the response of confined degenerate electron gas and we show that a series of sharp resonances may emerge in the conductivity spectrum (Section 5.2). We further show that these resonances couple with the plasmon in isolated systems; this coupling is qualitatively different in one-, two- and

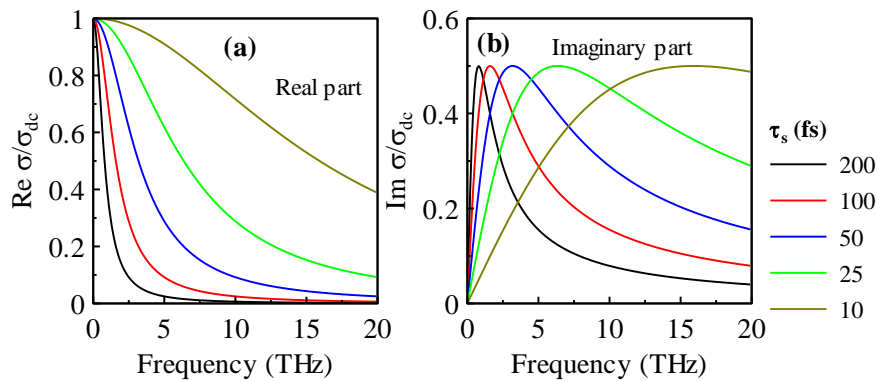


Fig. 5.1. Illustration of the Drude model (5.1) for several values of the scattering time  $\tau_s$ . The real part (a) is positive and exhibits a Drude peak with width  $1/\tau_s$  located at zero frequency. The conductivity decrease reflects the inertia of charges. The imaginary part (b) is positive and peaks at frequency  $1/(2\pi\tau_s)$ .



three-dimensional structures (Section 5.3). Finally, we employ the Monte-Carlo calculations to show that complicated features appear in conductivity spectra of systems with non-trivial shapes (Section 5.4). Our results concerning the degenerate electron gas and the chaotic systems were published in [83] and [84], respectively.

We note, that we represent the results in the form of either the conductivity  $\sigma$  or the charge mobility  $\mu$ . These quantities are linked together by Eq. (1.3). The presented results are also valid for the photoexcited systems (we just replace the conductivity  $\sigma$  with the photoconductivity  $\Delta\sigma$ ).

## 5.1 Non-degenerate electron gas

Majority of experimental works has been realized under conditions for which the confined carriers can be described by Maxwell-Boltzmann statistics (e.g. [5],[42],[70]-[82]). The linear THz conductivity spectrum then exhibits a single broad resonance (Fig. 5.2) with characteristic features in the real and imaginary parts – at low frequencies, the real part is positive and slowly increases while at the same time, the imaginary part is negative and decreases.

In the literature, the considered response is often reproduced in terms of the phenomenological Drude-Smith model [70]

$$\sigma(\omega) = \frac{\sigma_{\text{DS}}}{1 - i\omega\tau_{\text{DS}}} \left( 1 + \frac{c}{1 - i\omega\tau_{\text{DS}}} \right), \quad (5.2)$$

where  $\sigma_{\text{DS}}$  characterizes the conductivity amplitude,  $\tau_{\text{DS}}$  is the Drude-Smith scattering time (which can generally differ from the bulk scattering time  $\tau_s$ ) and  $c$  is a parameter which describes the level of carrier localization within nanostructure. The parameter  $c$  may have any value from the interval  $\langle -1, 0 \rangle$ . For  $c = 0$ , formula (5.2) simplifies into the Drude model (5.1). For  $c = -1$ , the dc conductivity is then fully suppressed. While the Drude-Smith model (5.2) can reproduce linear THz conductivity spectra of a large variety of materials (e.g. [70],[85],[86]), there are several drawbacks. Firstly, this model assumes that the first scattering event is different from the others and thus it does not respect the homogeneity of time (nevertheless, this assumption was supported in [71], where it was argued that in a spherical nanoparticle with dominating charge backscattering at its boundary, the charge velocity is perfectly randomized upon the second and further scattering events). Furthermore, this model is purely phenomenological and the microscopic interpretation of parameters  $\tau_{\text{DS}}$  and  $c$  is not clear (see e.g. a discussion in [27]). Most importantly, Eq. (5.2) does not explicitly depend on the important parameters such as structure dimensions or shape. These parameters are then encoded in an unknown way in the phenomenological parameters  $\tau_{\text{DS}}$  and  $c$ .

In [29] and [72], it was discussed that the low-frequency behavior of the conductivity is caused by a diffusive restoring current of scattered charges. On this basis, a semi-classical modified Drude-Smith formula for completely isolated nanoparticles was derived in [29]

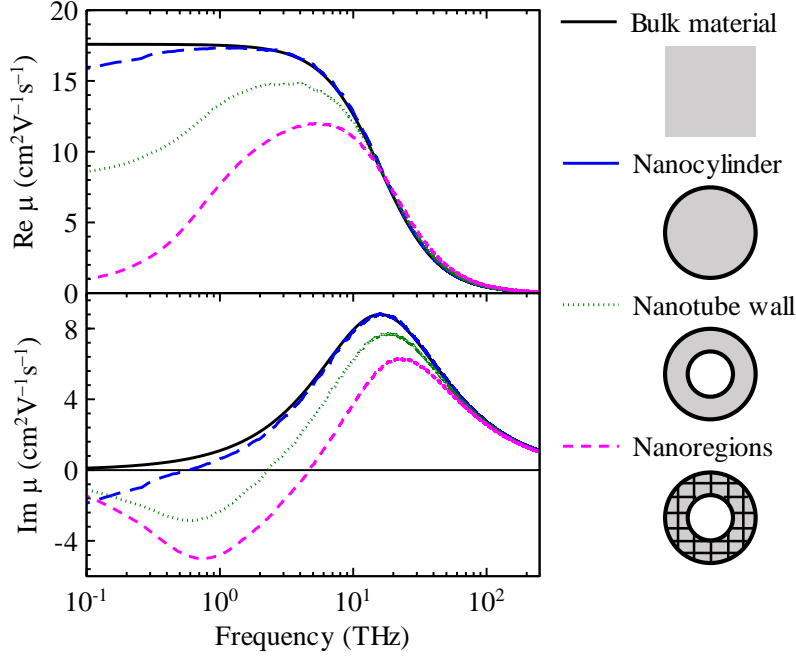


Fig. 5.2. Examples of the charge mobility spectra for various confining structures (outer diameter = 140 nm for all nanostructures, nanotube wall thickness = 10 nm, "Nanoregions" identify nanotube wall divided into cubic regions with dimensions 10 nm (see Section 8.3.1, Fig. 8.5(b)). The mobility spectra clearly deviate from the bulk response for low frequencies: the real parts are positive and increase with the frequency while the imaginary part is initially negative. All the spectra were calculated using the Monte-Carlo method based on Kubo formalism with following parameters:  $\tau_s = 10$  fs,  $m = m_e$ ,  $T = 300$  K.

$$\sigma(\omega) = \frac{Ne_0^2 \tau'}{m} \frac{1}{1 - i\omega \tau'} \left( 1 - \frac{1}{1 - i\omega \tau_{\text{diff}}} \right), \quad (5.3)$$

where  $\tau'$  is the effective scattering time and  $\tau_{\text{diff}}$  is the diffusion time which specifies how long does the carrier need to diffuse across the nanoparticle. These two times read

$$\tau' = \left( \frac{1}{\tau_s} + \frac{2v_{\text{th}}}{l} \right)^{-1} \quad (5.4.1)$$

$$\tau_{\text{diff}} = \frac{l}{12v_{\text{th}}} \left( 2 + \frac{l}{\tau_s v_{\text{th}}} \right), \quad (5.4.2)$$

where  $v_{\text{th}} = \sqrt{k_B T / m}$  is the thermal velocity and  $l$  is the confining length. The "original" Drude-Smith model (5.2) is then a special case of the above equation (for  $\tau_{\text{diff}} = \tau'$ ).

For a thorough understanding of smaller structures, a quantum-mechanical treatment is necessary [72]. In [73], it was shown that the conductivity of a non-degenerate electron gas confined in an infinitely deep rectangular potential well reads

$$\sigma(\omega) = -\frac{8\sqrt{2}ie_0^2 M l}{\pi^3 m v_{th}} \sum_{p \text{ odd}} \frac{\xi_p}{p^3} \left[ 1 - \frac{1}{1 - i\omega/\gamma} \frac{1}{1 - i\omega/p^2 \Gamma_D} \right] \left[ 1 + i\sqrt{\pi} \xi_p \operatorname{erfcx}(-i\xi_p) \right], \quad (5.5)$$

where  $\Gamma_D = D_{\text{diff}} \pi^2 / l^2$  is the diffusion rate and  $\xi_p$  is the dimensionless parameter  $\xi_p = (\omega + i\gamma)t_{th}/p$  (where  $t_{th} = l/\pi\sqrt{2}v_{th}$ ). The complex scaled complementary error function  $\operatorname{erfcx}$  is defined in terms of standard error function  $\operatorname{erf}$  as

$$\operatorname{erfcx} z \approx \exp(z^2)(1 - \operatorname{erf} z), \quad (5.6)$$

The absolute value of the terms under the sum in (5.5) rapidly decreases with increasing  $p$  and often it is sufficient to consider  $p \leq 5$ . If we approximate the complementary error function for large  $|z|$  as

$$1 - \operatorname{erf} z \approx \frac{\exp(-z^2)}{\sqrt{\pi} z} \left( 1 - \frac{1}{2} \frac{1}{z^2 + 1} \right), \quad (5.7)$$

the series in (5.5) can be further summed up and the result has the form of the modified Drude-Smith model (5.3) [2], although with different diffusion time  $\tau_{\text{diff}}$  [73]

$$\tau_{\text{diff}} \approx \frac{l^2}{12D_{\text{diff}}} = \frac{l^2}{12v_{th}^2 \tau_s}. \quad (5.8)$$

## 5.2 Degenerate electron gas confined in infinitely deep rectangular well

Here, we investigate a linear terahertz conductivity of a degenerate electron gas ( $k_B T \ll E_F$ , implying a low temperature or elevated Fermi energy) confined in an infinitely deep rectangular potential well (Fig. 5.3(a)). We consider ballistic (or close to ballistic, i.e. we assume very long bulk scattering time  $\tau_s$ ) motion of non-interacting carriers. In the first part, we treat this problem in both the semi-classical and quantum-mechanical way and we show that a series of geometrical resonances emerges in the mobility spectrum. This also allows us to interpret the response of non-degenerate electron gas as a coalescence of the resonances into a single broad-band. We published these results in [83].

### 5.2.1 Semi-classical calculations

Our theoretical analysis is based on the semi-classical Kubo formula (2.4). We consider very long scattering times  $\tau_s$  (e.g.  $\tau_s = 10$  ps was reported for high-quality GaAs [88]) which favor the role of carrier interaction with well boundaries over bulk scattering. We assume that the carriers reflect from the well boundary elastically and specularly and we thus neglect a possible influence of surface roughness [89].

We start with the one-dimensional (1D) well (Fig. 5.3(a)). Geometrically, this problem is equivalent to carriers bouncing between two straight parallel planes. In the limit  $T \rightarrow 0$  K, the distribution  $(-\partial F/\partial E)$  (see (2.2)) reduces to Dirac delta function and thus only carriers initially moving with Fermi velocity  $v_F$  contribute to the autocorrelation function in (2.4). The velocity  $v_x$  of conducting charges thus periodically switches between  $+v_F$  and  $-v_F$  as the carriers

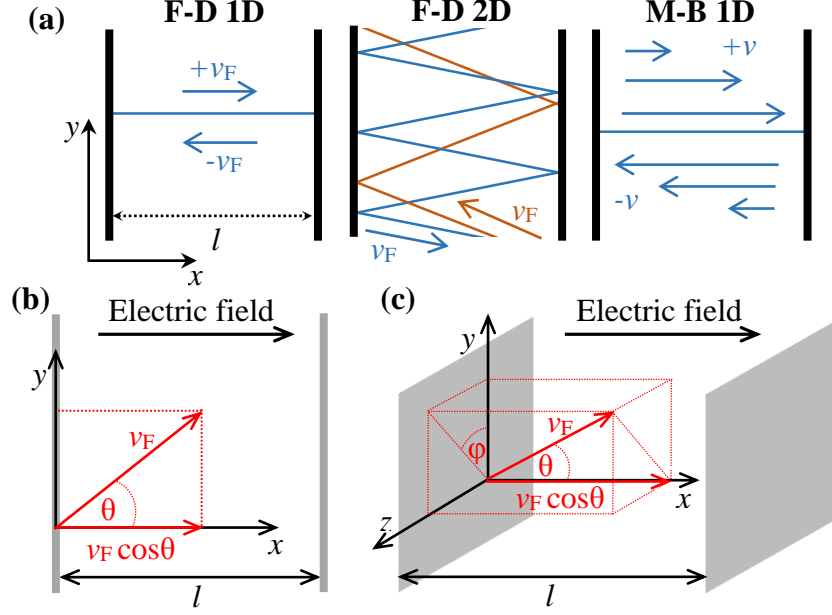


Fig. 5.3. (a) Schematics of the charge motion in an infinitely deep rectangular potential wells for Fermi-Dirac (F-D) and Maxwell-Boltzmann (M-B) statistics. For Fermi-Dirac statistics, only carriers with velocity close to the Fermi velocity  $v_F$  contribute to the conductivity. In case of Maxwell-Boltzmann statistics, the conductive charges exhibit a broad distribution of velocities. (b),(c) Geometries used for the calculations of THz conductivity in 2D (panel (b)) and 3D (panel (c)) cases. We assume that charge reflections at the boundaries are elastic and specular. Therefore, the presence/absence of enclosure in the  $y$ - and  $z$ - directions does not affect the response in the  $x$ -direction.

bounce between the planes. The period of this motion is the round-trip time  $t_r = 2l/v_F$  where  $l$  is the distance between the planes. The product  $v_x(0)v_x(t)$  in the autocorrelation function is then a square wave oscillating between  $\pm v_F^2$  with period  $t_r$  (Fig. 5.4(a)). The phase shift of this square wave depends on the initial positions in the phase space and it may have any value just from the interval  $\langle 0, \pi \rangle$  as  $v_x^2(0)$  is always positive (Fig. 5.4(b)). The averaging over all initial positions then yields a triangle wave shape  $\Lambda(t/t_r)$  of the autocorrelation function (Figs. 5.4(c) and 5.5(a); the symbol  $\Lambda(x)$  denotes a triangle function oscillating between  $+1$  and  $-1$  with period 1). After substitution into the Kubo formula (2.4) we obtain the corresponding charge mobility (without bulk scattering)

$$\text{Re } \mu_{xx}(f) = \frac{e_0}{m} \cdot \frac{2}{\pi^2} \sum_{k=-\infty}^{\infty} \frac{\delta[f - (2k+1)f_r]}{(2k+1)^2} \quad (5.9.1)$$

$$\text{Im } \mu_{xx}(f) = -\frac{e_0}{m} \cdot \frac{2}{\pi^3} \sum_{k=-\infty}^{\infty} \frac{1}{f - (2k+1)f_r} \cdot \frac{1}{(2k+1)^2}. \quad (5.9.2)$$

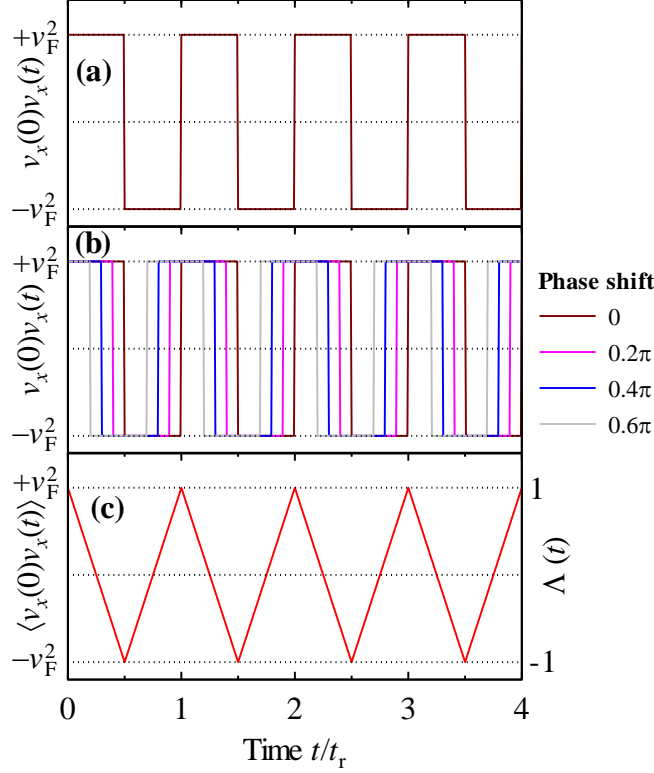


Fig. 5.4. Derivation of the autocorrelation function for degenerate electron gas in a 1D potential well. A carrier bounces between two straight parallel planes; for a single charge, the product  $v_x(0)v_x(t)$  then takes form of a square wave with phase shift determined by the initial charge position and period given by the round-trip time  $t_r$  of carriers in the well (a). The averaging takes place over all possible initial positions which are represented by different phase shifts (a few of them are illustrated in panel (b)). Integration over all possible initial phases of movement then yields the triangle wave shape of the autocorrelation function (c).

The real part of mobility (5.9.1) consists of a sum of Dirac delta functions  $\delta$  which are located at the fundamental frequency corresponding to the round-trip movement with frequency  $f_r = 1/t_r$  and its odd harmonics (Fig. 5.5(b)). The higher harmonics originate from the anharmonic shape of the confining potential, which causes an anharmonic character of carrier trajectories. In the quantum-mechanical approach (Section 5.2.2), we will show that these harmonics are linked to dipolar transitions to higher unoccupied levels.

In a two-dimensional (2D) well, the charges can move at an oblique angle  $\theta$  with respect to the well boundaries (Fig. 5.3(b)). This prolongs the round-trip time compared to the 1D case which now reads  $t_r/\cos \theta$ . The velocity component parallel with the probing electric field is then a projection of the Fermi velocity to the  $x$ -axis (perpendicular to the confining planes), i.e.  $v_x(0) = v_F \cos \theta$ . In analogy to the 1D well, averaging over all initial positions leads to a triangular time evolution of velocity

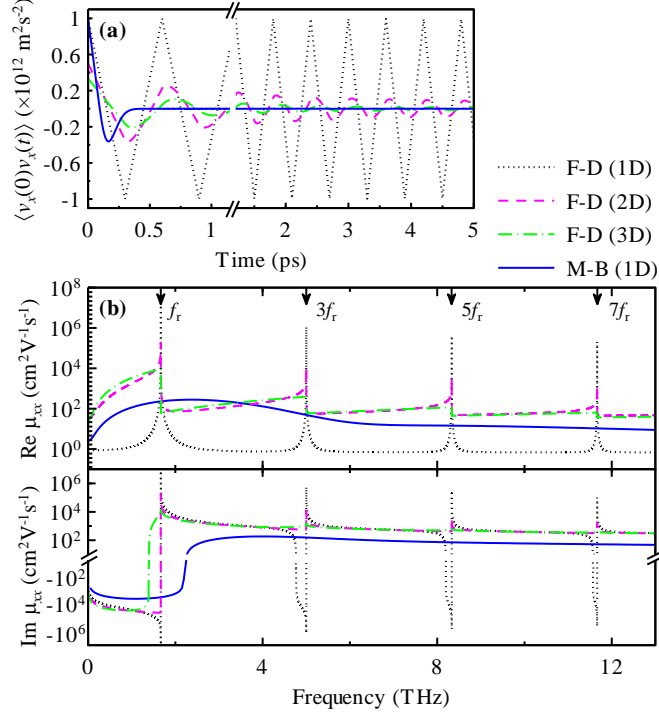


Fig. 5.5. (a) Velocity autocorrelation functions in the time-domain of carriers bouncing in a multidimensional infinitely deep rectangular potential well with width  $l = 300$  nm. The carriers were described either with Fermi-Dirac statistics (F-D) ( $v_F = 1000$  m/s,  $E_F = 0.20$  eV,  $T = 0$  K) or Maxwell-Boltzmann statistics (M-B) (to allow a direct comparison, the mean square velocity in the Maxwell-Boltzmann statistics is set to  $v_F^2$ , i.e.  $T = 4620$  K; to transfer the results towards realistic temperatures, the frequency would need to be scaled with  $\sqrt{T}$ ). (b) Mobility spectra corresponding to the velocity autocorrelation functions from panel (a) calculated using the Kubo formula (2.4). For the purpose of plotting, we phenomenologically introduced a bulk scattering time  $\tau_s = 1$  ns (i.e. the triangle wave from panel (a) is multiplied by  $\exp(-t/\tau_s)$ ). The Dirac delta functions are then replaced by a narrow Lorentzians for 1D Fermi-Dirac statistics and also the divergences are prevented in the 2D case. The unrealistically long scattering time allows us to clearly distinguish the intrinsic damping in the 2D and 3D systems (picosecond time scale) from the artificial extrinsic losses (decay time of 1 ns). Other parameters:  $m = 0.07m_e$ .

$$v(t) = v_F \cos \theta \cdot \Lambda \left( \frac{t}{t_r / \cos \theta} \right). \quad (5.10)$$

To find the velocity autocorrelation function in the time-domain, we have to average over all possible directions of movement (represented by  $\theta$  ranging from 0 to  $2\pi$ )

$$\langle v_x(0)v_x(t) \rangle = \frac{\int_0^{2\pi} v_F^2 \cos^2 \theta \cdot \Lambda\left(\frac{t}{t_r} \cos \theta\right) d\theta}{\int_0^{2\pi} d\theta}. \quad (5.11)$$

The oscillations of the above autocorrelation function (the inner integral) are damped due to dephasing of the triangle functions corresponding to carriers moving under different angles  $\theta$  (Fig. 5.5(a)). Substitution of (5.11) into the Kubo formula (2.4) and considering that  $E_F = mv_F^2/2$  then yields the mobility of carriers

$$\mu_{xx}(f) = \frac{e_0}{m} \frac{1}{\pi} \int_0^\infty e^{2\pi i f t} \int_0^{2\pi} \Lambda\left(\frac{t}{t_r} \cos \theta\right) \cos^2 \theta d\theta dt. \quad (5.12)$$

As in the 1D case, the mobility spectrum contains a series of odd harmonics with fundamental frequency  $f_r$  (Fig. 5.5(b)). However, the corresponding peaks are intrinsically broadened due to the damped character of the autocorrelation function (intrinsic peak broadening due to a distribution of trajectory lengths was predicted also for nanodiscs [89],[90]). The low-frequency tails then emerge due to carriers with non-zero velocity component along the boundaries. The round-trip of such carriers lasts necessarily longer which implies a lower bouncing frequency. Similar broadening towards higher frequencies cannot appear since no trajectory has a period shorter than  $t_r$ . Instead, the diverging conductivity at the frequency  $f_r = 1/t_r$  is followed by a sharp cut-off.

For carriers confined in three-dimensional (3D) well, there is an additional degree of freedom (Fig. 5.3(a)). The transformation into spherical coordinates then reveals that both the carrier round-trip time  $t_r$  and the  $x$ -component of velocity  $v_x$  are determined just by the polar angle  $\theta$ . However, the additional degree of freedom appears as the Jacobian  $\sin \theta$  in the coordinate transformation and the autocorrelation function thus reads

$$\langle v_x(0)v_x(t) \rangle = \frac{\int_0^{2\pi} d\varphi \int_0^\pi v_F^2 \cos^2 \theta \cdot \Lambda\left(\frac{t}{t_r} \cos \theta\right) \sin \theta d\theta}{\int_0^{2\pi} d\varphi \int_0^\pi \sin \theta d\theta}, \quad (5.13)$$

where  $\varphi$  is the azimuthal angle. Trivial integrations followed by the substitution into the Kubo formula (2.4) then yield

$$\mu_{xx}(f) = \frac{3e_0}{2m} \int_0^\infty e^{2\pi i f t} \int_0^\pi \Lambda\left(\frac{t}{t_r} \cos \theta\right) \cos^2 \theta \sin \theta d\theta dt. \quad (5.14)$$

The time-domain velocity autocorrelation and the corresponding mobility spectrum exhibit similar features as in the 2D case. The additional degree of freedom, however, leads to a broader distribution of the  $x$ -components of velocity  $v_x$ . Therefore, the oscillations in the

time-domain autocorrelation are damped faster (Fig. 5.5(a)). The mobility then does not diverge at the frequency  $f_r$  and its odd harmonics and there are just discontinuities.

For a given well width  $l$ , the resonant frequency  $f_r$  depends just on the Fermi velocity  $v_F$  and thus also on the charge density  $n$ . In the semi-classical limit, the density of states is continuous and thus  $v_F \sim n^{1/D}$  where  $D$  is the dimension. All the resonant frequencies in our model are then directly proportional to  $n^{1/D}$  (Fig. 5.10(a)-(c)). The proportionality constant is determined just by the geometry and scales with the reciprocal size of the nanostructure. For this reason, we call these resonances "geometrical". We note that the  $1/D$ -power dependence is universal; it does not depend on the particular nanostructure shape.

Within the developed framework, we now revisit the calculations of the conductivity of confined non-degenerate electron gas. In such system, the conducting carriers exhibit a broad distribution of thermal velocities (according to the Maxwell-Boltzmann statistics). Averaging over the velocity amplitudes is then required and the carrier mobility thus reads

$$\mu_{xx}(f) = \frac{e_0}{k_B T} \cdot \sqrt{\frac{2m}{\pi k_B T}} \int_0^\infty e^{2\pi i f t} \int_0^\infty \Lambda\left(\frac{v_x t}{2l}\right) v_x^2 \exp\left(-\frac{m v_x^2}{2k_B T}\right) dv_x dt. \quad (5.15)$$

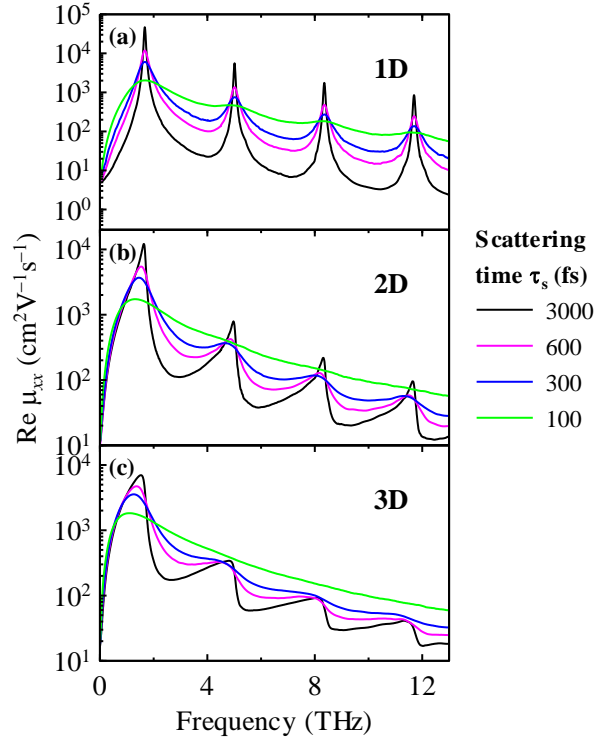


Fig. 5.6. Mobility spectra of a degenerate electron gas confined in an infinitely deep rectangular potential well in the presence of finite bulk scattering time  $\tau_s$ . Following parameters were considered:  $l = 300$  nm,  $v_F = 1000$  m/s,  $E_F = 0.20$  eV,  $T = 0$  K,  $m = 0.07m_e$ . The round-trip time is then  $t_r = 600$  fs. Individual geometrical resonances can be resolved for  $\tau_s$  as short as one half of  $t_r$ .



The inner integral is the time-domain velocity autocorrelation exhibiting very rapidly damped oscillations (Fig. 5.5(a)). The mobility spectrum is then very broad and it is essentially identical to the behavior of confined charges described in Section 5.1. This emphasizes the key role of the broad velocity distribution. Even though there is no bulk scattering, the effective damping and associated resonance width induced by the carrier dephasing are large enough to form a single broad absorption band.

We now discuss the conditions under which we can clearly resolve individual geometrical resonances. It is obvious that the electron gas must be degenerate (i.e.  $k_B T \ll E_F$ ). In such case, the response is dominated by carriers which move perpendicularly to the surface, while the influence of carriers moving under an oblique angle  $\theta$  (and thus contributing to the low-frequency tails) is suppressed by the factors  $\cos^2\theta$  and  $\cos^2\theta \sin \theta$  in 2D (5.12) and 3D (5.14) case, respectively. In the non-degenerate electron gas, however, the entire distribution of velocities contributes (independently of dimension) and the mobility spectrum is dominated by a single broad band. The weak background above this broad band ( $f \gtrsim 6$  THz in Fig. 5.5(b)) can be attributed to the onset of the high harmonics.

The degeneracy of the electron gas, however, is not a sufficient condition for clear resolution of individual geometrical resonances. In real materials, the spectra would be further smeared due to the inherent bulk scattering and inhomogeneous broadening. Our calculations show, that the scattering time  $\tau_s$  exceeding one half of the round-trip time  $t_r$  is required (Fig. 5.6). This condition can be easily satisfied in 2DEG-based nanostructures at low temperature (long  $\tau_s$ ) or in nanometer-sized metallic particles (short  $t_r$  due to high Fermi velocity  $v_F$ ). The large spectral separation of individual geometrical resonances also weakens the demand on monodispersity. We estimate that the fundamental and third harmonic resonance should be distinguished even for a size distribution with full width reaching 100% of the mean value. Considerably better structures can be routinely prepared by lithography-based methods [91],[92].

### 5.2.2 Quantum-mechanical calculations

Here, we treat the conductivity of degenerate electron gas confined in a rectangular potential well (Fig. 5.3(a)) using quantum-mechanical approach. This allows us to discuss the limits of the semi-classical model developed in previous section.

To calculate the conductivity, we will recall the approach developed in [72]. We first consider the well-known Kubo-Greenwood formula for conductivity in a relaxation time approximation [82]

$$\sigma(\omega) = \frac{2e_0^2 \hbar}{m^2 \mathcal{V}} \sum_{jk} \frac{|\langle \psi_k | \vec{e} \cdot \hat{p} | \psi_j \rangle|^2}{E_k - E_j} \frac{i[F(E_k) - F(E_j)]}{E_k - E_j - \hbar\omega - i\hbar/\tau}, \quad (5.16)$$

where  $\hat{p}$  is the momentum operator,  $\vec{e}$  is the unit vector pointing in the direction of the probing electric field,  $\psi_i$  and  $E_i$  are the wave function and energy corresponding to the  $i$ -th state, indices  $j$  and  $k$  denote the initial and final states, respectively,  $F(E)$  is the distribution function, and  $\mathcal{V}$

is the volume of the nanocrystal. The term  $\hbar/\tau$  then accounts for all scattering processes and ensures a finite line width. The above formula can be safely applied for optical frequencies. In the THz range, however, (5.16) always yields a non-zero dc conductivity which is unphysical for finite isolated objects. In [72], a restoring diffusion current of scattered charges was considered and an appropriate correction to quantum Kubo formula was found. The conductivity of electrons confined in a three-dimensional infinitely deep rectangular well (the probing electric field is polarized along the  $x$ -axis) then reads [72]

$$\sigma_{xx}(\omega) = \frac{e_0^2}{\hbar l^3} \sum_{j,k} \frac{f_j - f_k}{\omega - \omega_{jk} + i\gamma} \times \left[ \sum_{n \text{ odd}} \frac{2D_{\text{diff}} \gamma l S_{jkn} x_{jk}}{D_{\text{diff}} \pi^2 n^2 - i\omega l^2} - i\omega_{jk} |x_{jk}|^2 \right], \quad (5.17)$$

$$S_{jkn} = \delta_{j_y, k_y} \delta_{j_z, k_z} (\delta_{n, j_x - k_x} + \delta_{n, k_x - j_x} - \delta_{n, j_x + k_x}),$$

where  $j = (j_x, j_y, j_z)$  and  $k = (k_x, k_y, k_z)$  are multi-indices with positive integers  $j_i$  and  $k_i$  ( $i = x, y, z$ ) denoting the quantum states of electrons in the appropriate directions,  $f_i$  is the occupation of state  $i$  (given by Maxwell-Boltzmann or Fermi-Dirac statistics),  $l$  is the well width in the  $x$ -direction,  $\gamma$  is the scattering rate (related to the scattering time  $\tau_s$  as  $\gamma = 1/\tau_s$ ) and  $e_0 x_{jk} = e_0 \langle \psi_j | \hat{x} | \psi_k \rangle$  is the dipole matrix element.  $D_{\text{diff}}$  is the diffusion constant which is given by the Einstein's relation  $D_{\text{diff}} = k_B T / (m\gamma)$  (for degenerate electron gas,  $k_B T$  should be replaced by  $N(\partial E_F / \partial N)$  where  $N$  is the concentration of carriers in the conduction band) [87]. The energy levels in the infinitely deep rectangular quantum well are

$$E_{(k_x, k_y, k_z)} = \frac{\pi^2 \hbar^2 (k_x^2 + k_y^2 + k_z^2)}{2ml^2}. \quad (5.18)$$

The angular frequency  $\omega_{jk}$  corresponding to the transition between two states  $j$  and  $k$  then reads

$$\hbar \omega_{jk} = \frac{\pi^2 \hbar^2 (j_x^2 - k_x^2)}{2ml^2}. \quad (5.19)$$

For large nanocrystals in the semi-classical limit, it was shown in [72] that (5.17) yields same results as the Monte-Carlo calculations based on Kubo formalism.

In order to resolve the geometrical resonances in the mobility spectra, we have to meet generally two conditions. First, the nanostructure size should significantly exceed the de Broglie wavelength of electrons at Fermi level. In such case, the Fermi velocity  $v_F$  satisfies

$$v_F \gg \frac{\hbar}{ml}, \quad (5.20)$$

where  $\hbar$  is the Planck constant. Since  $v_F$  is directly proportional to the power of charge density  $n$  ( $v_F \sim n^{1/D}$ , where  $D$  is the dimension), the above relation implies that the semi-classical approach can be applied only for high enough carrier concentrations. As an example, we consider potential wells with width  $l = 300$  nm, for which we find

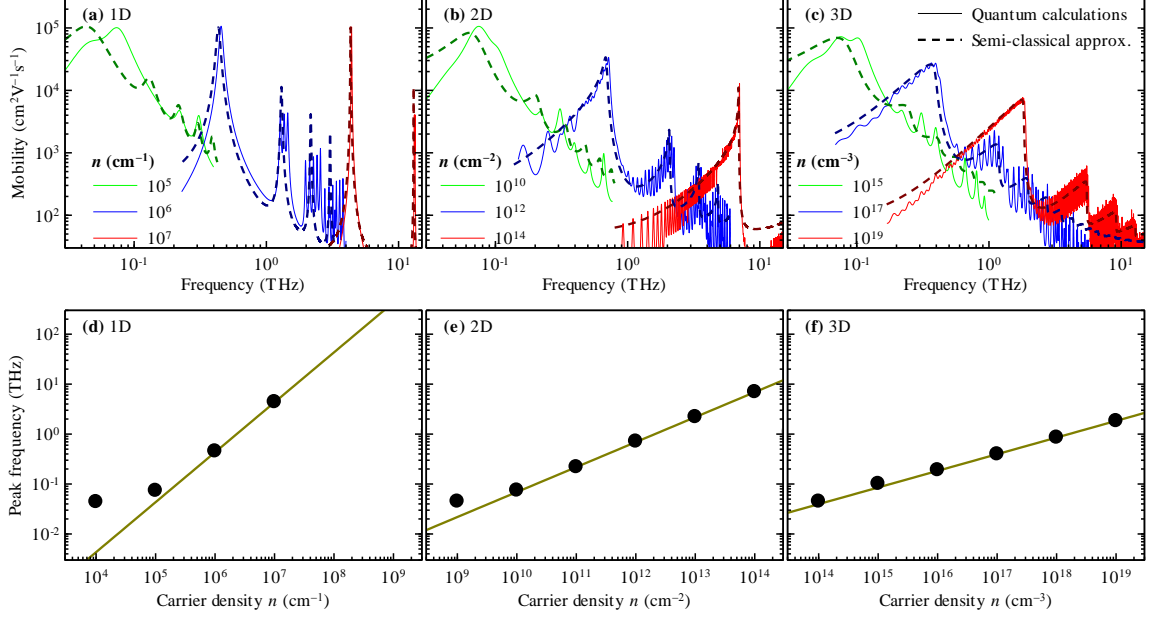


Fig. 5.7. (a)-(c) Comparison of real parts of mobility spectra calculated using the quantum formula (5.17) (thin solid lines) and the semi-classical model from Section 5.2.1 (Eqs. (5.9.1), (5.12) and (5.14); thick dashed lines) for various charge densities  $n$  ( $l = 300 \text{ nm}$ ,  $T = 0 \text{ K}$ ,  $\tau_s = 10 \text{ ps}$ ,  $m = 0.07m_e$ ). (d)-(f) Comparison of the frequency of the first peak from panels (a)-(c) (symbols) and the frequency of the fundamental geometrical resonance ( $\sim n^{1/D}$  where  $D$  is dimension (Fig. 5.10)) in the semi-classical description (lines).

$$3\text{D} : n \gg \frac{8\pi}{3l^3} = 3 \times 10^{14} \text{ cm}^{-3} \quad (5.21.1)$$

$$2\text{D} : n \gg \frac{2\pi}{l^2} = 7 \times 10^9 \text{ cm}^{-2} \quad (5.21.2)$$

$$1\text{D} : n \gg \frac{4}{l} = 1 \times 10^5 \text{ cm}^{-1} . \quad (5.21.3)$$

Second, the quantum transitions should be smeared enough so that density of states could be regarded as a continuum. This is achieved for scattering times  $\tau_s$  for which  $\hbar/\tau_s$  is at least comparable with the energy-level spacing around  $E_F$ .

In Fig. 5.7, we show that the first geometrical resonance is clearly resolved even close to the critical concentrations (5.21) in the quantum-mechanical results. Its frequency then coincides with that predicted in the semi-classical model (for higher charge densities, they match each other perfectly). Higher-order geometrical resonances are then resolvable for higher charge densities (we can identify them by comparison with the semi-classical results). The corresponding peaks split due to the discrete character of density of states. This becomes suppressed with increasing density of carriers or for a stronger damping which would smear the individual transition lines. In this sense, we thus confirm the existence of higher-order geometrical resonances also in the quantum-mechanical view. We note that the differences

between semi-classical and quantum description are less pronounced for 3D well due to higher density of states.

We now further discuss the origin of the predicted peaks from the quantum-mechanical view. The frequencies corresponding to the transition between quantum energy levels in the infinitely deep rectangular well are given by (5.19). The dipole selection rules then allow just the transitions from the state  $k_x$  to the state  $j_x = k_x + 1 + 2q$ , where  $q$  is a non-negative integer. The transition frequency can be thus written as

$$f_{jk} = \frac{\pi\hbar}{4ml^2} (2k_x + 2q + 1)(2q + 1). \quad (5.22)$$

At zero temperature, the states are occupied up to the Fermi energy which thus determines the highest value of  $k_x$ . For large structure size  $l$ , the states are dense and approach continuum. Degeneracy of the electron gas then implies large value of such  $k_x$ . Dipole matrix elements rapidly decrease with increasing  $q$  and thus only transitions close to the Fermi level contribute to the response (i.e.  $q \ll k_x, j_x$ ). We can thus approximate  $2k_x + 2q + 1$  by  $2k_x$  and find

$$f_{jk} \approx \frac{v_F}{2l} (2q + 1), \quad (5.23)$$

which is equivalent to the semi-classical result. The odd harmonics accompanying the semi-classical motion thus have their origin in quantum transitions to higher energy levels.

### 5.3 Coupling between geometrical and plasmonic resonances

The conductivities calculated in Section 5.2.1 describe the response to the local probing electric field. As we discussed in Section 3, however, the nanostructures are inherently inhomogeneous systems where the depolarization fields cause the local field to be different from the applied one. The measured (effective) spectra then generally differ from the local conductivity spectra (Section 3.2). We now investigate how does the effective medium influence the geometrical resonances. For the sake of simplicity, we will use the semi-classical description of local conductivity from previous section. We published these results in [83].

In Section 3.1.3, we discussed that non-existence of percolation (in the direction of the polarization of the probing electric field) leads to a build-up of a plasmonic resonance in the effective conductivity spectrum. Qualitatively, this behavior is identical for any non-percolated morphology (particular layout would affect just quantitative properties). Therefore, we consider the structures from Fig. 5.8(a)-(c) which consist of blocks filled with nanostructures (surrounded by infinitesimally thin isolating barriers) separated by insulating layers with finite thickness. There is obviously no percolation in the direction of the probing electric field ( $x$ -direction) and the symmetry further ensures that there are no induced net fields in the  $y$ - and  $z$ -directions. We can thus equivalently consider a structure consisting of alternating conductive and nonconductive laterally infinite blocks (Fig. 5.8(d)) which is described by the brick-wall model (Section 3.1.2). In 2D and 1D case, we have to additionally consider the number of nanosheets per unit length  $\eta_2$  and the number of nanowires per unit area  $\eta_1$ , respectively.

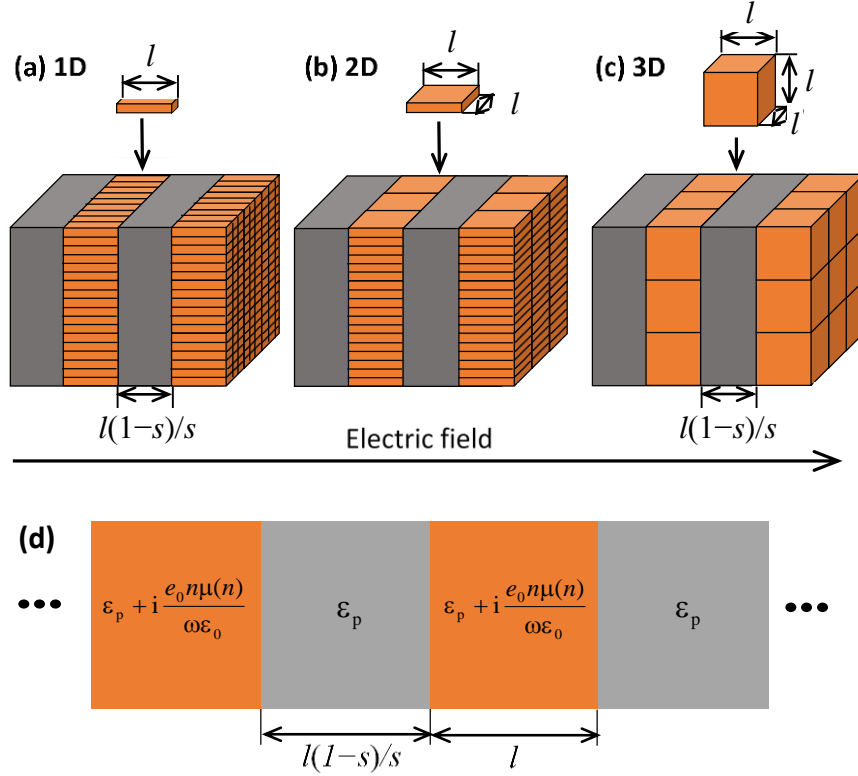


Fig. 5.8. Scheme of structures used for the study of coupling between geometrical and plasmonic resonances. Mutually isolated conducting 1D, 2D and 3D nanostructures (orange) are separated by thick nonconductive blocks (gray,  $\epsilon_p = 12.6$ ) (a)-(c). The percolation along the direction of the probing field is broken which allows the plasmonic resonance to build up. The effective response of all these geometries is equivalent to the structure in (d) which consists of alternating conducting (thickness  $l$ ) and nonconductive blocks. The blocks are infinite in the lateral directions. Such structure is then described within the brick-wall model (i.e. analogy with capacitors connected in series; Section 3.1.2). To guarantee the correct filling factor  $s$  of the conducting material, we have to scale the thickness of nonconductive blocks by factor  $(1-s)/s$ .

These parameters (together with the carrier concentration in the nanostructures) control at which (volume) charge density the plasmonic resonance meets the geometrical one.

We assume that the nonconductive parts have a purely real constant permittivity  $\epsilon_p$ . The permittivity of the conductive parts is considered in the form  $\epsilon_p + i e_0 N \mu_{xx}(f, n) / (2\pi f \epsilon_0)$ . Here,  $N$  is the average number of charges per unit *volume* of the block, whereas  $n$  is the number of charges per unit *length*, *surface* and *volume* in one, two and three dimensions, respectively. In 3D case, obviously  $N = n$ . For 2D and 1D nanostructures,  $N = \eta_2 n$  and  $N = \eta_1 n$ , respectively. The effective conductivity  $\sigma_{\text{eff}}$  of the structure is given by Eq. (3.10). We further represent the results in the form of normalized effective conductivity  $\sigma_{\text{eff}}/e_0 N$  which describes effective response of a single carrier (i.e.  $\sigma_{\text{eff}}/e_0 N$  can be identified with the electron mobility in homogeneous systems). The plasma frequency  $f_{\text{pl}}$  is controlled by the concentration  $N$  and it reads [33]

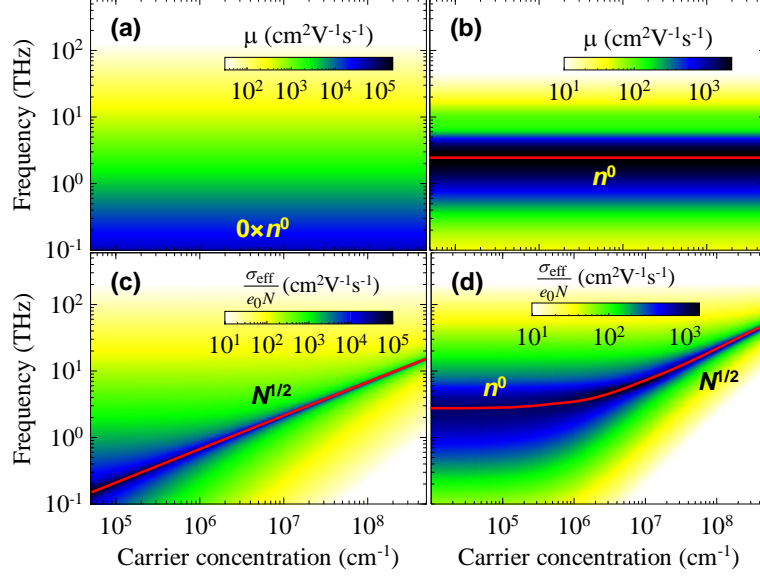


Fig. 5.9. (a) Drude mobility spectrum (5.1) (nanostructure size  $l \rightarrow \infty$ ) exhibits a peak at zero frequency. The spectrum shape does not depend on the carrier density  $n$ . (b) Mobility spectrum  $\mu_{xx}$  of non-degenerate electron gas confined in an infinitely deep rectangular potential well (width  $l = 300$  nm) calculated using (5.15). (c),(d) Normalized effective conductivities of the structure from Fig. 5.8(d) corresponding to mobilities from panels (a) and (b), respectively. Solid red lines serve as a guide for the eye for the resonances (represented by the maxima of  $|\Delta\sigma|$ ) – the parts following the  $N^{1/2}$ -dependence represent the plasmonic resonance. Following parameters were considered:  $T = 4620$  K,  $\tau_s = 10$  ps,  $s = 0.5$ ,  $m = 0.07m_e$ . In panel (d), the density of nanowires is  $\eta_1 = 10^{11}$  cm $^{-2}$ . All panels show the amplitudes of the complex spectra.

$$f_{pl} = \frac{1}{2\pi} \sqrt{\frac{e_0^2 N(1-s)}{m\epsilon_0\epsilon_p}}, \quad (5.24)$$

where  $s$  is the filling factor of conducting material.

For large nanostructures (i.e.  $l \rightarrow \infty$ ), the local conductivity approaches the Drude model (5.1) (Fig. 5.9(a)) – there is a peak at the zero frequency independently of charge density. In the effective conductivity, this peak is preserved just in the limit  $N \rightarrow 0$  while for higher  $N$ , the spectrum is dominated by the plasmonic resonance with the frequency following  $N^{1/2}$ -dependence (Fig. 5.9(c)). This behavior was already discussed in [32].

Response of confined non-degenerate electron gas exhibits similar behavior. The geometrical resonance in the local conductivity does not depend on the carrier density (Fig. 5.9(b)). In the effective conductivity (Fig. 5.9(d)), this broad geometrical resonance dominates at low charge densities. The plasmonic resonance follows the  $N^{1/2}$ -dependence and takes over at higher carrier densities.

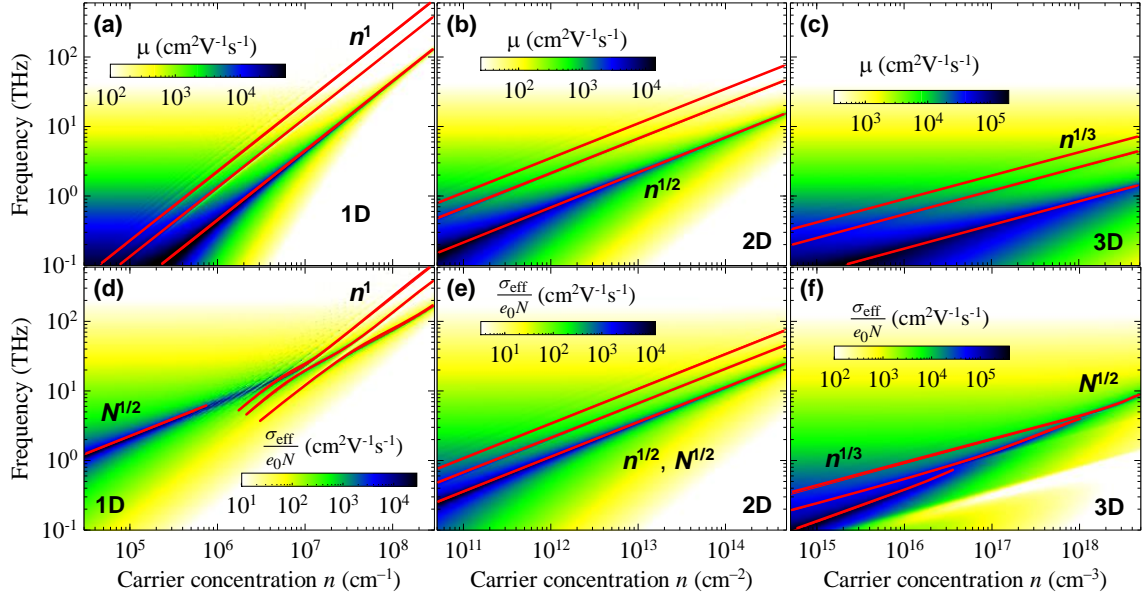


Fig. 5.10. (a)-(c) Mobilities of  $D$ -dimensional degenerate electron gas confined in an infinitely deep rectangular potential well with width  $l = 300$  nm ( $T = 0$  K,  $\tau_s = 10$  ps,  $m = 0.07m_e$ ). The geometrical resonant frequencies are directly proportional to the  $n^{1/D}$ . (d)-(f) Normalized effective conductivities of the structure from Fig. 5.8(d) corresponding to the mobilities from panels (a)-(c). Solid red lines serve as a guide for the eye to indicate the behavior of a few lowest resonances – the parts following  $N^{1/2}$ -dependence represent the plasmonic resonance while those with  $n^{1/D}$ -trend represent the geometrical modes. In panel (d), the density of nanowires  $\eta_1 = 10^{12}$  cm $^{-2}$  was considered. The density of nanosheets in panel (e) is  $\eta_2 = 10^5$  cm $^{-1}$ . The filling factor is  $s = 0.5$  in panels (d) and (e), and  $s = 0.944$  in panel (f). All panels show the amplitudes of the complex spectra.

For degenerate electron gas (Section 5.2.1), the frequency  $f_r$  of geometrical resonances in local conductivity is directly proportional to  $n^{1/D}$  (Fig. 5.10(a)-(c)). The plasmonic frequency  $f_{pl}$ , however, is directly proportional to  $N^{1/2}$ . The effective conductivity thus exhibits clear signatures of a coupling between the geometrical and plasmonic resonances (Fig. 5.10(d)-(f)). In the 3D case (Fig. 5.10 (f)), individual geometrical resonances exist for low carrier concentrations and they are not influenced by the plasmonic resonance. With increasing carrier density, mixing with the plasmonic mode becomes important. The plasmonic resonance then takes completely over at high concentrations. This behavior is similar to the one observed for local Drude response and non-degenerate electron gas. In 1D and 2D case, however, this coupling is strikingly different.

In 1D systems, it is the plasmonic resonance which dominates for low charge densities (Fig. 5.10(d)). With increasing concentration, mixed modes appear and they successively transform into the geometrical modes at high concentrations.

The 2D systems are then specific since both the geometrical and plasmonic resonances depend on the charge density in the same manner. The resonant frequencies of the mixed modes thus keep the square-root dependence on the carrier concentration. In comparison with

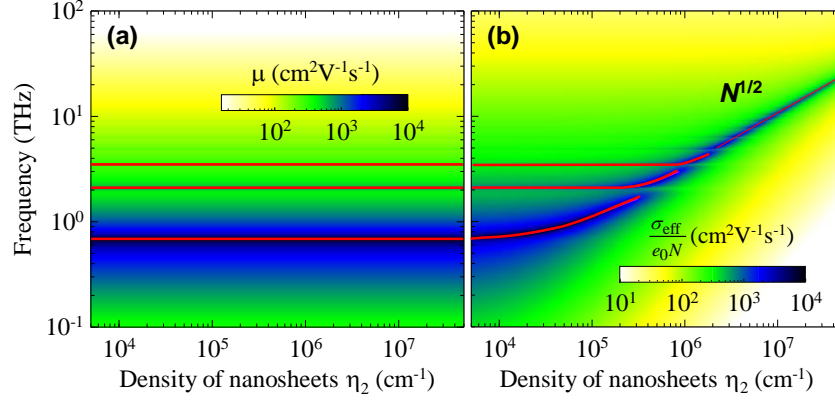


Fig. 5.11. Amplitudes of complex local and effective conductivity of confined 2D degenerate electron gas as a function of the density of nanosheets  $\eta_2$ . (a) Mobility spectrum does not depend on the nanosheet density  $\eta_2$  (it varies just with carrier density in the nanosheets  $n$ ). (b) Normalized effective conductivity of the structure from Fig. 5.8(d) corresponding to the mobility from panel (a). Solid red lines serve as a guide for the eye to indicate the behavior of the three lowest resonances – the parts following  $N^{1/2}$  trend represent the plasmonic mode while the constant parts (i.e. independent of  $\eta_2$ ) represent the geometrical modes. Following parameters were considered:  $l = 300$  nm,  $n = 10^{12}$  cm $^{-2}$ ,  $s = 0.5$ ,  $\tau_s = 10$  ps,  $m = 0.07m_e$ .

the geometrical resonances in the local conductivity, the mixed effective resonances are only scaled (shifted in the logarithmic scale in Fig. 5.10(e)) and their line shape is altered. To further understand this mixing, we investigate the dependence on the density of nanosheets  $\eta_2$  (Fig. 5.11). In the effective conductivity, the geometrical modes exist for small nanosheet densities. For higher densities  $\eta_2$ , these modes then progressively transform into a single plasmonic resonance.

The first geometrical mode and the plasmonic mode cross at the carrier density for which the corresponding frequencies are equal. These crossover charge densities  $n_{\text{cross}}$  read

$$n_{\text{cross}} = \frac{\eta_l m l^2}{\epsilon_p} (1-s) \frac{4e_0^2}{\pi^4 \hbar^2 \epsilon_0} \quad \text{for 1D nanostructures,} \quad (5.25.1)$$

$$n_{\text{cross}} = \left( \frac{\epsilon_p}{m l^2} \right)^3 \frac{1}{(1-s)^3} \frac{9\pi^{10} \hbar^6 \epsilon_0^3}{e_0^6} \quad \text{for 3D nanostructures.} \quad (5.25.2)$$

The above relations show that the crossover is controlled by a large number of parameters ( $m$ ,  $s$ ,  $l$ ,  $\epsilon_p$  and  $\eta_l$ ). This allows us to tune  $n_{\text{cross}}$  and the corresponding frequency as desired. Importantly, this permits to find such material and conditions for which the assumptions of semi-classical description are satisfied. We note that in real situations, we would also need to consider the dependence of scattering time on the charge density and the temperature. This



time has to be long enough to resolve the resonances, and at the same time sufficiently short to avoid the dominance of quantum effects.

## 5.4 Degenerate electron gas confined in further model 2D nanostructures

In this section, we calculate the linear terahertz conductivity of degenerate electron gas confined in various further 2D model nanostructures (periodically perturbed parallel planes, and chaotic behavior in oval Bunimovich stadium [93] and Lorentz gas potential [94]) using the Monte-Carlo calculations based on Kubo formalism (Section 2.1). We thus describe the response just at the semi-classical level (complex quantum effects were described e.g. for 2D nanodiscs in [90]). As previously, we assume a close to ballistic motion of non-interacting carriers (i.e. very long scattering times). This favors the influence of interaction with nanostructure boundaries over the bulk scattering and thus allows to resolve distinct features in the conductivity spectra. Also, we assume that the carriers reflect elastically and specularly from the boundary. We published these results in [84].

We first investigate a 2D potential well with boundaries periodically perturbed by elliptically curved segments (Fig. 5.12(a)). The geometrical resonances observed for

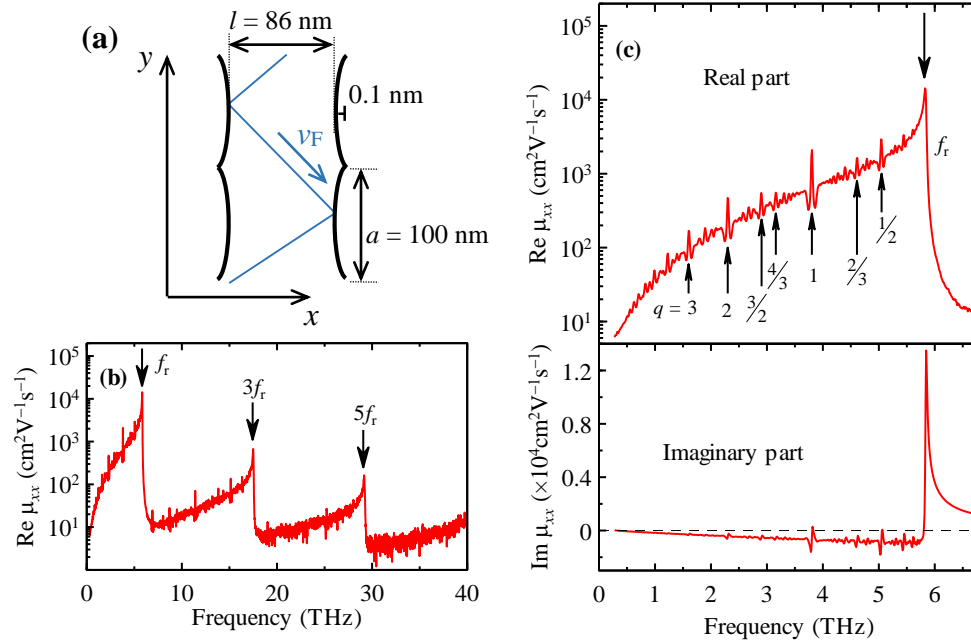


Fig. 5.12. (a) Scheme of the 2D well with periodically perturbed boundaries. The boundary segments are elliptically curved and the difference between the longest and shortest distance between boundaries is 0.1 nm. (b) Mobility spectrum  $\mu_{xx}$  corresponding to carriers bouncing between the curved planes from (a). Despite the perturbation, the geometrical resonances at the round-trip frequency  $f_r$  and its odd harmonics (Section 5.2.1) are clearly resolved. (c) Detail of the low-frequency tail of the fundamental geometrical resonance. The arrows indicate secondary resonances for given pitch  $q$  (5.26). The mobility spectrum was assessed using the Monte-Carlo calculations based on Kubo formalism. Following parameters were considered:  $v_F = 1000$  m/s,  $E_F = 0.20$  eV,  $T = 4$  K,  $\tau_s = 1$  ns,  $m = 0.07m_e$ .

unperturbed rectangular well (Fig. 5.5(b)) are quite stable with respect to the perturbation and remain clearly resolved (Fig. 5.12(b)). However, a careful examination reveals a presence of a fine structure of the low-frequency tail (Fig. 5.12(c)). We provide the following explanation. The concave parts of the boundaries focus charge trajectories towards stable periodic orbits. These stable pathways are characterized by frequencies

$$f = \frac{v_F}{2\sqrt{l^2 + (qa)^2}}, \quad (5.26)$$

where  $l$  is the distance between the planes,  $a$  is the period of the curvature (Fig. 5.12(a)) and the rational number  $q$  describes the pitch of the motion. The narrow peaks in the low-frequency tail then appear at the above frequencies. Trajectories close to these periodic orbits rapidly converge to these stable pathways. Therefore, the conductivity is depleted close to the frequencies (5.26) and side minima around the peaks appear (Fig. 5.12(c)). This example shows, that even a very small perturbation can lead to presence of new spectral features (in Fig. 5.12, the difference between the longest and shortest between the boundaries is just 0.1 nm, compared to the 100-nm characteristic size).

Much more complicated conductivity spectra are expected for systems with chaotic behavior where a very complex charge motion may occur. We start with the Bunimovich

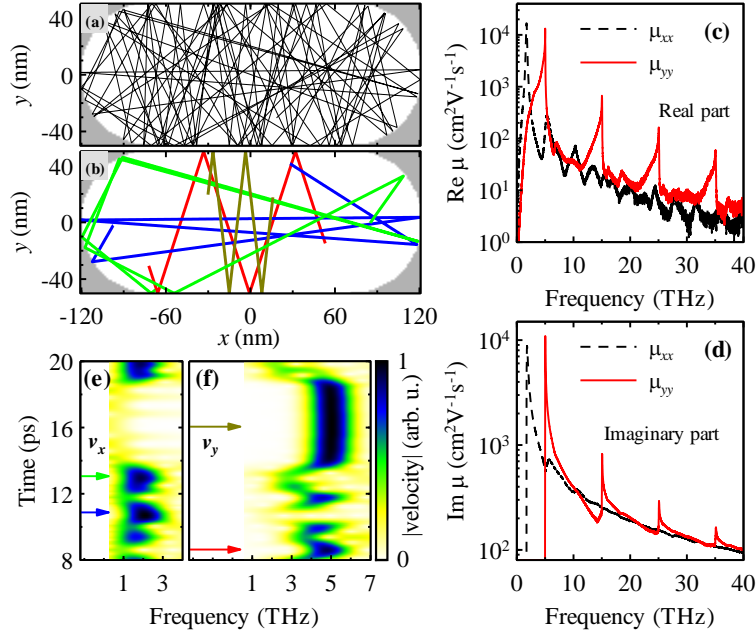


Fig. 5.13. (a),(b) Oval geometry with an example of chaotic thermal trajectory (a) and its marked sections (b). (c),(d) Real and imaginary parts of the mobility spectra  $\mu_{xx}$  and  $\mu_{yy}$  of degenerate electron gas confined in the geometry from panel (a). The spectra were calculated using the Monte-Carlo method based on Kubo formalism ( $v_F = 1000$  m/s,  $E_F = 0.20$  eV,  $T = 4$  K,  $\tau_s = 1$  ns,  $m = 0.07m_e$ ). (e),(f) The windowed Fourier transforms of the velocity components  $v_x(t)$  and  $v_y(t)$  corresponding to the chaotic trajectory from panel (a). The arrow colors match the trajectory sections in panel (b).

stadium (Fig. 5.13) [93]. The mobility tensor component  $\mu_{yy}$  corresponds mainly to the bouncing of carriers between the vertical planes. Its spectrum (Fig. 5.13(c),(d)) is then similar to that of the 2D rectangular well (Fig. 5.5(b)) as it also exhibits a series of geometrical resonances. Qualitatively similar, but less pronounced features appear in the spectrum of  $\mu_{xx}$ . Here, we can resolve the fundamental geometrical resonance ( $\sim 1.7$  THz) which corresponds to the horizontal bouncing of charges between the semicircular parts. The peak at third harmonic frequency (slightly above 5 THz) is also pronounced. However, the higher harmonics are replaced by a series of irregularly spaced peaks.

To further confirm the origin of the peaks in the mobility spectrum (Fig. 5.13(c),(d)), we simulate a long trajectory of a single carrier. Then, we calculate a windowed Fourier transform (with a Gaussian window) of the temporal profile of velocity components  $v_x(t)$  and  $v_y(t)$  and plot the results as a 2D frequency-time maps (Fig. 5.13(e),(f)). This allows us to link the peaks in the velocity spectra with trajectory sections in time. The fundamental peak in the spectrum of  $\mu_{xx}$  then indeed originates from the bouncing of carriers between the semicircular oval parts. This motion is frequently interleaved by longer periods during which the carriers bounce between the vertical planes. The latter type of movement then leads to the geometrical resonances in the mobility  $\mu_{yy}$ . The presented analysis reveals that there is a broad distribution of quasi-periodic trajectories in this chaotic system. The corresponding peaks in the mobility spectrum are then rather broad. However, we can still clearly resolve them as they do not merge into a single broad-band as in the case of non-degenerate electron gas (Fig. 5.5(b)).

Further, we investigate the conductivity of 2D Lorentz gas potential in which the carriers scatter on periodically distributed cylinders arranged in a hexagonal lattice (Fig. 5.14(a)). This billiard model is used to simulate the thermal and electric conductivity of metals and it resembles the Drude model with random intervals between scattering events [94],[95]. Our calculations confirm this for smaller cylinder radii – the calculated spectra are dominated by a very narrow Drude peak at zero frequency (Fig. 5.14(b); due to hexagonal symmetry  $\mu_{xx} = \mu_{yy}$ ). With increasing cylinder radius, the mean time between scattering events becomes shorter and the Drude peak thus broadens and decreases. When the cylinders touch each other, the long-range transport is no longer possible and dc conductivity necessarily drops to zero. Above the Drude peak, the spectra exhibit an irregular series of peaks.

To find the origin of the irregular peaks in the mobility spectrum (Fig. 5.14(b)), we calculate the windowed Fourier transform of single-carrier trajectory (Fig. 5.14(d)). Here, we focus on the cylinder radius 30 nm, analogical conclusions would apply also for other cylinder radii. We first consider the pronounced peak located at  $\sim 12$  THz. The shortest possible distance between two cylinders is 40 nm. For the considered Fermi velocity ( $v_F = 1000$  m/s), this corresponds to the round-trip frequency of 12.5 THz. This implies that the considered peak in the spectrum originates from the carrier bouncing between the neighboring cylinders (this is also confirmed by the windowed Fourier transform – see the appropriate sections in the trajectory in Fig. 5.14(c)). The peaks at higher frequencies then cannot be linked to a specific quasi-periodic trajectories and they rather originate from the complex anharmonic character of thermal charge trajectories. Another feature in the mobility spectrum is the shoulder at  $\sim 3$  THz which is due to bouncing of carriers among more distant cylinders (Fig. 5.14(c),(d)).

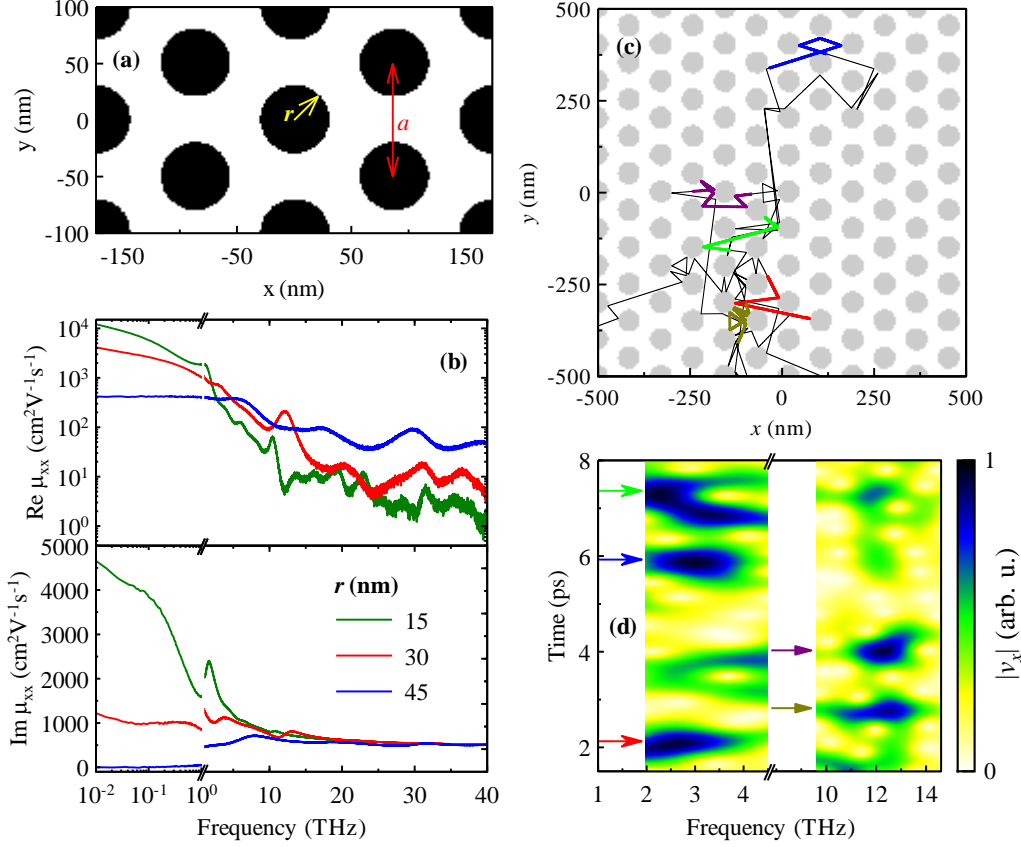


Fig. 5.14. (a) Scheme of hexagonal Lorentz gas potential for the calculations of mobility (period  $a = 100$  nm). (b) Mobility spectra  $\mu_{xx}$  of degenerate electron gas confined in the geometry from panel (a). The spectra were calculated using the Monte-Carlo method based on Kubo formalism for various cylinder radii  $r$  ( $v_F = 1000$  m/s,  $E_F = 0.20$  eV,  $T = 4$  K,  $\tau_s = 1$  ns). The hexagonal symmetry ensures that  $\mu_{xx} = \mu_{yy}$ . To emphasize the Drude-like peak at zero frequency, the scale up to 1 THz is logarithmic while the rest of the spectra is in the linear scale. (c) Example of the chaotic single-carrier trajectory in the geometry from panel (a). (d) Windowed Fourier transform (with a Gaussian window) of velocity component  $v_x(t)$  corresponding to the trajectory in panel (c). The color arrows then correspond to the sections marked in the trajectory in panel (c). The cylinders are smooth in the calculation whereas here they appear rasterized due to problems with rendering.

## 5.5 Conclusions

In this section, we calculated the linear terahertz conductivity spectra of carriers moving classically in various model nanostructures. We thoroughly analyzed the situation when most sources of broadening are suppressed. This essentially required us to consider a degenerate electron gas in which only the carriers close to the Fermi level contribute to the conductivity. The conductivity spectra then may exhibit specific features:

- For structures with rectangular geometries, the conductivity spectra exhibit a series of geometrical resonances which are directly associated with the frequency of the

round-trip bouncing and also with its higher harmonics due to anharmonic character of charge motion.

- The roundness of the structure surfaces can lead to emergence of complex patterns in the conductivity spectra. The origin of these features can be linked to complex trajectories and their higher harmonics.

Under common experimental conditions, the mobile charges form a non-degenerate electron gas. A broad distribution of charge velocities (and to a lesser extent also the bulk scattering and distribution of nanoelement sizes) then smears the sharp geometrical resonances into a single broad resonance.

In mutually isolated nanoelements, a plasmonic resonance develops and couples with the observed spectral features. In 1D nanostructures, the plasmonic mode dominates the response only at low carrier densities. In 3D systems, the plasmonic resonance then dominates in the spectra only at high enough carrier concentrations. The 2D nanostructures are then specific as the geometrical and plasmonic modes couple independently of the charge density.

## 6. Nonlinear THz conductivity of 1D confined electron gas

In section 5, we thoroughly explained the fundamental aspects of linear THz conductivity of confined degenerate and non-degenerate electron gases. Here, we expand these studies on the case of nonlinear response. For simplicity, however, we focus just on the microscopic conductivity of one-dimensional systems. In Section 7, we will cover the influence of the effective medium and also calculate the corresponding transient signals which can be measured in experiments.

### 6.1 Non-degenerate electron gas

In this part, we use the non-perturbative Monte-Carlo calculations to study the nonlinear conductivity of non-degenerate electron gas confined in a one-dimensional (1D) infinitely deep rectangular potential well with width  $l$  (Fig. 6.1(a)). In the calculations, we start with an equilibrium ensemble of carriers. At zero time, a monochromatic wave

$$E(t) = E_0 \cos(\omega_0 t), \quad (6.1)$$

with amplitude  $E_0$  starts to drive carriers out of the equilibrium. After a transient regime, which lasts a few times the scattering time, the mean carrier velocity  $\langle v(t) \rangle$  attains stationary oscillations (Fig. 6.1(b)) [29]. For sufficiently low electric fields (red curve in Fig. 6.1(b)), the linear response dominates and the oscillations of the mean velocity are thus monochromatic, generally phase shifted with respect to the driving field. With increasing electric field, the

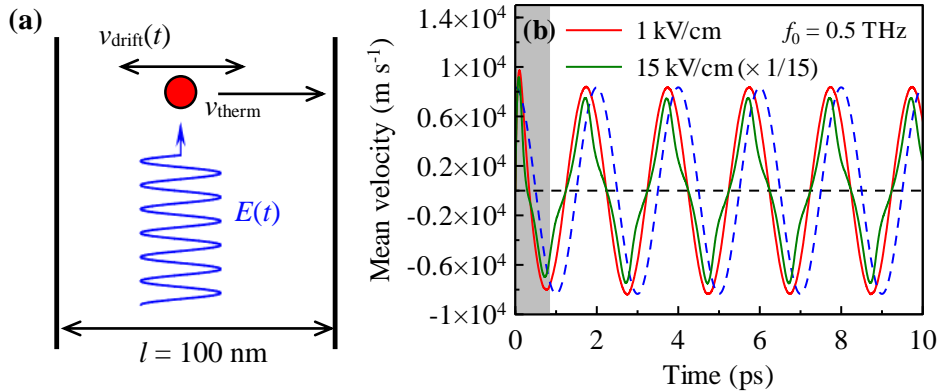


Fig. 6.1. (a) Schematic illustration of the investigated confined 1D non-degenerate electron gas subjected to a monochromatic wave (6.1). The net velocity of a single carrier is a superposition of the random thermal velocity  $v_{\text{therm}}$  and the drift velocity  $v_{\text{drift}}(t)$  induced by the electric field. (b) Solid lines: the time evolution of the carrier mean velocity for different amplitudes  $E_0$  of the driving electric field (dashed lines, arbitrary units). For lower fields, the harmonic profile of the oscillations is retained (red), while with increasing electric field the deviations from the harmonic profile become prominent (green). Gray area: Transient behavior of the mean velocity due to the sudden switch-on of the driving electric field. Following parameters were considered in the calculations:  $T = 300$  K,  $\tau_s = 100$  fs,  $m = 0.07m_e$ ,  $l = 100$  nm.

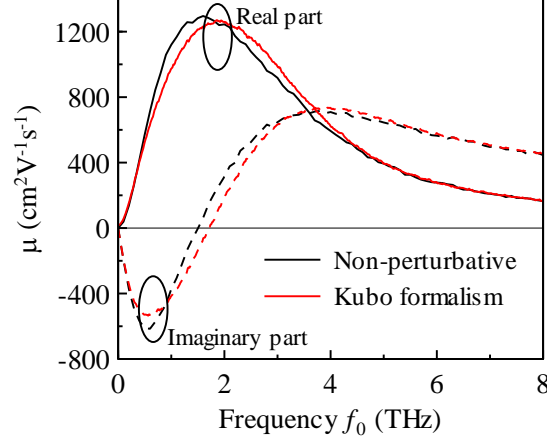


Fig. 6.2. Comparison between the linear responses of a 1D non-degenerate electron gas confined in an infinitely deep rectangular potential well calculated by the Kubo formalism calculations without the electric field [27] and the developed non-perturbative calculations, where the charges are driven by monochromatic waves with a low amplitude ( $E_0 = 0.1$  kV/cm). Parameters of the calculations:  $T = 300$  K,  $\tau_s = 100$  fs,  $l = 100$  nm,  $m = 0.07m_e$ .

oscillatory behavior is retained but the deviations from the harmonic time profile become prominent (green curve in Fig. 6.1). Spectral decomposition of the mean velocity (analogous to (1.12)) then straightforwardly yields the complex harmonic amplitudes  $v^{[m]}$  which can be further transformed into distinct non-linear orders  $v^{(a)}$ . The nonlinear mobilities  $\mu^{(a)}$  are then calculated by the framework described in Section 1.2. To obtain their entire spectra, it is necessary to calculate the conductivity for a set of discrete frequencies of the driving monochromatic wave.

### 6.1.1 Linear response

We start with the calculations with the field amplitude  $E_0 = 0.1$  kV/cm which is sufficiently weak for the charge transport to be linear (thermal velocity  $v_{\text{therm}} \sim 2.5 \times 10^5$  m.s<sup>-1</sup> for 300 K is much higher than the drift velocity  $v_{\text{drift}} \sim \mu E_0 \sim 2 \times 10^3$  m.s<sup>-1</sup>; moreover, we verified that the shape of the spectrum does not change noticeably for fields up to 1 kV/cm). In Fig. 6.2, we present the comparison of the linear mobility spectra  $\mu(\omega) (\equiv \mu^{(1)}(\omega))$  obtained by the Kubo formalism calculations (i.e. thermal motion without the electric field) [27] and the non-perturbative calculations (i.e. with the electric field) developed here. Both spectra show qualitatively the same resonant-like behavior typical for the response of confined carriers. Quantitatively, however, the shapes of the spectra slightly differ. This can be ascribed to the influence of the electric field on the statistical distribution, which we do not consider in our approach. In linear calculations, where no electric field is present, the equilibrium Boltzmann statistics is well defined. In the nonlinear calculations, however, we require the presence of a time-varying electric field which pushes the system out of the equilibrium. This leads to the modification of the statistical distribution function in time which influences the carrier ensemble properties and thus can alter the shape of the mobility spectrum. Furthermore, we

assume that the carriers become thermalized after the bulk scattering event. The presence of the electric field, however, changes the conditions under which the scattering occurs and may in reality lead to a non-equilibrium distribution.

### 6.1.2 Nonlinear response – high harmonics generation

Here, we consider the nonlinear response of the confined non-degenerate electron gas. In analogy to linear response (1.4), we define the harmonic mobility  $\mu^{[m]} = v^{[m]}/E_0$ . In Fig. 6.3, we show an example of the calculated spectra of  $\mu^{[m]}$ . In contrast to the weakly nonlinear regime known from the nonlinear optics, we observe nonlinearities of much higher orders – here, for the strongest presented electric field of 200 kV/cm, harmonic orders exceeding 91 with strengths of  $10^{-4}$  of the first harmonic order can be still recognized. We are aware that for fields exceeding a few times 10 kV/cm, other nonlinear effects may emerge, such as the intervalley scattering and intravalley dynamics [18]-[20] or ultrafast dynamics of polarons [96]. Nevertheless, our theoretical calculations predict an efficient high harmonics generation from a semiconductor nanostructure as a consequence of carrier confinement (4.11).

High harmonics generation is a well-known effect which was experimentally observed in the THz spectral range for bulk semiconducting GaSe [24], where the dynamical Bloch oscillations of the electron wave packet in the band structure combined with coherent interband excitation were identified as its origin. In contrast, we do not consider any quantum effects in our calculations where the carriers move strictly according to the classical Newton's equations of motion (2.5).

High harmonics generation is also achieved in atomic gases where it is usually described by a semi-classical three-step model [99]. In the first step, electrons are ionized from the atomic shell, then they are accelerated in the free space by an external laser electric field and finally they recombine with the original ion; the excess electron energy is then emitted in the form of the high-harmonic photon. This model is thus similar to our situation, in the sense that it also considers classical movement under a time-varying electric field. The difference, however, lies within the generation of high-harmonic photons. The three-step model considers recombination of electrons with ions while in our case, the generation is due to the time-varying electric current.

We thus predict another mechanism leading to high harmonics generation – the interplay between the oscillatory movement of carriers and the charge confinement. While the two other mechanisms require electric fields comparable to the atomic fields ( $\sim$  MV/cm) to enable efficient high harmonics generation, we achieve it for much lower fields of several tens of kV/cm.

### 6.1.3 Qualitative properties of harmonic mobility spectra

The response at the fundamental frequency  $\mu^{[1]}(f_0)$  (Fig. 6.3(a)) exhibits the behavior typical for the response of confined carriers. The resonant peak in the real part clearly decreases, blueshifts and broadens with the increasing electric field while the spectral weight



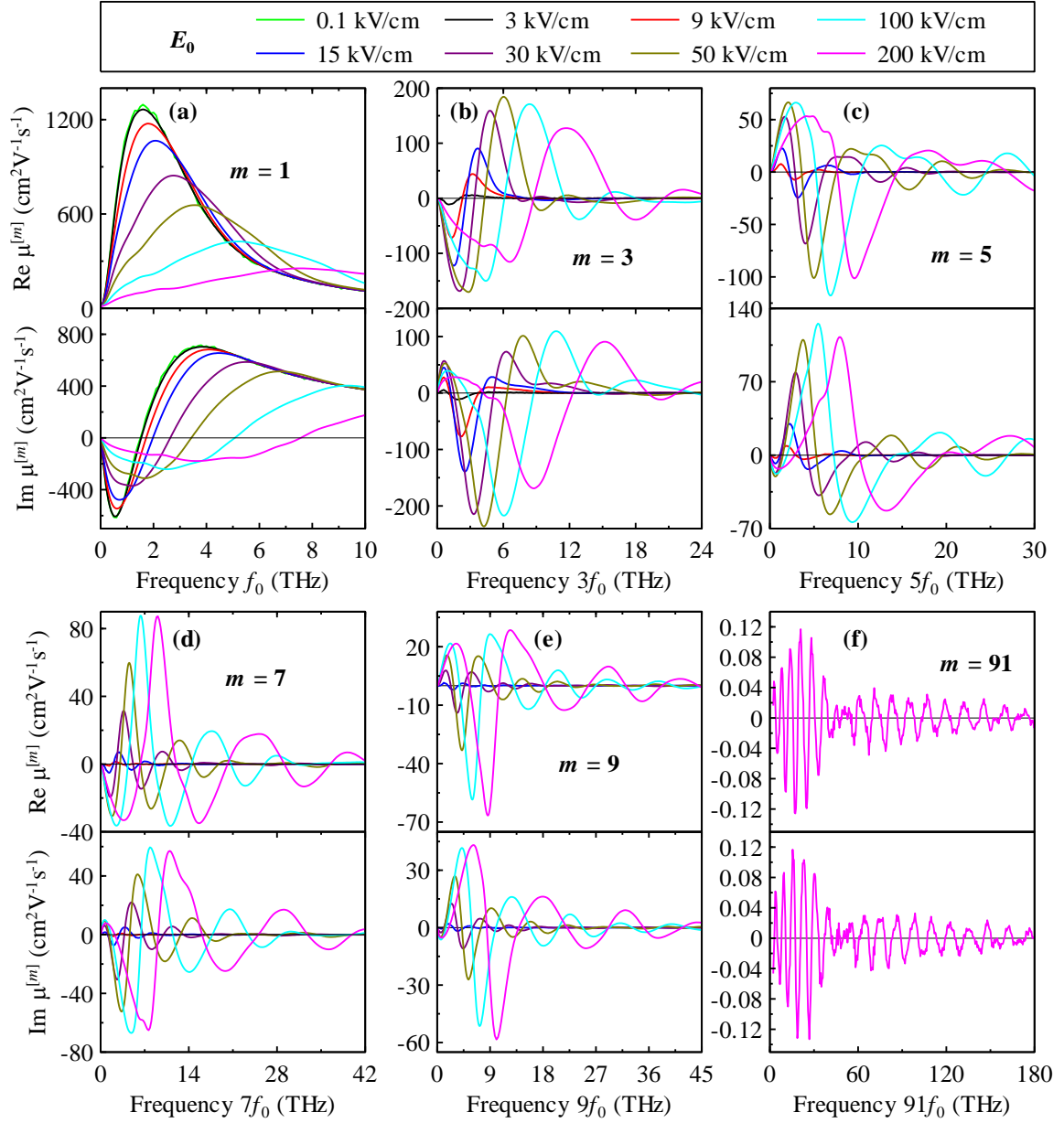


Fig. 6.3. Spectra of harmonic mobility amplitudes  $\mu^{[m]}$  obtained by the non-perturbative Monte-Carlo calculations for the 1D non-degenerate electron gas confined in an infinitely deep rectangular potential well and subjected to a monochromatic electric field (6.1). Following parameters were considered in the calculations:  $T = 300$  K,  $\tau_s = 100$  fs,  $m = 0.07m_e$ ,  $l = 100$  nm.

remains conserved. When the electric field is very weak, the frequency of this peak is proportional to the thermal velocity of carriers  $v_{\text{therm}}$  [27]

$$f_{\text{peak}} = \frac{v_{\text{therm}}}{2\alpha l}, \quad (6.2)$$

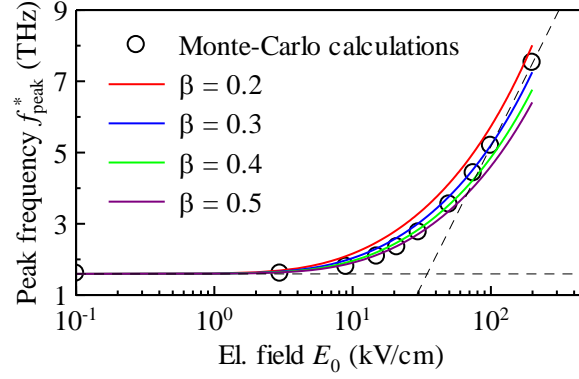


Fig. 6.4. Dependence of the frequency  $f_{\text{peak}}^*$  of the spectral peak in  $\mu^{[1]}$  from Fig. 6.3(a) on the amplitude of the electric field  $E_0$ . Circles: results of the Monte-Carlo calculations, lines: dependencies calculated from (6.6) for various values of geometrical factor  $\beta$ . The geometrical factor  $\alpha = 0.8$  was determined from the spectrum calculated for the lowest electric field. Dashed lines represent the slopes of the depicted dependence for low and high electric field limits.

where  $\alpha$  is an empirical factor related to the shape of the confining potential and the distribution of thermal velocities. A strong electric field induces a drift contribution to the carrier velocity  $v_{\text{drift}}$  which we estimate as a time-average of the solution of Newton's equations (2.5) over the period of the electric field

$$v_{\text{drift}}^2 = \frac{1}{T} \int_0^T v^2(t) dt = \frac{1}{T} \int_0^T \frac{e_0^2 E_0^2}{m^2} \sin^2(2\pi f_0 t) dt = \frac{e_0^2 E_0^2}{8\pi^2 m^2 f_0^2}, \quad (6.3)$$

where  $T = 1/f_0$  is the period of the electric field. The net velocity  $v$  of carrier then consists of both the thermal and the drift components, respectively, which sum up incoherently and thus

$$v = \sqrt{\frac{v_{\text{therm}}^2}{\alpha^2} + \frac{v_{\text{drift}}^2}{\beta^2}}, \quad (6.4)$$

where we introduce a factor  $\beta$  to account for the geometry and exact shape of distribution of thermal velocities. The peak frequency then changes to

$$f_{\text{peak}}^* = \frac{v}{2\alpha l}. \quad (6.5)$$

The substitution of (6.4) (with the frequency  $f_{\text{peak}}^*$  in the field term  $v_{\text{field}}$ ) into (6.5) leads to a quadratic equation for the shifted peak frequency  $f_{\text{peak}}^*$ . Its solution then yields the relation between the peak frequency and the amplitude of the electric field

$$f_{\text{peak}}^* = \frac{\sqrt{\frac{v_{\text{therm}}^2}{\alpha^2}} + \sqrt{\frac{v_{\text{therm}}^4}{\alpha^4} + 2\alpha^2 l^2 \frac{e_0^2 E_0^2}{\pi^2 \beta^2 m^2}}}{2\sqrt{2}\alpha l}. \quad (6.6)$$

For the parameters used in the presented calculations ( $T = 300$  K,  $m = 0.07m_e$ ), the thermal velocity is  $v_{\text{therm}} \sim 2 \times 10^5$  m.s<sup>-1</sup>. Comparison of (6.2) with the spectrum for the lowest electric field (Fig. 6.3(a)) gives an estimate  $\alpha \sim 0.8$  and the geometrical factor  $\beta$  thus remains the only unknown parameter in the above formula. Its fitting allows us to reproduce peak positions obtained by the Monte-Carlo calculations (Fig. 6.4). We can qualitatively distinguish several regimes in this dependence. For the lowest electric fields, their influence is negligible and the thermal velocity thus solely governs the peak position which thus remains constant. When the field increases, its contribution to the velocity of carriers becomes comparable to the thermal one and departure from the constant value is observed. Finally, the field contribution completely takes over for the strongest fields and peak frequency thus starts to follow the square-root dependence on field amplitude.

We now address the response at higher harmonic frequencies  $\mu^{[m]}(mf_0)$  ( $m > 1$ , Fig. 6.3(b)-(f)). Since the studied system has a center of symmetry, the even harmonic and nonlinear orders are not present. The nonlinear spectra show more complicated behavior than their linear counterparts (Fig. 6.3(a)). They clearly broaden and blueshift with increasing electric field while their amplitude changes in a more complex way, however, no other significant changes in their shape are observed.

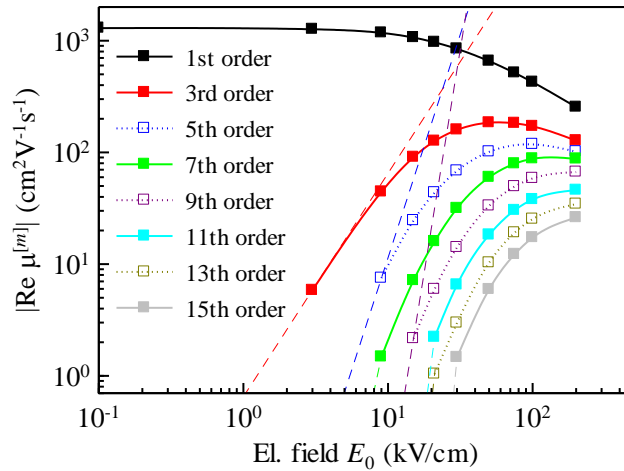


Fig. 6.5. Dependence of the absolute value of the first extreme of the real part of the harmonic spectra in Fig. 6.3 on the amplitude of the electric field  $E_0$ . With increasing electric field, the amplitude of the first harmonics decreases at the expense of higher harmonics. The amplitudes of the higher harmonics rapidly increase with electric field until reaching a saturated state. For the lowest harmonics, we also observe the beginning of their depletion. Filled symbols: first maximum in the spectrum, hollow symbols: first minimum in the spectrum. Dashed indicate the  $E_0^{(m-1)}$ -dependence which the peaks should follow in weak electric field.

Based on the above observations, we quantify the dependence of the harmonic spectra (Fig. 6.3) on the electric field by the absolute value of the first extreme in the real part of the mobility  $\mu^{[m]}$ , i.e. the local minimum or maximum of the real part of  $\mu^{[m]}$  which lies at the lowest non-zero frequency (Fig. 6.5). The peak of the linear amplitude  $\mu^{[1]}$  is initially constant but with increasing electric field, it decreases due to the spectral broadening. Meanwhile, the higher harmonic amplitudes  $\mu^{[m]}$  exhibit three different regimes in their dependence on the electric field. Initially, the nonlinearities rapidly increase with the  $m$ -th power of the electric field  $E_0^m$  (in Fig. 6.5, due to the normalization by field amplitude  $E_0$ , the nonlinearities increase with  $E_0^{m-1}$ ). This power dependence is followed even for low electric fields where we cannot resolve the mobilities  $\mu^{[m]}$  due to the noise in the calculations. Eventually, the strong dependence on the electric field disappears and the nonlinear velocity becomes saturated. For the lowest orders ( $m = 3, 5$ ), we also observe the third regime, where the decrease due to the spectral broadening begins for the strongest electric fields.

#### 6.1.4 Analogy with an anharmonic oscillator

Using the framework developed in Section 1.2, we calculate the odd nonlinear mobilities  $\mu^{(a)}$  from the spectra of harmonics  $\mu^{[m]}$  in Fig. 6.3 corresponding to a motion of charges in an infinitely deep rectangular potential well. The mobility spectra  $\mu^{(a)}$  up to the fifth order are shown in Fig. 6.6. The spectrum of  $\mu^{(5)}(-\omega_0, -\omega_0, \omega_0, \omega_0, \omega_0)$  is not shown because its peak amplitude is comparable with the noise originating from the calculations. We emphasize the frequency arguments of the discussed quantities. Whereas the harmonic mobilities  $\mu^{[m]}$  are naturally functions of the  $m$ -th harmonic frequency  $m\omega_0$ , we display the nonlinear mobilities  $\mu^{(a)}$  as functions of the fundamental frequency  $\omega_0$ . The first-order mobility  $\mu^{(1)}(\omega_0)$  (Fig. 6.6(a)) is essentially the same as the linear mobility (Fig. 6.2) and its spectrum reflects the carrier confinement, while the spectra of the third- and the fifth-order mobility are more complicated (Fig. 6.6(b),(c)). The mobility spectra are expected to be smooth – their roughness in Fig. 6.6 is due to the noise originating from Monte-Carlo calculations which is amplified due to ill-conditioning of the matrices in (1.18) and (1.19) (as we discussed in Section 1.2).

The nonlinear mobility spectra  $\mu^{(a)}$  in Fig. 6.6 can be interpreted qualitatively in terms of a classical anharmonic oscillator (i.e. nonlinear Lorentz model) [28]. In the linear Lorentz model, electrons oscillate around a minimum in a parabolic potential. The nonlinear behavior is then accounted for by an anharmonic correction to this potential. Here, we assume nonlinearities up to the fifth order, for which the binding potential reads  $V(x) = m\Omega_{\text{osc}}^2 x^2/2 - mbx^4/4 - mcx^6/6$ , where  $\Omega_{\text{osc}}$  is the resonant oscillator angular frequency and  $b$  and  $c$  are parameters characterizing the strength of the nonlinearity (i.e. the deviation from the parabolic binding potential). The sign of parameter  $b$  is arbitrary while  $c$  must be negative to guarantee the binding character of the potential. If we introduce  $\mathcal{N}(\omega_0) = \Omega_{\text{osc}}^2 - \omega_0^2 - 2i\omega_0\gamma$ , where  $\gamma$  is the oscillator damping rate, the pertinent mobilities of the anharmonic oscillator read (see appendix B for the derivation)

$$\mu^{(1)}(\omega_0) = -i\omega_0 \frac{e_0}{m} \frac{1}{\mathcal{N}(\omega_0)} \quad (6.7.1)$$

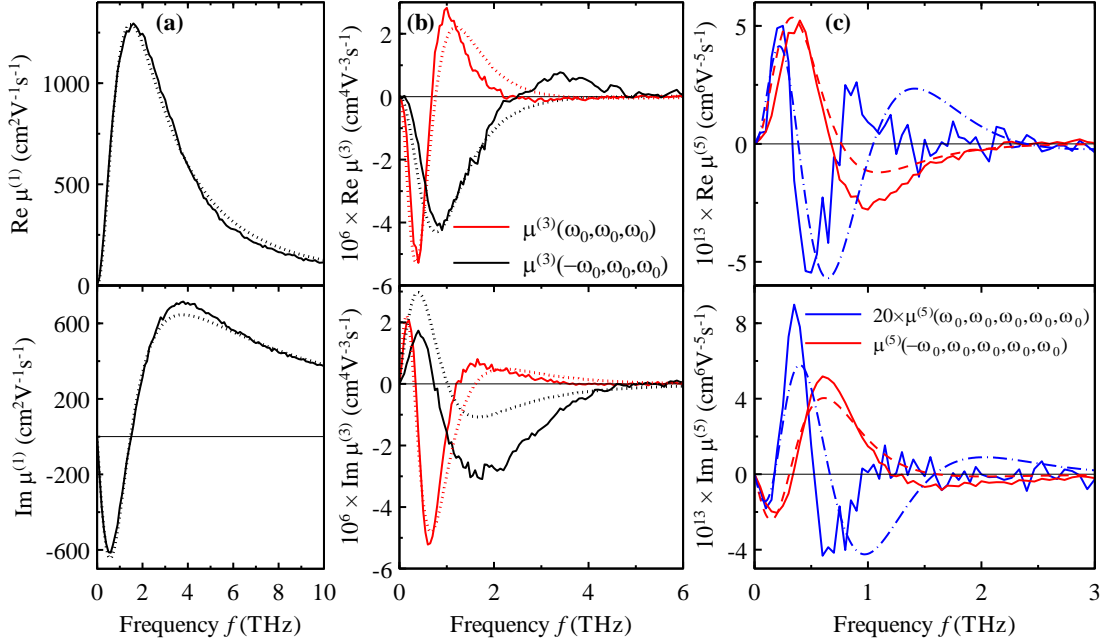


Fig. 6.6. Nonlinear mobilities  $\mu^{(a)}$  of carriers from the non-degenerate electron gas confined in an infinitely deep rectangular potential well. Solid lines: spectra calculated from the harmonic mobilities  $\mu^{[m]}$  in Fig. 6.3 using the framework developed in Section 1.2 (spectra for 0.1 kV/cm, 3 kV/cm and 5 kV/cm were used for the decomposition). The spectrum of  $\mu^{(5)}(-\omega_0, -\omega_0, \omega_0, \omega_0, \omega_0)$  is not shown because its peak amplitude is comparable with the noise originating from the calculations. Dotted lines: spectra predicted by the anharmonic oscillator model (6.7.1)-(6.7.3). The spectra were normalized individually to match the peak amplitude of the extracted mobilities  $\mu^{(a)}$ . Dashed line: normalized spectrum of the  $c$ -term from (6.7.5). Dot-dash line: linear combination of  $c$ -term and net  $b$ -term from (6.7.4). Both terms were normalized to peak mobility amplitude and then the  $c$ -term was subtracted ( $c < 0$ ) from the net  $b$ -term which was taken with the weight of 1.5. Following parameters of the anharmonic oscillator were assumed:  $\Omega_{\text{osc}} = 1.5$  THz,  $\gamma = 10$  ps<sup>-1</sup>.

$$\mu^{(3)}(\omega_0, \omega_0, \omega_0) = -i3\omega_0 \frac{e_0^3}{4m^3} \frac{b}{\mathcal{N}(3\omega_0)\mathcal{N}^3(\omega_0)} \quad (6.7.2)$$

$$\mu^{(3)}(-\omega_0, \omega_0, \omega_0) = -i\omega_0 \frac{e_0^3}{4m^3} \frac{3b}{\mathcal{N}(\omega_0)\mathcal{N}^2(\omega_0)\mathcal{N}(-\omega_0)} \quad (6.7.3)$$

$$\begin{aligned} \mu^{(5)}(\omega_0, \omega_0, \omega_0, \omega_0, \omega_0) = & -i5\omega_0 \frac{e_0^5}{16m^5} \left[ \frac{c}{\mathcal{N}(5\omega_0)\mathcal{N}^5(\omega_0)} + \right. \\ & \left. + \frac{3b^2}{\mathcal{N}(5\omega_0)\mathcal{N}^2(\omega_0)\mathcal{N}(3\omega_0)\mathcal{N}^3(\omega_0)} \right] \end{aligned} \quad (6.7.4)$$

$$\begin{aligned} \mu^{(5)}(-\omega_0, \omega_0, \omega_0, \omega_0, \omega_0) = & -i3\omega_0 \frac{e_0^5}{16m^5} \left[ \frac{5c}{\mathcal{N}(3\omega_0)\mathcal{N}^4(\omega_0)\mathcal{N}(-\omega_0)} + \right. \\ & + \frac{3b^2}{\mathcal{N}(3\omega_0)\mathcal{N}^2(\omega_0)\mathcal{N}(\omega_0)\mathcal{N}^2(\omega_0)\mathcal{N}(-\omega_0)} + \\ & \left. + \frac{6b^2}{\mathcal{N}(3\omega_0)\mathcal{N}(\omega_0)\mathcal{N}(-\omega_0)\mathcal{N}(3\omega_0)\mathcal{N}^3(\omega_0)} \right] \end{aligned} \quad (6.7.5)$$

$$\begin{aligned} \mu^{(5)}(-\omega_0, -\omega_0, \omega_0, \omega_0, \omega_0) = & -i\omega_0 \frac{e_0^5}{16m^5} \left[ \frac{10c}{\mathcal{N}(\omega_0)\mathcal{N}^3(\omega_0)\mathcal{N}^2(-\omega_0)} + \right. \\ & + \frac{3b^2}{\mathcal{N}(\omega_0)\mathcal{N}^2(-\omega_0)\mathcal{N}(3\omega_0)\mathcal{N}^3(\omega_0)} + \\ & \left. + \frac{9b^2}{\mathcal{N}(\omega_0)\mathcal{N}^2(\omega_0)\mathcal{N}(-\omega_0)\mathcal{N}^2(\omega_0)\mathcal{N}(-\omega_0)} \right] \end{aligned} \quad (6.7.6)$$

The shape of the first-order mobility  $\mu^{(1)}(\omega_0)$  is well reproduced by (6.7.1) for  $\Omega_{\text{osc}} = 1.5$  THz and  $\gamma = 10$  ps<sup>-1</sup> (Fig. 6.6(a)). However, the anharmonic oscillator model predicts five times lower amplitude. This stems from the difference between the polynomial potential of the anharmonic oscillator and the rectangular potential used in the Monte-Carlo calculations. For the considered parameters  $\Omega_{\text{osc}}$  and  $\gamma$ , a good qualitative match in the spectral shapes is obtained also for the third-order mobilities  $\mu^{(3)}(\omega_0, \omega_0, \omega_0)$  and  $\mu^{(3)}(-\omega_0, \omega_0, \omega_0)$ , respectively (Fig. 6.6(b)). Similarly to the linear case, both models predict different spectral amplitudes. Furthermore, the anharmonic oscillator model does not correctly scale  $\mu^{(3)}(-\omega_0, \omega_0, \omega_0)$  with respect to  $\mu^{(3)}(\omega_0, \omega_0, \omega_0)$ . Similar analysis of the fifth-order mobilities is more complicated due to the presence of several terms with different frequency dependence (6.7.4)-(6.7.6). Nevertheless, the shape of the spectra can be also understood within this framework – the spectrum of  $\mu^{(5)}(-\omega_0, \omega_0, \omega_0, \omega_0, \omega_0)$  is qualitatively matched just by the  $c$ -term from (6.7.5), while the shape of  $\mu^{(5)}(\omega_0, \omega_0, \omega_0, \omega_0, \omega_0)$  is reproduced by (6.7.4) if we consider  $c < 0$  and take the net  $b$ -term with the weight of 1.5.

The real and imaginary parts of the first-order mobility must always satisfy the Kramers-Kronig (K-K) relations. Their applicability for the nonlinearities is discussed in detail in [28] and [100]. On the one hand, the K-K relations still apply for the mobilities  $\mu^{(3)}(\omega_0, \omega_0, \omega_0)$  and  $\mu^{(5)}(\omega_0, \omega_0, \omega_0, \omega_0, \omega_0)$ . On the other hand, they are not valid for the mobilities  $\mu^{(3)}(-\omega_0, \omega_0, \omega_0)$ ,  $\mu^{(5)}(-\omega_0, \omega_0, \omega_0, \omega_0, \omega_0)$  and  $\mu^{(5)}(-\omega_0, -\omega_0, \omega_0, \omega_0, \omega_0)$ , respectively, with respect to the frequency  $\omega_0$ .

## 6.2 Degenerate electron gas

In this section, we turn to the nonlinear response of a degenerate electron confined in a one-dimensional infinitely deep rectangular potential well with width  $l$  (Fig. 6.1(a)). In Section 5.2, we have shown that the linear mobility of such system consists of a series of peaks which are located at the frequency  $f_r = 1/t_r$ , where  $t_r$  is the round-trip time of the carriers

inside the well, and its odd harmonics. In analogy with the non-degenerate case, we calculate the response to a monochromatic wave (6.1). For simplicity, we limit the incident frequencies to  $f \leq 2f_r = 10$  THz, thus focusing on the response just around the peak at the fundamental frequency  $f_r$ .

In Fig. 6.7 we show the calculated spectra of the harmonic mobility  $\mu^{[m]}$ . In comparison to the non-degenerate electron gas (Fig. 6.3), we observe a much stronger dependence on the electric field. Indeed, while the response for the field 0.1 kV/cm can be considered linear in the non-degenerate case, here we can resolve nonlinearities up to the fifth order. Such strong nonlinear response appears since the driving field is in resonance with the motion of carriers inside the well. This, however, means that the linear regime is practically unattainable by the non-perturbative Monte-Carlo calculations (for fields below  $\sim 0.1$  kV/cm, the results are hindered by noise). We thus calculate the linear mobility  $\mu$  using the Kubo-based formalism (we have to be aware of the slight quantitative differences between the spectra calculated by both approaches (Fig. 6.2)). Furthermore, it is not possible to obtain the nonlinear mobilities  $\mu^{(a)}$  using the framework from Section 1.2 since the harmonic series cannot be truncated (higher orders are important even for low fields). We thus further focus just on the characteristics of the harmonic spectra from Fig. 6.7.

For the response at the fundamental frequency  $\mu^{[1]}(f_0)$  (Fig. 6.7(a)), the resonant peak at the frequency  $f_r$  is preserved only for the lowest electric fields considered. For higher fields ( $\geq 1$  kV/cm), this peak splits into a doublet. We will later explain this splitting qualitatively.

The main feature of spectra of higher harmonics  $\mu^{[m]}(mf_0)$  ( $m > 1$ ) are peaks located at the odd harmonic frequencies  $mf_r$  which further split into multiplets with increasing  $E$  (Fig. 6.7(b)-(d)). The number of sub-peaks within the multiplet increases with the harmonic order  $m$ . Similarly to the response of the first order, these sub-peaks broaden and move away from the central frequency  $mf_r$ .

For fields stronger than  $\sim 1$  kV/cm, we can in each spectrum of  $\mu^{[m]}$  resolve further peaks located close to frequencies  $nf_r$ , where  $n$  is an integer lower than  $m$  (insets in Fig. 6.7(b)-(d)). These peaks appear due to the resonant character of carrier motion inside the well. With increasing field, they broaden and blueshift. For high enough fields, there is necessarily an overlap with the redshifting multiplets around  $mf_r$  described above. Furthermore, the whole spectra blueshift for sufficiently strong fields. This shift is most obvious in the response of the first order (Fig. 6.7(a)). The nonlinear response of the confined degenerate electron gas is thus clearly very complicated and development of a model quantitatively explaining all observed features lies beyond the scope of this work.

### 6.2.1.a) Geometrical model describing the first order response

For a qualitative explanation of the splitting in the first-order harmonic spectra from Fig. 6.7(a), we develop a geometric model based on the classical movement of carriers subjected to a monochromatic wave (6.1) inside the well.

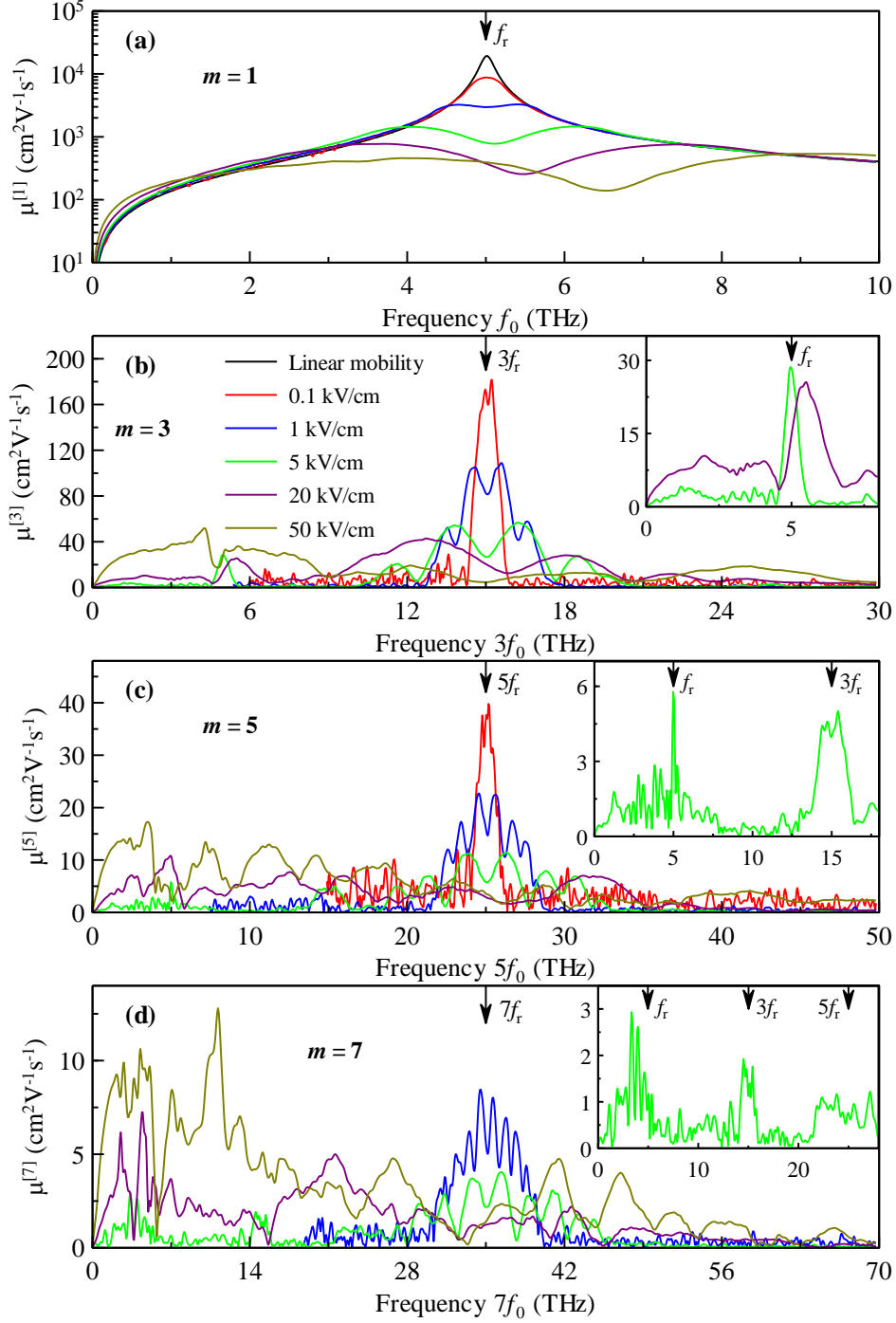


Fig. 6.7. Spectra of the harmonic mobility  $\mu^{[m]}$  obtained by the non-perturbative Monte-Carlo calculations for 1D degenerate electron gas confined in an infinitely deep rectangular potential well and subjected to a monochromatic electric field. Following parameters were considered:  $v_F = 10^6$  m/s,  $E_F = 0.2$  eV,  $T = 4$  K,  $\tau_s = 1$  ps,  $m = 0.07m_e$ ,  $l = 100$  nm. Real and imaginary parts of these spectra are shown in the Appendix C. The spectrum of the linear mobility was calculated by the Monte-Carlo calculations based on Kubo formalism. Insets: details of the secondary peaks in the nonlinear spectra located at frequencies  $nf_r$ .



We start with a carrier located at the left side of the well (i.e.  $x = 0$ , Fig. 6.8) in time  $t = 0$ . Its (drift) velocity evolves according to the equation of motion

$$\frac{dv(t)}{dt} + \frac{1}{\tau_s} [v(t) - v_F] = \frac{e_0 E_0}{m} \cos(\omega_0 t + \varphi_0), \quad (6.8)$$

where  $v_F$  is the Fermi velocity and  $\varphi_0$  represents the initial phase shift between the applied field and the carrier movement. The solution reads

$$v(t) = v_F + v_0 e^{-t/\tau_s} + \frac{e_0 E_0 \tau_s}{m} \operatorname{Re} \left\{ \frac{e^{i(\omega_0 t + \varphi_0)}}{1 + i\omega_0 \tau_s} \right\}, \quad (6.9)$$

where  $v_0$  is the drift velocity acquired during the previous driven motion (on top of the Fermi velocity). If we turned off the electric field,  $v(t)$  would decay towards  $v_F$  with the time constant equal to the scattering time  $\tau_s$ .

Using (6.9), we now describe the movement of charges inside the well for a given initial phase  $\varphi_0$ . First, we find the time  $t_1$  at which the carrier reaches the opposite well wall, i.e. it travels the distance  $l$  (Fig. 6.8). We assume low enough fields which prevent multiple bouncing of carriers by a single wall during their round-trips. Integration of (6.9) yields

$$v_F t_1 + v_0 \tau_s (1 - e^{-t_1/\tau_s}) + \frac{e_0 E_0 \tau_s}{m} \operatorname{Re} \left\{ \frac{e^{i(\omega_0 t_1 + \varphi_0)} - e^{i\varphi_0}}{i\omega_0 (1 + i\omega_0 \tau_s)} \right\} - l = 0, \quad (6.10)$$

which is a transcendental equation for  $t_1$  which has to be solved numerically. The carrier then reaches the right wall with velocity  $v_F + v_1$ , where the drift component  $v_1 = v(t_1)$  is given

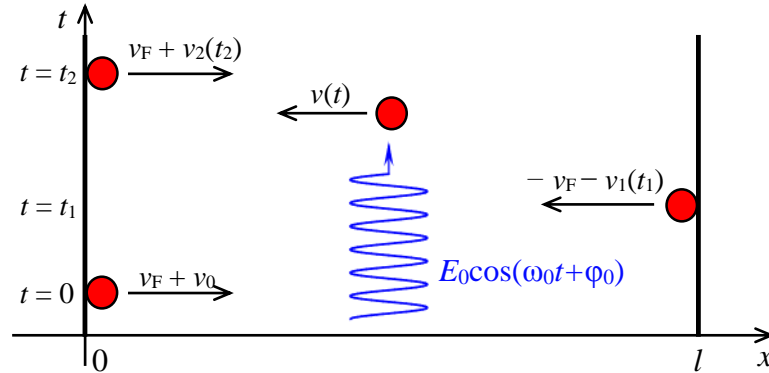


Fig. 6.8. Illustration of the carrier movement within the well under the monochromatic electric field  $E_0 \cos(\omega_0 t + \varphi_0)$ . At zero time, the carrier is located at the left well wall ( $x = 0$ ) and moves with velocity  $v_F + v_0$ . At the time  $t_1$ , the carrier reaches the right well wall and upon the reflection, it moves back with velocity  $-v_F - v_0(t_1)$ . Finally, the carrier returns to the left wall at  $t = t_2$  and upon reflection, it has velocity  $v_F + v_2(t_2)$ . In reality, the carrier dimensions are negligible with respect to the well width  $l$ .

by (6.9). Upon reflection, the carrier moves back towards the original wall and reaches it at the time  $t_2$  which satisfies transcendental equation

$$l - v_F(t_2 - t_1) + v_1 \tau_s \left( e^{\frac{t_2 - t_1}{\tau_s}} - 1 \right) + \frac{e_0 E_0 \tau_s}{m} \operatorname{Re} \left\{ \frac{e^{i(\omega_0 t_2 + \varphi_0)} - e^{i(\omega_0 t_1 + \varphi_0)}}{i\omega_0(1 + i\omega_0 \tau_s)} \right\} = 0. \quad (6.11)$$

Just after the reflection from the left well wall, the drift component  $v_2$  reads

$$v_2 = v_1 e^{-\frac{t_2 - t_1}{\tau_s}} - \frac{e_0 E_0 \tau_s}{m} \operatorname{Re} \left\{ \frac{e^{i(\omega_0 t_2 + \varphi_0)}}{1 + i\omega_0 \tau_s} \right\}. \quad (6.12)$$

The motion of carriers described above will lead to a resonant behavior when two conditions are met. First, the period of the carrier movement must match the period of the field

$$t_1 + t_2 = \frac{2\pi}{\omega_0}. \quad (6.13)$$

Second, the described motion must be stationary. This requires the equality of the drift components at the beginning and at the end of the period

$$v_0 = v_2. \quad (6.14)$$

In Fig. 6.9, we show the frequency  $f_0 = 2\pi/\omega_0$  and the drift velocity  $v_0$ , which satisfy the conditions (6.13) and (6.14) simultaneously, as functions of the initial phase shift  $\varphi_0$  for several lowest electric fields. For  $0 \leq \varphi_0 \leq \pi$ , the resonant frequencies  $f_0$  are below  $f_r$  (Fig. 6.9(a)) and thus correspond to the lower-frequency peak in the doublet (Fig. 6.7(a)). Since

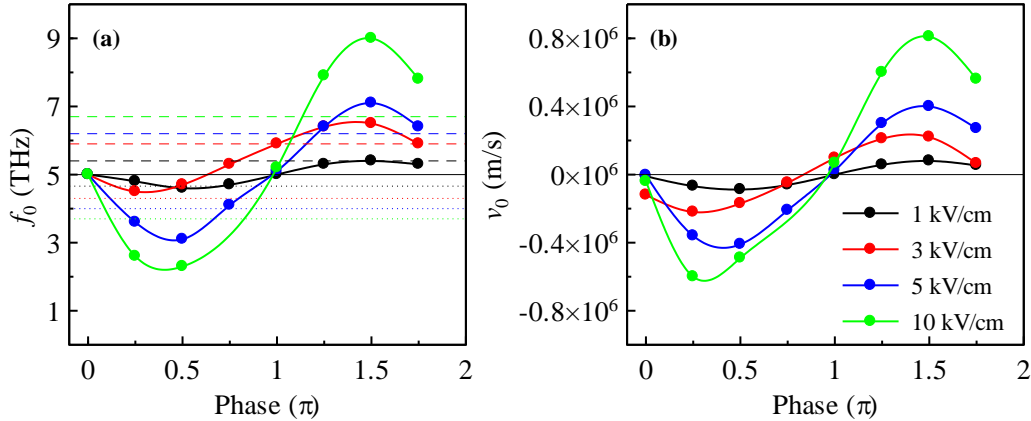


Fig. 6.9. Solution of the geometric model (Eqs. (6.9)-(6.14)) which explains the existence of the doublet in the first-order harmonic spectra of confined 1D degenerate electron gas (Fig. 6.7(a)). For the lowest electric field, the model also predicts the doublet frequencies. Dashed and dotted lines: doublet frequencies obtained by the Monte-Carlo calculations. Solid line in panel (a): the frequency of the fundamental geometrical resonance in the linear spectra (Fig. 5.5(b)).

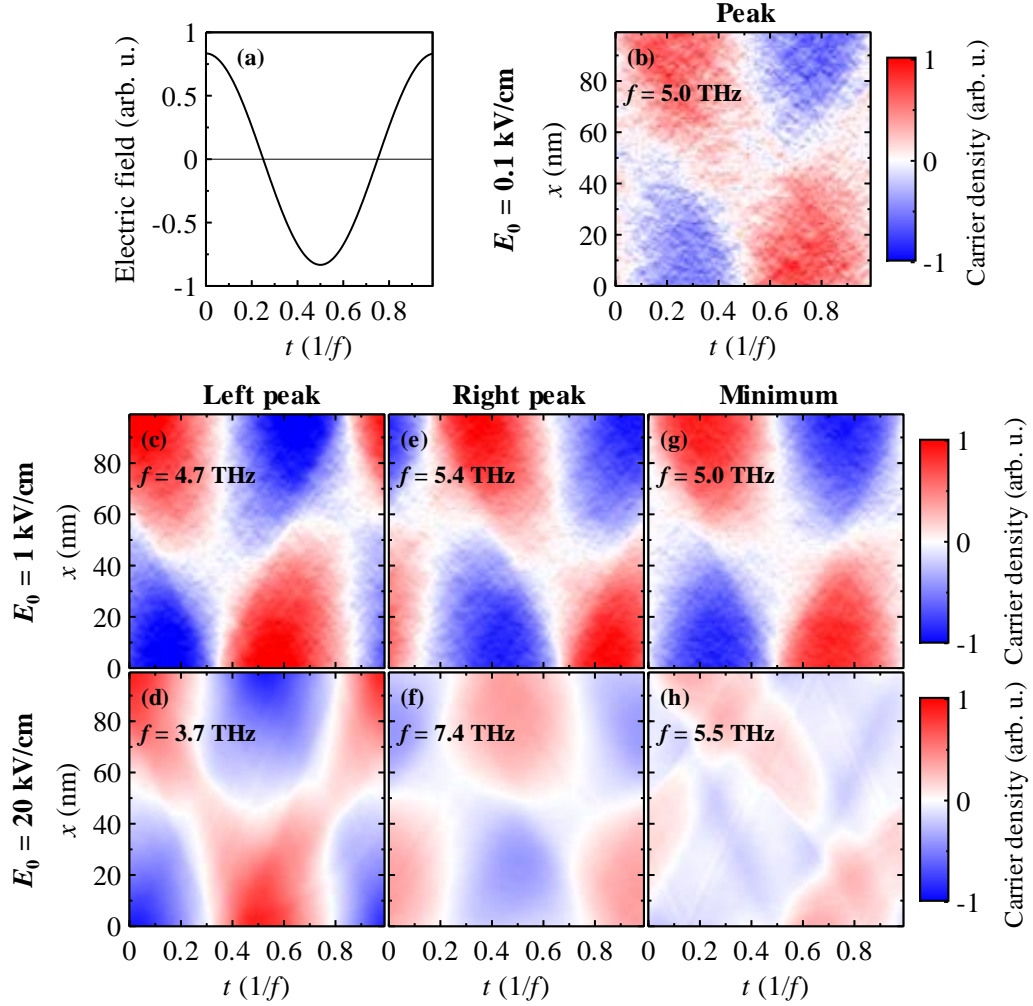


Fig. 6.10. Charge densities of the confined 1D degenerate electron gas for field amplitudes 0.1 kV/cm (panel (b)), 1 kV/cm (middle row) and 20 kV/cm (lower row) calculated using the non-perturbative Monte-Carlo calculations. The carriers were subjected to a monochromatic electric field 6.1. For 0.1 kV/cm, the field frequency  $f_0 = 5.0$  THz matches the peak position in the first order response (Fig. 6.7(a)). For higher fields, the selected frequencies  $f_0$  match the characteristic features of the doublet observed in the first order response: the redshifted sub-peak ((c),(d)), blueshifted sub-peak ((e),(f)) and the minimum ((g),(h)). Zero charge density in the maps represents the equilibrium value. The graph in panel (a) shows the time profile of the driving electric field.

the corresponding drift velocity  $v_0$  is negative (Fig. 6.9(b)), the carriers are effectively slowed down during their round-trip (with respect to the equilibrium Fermi velocity) and their velocity spectra thus redshift. On the other hand, for  $\pi \leq \varphi_0 \leq 2\pi$ , the resonant frequencies  $f_0$  are above  $f_r$  which leads to the emergence of the higher-frequency peak in the doublet as the carriers are moving faster ( $v_0 > 0$ ).

The solution of the geometric model gives the resonant frequency  $f_0$  as a continuous function of the phase shift  $\varphi_0$  (Fig. 6.9(a)). The resonant frequencies predicted by the

non-perturbative Monte-Carlo calculations (Fig. 6.7(a)) then correspond to  $\varphi_0$  for which the carrier movement occurs in stable periodic pathways. For other  $\varphi_0$ , the corresponding trajectories are unstable and rapidly converge into the stable pathways (i.e. due to the scattering). The exact evaluation of the stability conditions, however, would require further analysis which we do not cover here.

For a further insight, we tracked also the charge density within the well in the non-perturbative Monte-Carlo calculations (Fig. 6.10). For low enough electric fields ( $\lesssim 0.1$  kV/cm), the peak in  $\mu^{[1]}(f_0)$  does not split (Fig. 6.7(a)). For the peak frequency, the charge movement is in-phase with the driving field – the charges are located at the right well wall ( $x = 100$  nm) for the maximum field and at the left wall ( $x = 0$  nm) when the field reaches the lowest negative value (Fig. 6.10(b)). For higher fields, this behavior is preserved for frequencies around the redshifted sub-peak (Fig. 6.10(c),(d)). For frequencies near the blueshifted sub-peak, however, the charge movement is out-of-phase (Fig. 6.10(e),(f)). These features are well preserved with increasing electric field. The behavior around the minimum between the doublet peaks, however, becomes more complicated (Fig. 6.10(g),(h)).

### 6.3 Conclusions

We used the non-perturbative Monte-Carlo calculations to investigate the nonlinear THz conductivity of 1D confined non-degenerate and degenerate electron gases under monochromatic electric field. The response of both systems is well beyond the perturbative regime: we predicted an efficient high harmonics generation due to charge confinement.

Nonlinear THz conductivity spectra of the non-degenerate electron gas are qualitatively compatible with the response of an anharmonic oscillator. The conductivity spectra broaden and blueshift with the increasing electric field due to increasing mean charge velocity. The response of the degenerate electron gas is much more complicated. For low electric fields, the conductivity spectra contain peaks centered around the harmonic frequencies  $mf_r$  ( $f_r$  corresponds to the equilibrium round-trip time). With increasing electric field, each of these peaks splits into multiplets. At the same time, other complicated features emerge in the spectra due to the resonant character of the carrier motion inside the well.

## 7. Nonlinear THz response of semiconductor nanostructures

In section 6, we studied the nonlinear THz conductivity of confined one-dimensional electron gas. Here, we expand the calculations on selected multi-dimensional structures and more importantly employ the developed theory of wave propagation in nonlinear media (Section 4) to find measurable signals related to the nonlinearities. We thus provide a theoretical feasibility study for an experimental observation of nonlinear THz photoconductivity in nanostructures using free space THz radiation. We namely focus on non-percolated structures as percolation weakens the charge confinement and thus also the corresponding nonlinearities.

Table-top optical pump-THz probe time-domain spectroscopy usually utilizes THz pulses generated by optical rectification in nonlinear crystals. Fields generated this way, however, are not always strong enough to induce nonlinearities in the studied systems. We thus consider sources which can generate pulses with high enough field amplitudes for nonlinearities to occur – three different apparatuses will be examined in detail:

- **Tilted-wavefront optical rectification in lithium niobate**

Lithium niobate ( $\text{LiNbO}_3$ ) is a crystal with high nonlinear coefficient. However, the phase-matching condition in this material cannot be satisfied in a colinear scheme. To generate intense THz radiation, it is necessary to tilt the pump pulse wavefront using e.g. a diffraction grating [6]-[8]. This allows generation of pulses with peak amplitudes up to 1 MV/cm [14]. The generated THz pulse profiles and spectra strongly depend on the parameters of the employed optical pumping and the tilt angle [7],[101]-[104]. For simplicity, we perform the calculations with a model THz pulse with rather narrow spectrum (Fig. 7.1(a),(b)).

- **Generation from air-based plasma ("multi-THz")**

Above a certain intensity threshold, a laser pulse focused in air generates a plasma. A nonlinear interaction between the pulse at the fundamental frequency  $\omega$  and its second harmonics  $2\omega$  inside such plasma can be utilized to generate strong THz radiation [9]-[13]. The THz pulses generated this way exhibit very broad spectra ranging from about 1 THz to several tens of THz and their peak amplitudes can reach values over 100 kV/cm. These pulses are sometimes referred to as multi-THz. For the calculations of nonlinear conductivity, we use a multi-THz pulse measured in our experimental setup (without deconvoluted instrumental response) [47]. Its temporal profile with peak amplitude  $\sim 120$  kV/cm and spectrum containing frequencies up to 20 THz are shown in Fig. 7.1(c),(d).

- **Free electron lasers**

Free electron lasers are large-scale facilities which utilize a beam of relativistic electrons to generate tunable high-intensity radiation [15]-[17]. In this work, we focus on the FELBE facility located in Forschungszentrum Dresden-Rossendorf, Germany [106]-[108]. This laser operates in the far-infrared spectral range and allows generation of frequencies from  $\sim 1.2$  THz to  $\sim 75$  THz. The estimated peak electric fields are of the order of hundreds kV/cm and they are summarized in Fig. 7.2. The generated THz pulses

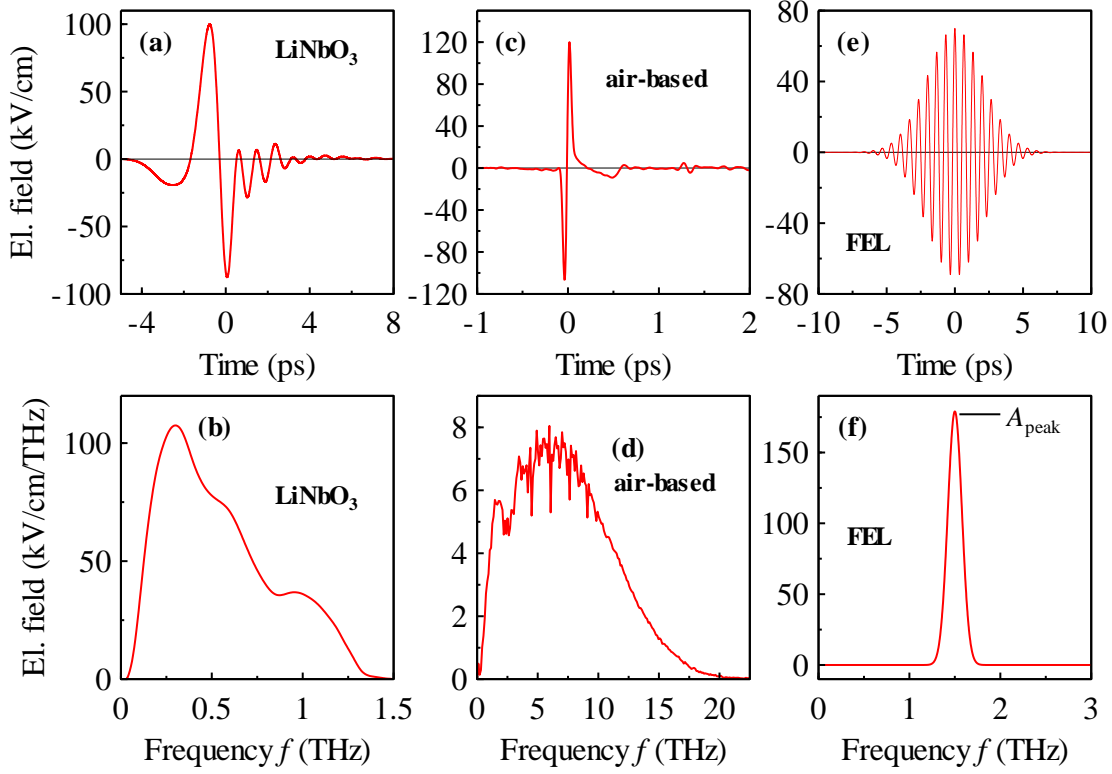


Fig. 7.1. Temporal profiles (upper row) and spectra (lower row) of high-field THz pulses used for the theoretical study of nonlinear response. (a),(b) Model of a pulse generated in a LiNbO<sub>3</sub> crystal. From historic reasons, we modelled it by broadening a THz pulse generated by optical rectification in ZnTe in time so it lasts twice longer. The resulting pulse spectrum is similar to that of LiNbO<sub>3</sub> in Ref. [105]. (c),(d) Multi-THz pulse generated in the air-based plasma measured in our experimental setup [47]. (e),(f) Model pulse generated by free electron laser. The pulse shape is described by Eq. (7.1) for following paramers:  $f_0 = 1.5$  THz,  $\sigma_{\text{FWHM}} = 4$  ps.  $A_{\text{peak}}$  denotes the peak spectral amplitude.

are narrowband and we model them as monochromatic pulses modulated by a Gaussian envelope

$$E(t) = E_0 \exp\left(-\frac{4 \ln 2}{\sigma_{\text{FWHM}}^2} t^2\right) \cos(2\pi f_0 t), \quad (7.1)$$

where  $E_0$  is the peak amplitude of the electric field,  $\sigma_{\text{FWHM}}$  is the pulse full width at half maximum and  $f_0$  is the central pulse frequency. Based on the laser parameters, we assume  $\sigma_{\text{FWHM}} = 4$  ps a  $f_0 \geq 1.5$  THz in our calculations. An illustration of the model pulse for the lowest frequency and peak amplitude 70 kV/cm is shown in Fig. 7.1(e),(f).

We now turn to the theoretical investigation of nonlinear THz conductivity. First, we recall the general theoretical way to assess the response linked with nonlinear THz conductivity. Then, we study the response of selected semiconductor nanostructures under the high-field sources mentioned above. We namely focus on the nanostructures of GaAs

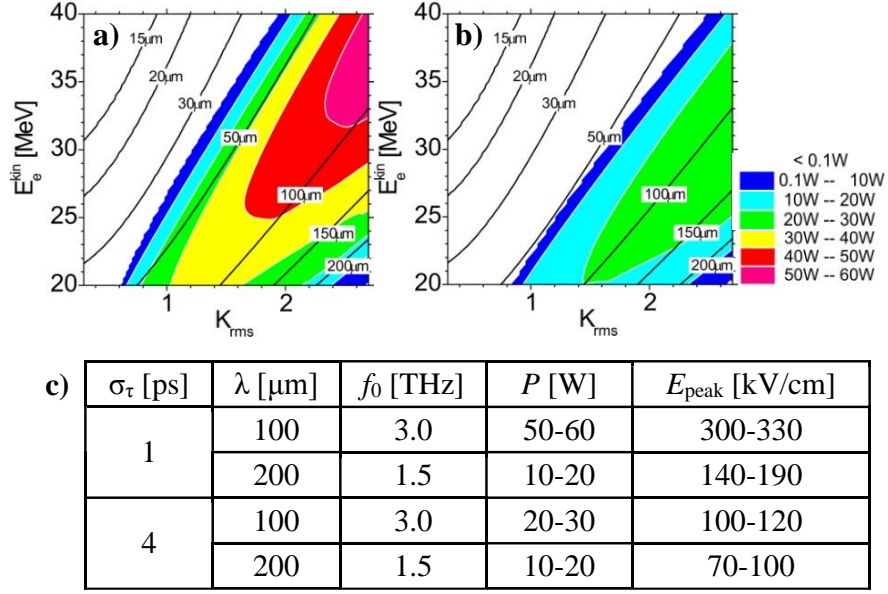


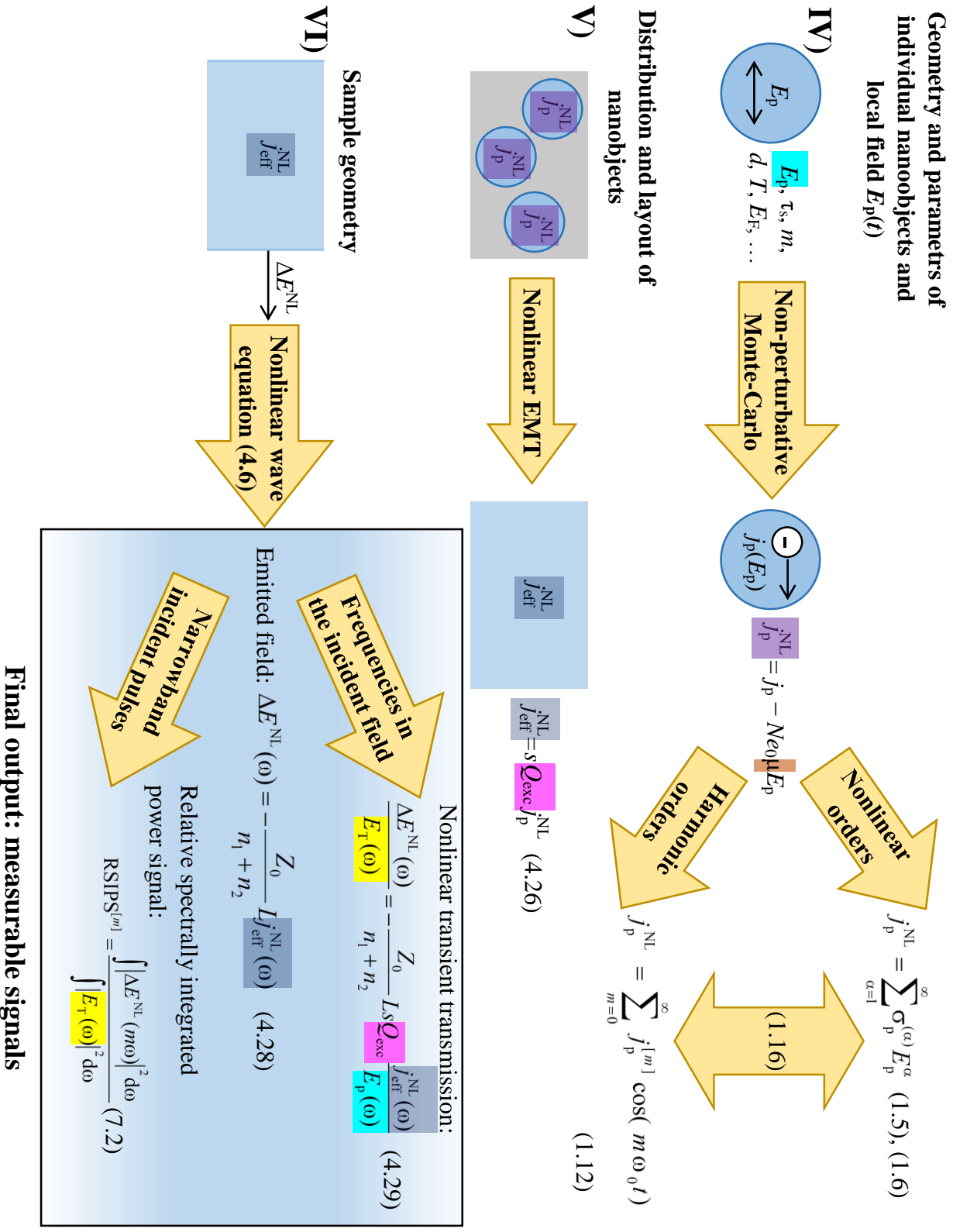
Fig. 7.2. Parameters of FELBE facility pulses. (a), (b) Dependence of the average pulse power  $P$  on the undulator parameter  $K_{\text{rms}}$  and the kinetic energy of electrons  $E_e^{\text{kin}}$  for electron pulse lengths  $\sigma_\tau$  1 ps (a) and 4 ps (b) and for the outcoupling hole diameter 7.0 mm. The graphs were taken from Ref. [109]. (c) Estimated peak electric fields  $E_{\text{peak}}$  corresponding to the graphs from panels (a),(b) for pulses focused into a spot with radius  $r = 1$  mm. The peak fields were then calculated from the Poynting vector as  $E_{\text{peak}} = \sqrt{2P/(\pi r^2 c \epsilon_0 \sigma_t f_{\text{rep}})}$ , where  $f_{\text{rep}} = 13$  MHz is the repetition rate of the laser.

(nanobars, nanowires and slits between metallic blocks) which provide a very promising material towards the experimental observation of nonlinear conductivity. We also examined ZnO nanoparticles [27],[110] and CdS nanocrystals [111],[112] which can be prepared by considerably easier methods. Finally, we compare the estimated strength of nonlinearities with known nonlinear phenomena in bulk materials. Based on our experience with setups utilizing ZnTe for generation and detection of THz radiation ( $0.1 \text{ THz} \lesssim f \lesssim 2.5 \text{ THz}$ ), we assume that transient transmissions as low as  $\sim 10^{-5}$  can be detected [42],[47],[113].

## 7.1 Theoretical assessment of nonlinear THz signal

In this part, we draw a general way to calculate the signal linked with the nonlinear THz conductivity. The thorough assessment of the measurable nonlinear signal is very complex and requires careful application of the methods introduced earlier – namely the theories of wave propagation in both the linear and nonlinear inhomogeneous media (Sections 3 and 4) and the Monte-Carlo calculations of conductivity (Section 2). We depict our entire approach schematically in Fig. 7.3.

Fig. 7.3. Scheme of the calculations of measurable signals linked with the nonlinear THz conductivity due to charge confinement.

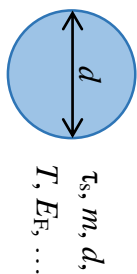




## Input

Geometry and parametrs of individual nanoobjects

## Output



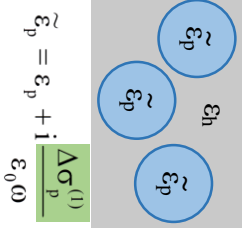
Monte-Carlo

Mobility spectrum:  $\mu$   
Transient photoconductivity:  $\Delta\sigma_p^{(1)} = Ne_0\mu$  (1.3)

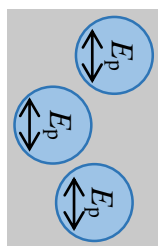
## Linear response

Distribution and layout of nanoobjects

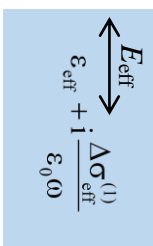
II)



Linear EMT



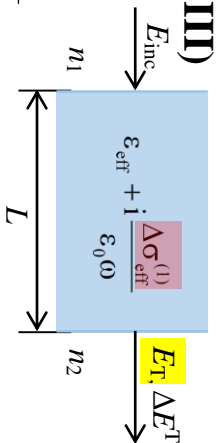
Without photoexcitation ( $\Delta\sigma_p^{(1)} = 0$ ):  $E_p = Q E_{\text{eff}}$   
Photoexcitation ( $\Delta\sigma_p^{(1)} \neq 0$ ):  $E_p = Q_{\text{exc}} E_{\text{eff}}$   
Field-enhancement factors:  $Q$  (3.13)  $Q_{\text{exc}}$  (3.14)



Effective permittivity:  $\epsilon_{\text{eff}}$  (3.6), (3.9)  
Transient effective photoconductivity:  $\Delta\sigma_{\text{eff}}^{(1)}$

Sample geometry

III)



Wave equation (3.20)

Linear transient transmission (thin sample limit):  
$$\frac{\Delta T}{T} = \frac{\Delta E_T}{E_T} = -\frac{Z_0}{(n_1 + n_2)} L \Delta\sigma_{\text{eff}}^{(1)} \quad (3.49) \text{ or } (4.29, 2)$$
  
Local field  $E_p$  (thin sample limit):  
$$E_p = \frac{2n_1}{n_1 + n_2} Q_{\text{exc}} E_{\text{inc}} \quad (4.16)$$

## Calculations of nonlinear response

For each structure, our analysis starts with the evaluation of the linear THz response (parts I)-III) in Fig. 7.3). This requires not only to evaluate the effective linear photoconductivity of the nanostructure, but also the local field in the photoconductive parts which we use later in the calculations of the nonlinear response:

- I) First, we consider the geometry and parameters of individual nanoobjects and we calculate the linear THz mobility  $\mu$  and the corresponding linear THz photoconductivity  $\Delta\sigma_p^{(1)}(\omega_0) = Ne_0\mu$  of confined carriers using the non-perturbative Monte-Carlo calculations (Section 2.2) for a sufficiently weak electric field (typically  $\sim 0.1$  kV/cm). The temporal profile of this field is arbitrary since the linear response is field-independent; only a wide enough spectral bandwidth is required. For the structures covered here, we verified that these calculations yield same results as the established approach based on Kubo formalism.
- II) Depending on the distribution and layout of the nanoobjects, we next apply a suitable effective medium theory<sup>1</sup>. We thus calculate the linear effective photoconductivity  $\Delta\sigma_{\text{eff}}$  for various concentrations of photoexcited carriers  $N$  (using (3.7) or (3.10)) and also the field-enhancement factors  $Q$  (3.13) and  $Q_{\text{exc}}$  (3.14) which link the local electric field  $E_p$  in the nanoobjects with the effective electric field in the homogenized sample in equilibrium and upon photoexcitation, respectively.
- III) Finally, we apply the solution of the linear wave equation (3.20) in small-signal and thin-sample limits (i.e.  $kL \ll \alpha_{\text{eff}}L \ll 1$ , see Section 3.2.2). Using (3.49), we then determine the linear transient transmission  $\Delta T/T$  which we later compare with the estimated measurable nonlinear signals. For a given incident THz electric field<sup>2</sup>  $E_{\text{inc}}$ , we also calculate the local field  $E_p$  in the photoexcited photoconductive parts using (4.16). This transformation necessarily changes the field amplitude and may also change the pulse profile due to the dispersion of material parameters. Furthermore, since the field-enhancement factor  $Q_{\text{exc}}$  in (4.16) depends on the linear photoconductivity, the local field amplitude and waveform will differ for various carrier concentrations  $N$ . As the pulse shape is expected to strongly influence the nonlinear carrier response, the described transformation has to be applied very carefully.

In the above steps, we prepared ground for the calculations of nonlinear THz response (parts IV)-VI) in Fig. 7.3) which itself consists of the following steps:

- IV) For the geometry and parameters from step I) and the known local field  $E_p$  (evaluated in the step III)), we employ the non-perturbative Monte-Carlo calculations to determine the total local electric current density  $j_p$ . For further analysis, however, we have to provide the decomposition (4.20) of  $j_p$  into the linear  $j_p^{(1)}$  and nonlinear  $j_p^{\text{NL}}$  contributions. We calculate the linear component  $j_p^{(1)}$  from the linear mobility determined in step I) easily as  $j_p^{(1)} = Ne_0\mu E_p$ . The nonlinear electric current density is then the difference

---

<sup>1</sup> Here, we consider either the Maxwell-Garnett effective medium theory (Section 3.1.2) or the brick-wall model (Section 3.1.3).

<sup>2</sup> In this work, we always assume one of the model pulses from Fig. 7.1.

$j_p^{\text{NL}}(E_p) = j_p(E_p) - j_p^{(1)}(E_p)$ . Using a nonlinear effective medium theory for the specified geometry and layout of the nanostructure, we transform the local electric current densities  $j_p, j_p^{(1)}$  and  $j_p^{\text{NL}}$  into their effective counterparts  $j_{\text{eff}}, j_{\text{eff}}^{(1)}$  and  $j_{\text{eff}}^{\text{NL}}$  using (4.22), (4.26) and (4.27), respectively.

V) Finally, we wish to link the effective electric current densities  $j_{\text{eff}}, j_{\text{eff}}^{(1)}$  and  $j_{\text{eff}}^{\text{NL}}$  with measurable signals (i.e. solution of the nonlinear wave equation (4.6)). In the linear case, the results of experiments are usually represented as the transient transmission (3.49). Since nonlinear processes can generate signals at frequencies which are not present in the driving THz pulse (and thus neither in the reference wave), we cannot straightforwardly apply the concept of the transient transmittance from the linear case. We therefore propose three different representations of the results obtained in a nonlinear regime:

- Generally, it is always possible to calculate the transient waves which are just leaving the output surface of the sample. For known effective electric current densities, we thus apply equation (4.28) which yields the sought transient waves  $\Delta E^{\text{T}}, \Delta E^{(1)}$  and  $\Delta E^{\text{NL}}$ . The comparison of the transient waves calculated for different amplitudes of the driving field then gives the estimate of the strength of involved nonlinear phenomena. The final link with experimental results requires to account for the instrumental response functions  $\mathcal{P}(\omega)$  and  $\mathcal{D}(\omega)$  introduced in (3.25) (we skip this step for simplicity).
- For frequencies contained in a broadband THz pulse  $E_{\text{T}}(\omega)$  transmitted through sample in equilibrium, we can define the total and nonlinear transient transmissions  $\Delta E^{\text{T}}/E_{\text{T}}$  and  $\Delta E^{\text{NL}}/E_{\text{T}}$  (4.29), respectively.  $\Delta E^{\text{NL}}/E_{\text{T}}$  reveals the presence and strength of the signal due to nonlinearities. The comparison of  $\Delta E^{\text{T}}/E_{\text{T}}$  with the linear transient transmission calculated in the step III) then allows us to discuss the feasibility of experimental observation of the nonlinear response. We note that for fields low enough to induce just the linear response, Eq. (4.29) will essentially yield the same results as Eq. (3.49) used in step III). Outside the transmitted spectrum of  $E_{\text{T}}(\omega)$  (i.e.  $E_{\text{T}}(\omega) = 0$  within the noise floor),  $\Delta E^{\text{T}}/E_{\text{T}}$  cannot be calculated directly. In this case, we estimate the corresponding signal as  $\Delta E^{\text{T}}/E_{\text{T,peak}}$  where  $E_{\text{T,peak}}$  is the peak spectral amplitude of the field transmitted through the sample in equilibrium.
- For narrowband THz sources, the individual nonlinearities can be spectrally separated, therefore the spectral decomposition of the electric current density (12) can be performed. Using (4.27) and (4.28), we then calculate the corresponding transient fields  $\Delta E_m^{\text{T}}$ . To estimate the strength of the measurable nonlinear signal, we further introduce a relative spectrally integrated power signal of the  $m$ -th harmonics (RSIPS<sup>[m]</sup>) as the ratio between the powers of the field  $\Delta E_m^{\text{T}}$  at the harmonic frequency  $m\omega$  and the field  $E_{\text{T}}$  transmitted through the structure in the equilibrium

$$\text{RSIPS}^{[m]} = \frac{\int |\Delta E_m^{\text{T}}(m\omega)|^2 d\omega}{\int |E_{\text{T}}(\omega)|^2 d\omega} . \quad (7.2)$$

We developed this construction since there is no THz detector with sufficient spectral resolution and we thus essentially always measure an integral over a continuous spectral interval. Also, it represents a more appropriate quantity with respect to possible measurements at the FELBE facility where most of the experiments are not phase-sensitive as they utilize power detectors [108],[116]-[120]. We note that if the calculations were provided for multiple amplitudes of the driving field, it would be possible to apply framework analogous to the one from Section 1.2 and thus assess the strength of individual nonlinear phenomena contributing to the response.

## 7.2 Nanostructures of GaAs

Gallium arsenide is a semiconducting material on which a plethora of high-field THz studies in the bulk has been conducted recently. This includes among others the studies of intervalley scattering and intravalley dynamics [18]-[20], reports on the ultrafast dynamics of excitons [26] and polarons [96] and observation of phase-coherent stimulated emission from impurities [97]. Regarding the charge transport, there are observations of field-induced tunnelling between valence and conduction bands [98], partial Bloch oscillations [21] and transition from ballistic to drift-like transport in electron-hole plasma under high THz field [22].

Since the bulk scattering time in GaAs is rather long ( $\tau_s = 270$  fs) and carrier effective mass is rather low ( $m = 0.07m_e$  in the  $\Gamma$ -valley), it constitutes a very promising material towards the experimental observation of nonlinear THz conductivity in nanostructures. However, we have to be aware of the nonlinear bulk phenomena mentioned above. For our work, the most important of these effects is the acceleration of electrons in the conduction band of GaAs by the THz electric field which allows the scattering into L- and X-valleys where the electron effective mass is higher (which results in much smaller mobility and in turn much smaller absorption of THz pulse) [18]-[20]. This effect can be considerably strong (according to [20], the absorption may decrease by up to 80% with respect to the linear response for very high THz fields of  $\sim 150$  kV/cm, see Fig. 7.22(a) in Section 7.5) and will thus likely accompany any nonlinearities arising due to the charge confinement. Within the incident pulse bandwidth, the resulting signal will be then a mixture of signals of different origin and careful discussion would be required to identify the dominant contribution. Above this bandwidth, however, it is currently unknown to which degree the intervalley scattering yields any signal as there are no reports in the literature for GaAs (emerging high-frequency signals were observed in InGaAs [23]). In Section 7.5, we estimate the strength of this effect and compare it with the nonlinearities due to charge confinement.

Using the framework described above, we will investigate the nonlinear responses only due to charge confinement in two different nanostructures of GaAs (Fig. 7.4) – nanobars and nanowires:

- The GaAs nanobars have width 250 nm and are separated by 350 nm gaps (Fig. 7.4(a)). The layer is 1  $\mu$ m thick and placed on GaAs substrate. We already verified that such

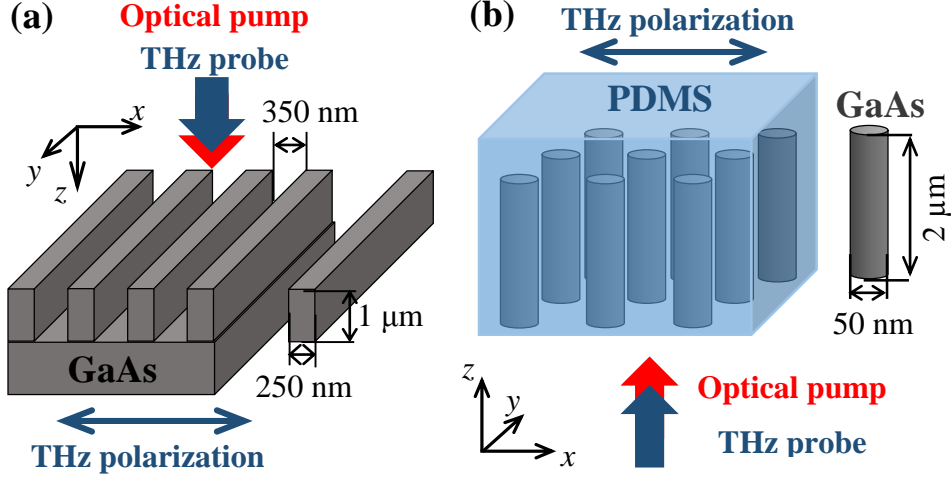


Fig. 7.4. Schematic illustration of GaAs nanostructures used for the theoretical study of nonlinear THz photoconductivity – nanobars (panel (a)) and nanowire array embedded in PDMS matrix (panel (b)). Filling factor of the nanowires: 7%. Both optical pump and THz probe beams propagate along  $z$ -axis. THz electric field is polarized in the  $x$ -direction.

a kind of structure can be prepared by a molecular beam epitaxy followed up by a lithography.

- The GaAs nanowires form an array embedded in a polydimethylsiloxane (PDMS) matrix (Fig. 7.4(b)). The nanowires are  $2\ \mu\text{m}$  long, have  $50\ \text{nm}$  diameter and their volume filling fraction  $s$  is 7%. PDMS is a polymer transparent in both the optical and THz range and has terahertz permittivity  $\epsilon_{\text{PDMS}} \sim 2.56$  [121]. Linear response of a similiar array of heavily  $n$ -doped InP nanowires was studied in [92].

The linear (3.49) and nonlinear (4.29) signals are both limited by the filling factor of GaAs and the structure thickness  $L$ . For the nanobars, it is possible to significantly increase the filling factor by tayloring their width and mutual spacing. However, the achievable aspect ratio between the layer thickness and the gap width is limited in the current fabrication process. In contrast, the filling factor of the nanowires is strongly limited by the growth process. On the other hand, their prolongation is feasible and thus could be exploited to enhance the measurable signals.

To simplify the analysis, we neglect the dispersion of all equilibrium material parameters. While this approximation is valid for most frequencies, it inevitably fails in the reststrahlen band of GaAs between the TO and LO phonon modes at the frequencies  $8\ \text{THz}$  and  $8.7\ \text{THz}$ , respectively [122]. In all Monte-Carlo calculations used in this part, we assume Boltzmann statistics and the following parameters:  $\tau_s = 270\ \text{fs}$ ,  $m = 0.07m_e$ ,  $T = 300\ \text{K}$ . The electric field is always assumed to be propagating along the  $z$ -axis and polarized in the  $x$ -direction. Any nonlinearity is thus fully described by the  $x$ -component of the electric current density  $j_x$  as symmetry prohibits a non-zero response in the other directions. For the effective medium theory, we consider  $\epsilon_p = \epsilon_{\text{GaAs}} \sim 12.6$ .

As the nanobars and the substrate are formed by the same material, experimental study of this structure may be problematic due to an unwanted signal from the substrate. The unwanted signal may be very high compared to the signal from the nanostructure (compare bulk mobility of GaAs  $\mu \sim 7 \times 10^3 \text{ cm}^2 \text{V}^{-1} \text{s}^{-1}$  with the normalized effective photoconductivity of nanobars ( $\lesssim 30 \text{ cm}^2 \text{V}^{-1} \text{s}^{-1}$ ) in Fig. 7.5(b)). This signal could be reduced by a deposition of a reflective coating onto the substrate prior to the GaAs growth. Even better, the nanowires may be embedded in PDMS and separated from the substrate which eliminates the discussed problem completely.

### 7.2.1 Linear response

The linear mobility  $\mu$  of carriers inside both the nanobars and nanowires (Fig. 7.5(a),(d)) was calculated using the Monte-Carlo calculations based on Kubo formalism (Section 2.1). The spectrum for the nanowires is blueshifted and has lower amplitude since the confining length is shorter. To assess the effective response, we used the brick-wall model ((3.14) for  $K = 0$  and (4.17)) for the nanobars and the Maxwell-Garnett theory ((3.14) and (4.17)) for the nanowires. The calculated normalized effective photoconductivities  $\Delta\sigma_{\text{eff}}/(Ne_0)$  are shown in Fig. 7.5(b),(e). For low enough carrier concentrations ( $N \lesssim 10^{14} \text{ cm}^{-3}$  for the nanobars and  $N \lesssim 10^{16} \text{ cm}^{-3}$  for the nanowires), the effective conductivity is directly proportional to the microscopic conductivity. For higher concentrations, a plasmonic resonance develops and blueshifts with increasing number of photoexcited carriers.

In experiments, the linear response is characterized by the transient transmission  $\Delta T/T$ . In our case, the thin-film limit is satisfied and  $\Delta T/T$  is thus directly proportional to the effective photoconductivity  $\Delta\sigma_{\text{eff}}$  (3.49). The normalized effective photoconductivity  $\Delta\sigma_{\text{eff}}/(Ne_0)$  then represents the effective mobility of the structured system and in this case, it is two orders of magnitude lower than the mobility of bulk GaAs ( $\mu \sim 7 \times 10^3 \text{ cm}^2 \text{V}^{-1} \text{s}^{-1}$ ). While response of bulk GaAs is easily measurable [123], the conductivity measurement of the considered structured systems then provides a greater challenge. Indeed, for the intermediate carrier concentration  $N = 10^{16} \text{ cm}^{-3}$ , the absolute values of the measurable transient transmissions are  $\lesssim 3 \times 10^{-4}$  (Fig. 7.5(c),(f)), which is just an order of magnitude above the detection limit of common setups [42],[47],[113]. The transient transmission of the nanowires is comparable with the values measured for a similar array of heavily *n*-doped InP nanowires [92].

### 7.2.2 Nonlinear response under broadband THz and multi-THz pulses

#### 7.2.2.a) THz pulses

Here, we investigate the nonlinear response of the GaAs nanobars and nanowires induced by the high-field broadband low-frequency THz pulses. We will assume that a pulse from Fig. 7.1(a) with peak amplitude 100 kV/cm is incident on the structure. Using the linear effective medium theory (Eqs. (4.16) and (3.14)), we first calculate temporal profile and spectrum of the field  $E_p$  inside a single photoconductive constituent for various concentrations of photoexcited carriers. The resulting pulse amplitudes are significantly smaller than the amplitude of the incident electric field (Fig. 7.6). This striking decrease is mainly due to the high contrast between the permittivities of GaAs and the surrounding non-conducting material,

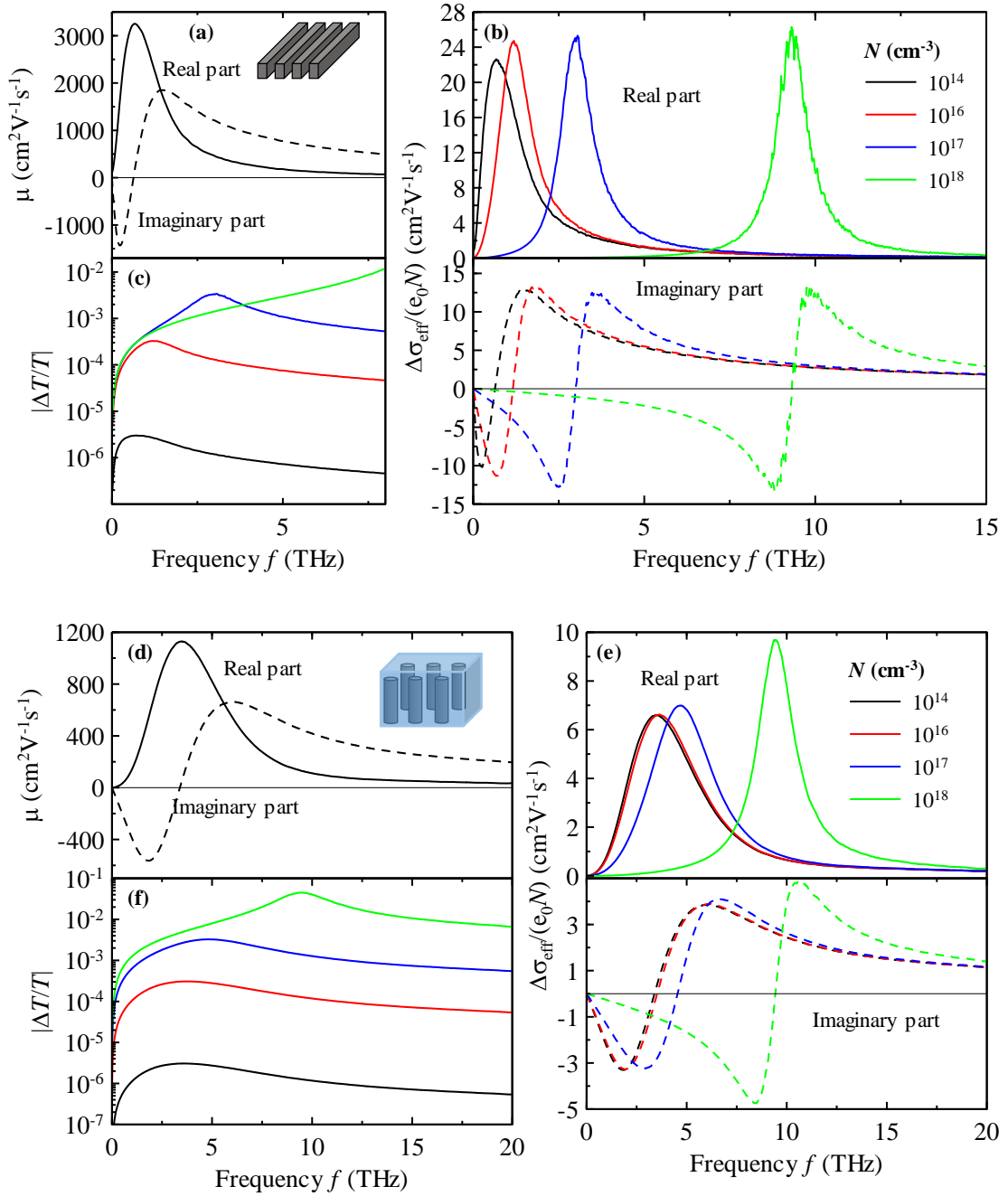


Fig. 7.5. Linear responses of the GaAs nanobars ((a)-(c)) and nanowires ((d)-(f)). (a),(d) Linear mobilities of carriers confined within the considered structures calculated using the Monte-Carlo calculations based on Kubo formalism. (b),(e) Normalized effective photoconductivity spectra for various concentrations  $N$  of photoexcited carriers calculated using Eqs. (3.14) and (4.17). For low enough concentrations, the spectra are directly proportional to the microscopic conductivity. With increasing carrier concentration, a plasmonic resonance develops and blueshifts. (c),(f) Linear transient transmission spectra calculated from panels (b) and (e), respectively, using Eq. (3.49).

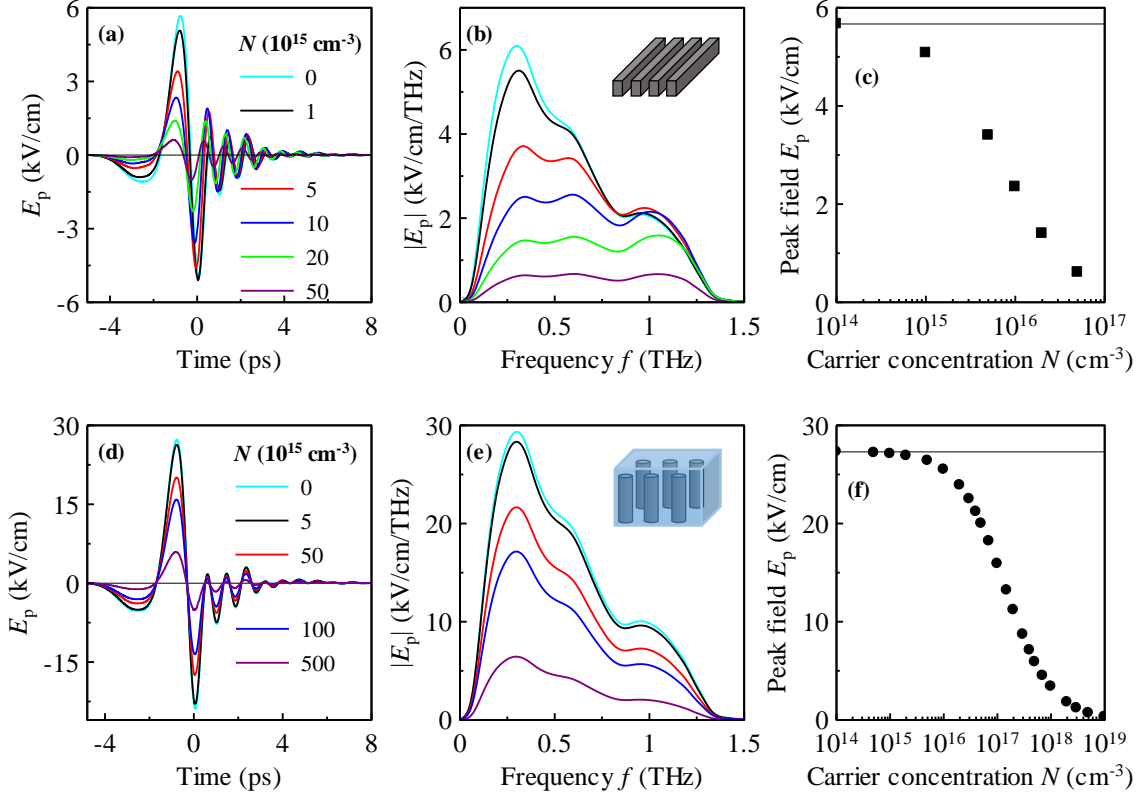


Fig. 7.6. THz waveforms inside GaAs nanobars (a),(b) and nanowires (d),(e) induced by an incident high-field pulse from Fig. 7.1(a) with peak amplitude of 100 kV/cm. The peak amplitude decreases with the increasing carrier concentration  $N$  due to the screening caused by free charges (c),(f). The temporal profile shape then slightly changes due to the linear photoconductivity dispersion of the nanobars. Solid lines in panels (c) and (f): amplitude of  $E_p$  without photoexcitation.

and to a lesser extent due to the small filling factor of GaAs. The higher permittivity of PDMS (and thus a smaller permittivity contrast) ensures that local fields in the nanowires are stronger than in the bare nanobars. Note that the pulse shape slightly changes due to the linear photoconductivity dispersion. We also emphasize that the transformation (4.16) is linear in the electric field, therefore it does not introduce any new spectral components (Fig. 7.6(b),(e)).

For low enough concentrations  $N$ , the local field amplitude is almost constant and it is close to the value reached without photoexcitation (Fig. 7.6(c),(f)). Carrier concentrations exceeding  $10^{14} \text{ cm}^{-3}$  then start to cause a screening of the incident electric field and thus a rapid drop of  $E_p$ . The decrease is the most pronounced for the concentrations which coincide with the build-up of the plasmonic resonance in the effective response (Fig. 7.5(b),(e)). Finally, for the highest concentrations, the field is almost completely screened and  $E_p$  approaches zero. We emphasize that this screening becomes inefficient for frequencies close to the plasmonic resonance as the local field is enhanced due to the coupling with the plasmon (Fig. 7.9).



Using the non-perturbative Monte-Carlo calculations with fields from Fig. 7.6, we assess the nonlinear response of the nanostructures (Fig. 7.7). Despite the rather low fields inside the nanobars (Fig. 7.6(a)-(c)), a non-zero nonlinear electric current density  $j_x^{\text{NL}}$  is clearly resolved (Fig. 7.7(c)). The nonlinearity is seen as a departure from the linear response (i.e. the decrease of the total electric current density with respect to the linear component) and also as the tail emerging above the incident frequencies. The responsible nonlinear process is a general four-wave mixing between individual spectral components of the driving THz pulse. The relative strength of the nonlinearity is clearly the highest for the lowest carrier concentration of  $1 \times 10^{15} \text{ cm}^{-3}$  (i.e. the highest electric field inside the nanobars) and decreases with increasing concentration (Fig. 7.7(c)) which is in agreement with the same dependence of the local field

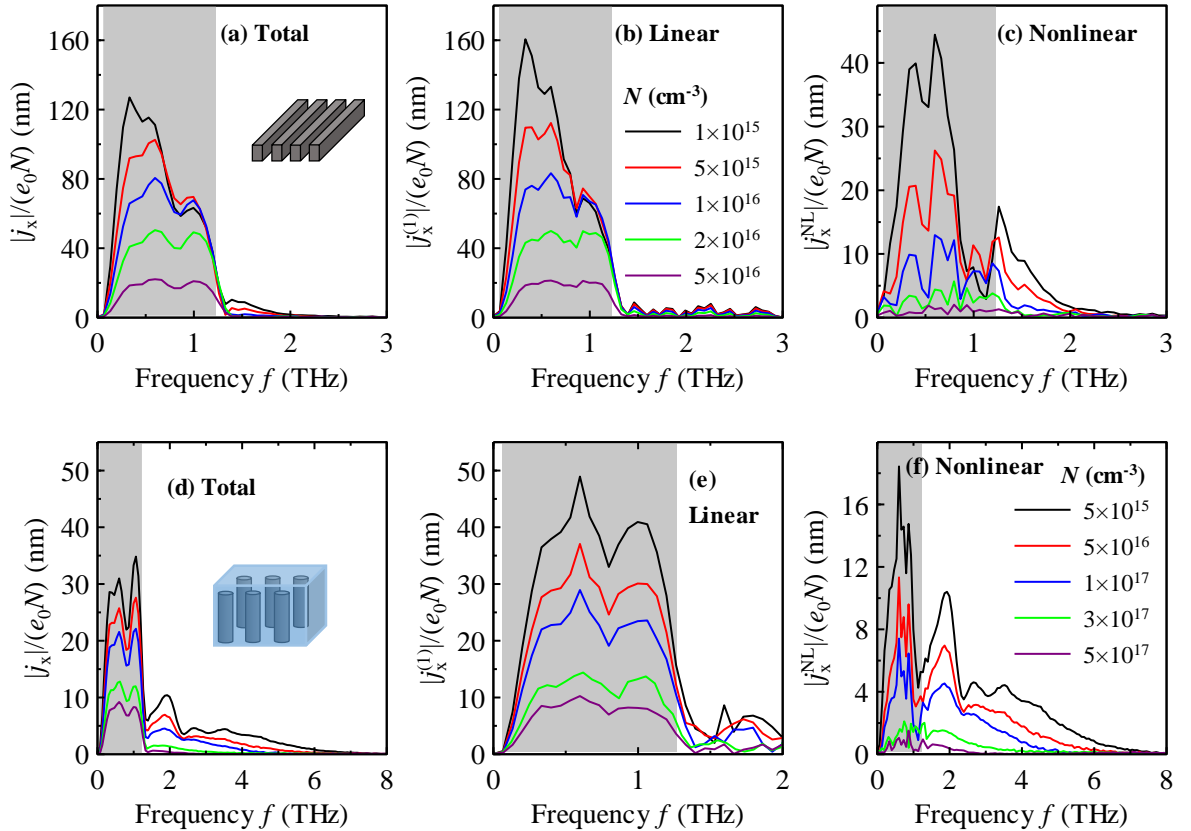


Fig. 7.7. Amplitudes of the electric current density induced inside GaAs nanobars ((a)-(c)) and nanowires ((d)-(f)) by the incident THz pulses from Fig. 7.1(a) with peak amplitude 100 kV/cm for various concentrations of carriers  $N$  calculated using the non-perturbative Monte-Carlo calculations. Clear departure from the linear response  $j_x^{(1)}$  and presence of tail in the nonlinear component  $j_x^{\text{NL}}$  above the incident frequencies (gray areas) are observed for  $N \leq 10^{16} \text{ cm}^{-3}$  (nanobars) and  $N \leq 3 \times 10^{17} \text{ cm}^{-3}$  (nanowires), respectively. For the linear component, the data above the incident frequencies are just a noise originating from the calculations. Real and imaginary parts of the spectra are shown in the Appendices D and E, respectively. We note, that the normalized electric current density  $j_x/(e_0 N)$  represents the velocity of carriers. The Fourier transform then reduces the unit of velocity from meters per second just to meters.

(Fig. 7.6(c)). This decrease is then rather steep and the nonlinearity can be hardly resolved already for  $N \gtrsim 2 \times 10^{16} \text{ cm}^{-3}$ . This corresponds to local fields  $E_p \lesssim 1.5 \text{ kV/cm}$  (Fig. 7.6) and the response of the nanobars can be then described solely by the linear theory.

For the nanowires, the local fields are higher than for the nanobars and the nonlinearities are thus more pronounced (Fig. 7.7(f)). The nonlinear electric current density  $j_x^{\text{NL}}$  clearly contains the third harmonics of the incident spectrum followed by a tail. In comparison with the nanobars, the tail here extends up to  $\sim 8 \text{ THz}$  which implies the involvement of nonlinear phenomena of up to the 7th order. The relative strength of the nonlinearity decreases with increasing concentration of photoexcited carriers.

The electric current densities  $j_x^{(1)}$ ,  $j_x^{\text{NL}}$  and  $j_x$  calculated so far (Fig. 7.7) characterize just the local response of a single constituent within the structure. To evaluate the effective response of the entire structure, it is necessary to transform them into the effective electric current densities  $j_{\text{eff},x}^{(1)}$ ,  $j_{\text{eff},x}^{\text{NL}}$  and  $j_{\text{eff},x}$  using (4.22), (4.26) and (4.27), respectively. The net effective electric current density  $j_{\text{eff},x}$  then gives rise to the transient electric field  $\Delta E^{\text{T}}$  at the output sample surface according to (4.28). This field contains both linear and nonlinear contributions  $\Delta E^{(1)}$  and  $\Delta E^{\text{NL}}$ , respectively, linked with the partial electric current densities  $j_{\text{eff},x}^{(1)}$  and  $j_{\text{eff},x}^{\text{NL}}$ , respectively. We emphasize that if the response of the nanostructure were solely linear, only the field  $\Delta E^{(1)}$  would exist while  $\Delta E^{\text{NL}}$  would vanish. The comparison of the total transient signal  $\Delta E^{\text{T}}$  and the linear contribution  $\Delta E^{(1)}$  thus allows to assess the role of the nonlinearities.

The calculated transient amplitudes  $\Delta E^{\text{T}}$ ,  $\Delta E^{(1)}$  and  $\Delta E^{\text{NL}}$  are shown in Fig. 7.8(a),(c). For frequencies within the incident pulse bandwidth ( $f \lesssim 1.3 \text{ THz}$ ), there are differences between the linear and total responses which indicate the presence of a non-zero nonlinear component  $\Delta E^{\text{NL}}$  (dotted lines in Fig. 7.8):

- For the nanobars (Fig. 7.8(a)), this nonlinearity can be resolved for carrier concentrations lower than  $1 \times 10^{16} \text{ cm}^{-3}$ . It is the most distinct for  $N = 1 \times 10^{15} \text{ cm}^{-3}$ , for which the total transient field  $\Delta E^{\text{T}}$  is by  $\sim 20 \%$  lower than the linear transient wave  $\Delta E^{(1)}$ . With increasing concentration, the difference between the total and linear transient waves becomes less pronounced.
- For the nanowires (Fig. 7.8(c)), the total and linear field components differ for  $N \leq 10^{17} \text{ cm}^{-3}$ . The nonlinearity is the most pronounced for  $N = 5 \times 10^{15} \text{ cm}^{-3}$ , for which the transient signal decreases by one third with respect to the linear response. The relative strength of the nonlinearity decreases with increasing carrier concentration and for  $N \gtrsim 3 \times 10^{17} \text{ cm}^{-3}$  almost no difference between  $\Delta E^{\text{T}}$  and  $\Delta E^{(1)}$  is observed.

Above the incident pulse bandwidth ( $f \gtrsim 1.3 \text{ THz}$ ), the linear transient amplitude  $\Delta E^{(1)}$  sharply decreases below the noise floor of the calculations (Fig. 7.8(a),(c)). In contrast, the total transient amplitudes  $\Delta E^{\text{T}}$  exhibit high-frequency components (similarly to the electric current densities from Fig. 7.7) which thus appear solely due to the nonlinear response. For the nanowires (Fig. 7.8(c)), the initially decreasing high-frequency tail is followed by a resonant

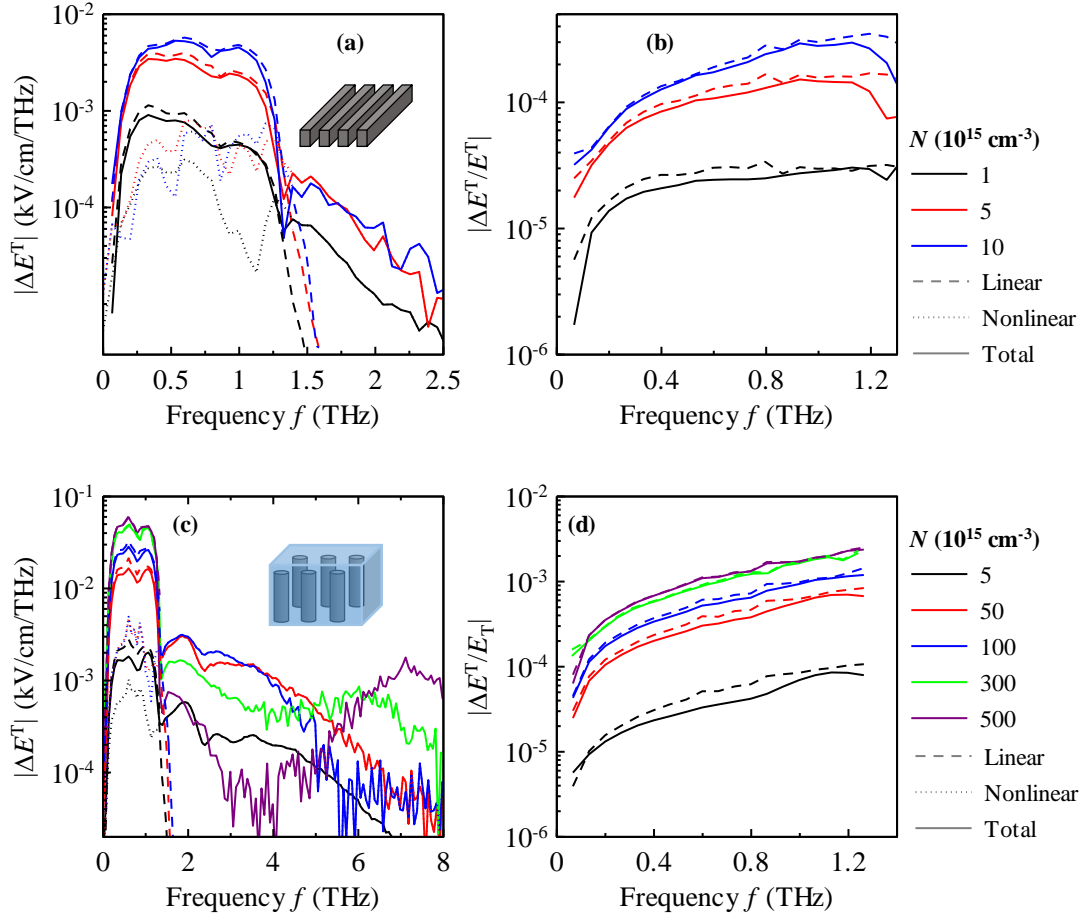


Fig. 7.8. (a),(c) Transient amplitudes  $\Delta E^T$  (solid),  $\Delta E^{(1)}$  (dashed) and  $\Delta E^{NL}$  (dotted) at the output surface of the investigated nanobar structure (a) and nanowire array (c) for various concentrations  $N$  of photoexcited carriers. The structures were subjected to the model broadband low-frequency THz pulse (Fig. 7.1(a)) with peak amplitude 100 kV/cm. The transient amplitudes were calculated from the electric current densities in Fig. 7.7. (b) The transient transmission spectra of the nanobars (b) and nanowires (d) in the linear (dashed) and the nonlinear regime (solid) calculated using (4.29).



behavior for  $N \gtrsim 3 \times 10^{17} \text{ cm}^{-3}$ . This field enhancement stems from the interaction with the plasmonic resonance (Fig. 7.5(e)) which overlaps with transient field spectrum for these concentrations.

From the experimental point of view, there are two phenomena available for the measurements – the change of the transient signal for the frequencies within the incident pulse bandwidth (i.e. dependence of the transient signal on the local electric field), or the emergence of the signal at higher frequencies. As noted in the introduction of this section, we will consider that transient transmissions  $\Delta T/T$  as low as  $\sim 10^{-5}$  is detectable.

Within the bandwidth of the pulse  $E_T$  transmitted through the samples in equilibrium (i.e.  $f \lesssim 1.3 \text{ THz}$ ), we calculate the transient transmissions  $\Delta E^T/E_T$ ,  $\Delta E^{(1)}/E_T$  and  $\Delta E^{NL}/E_T$

directly using (4.29) (Fig. 7.8(b),(d)). Since  $\Delta E^{(1)}/E_T$  is essentially the same as  $\Delta T/T$  defined by (3.49) (the calculated data match each other within the precision of used Monte-Carlo calculations), we directly obtain comparison between the measurable linear and nonlinear signals (Tab. 7.1). Experimentally, this would require to measure both the linear and nonlinear responses and then calculate their difference. In principle, there are two possible approaches. The first one is to provide separate measurements in two different setups optimized for low and high THz fields, respectively. However, the resulting nonlinear transient transmission would then be strongly influenced by inevitable systematic experimental errors (e.g. different temporal windowing, different parasitic reflections, different Gouy shift correction etc.). The other option is to measure both responses in a single setup. The low field for the linear response would be obtained by detuning the source of THz radiation. However, this detuning would necessarily increase the noise. To judge the experimental feasibility, it is then necessary to consider not only the absolute value of the nonlinear transient transmission  $\Delta E^{NL}/E_T$  but also its relative strength with respect to the linear transient transmission  $\Delta E^{(1)}/E_T$ .

For the nanobars, the highest nonlinear transmission  $\Delta E^{NL}/E_T \sim 10^{-5}$  is reached for the carrier concentrations  $5 \times 10^{15} \text{ cm}^{-3}$  and  $10^{16} \text{ cm}^{-3}$ . The corresponding linear signals are then one order of magnitude higher (Tab. 7.1). The considered nonlinear response of the nanobars is then rather weak and we cannot realistically expect its observation in experiments. The nanowires then seem to be more promising. However, even for the theoretically most suitable carrier concentration  $5 \times 10^{16} \text{ cm}^{-3}$  ( $\Delta E^{NL}/E_T \sim 7 \times 10^{-5}$  while  $\Delta E^{(1)}/E_T \sim 3 \times 10^{-4}$ ), it would require

<b>(a)</b> 	$N \text{ (cm}^{-3}\text{)}$	$ \Delta E^{(1)}/E_T $ (0.5 THz)	$ \Delta E^{NL}/E_T $ (0.5 THz)	$ \Delta E^{NL}/E_{T,\text{peak}} $ (1.5 THz)	
	$10^{15}$	$3 \times 10^{-5}$	$6 \times 10^{-6}$	$2 \times 10^{-6}$	
	$5 \times 10^{15}$	$10^{-4}$	$10^{-5}$	$6 \times 10^{-6}$	
	$10^{16}$	$2 \times 10^{-4}$	$10^{-5}$	$5 \times 10^{-6}$	
<b>(b)</b> 	$N \text{ (cm}^{-3}\text{)}$	$ \Delta E^{(1)}/E_T $ (0.6 THz)	$ \Delta E^{NL}/E_T $ (0.6 THz)	$ \Delta E^{NL}/E_{T,\text{peak}} $ (1.8 THz)	$ \Delta E^{NL}/E_{T,\text{peak}} $ (7.0 THz)
	$5 \times 10^{15}$	$5 \times 10^{-5}$	$2 \times 10^{-5}$	$3 \times 10^{-5}$	—
	$5 \times 10^{16}$	$3 \times 10^{-4}$	$7 \times 10^{-5}$	$5 \times 10^{-5}$	—
	$10^{17}$	$5 \times 10^{-4}$	$8 \times 10^{-5}$	$6 \times 10^{-5}$	—
	$3 \times 10^{17}$	$9 \times 10^{-4}$	$3 \times 10^{-5}$	$3 \times 10^{-5}$	$6 \times 10^{-6}$
	$5 \times 10^{17}$	$10^{-3}$	$2 \times 10^{-5}$	$10^{-5}$	$2 \times 10^{-5}$

Tab. 7.1. Summary of the linear  $\Delta E^{(1)}/E_T$  and nonlinear transient transmissions  $\Delta E^{NL}/E_T$  and  $\Delta E^{NL}/E_{T,\text{peak}}$  for the GaAs nanobars (a) and nanowires (b) for various concentration of photoexcited carriers  $N$ . Both structures were subjected to the model THz pulse from Fig. 7.8(a) with peak amplitude 100 kV/cm. The frequencies were selected to reflect the position of the third harmonics peak.

precise measurements of the responses in both regimes followed by a proper analysis of the experimental errors.

A more prospective might be the observation of the high-frequency tail present in the total transient field  $\Delta E^T$  (Fig. 7.8(a)) as linear signal cannot appear above the pulse bandwidth (i.e. only noise would be present in the linear response). The experiments would be then much simpler then in the previous case – we would have to measure just the high-frequency response for a long enough time to reduce the noise which should confirm an existence of the signal. Since the transient transmission cannot be calculated directly in this case, we estimate the corresponding signal as  $\Delta E^T/E_{T,\text{peak}}$  where  $E_{T,\text{peak}}$  is the peak spectral amplitude of the field transmitted through the sample in equilibrium (Tab. 7.1).

For the nanobars, the estimated maximum transient transmission corresponding to the high-frequency tail  $\Delta E^{\text{NL}}/E_{T,\text{peak}} \sim 6 \times 10^{-6}$  is reached for  $N = 5 \times 10^{15} \text{ cm}^{-3}$ . Since this value is below the detection limit of  $10^{-5}$ , we do not believe that the experimental confirmation of this nonlinearity is feasible. Regarding the nanowires, for concentrations up to  $3 \times 10^{17} \text{ cm}^{-3}$  we consider mainly the peaks located at the third harmonic frequencies ( $f \sim 1.8 \text{ THz}$ ). The estimated corresponding signals  $\Delta E^{\text{NL}}/E_{T,\text{peak}}$  are above the detection limit (Tab. 7.1) and thus detectable (the highest signal  $6 \times 10^{-5}$  is reached for  $N = 10^{17} \text{ cm}^{-3}$ ). We estimate, that the measurement of such signals would last at least 16 hours. Furthermore, these nonlinear signals do not depend strongly on the concentration of carriers which could be further exploited to confirm that the experimentally observed signal is due to the nonlinear conductivity. For  $N = 5 \times 10^{17} \text{ cm}^{-3}$ , we may consider also the resonance at  $f \sim 7 \text{ THz}$  caused by the interaction with plasmon. The estimated corresponding transient transmission is  $\Delta E^{\text{NL}}/E_{T,\text{peak}} \sim 2 \times 10^{-5}$ . However, we do not have an estimate of detection sensitivity for such high frequencies.

Even though we are assuming high incident field of  $100 \text{ kV/cm}$ , the corresponding nonlinear signals are rather low. Here we briefly discuss possible modifications of the investigated nanobar structure which would provide an enhanced signal (these ideas can be applied to any non-percolated structure). There are two feasible possibilities – filling air gaps with nonconducting material transparent both in optical and THz range to reduce the permittivity contrast within the structure, or reduction of the spacing between the nanobars which would increase the nanobars aspect ratio. We now estimate how the change of the pertinent parameters affects the response. Since the electric field induces just the nonlinearities of the third order, we approximate the nonlinear electric current density as  $j_x^{\text{NL}} \sim \Delta \sigma_p^{(3)} E_p^3$  where  $\Delta \sigma_p^{(3)}$  is a nonlinear conductivity of the third order. Using (4.29.3) and (4.16), we then express the ratio of nonlinear transient transmissions  $\Delta E^{\text{NL}}/E_T$  as

$$\left| \frac{(\Delta E^{\text{NL}} / E_T)_2}{(\Delta E^{\text{NL}} / E_T)_1} \right| = \frac{s_2}{s_1} \left| \frac{Q_{\text{exc},2}}{Q_{\text{exc},1}} \right|^4, \quad (7.3)$$

where the index 1 is related to the originally investigated structure from Fig. 7.4(a) and index 2 denotes the modified structure. The fourth-power dependence implies that a significant

enhancement of the measured signal can be achieved<sup>1</sup>. We now provide several illustrations for  $N = 5 \times 10^{15} \text{ cm}^{-3}$ :

- First, we consider filling of the air gaps with PDMS which was already used as a matrix in the THz study of vertically aligned InP nanowires [92]. Its terahertz permittivity is  $\epsilon_{\text{PDMS}} \sim 2.56$  [121] which would increase the nonlinear signal 30 times. If the filling material had permittivity  $\epsilon = 5$ , the nonlinear transient transmission would be 270 times higher than for the bare nanobars.
- Reduction of the gap between the nanobars from 350 nm to 100 nm would change both  $s$  and  $Q_{\text{exc}}$ , and the nonlinear signal would then increase 20 times.
- If we filled the gaps with PDMS and reduced them to 100 nm at the same time, the nonlinear signal would be 300 times higher (the transient transmission does not depend linearly on the spacing and permittivity of the filling material).

Based on these illustrations, the signals depend more significantly on the permittivity contrast within the structure than on the nanobar aspect ratio. Filling with a suitable material is thus a more prospective way to signal enhancement. It is also more feasible since the reduction of the spacing between the nanobars is almost impossible in the current fabrication process.

### 7.2.2.b) Multi-THz pulses

The low-frequency THz pulses used in the previous section contain just the frequencies up to  $\sim 1.3 \text{ THz}$  (Fig. 7.1(b)). For higher carrier concentrations  $N$ , the measurable signal at these frequencies is limited by the plasmonic resonance (Fig. 7.5(b),(e)). In contrast, the very broad spectra of multi-THz pulses (Fig. 7.1(d)) cover the spectral range where the plasmonic resonances enhance the linear transmission (Fig. 7.5(b),(e)). The interaction with the plasmon could be then exploited to strongly enhance also the nonlinear response.

We assume that the multi-THz pulses from Fig. 7.1(c) are incident on the structures ( $E_{\text{inc}} \sim 120 \text{ kV/cm}$ ). Using (4.16), we first evaluate the local field  $E_p$  (Fig. 7.9). Without photoexcitation, the spectrum and temporal profile of the local field are directly proportional to those of the incident field due to the neglected dispersion of the material parameters. For higher concentrations examined here ( $N \geq 10^{17} \text{ cm}^{-3}$ ), the local field  $E_p$  then fundamentally changes and its spectrum becomes resonant-like. The resonance blueshifts with  $N$  while the peak value attains maximum for certain concentration of carriers ( $N = 7 \times 10^{17} \text{ cm}^{-3}$  for the nanobars and  $N = 10^{18} \text{ cm}^{-3}$  for the nanowires).

The complicated behavior described above stems from the interaction with the plasmon which inherently develops for high carrier concentrations. In order to fully understand it, we examine the spectra of the field-enhancement factor  $Q_{\text{exc}}$  (Fig. 7.9(b),(e)). The factor  $Q_{\text{exc}}$  is given by (3.14) and completely accounts for the sample influence in the applied transformation of the incident field (4.16). For  $N = 0 \text{ cm}^{-3}$  and dispersion-free equilibrium material parameters,  $Q_{\text{exc}}$  is a real constant. This corresponds with the proportionality between the incident and the

---

<sup>1</sup> We note that the field-enhancement factor  $Q_{\text{exc}}$  depends strongly on the permittivity contrast across the structure and to a lesser extent also on the filling factor  $s$ .

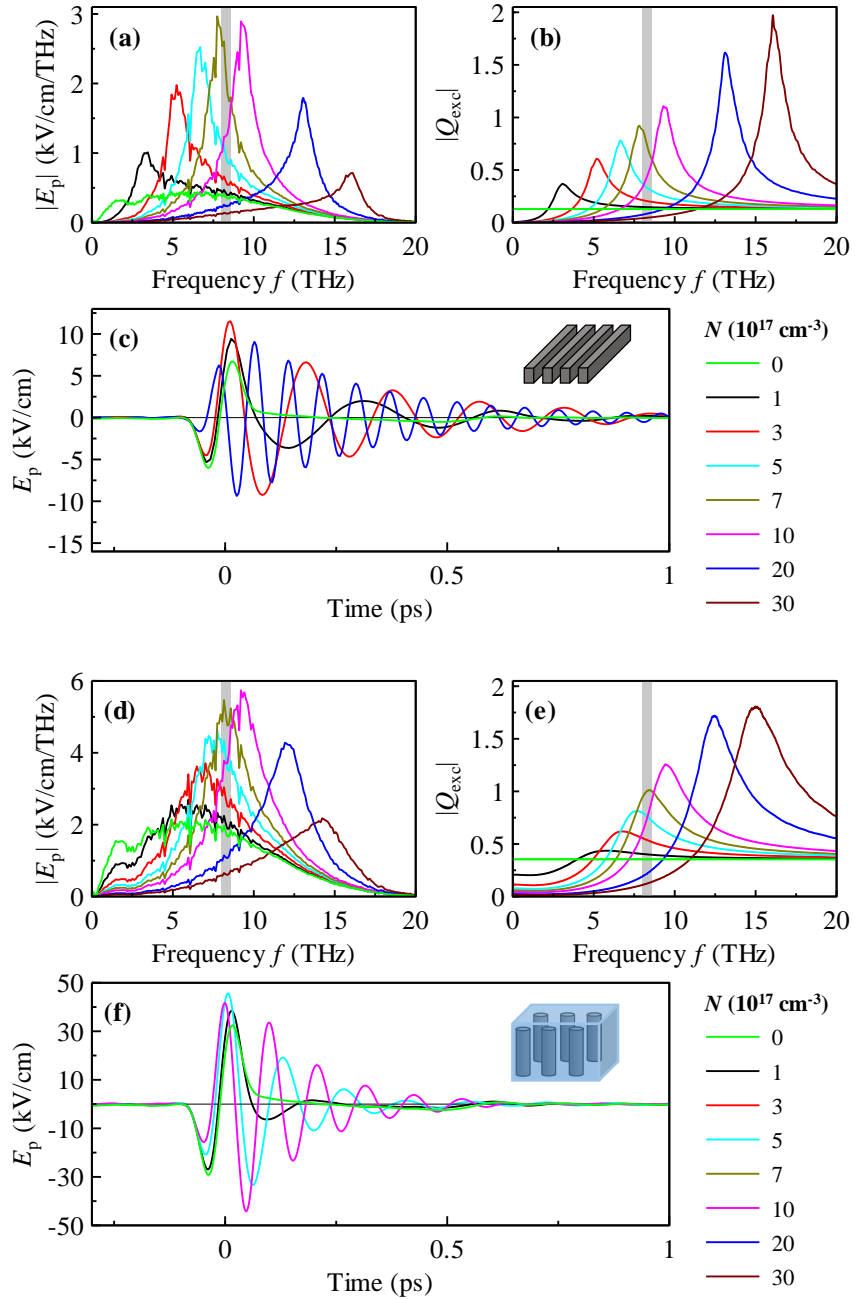


Fig. 7.9. Spectra of the electric field inside the GaAs nanobars (a) and nanowires (d) induced by a multi-THz pulse (Fig. 7.1(c)) with peak amplitude 120 kV/cm for various concentrations  $N$  of photoexcited carriers, calculated using (4.16). Without photoexcitation, the local field has same shape as the incident one. For  $N \gtrsim 10^{17} \text{ cm}^{-3}$ , the spectra exhibit a resonant character which stems from the interaction with the plasmon. The corresponding plasmonic resonances are captured in the field-enhancement factors  $Q_{exc}$  (panel (b) for nanobars and (e) for nanowires) which enter the transformation (4.16). The temporal profiles of the local fields (panels (c) and (f)) then consist of slowly damped oscillations which last much longer than the incident pulse. Gray areas: reststrahlen band of GaAs.

local fields observed above. For  $N \gtrsim 10^{17} \text{ cm}^{-3}$ , the spectra of  $Q_{\text{exc}}$  reflect the plasmonic resonance – the peak grows and blueshifts with increasing  $N$ . The observed asymmetry stems from the different behavior of  $Q_{\text{exc}}$  for low and high frequencies. In the dc-limit,  $Q_{\text{exc}}$  approaches 0 as no permanent electric current can flow through an isolated object. In the high-frequency limit,  $Q_{\text{exc}}$  converges to the equilibrium value since the term  $\Delta\sigma_p^{(1)}/\omega\epsilon_0$  can be neglected in (3.14).

We can now fully explain the shapes of the local field spectra (Fig. 7.9(a),(d)). In the frequency-domain, the field  $E_p$  is a product of the incident field  $E_{\text{inc}}$  (Fig. 7.1(d)) and the field-enhancement factor  $Q_{\text{exc}}$  (Fig. 7.9(b),(e)) (i.e. transformation (4.16)). Since the spectrum of  $E_{\text{inc}}$  is featureless, the resonant-like character of  $E_p$  (Fig. 7.9(a)) clearly originates from the plasmonic resonance which is captured in  $Q_{\text{exc}}$  (Fig. 7.9(b)). The non-monotonous dependence of peak amplitude of  $E_p$  on the carrier concentration then stems from different characteristics of spectra of  $Q_{\text{exc}}$  and  $E_{\text{inc}}$  (while the resonant amplitude of  $Q_{\text{exc}}$  increases and blueshifts with increasing  $N$ , the spectrum of  $E_{\text{inc}}$  is non-monotonous and obviously does not depend on  $N$ ). We note, that the interaction with the plasmon leads to the amplification of the local field spectral amplitude at certain frequencies in comparison to the equilibrium state. This feature could be possibly exploited to resonantly amplify the investigated class of nonlinear phenomena. However, we have to be aware of the reststrahlen band in real GaAs (gray areas in Fig. 7.9).

To provide the entire physical picture, we further examine the dependence of the field  $E_p$  on carrier concentration in the time-domain (Fig. 7.9(c),(f)). For the sample in the ground state, the local field is directly proportional to the incident field (under our assumptions, the factor  $Q_{\text{exc}}(\omega)$  does not depend on frequency in this case) and thus has the form of broadband practically single-cycle pulses. In the photoexcited case, however, the interaction with the narrow plasmon leads to a narrower spectrum which translates into long-lasting damped oscillations. The peak field amplitude follows a trend similar to the one in the frequency-domain – a maximum exists for certain concentration of carriers and the amplification with respect to the equilibrium is also observed.

With known the local multi-THz fields  $E_p$ , we can proceed with the assessment of the nonlinear conductivity using the non-perturbative Monte-Carlo calculations. From now on, we treat both considered structures separately.

We start with GaAs nanobars and consider a carrier concentration  $N = 3 \times 10^{17} \text{ cm}^{-3}$  for which the local field amplitude is sufficiently amplified and the corresponding maximum of  $E_p$  appears well below the reststrahlen band of GaAs (Fig. 7.9(a)). In Fig. 7.10, we show the spectra of local electric current densities calculated for various amplitudes of the electric field. For the lowest incident field of 10 kV/cm, the total current density  $j_x$  coincides with the linear density  $j_x^{(1)}$ , i.e. the response is purely linear. Strikingly, no nonlinearity is observed even for incident field as high as 120 kV/cm (i.e.  $E_p \sim 12 \text{ kV/cm}$ ). In contrast, twice lower local field was sufficient to induce nonlinear response in the case of THz pulses (Section 7.2.1.b)). To understand this, it is necessary to consider the spectra of the pertinent local fields together with the microscopic nonlinear coefficients (e.g. Fig. 6.6, although potential well width is different.



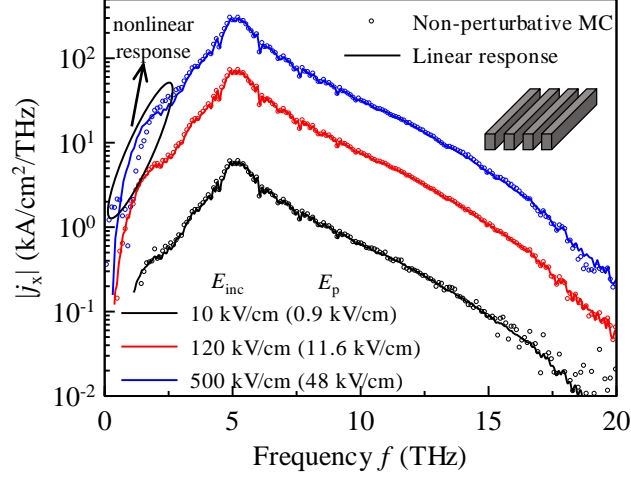


Fig. 7.10. Amplitude spectrum of the local electric current density  $j_x$  inside the GaAs nanobars induced by the multi-THz pulse for  $N = 3 \times 10^{17} \text{ cm}^{-3}$ . Various amplitudes of the electric field were considered. Symbols: spectra calculated using the non-perturbative Monte-Carlo calculations. Lines: spectra of the linear current density calculated as  $j_x^{(1)} = Ne_0\mu E_p$  where  $\mu$  is the linear mobility of the nanobars. Legend: amplitudes of the incident multi-THz field; parenthesis then contain the corresponding peak amplitude of the local field inside the nanobars.

The spectra for the nanobars would be redshifted). The THz pulses then essentially cover the spectral range where the nonlinear coefficients exhibit their maxima. The considered local multi-THz fields, however, are suppressed in this spectral range due to the plasmonic resonance, while the amplified local field maxima are located at higher frequencies for which the nonlinear coefficients already decrease towards zero values.

Based on the above discussion, the observation of nonlinear conductivity of the nanobars would require extremely strong multi-THz fields. As an example, we show the electric current density calculated for the incident field with amplitude 500 kV/cm (i.e. local field of  $\sim 48 \text{ kV/cm}$ ) in Fig. 7.10. Even such a strong field, however, induces just a weak nonlinearity for the frequencies  $\lesssim 2 \text{ THz}$  (appearing as the small systematic difference between the linear response and the result of non-perturbative Monte-Carlo calculations) while the response at high frequencies remains linear.

Regarding the experimental feasibility, the air-based multi-THz spectroscopy is not a suitable tool for the observation of nonlinear conductivity in the considered GaAs nanobars. For the commonly available fields (e.g.  $\lesssim 120 \text{ kV/cm}$  achievable in our lab), the response of the nanobars is still linear. Although we predicted a weak nonlinear response for extremely strong incident fields ( $\gtrsim 500 \text{ kV/cm}$ ), such high fields are not yet commonly obtainable by the air-based techniques [13]. Moreover, this nonlinearity appears at low frequencies (i.e.  $f \lesssim 2 \text{ THz}$ ) which can be better investigated using the high-field low-frequency THz pulses.

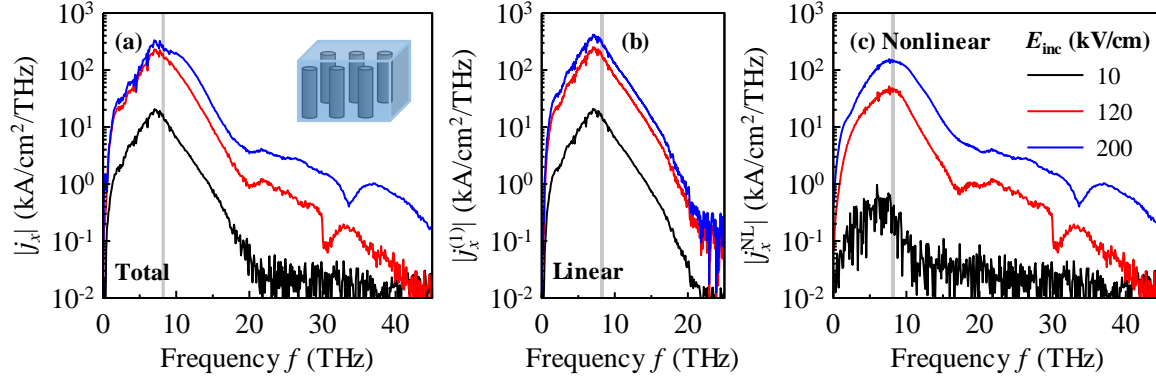


Fig. 7.11. Amplitudes of the local electric current density  $j_x$  induced in the GaAs nanowires induced by the multi-THz pulses for  $N = 5 \times 10^{17} \text{ cm}^{-3}$ . Various amplitudes of the electric field were considered. The total electric current density  $j_x$  (a) was calculated using the non-perturbative Monte-Carlo calculations. The linear current density  $j_x^{(1)}$  (b) was found as  $j_x^{(1)} = Ne_0\mu E_p$  where  $\mu$  is the linear mobility of the nanobars. The nonlinear component is then  $j_x^{\text{NL}} = j_x - j_x^{(1)}$  (c). Gray areas: reststrahlen band of GaAs. Incident fields 120 kV/cm and 200 kV/cm correspond to the local fields 45 kV/cm and 76 kV/cm, respectively.

For the GaAs nanowires, we will consider the carrier concentration  $N = 5 \times 10^{17} \text{ cm}^{-3}$  for which the amplified part of the local field still partly lies below the reststrahlen band of GaAs (Fig. 7.9(d)). The corresponding electric current densities are shown in Fig. 7.11. Unlike for the nanobars (Fig. 7.10), a strong nonlinear component exists for higher amplitudes of the electric field (Fig. 7.11(c)). This is due to the shorter confining length of the nanowires. The corresponding spectra of the nonlinear coefficients are then blueshifted and thus better overlap with the multi-THz pulses.

To describe the response of the entire nanowire array, we further transform the local electric current densities from Fig. 7.11 into their effective counterparts  $j_{\text{eff},x}^{(1)}$ ,  $j_{\text{eff},x}^{\text{NL}}$  and  $j_{\text{eff},x}$  using (4.22), (4.26) and (4.27), respectively, which are shown in Fig. 7.12. For the highest considered electric field, the spectra of  $j_{\text{eff},x}$  (Fig. 7.12(c)) and  $j_x$  (Fig. 7.11(a)) fundamentally differ as the peak at 7.2 THz splits in the effective response. This splitting is caused by the interaction with the plasmonic resonance. For proper understanding, we have to carefully examine the applied transformations. The effective and local linear current densities are mutually scaled by the equilibrium field-enhancement factor  $Q$  (4.22). Since we neglect the dispersion of equilibrium permittivities, the factor  $Q$  is constant and shape of the current density spectrum is thus preserved. The effective and local nonlinear current densities, however, are linked by the field-enhancement factor  $Q_{\text{exc}}$  for the photoexcited structure (4.26). For the considered carrier concentration, the factor  $Q_{\text{exc}}$  exhibits a resonant behavior (Fig. 7.9(e)) which enhances the effective nonlinear electric current density  $j_{\text{eff},x}^{\text{NL}}$  around the resonant frequency. The corresponding peaks in  $j_{\text{eff},x}^{(1)}$  and  $j_{\text{eff},x}^{\text{NL}}$  are then mutually shifted and for high enough fields, their amplitudes become comparable. The total effective electric current density follows  $j_{\text{eff},x} = j_{\text{eff},x}^{(1)} + j_{\text{eff},x}^{\text{NL}}$ . Since the linear and nonlinear components have different polarity (the total

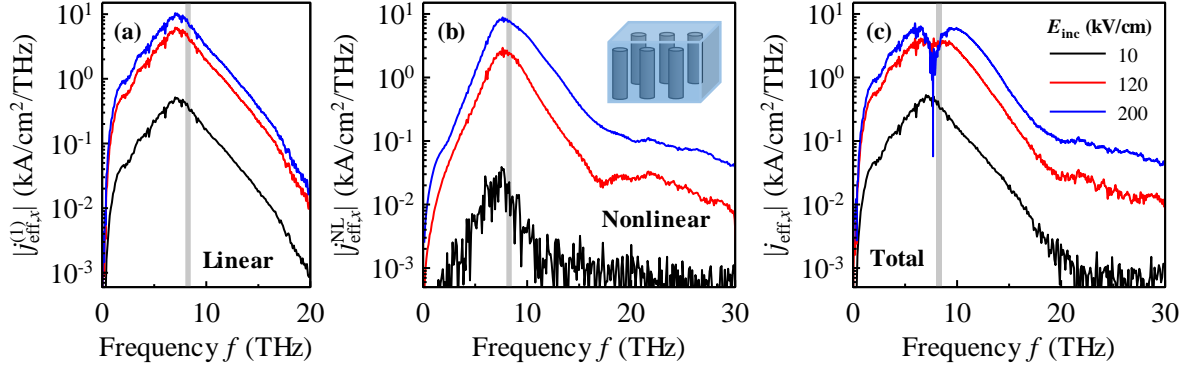


Fig. 7.12. Amplitudes of the effective electric current densities induced in the GaAs nanowires induced by the multi-THz pulses for  $N = 5 \times 10^{17} \text{ cm}^{-3}$ . Various peak amplitudes of the electric field were considered. The effective current densities were calculated from their local counterparts from Fig. 7.11 using the transformations (4.22), (4.26) and (4.27), respectively. The splitting of the main peak in the total effective electric current density  $j_{\text{eff},x}$  (c) appears for 200 kV/cm due to the interaction with the plasmon.

density is always lower than the linear density),  $j_{\text{eff},x}$  is here actually a difference of two close peaks of similar amplitudes which explains the observed splitting. We emphasize that the shift between the corresponding linear and nonlinear peaks depends on the concentration of photoexcited carriers. This feature could be exploited to avoid the reststrahlen band of GaAs in experiments.

In analogy to the broadband low-frequency THz pulses, we further evaluate the transient amplitudes  $\Delta E^{(1)}$  and  $\Delta E^T$  at the output sample surface (Fig. 7.13(a)) which are linked to the corresponding effective electric current densities according to (4.28). The linear signal  $\Delta E^{(1)}$  vanishes above  $\sim 20$  THz (there is just a noise which scales proportionally to the incident electric field). For higher incident electric fields, a pronounced high-frequency component emerges ( $f \gtrsim 20$  THz) in the total signal, thus indicating a strong nonlinear response. At the same time, the spectrum of transient amplitude fundamentally changes within the incident pulse bandwidth ( $f \lesssim 20$  THz).

We now discuss the calculated results with respect to potential experiments. Practically, it is possible to measure either the dependence of the transient signal on the electric field, or the emergence of the high-frequency signal. Previously, we considered that the common THz setups allow detection of transient transmissions as low as  $\sim 10^{-5}$ . For the air-based multi-THz setups, however, the sensitivity is necessary lower due to air fluctuations and inherent absorption in the water vapors [47]. Furthermore, a significant decrease of detector sensitivity is expected above the multi-THz pulse bandwidth as a result of limited gating laser pulse bandwidth.

Regarding the field-dependence of the signal within the incident pulse bandwidth (i.e.  $f \lesssim 20$  THz), we directly calculate the total  $\Delta E^T/E_T$ , linear  $\Delta E^{(1)}/E_T$  and nonlinear  $\Delta E^{\text{NL}}/E_T$  transient transmissions using (4.29) (Fig. 7.13(b)). In Tab. 7.2, we compare the transient transmissions  $\Delta E^{(1)}/E_T$  and  $\Delta E^{\text{NL}}/E_T$  for frequencies which correspond to the maximum of

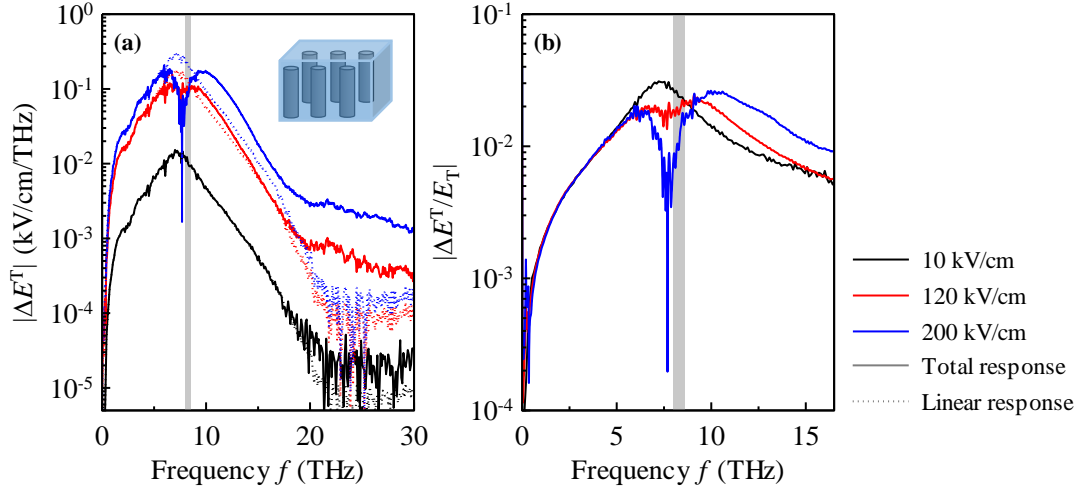
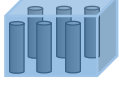


Fig. 7.13. (a) Total and linear transient amplitudes  $\Delta E^T$  (solid) and  $\Delta E^{(1)}$  (dotted), respectively, at the output surface of the investigated nanowire array for various peak amplitudes of the incident multi-THz pulse. Carrier concentration  $N = 5 \times 10^{17} \text{ cm}^{-3}$  was considered. The amplitudes were calculated from the effective electric current densities in Fig. 7.12 using (4.28). Above the incident pulse bandwidth ( $f \gtrsim 20 \text{ THz}$ ) the linear transient amplitudes  $\Delta E^{(1)}$  consist just of a noise originating from the measured multi-THz pulse. (b) The transient transmission spectra of the nanowires calculated from the transient fields in panel (a) using (4.29). The response for 10 kV/cm may be considered linear. Gray areas: reststrahlen band of GaAs.

linear signal ( $f = 7.3 \text{ THz}$ ) and to the peak which appears for 200 kV/cm due to the interaction with plasmon ( $f = 10.2 \text{ THz}$ ). In both cases, the linear and nonlinear signals are comparable to each other. Since the transient transmissions are of order  $10^{-2}$  and the their spectrum fundamentally changes with increasing field, the nonlinearity should be easily detectable by the measurement of both the linear and nonlinear responses in a single setup.

The other option is the emergence of the high-frequency response in the total transient field (Fig. 7.13(a)) for strong incident multi-THz fields. Similarly to the THz pulses, we estimate the corresponding signal as  $\Delta E^T/E_{T,\text{peak}}$  where  $E_{T,\text{peak}}$  is the peak spectral amplitude of the field transmitted through the sample without photoexcitation. The estimated corresponding nonlinear transient transmissions are of order  $10^{-4}$  (Tab. 7.2). As discussed above, the detection of such signals may be problematic in the current multi-THz setups.

The predicted high values of nonlinear transient transmission for GaAs nanowires appear promising for experiments. However, we will later argue (in Section 7.5) that the THz-induced intervalley scattering leads to comparable signals for nanostructures with dimensions  $\lesssim 50 \text{ nm}$  (Figs. 7.22(a) and 7.23(b)). The detected signal will then contain information on both nonlinear phenomena with no simple way to disentangle them from each other. For larger nanostructures, we can hardly resolve any nonlinearity due to charge confinement in the multi-THz range (Fig. 7.10). We thus conclude that the multi-THz

	$E_{\text{inc}}$ (kV/cm)	$f = 7.3$ THz		$f = 10.2$ THz		$f = 22.0$ THz
		$ \Delta E^{(1)}/E_T $	$ \Delta E^{\text{NL}}/E_T $	$ \Delta E^{(1)}/E_T $	$ \Delta E^{\text{NL}}/E_T $	$ \Delta E^{\text{NL}}/E_{T,\text{peak}} $
	120	$3 \times 10^{-2}$	$1.4 \times 10^{-2}$	$1.4 \times 10^{-2}$	$7 \times 10^{-3}$	$1 \times 10^{-4}$
	200		$2.4 \times 10^{-2}$		$2.0 \times 10^{-2}$	$4 \times 10^{-4}$

Tab. 7.2. Summary of the linear  $\Delta E^{(1)}/E_T$  and nonlinear transient transmissions  $\Delta E^{\text{NL}}/E_T$  and  $\Delta E^{\text{NL}}/E_{T,\text{peak}}$  for the GaAs nanowires for peak various amplitudes of the incident multi-THz pulse. Carrier concentration  $N = 5 \times 10^{17} \text{ cm}^{-3}$  was considered. The selected frequencies correspond to the maximum of the linear transient transmission ( $f = 7.3$  THz), the peak appearing for field 200 kV/cm due to the interaction with the plasmon ( $f = 10.2$  THz) and the high-frequency tail ( $f = 22.0$  THz).

spectroscopy is not a suitable technique for experimental confirmation of nonlinearities due to charge confinement in semiconductor nanostructures.

### 7.2.3 Nonlinear response under narrowband pulses generated by free electron laser

In this section, we study the nonlinear response of the GaAs nanobars and nanowires (Fig. 7.4) under the narrowband pulses generated by free electron lasers. Unlike the broadband THz and multi-THz pulses, the pulses generated by free electron laser are composed of several cycles which implies that the pulse reshaping due to the dispersion and phase change is unimportant. This allows a simplification of the computational procedure: we assume a fixed pulse shape *inside* the nanostructures (that from Fig. 7.1(e)) and then we find just the corresponding amplitude of the incident pulse for given concentration of carriers  $N$  (using (4.16)). This avoids the necessity to re-evaluate the incident pulse shape change for each carrier concentration. To evaluate the experimental signal, we have to further calculate the waves  $E_T$  transmitted through the sample without photoexcitation using (4.12.3).

Pertinent electric field parameters entering our calculations are estimated based on the outputs of the FELBE facility (Fig. 7.2) [106]–[108]. The other parameters depend on the investigated structure and are selected to correspond with the response of the high-field low-frequency THz pulses (Section 7.2.2.a)):

- For the nanobars, we assume local field with amplitude 5 kV/cm in the time-domain (i.e. peak spectral amplitude  $A_p \sim 1.3 \times 10^6 \text{ V/m/THz}$ ) and carrier concentration  $N = 5 \times 10^{15} \text{ cm}^{-3}$ . The corresponding incident fields are then  $E_{\text{inc}} \sim 80 \text{ kV/cm}$  (for  $1.5 \text{ THz} \leq f_0 \leq 1.8 \text{ THz}$ ).
- For the nanowires, we consider local fields with amplitude 20 kV/cm and carrier concentration  $N = 10^{17} \text{ cm}^{-3}$ . The amplitudes of  $E_{\text{inc}}$  then somewhat depend on the pulse central frequency  $f_0$  and are summarized in Tab. 7.3.

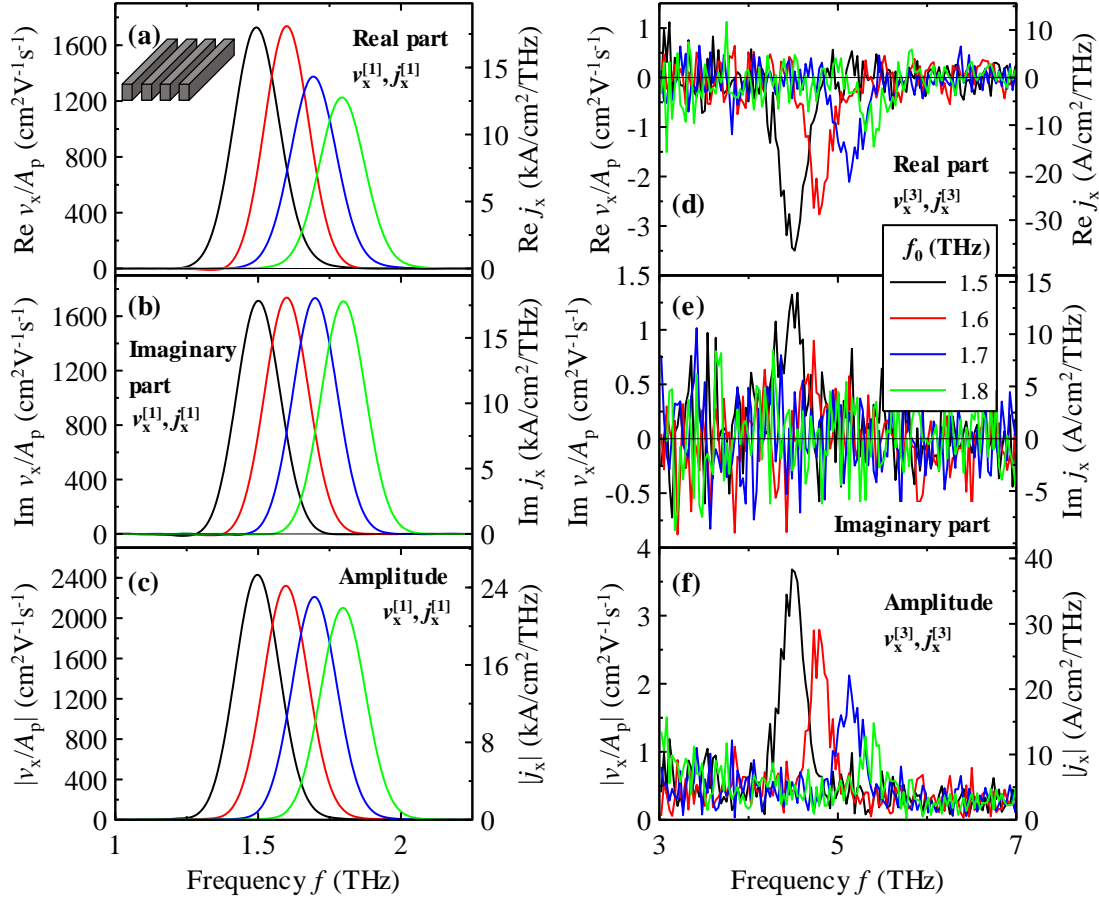


Fig. 7.14. Mean transverse velocity  $v_x$  of carriers inside the GaAs nanobars for several central frequencies  $f_0$  of the driving FELBE pulse ((7.1), Fig. 7.1(e),(f)) calculated by the non-perturbative Monte-Carlo calculations. The field amplitude inside the nanobars was always 5 kV/cm. The velocity spectra are normalized by the peak spectral amplitude  $A_p \sim 1.3 \times 10^6$  V/m/THz of the driving electric field. The ratio  $v_x/A_p$  gives a rough estimate of the mobility of carriers inside the nanobars. The corresponding current density  $j_x$  is evaluated for  $N = 5 \times 10^{15}$  cm $^{-3}$ . Panels (a)-(c) show the peak located at the fundamental frequency while panels (d)-(f) show response at the third harmonic frequency. We identify the latter peaks with the harmonic components of velocity  $v_x^{[3]}(3\omega_0)$  and electric current density  $j_x^{[3]}(3\omega_0)$ , respectively, which were introduced in Section 1.2.

$f_0$ [THz]	1.5	1.7	1.9	2.1	2.3	2.5	2.7	2.9
$E_{\text{inc}}$ [kV/cm]	128	125	122	118	115	108	105	98

Tab. 7.3. Incident electric fields  $E_{\text{inc}}$  required to obtain the local field 20 kV/cm inside the nanowires for  $N = 10^{17}$  cm $^{-3}$  and given central frequency  $f_0$  of the free electron laser pulses. The fields were calculated using the Maxwell-Garnett effective medium theory ((4.16) and (3.14)).

The conductivity of the both structures under the free electron laser pulses was assessed using the non-perturbative Monte-Carlo calculations. For the nanobars, the calculated electric current densities  $j_x$  contain a distinctive peak located at the fundamental frequency  $f_0$  (Fig. 7.14(a)-(c)) and another peak at the third harmonic frequency  $3f_0$  (Fig. 7.14(d)-(f)). Within the framework of the formalism developed in Section 1.2, we identify these peaks with the harmonic electric current density components  $j_x^{[1]}(\omega_0)$  and  $j_x^{[3]}(3\omega_0)$ . The amplitudes of higher harmonic components are at best comparable with the noise originating from the calculations and can be safely neglected. The third-order harmonic electric current density  $j_x^{[3]}(3\omega_0)$  is thus linked solely to the third harmonics generation while the first order component  $j_x^{[1]}(\omega_0)$  contains contributions arising due to the linear response and the third-order nonlinear process resulting in the frequency  $\omega_0 = \omega_0 - \omega_0 + \omega_0$ .

The response of the nanowires (Fig. 7.15) exhibits similar features and in addition, we can also resolve the peak located at the fifth harmonic frequency  $5f_0$  which we identify with the harmonic electric current density  $j_x^{[5]}(5\omega_0)$ . This implies that the response at the fundamental and the third harmonic frequencies is generally influenced also by the nonlinearities of the fifth order. Several third and fifth harmonic frequencies lie within the reststrahlen band of GaAs (gray areas in Fig. 7.15). Although the experimental observation of the signal at these frequencies is hindered due to the interaction with phonons, we keep the calculated data just for the illustration. The changes of the sign of real and imaginary parts of  $j_x^{[3]}(3\omega_0)$  and  $j_x^{[5]}(5\omega_0)$  are due to the phase of carrier motion which is different for each central frequency of the driving electric field.

In the following analysis, we focus on the third harmonics generation which should be in principle easily detectable in the experiments due to the frequency separation. For the nanobars, the third-order harmonic electric current density  $j_x^{[3]}(3\omega_0)$  is 600 times lower than the current density at the fundamental frequency (Fig. 7.14(e),(f)). Therefore, the response at the fundamental frequency is dominated by the linear conductivity and its change due to the nonlinearities is negligible. Similar conclusions hold also for the nanowires despite the higher efficiency of the third harmonics generation. In addition, we also neglect the influence of the fifth order nonlinearities.

The third harmonics generation gives rise to the transient field  $\Delta E_3^T(3\omega_0)$  emitted from the entire structure. Since we neglect nonlinear phenomena of higher orders, Eq. (4.27) and (4.28) together with the appropriate effective medium theories (brick-wall model (3.14.2) for the nanobars and Maxwell-Garnett theory (3.14.1) for the nanowires) yield

$$\Delta E_3^T(3\omega_0) = -\frac{Z_0}{1 + n_{\text{GaAs}}} \frac{\epsilon_{\text{air}} d_{\text{GaAs}}}{\left[ \epsilon_{\text{GaAs}} + i \frac{Ne_0 \mu(3\omega_0)}{\epsilon_0 3\omega_0} \right] d_{\text{air}} + \epsilon_{\text{air}} d_{\text{GaAs}}} L j_x^{[3]}(3\omega_0), \quad (7.4.1)$$



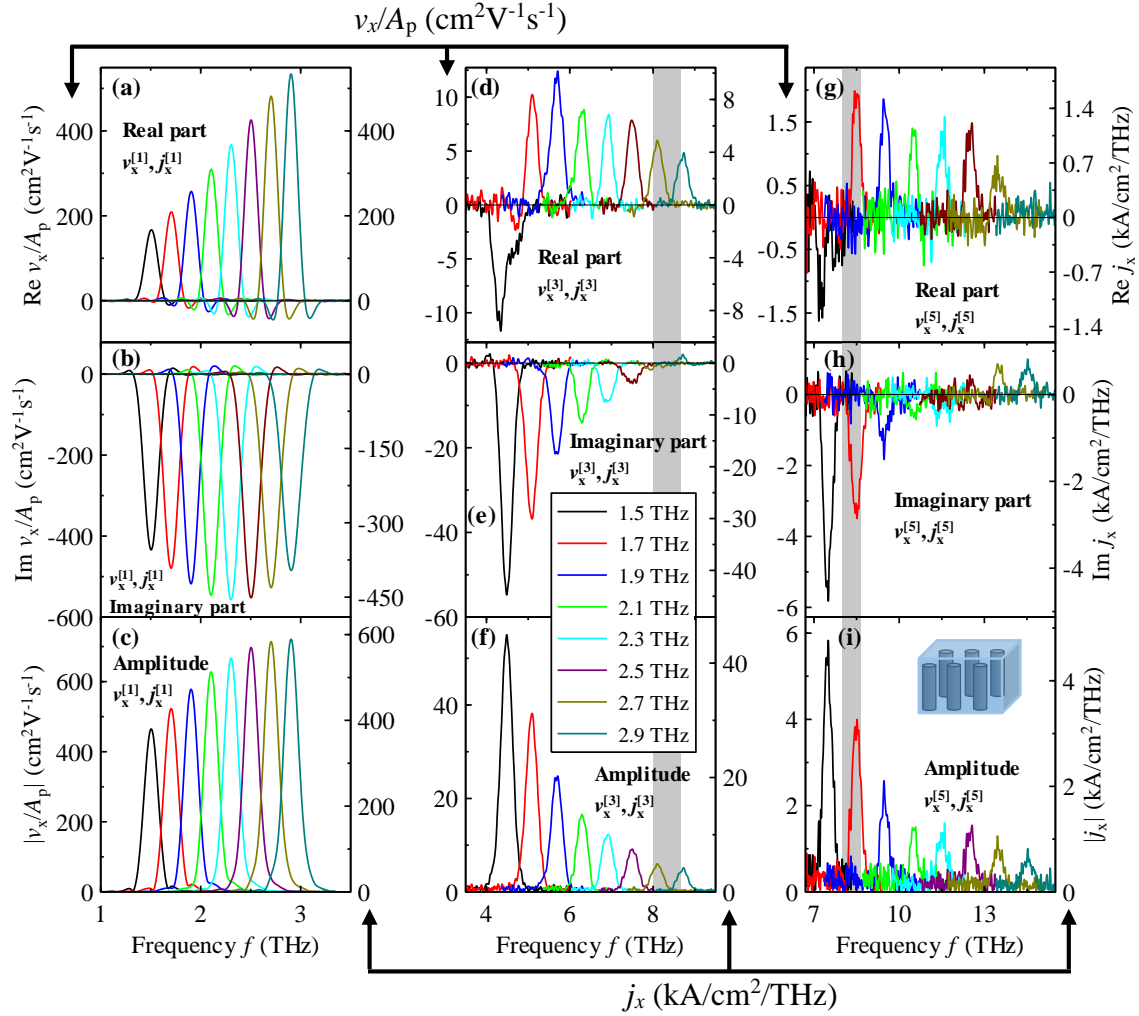


Fig. 7.15. Mean transverse velocity  $v_x$  of carriers inside the GaAs nanowires for several central frequencies  $f_0$  of the driving FELBE pulses ((7.1), Fig. 7.1(e),(f)) calculated by the non-perturbative Monte-Carlo calculations. The field inside the nanowires was always 20 kV/cm. The velocity spectra are normalized by the peak spectral amplitude  $A_p \sim 5.1 \times 10^6$  V/m/THz of the driving electric field. The ratio  $v_x/A_p$  gives rough estimate of the mobility of carriers inside the nanowires. The electric current density  $j_x$  corresponds to  $N = 10^{17} \text{ cm}^{-3}$ . Panels (a)-(c) show the peak located at the fundamental frequency while panels (d)-(f) and (g)-(i) show response at the third and fifth harmonic frequencies, respectively. We identify these peaks with the harmonic components of velocity  $v_x^{[m]}(m\omega_0)$  and electric current density  $j_x^{[m]}(m\omega_0)$ , respectively, which were introduced in Section 1.2. Gray areas: reststrahlen band of GaAs. Black arrows outside the graphs indicate the y-axes displaying the same quantity.

$$\Delta E_3^T(3\omega_0) = -\frac{Z_0}{1+n_{\text{PDMS}}} \frac{2\varepsilon_{\text{PDMS}}}{(1-s)\left[\varepsilon_{\text{GaAs}} + i\frac{Ne_0\mu(3\omega_0)}{\varepsilon_0 3\omega_0}\right] + (1+s)\varepsilon_{\text{PDMS}}} Ls j_x^{[3]}(3\omega_0), \quad (7.4.2)$$



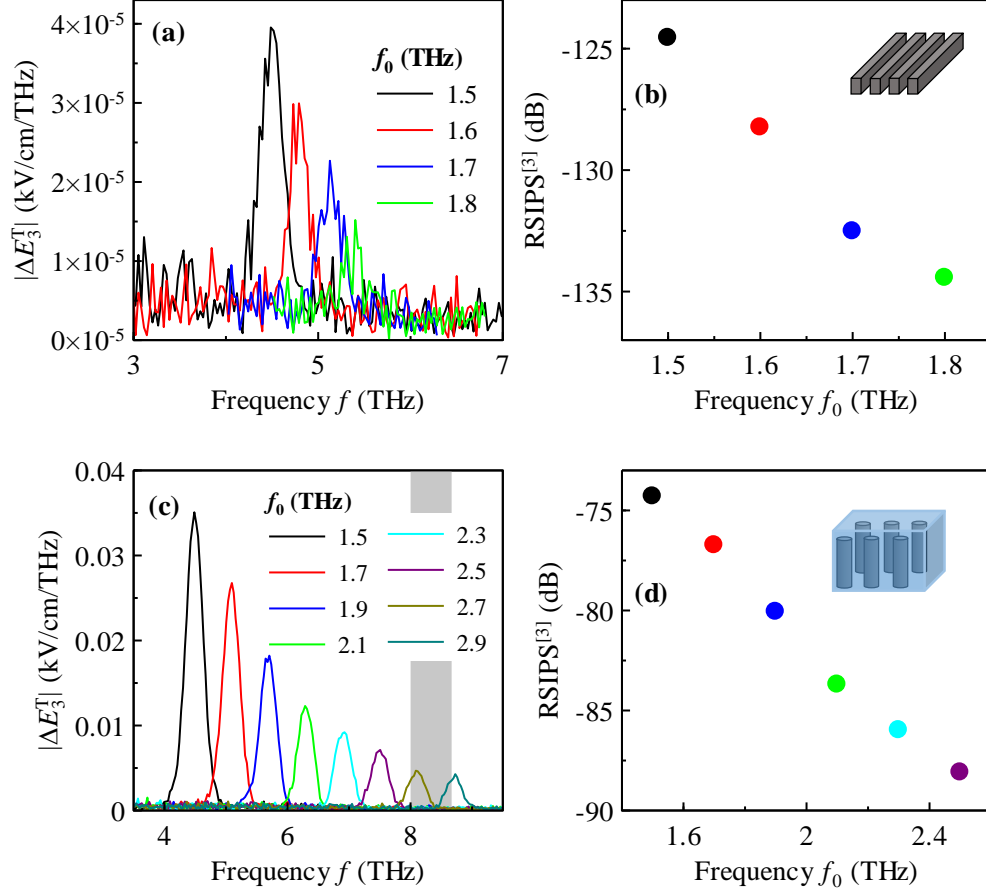


Fig. 7.16. (a),(c) Amplitudes of the third harmonics electric field  $\Delta E_3^T$  emitted from the GaAs nanobars (a) and the nanowires (c) for various frequencies  $f_0$  of the driving free electron laser pulses. The amplitudes were calculated from the electric current density  $j_x$  in Figs. 7.14 and 7.15, respectively, using (7.4). (b),(d) The relative spectrally integrated signal ( $RSIPS^{[3]}$ ) (7.2) corresponding to the third harmonics fields from panels (a) and (c). For the nanobars, we assumed  $E_p = 5$  kV/cm and  $N = 5 \times 10^{15} \text{ cm}^{-3}$ . For the nanowires,  $E_p = 20$  kV/cm and  $N = 10^{17} \text{ cm}^{-3}$  were considered.

where  $\epsilon_{\text{air}}$  is the permittivity of air,  $n_{\text{GaAs}}$  is the refractive index of GaAs,  $d_{\text{GaAs}}$  and  $d_{\text{air}}$  are the width of the nanobars and the spacing between them, respectively and  $\mu$  is the linear mobility of either the nanobars (7.4.1), or the nanowires (7.4.2) (Fig. 7.5(a),(d)). In comparison with the high-frequency tail in the response driven by the model high-field THz pulses (Fig. 7.1(a),(c)), the calculated field amplitudes reach similar values for the nanobars (Fig. 7.16(a)) and are an order of magnitude higher in the case of nanowires (Fig. 7.16(c)). We further evaluate the corresponding ( $RSIPS^{[3]}$ ) using the definition (7.2). In the covered spectral range, the expected signal decreases monotonously with the pulse frequency  $f_0$  (Fig. 7.16(b),(d)). The maximum  $RSIPS^{[3]}$  values are  $\sim 4 \times 10^{-13}$  for the nanobars and  $\sim 4 \times 10^{-8}$  for the nanowires.

To assess the feasibility of experiments, we first draw a comparison with the time-domain techniques. Since the presented RSIPS<sup>[3]</sup> is related to the power transported by the waves, we will consider its square root which roughly gives the transient change in the electric fields. For the nanobars, the maximum transient signal in the fields is then  $\Delta E^{\text{NL}}/E_{\text{T}} \sim 6 \times 10^{-7}$ . This is an order of magnitude lower than the nonlinear transient transmission predicted for the model high-field THz pulses (Tab. 7.1). The predicted third harmonics generation thus cannot be observed by the time-domain detection techniques, since the common setups allow the detection of signals as low as  $10^{-5}$  [42],[47],[113]. Regarding the power measurements, since the incident power is  $10 \text{ W} \lesssim P_{\text{inc}} \lesssim 20 \text{ W}$  (Fig. 7.2(c)), we estimate the power of the third harmonics as  $\sim 10 \text{ pW}$ . We do not believe that such a low power would be detectable with regard to the presence of much stronger background around the fundamental frequency  $f_0$ .

The nanowires are more promising since the RSIPS<sup>[3]</sup> is five orders of magnitude higher. In the electric fields, this would correspond to the nonlinear transient transmission  $\Delta E^{\text{NL}}/E_{\text{T}} \sim 2 \times 10^{-4}$  which would be easily detectable. In the power measurements, this would be equivalent to  $\sim 4 \text{ }\mu\text{W}$  (based on the data from Fig. 7.2(c)). Such powers can be measured by available power detectors. In reality, however, the free electron laser radiation itself exhibits a third harmonics component as a result of nonlinear interactions in optical elements which guide the radiation towards the sample. Since the powers of the FELBE pulses are between  $10 \text{ W}$  and  $30 \text{ W}$  in this case (Fig. 7.2(c)), it is unrealistic to expect that the "natural" third harmonics are comparable to or below the level of the predicted third harmonics generation from the nanowires. We thus conclude, that the FELBE facility is not suitable for the experimental observation of predicted nonlinear phenomena.

### 7.3 ZnO nanoparticles and CdS nanocrystals

While the nanostructures of GaAs (Section 7.2) are promising towards an experimental observation of nonlinearities due to the carrier confinement, their fabrication requires an application of advanced techniques (such as molecular beam epitaxy followed up by lithography). An important limitation of these fabrication processes are a low volume filling fraction of the photoconductive material and rather small dimensions of the samples. In this section, we consider structures which can be easily prepared by much simpler chemical methods. Also, such structures are typically much more tightly packed which significantly increases their filling factor and their thickness is scalable. However, the morphology of the entire system can become more complicated since percolation pathways may appear.

Here, we focus on the nonlinear response of films of ZnO nanoparticles with diameters  $30 \text{ nm}$  and  $50 \text{ nm}$  (which can be prepared by sol-gel technique [110]) and CdS nanocrystals with diameter  $6 \text{ nm}$  (which can be obtained by chemical bath deposition [112]). The linear THz responses of these systems (which are partly percolated) were covered in [27] and [111], respectively. We consider, that both structures are in the form of a thin film with thickness  $L = 1 \text{ }\mu\text{m}$  placed on a quartz substrate ( $n_s \sim 2$ ).

To account for percolation, we have to appropriately modify our non-perturbative Monte-Carlo calculations (Section 2.2) and our nonlinear effective medium theory (Section 4):

- In the Monte-Carlo method, we need to modify the carrier interaction with the nanoparticle boundary. We will assume that carriers are either reflected elastically and specularly with probability  $p_{\text{rel}}$ , or they pass through the boundary into a neighboring nanoparticle with probability  $p_t$  (while their velocity does not change during this process). It is obvious that  $p_{\text{rel}} + p_t = 1$ . In the calculations, we apply parameters from [27] and [111] (Tab. 7.4). In fully isolated nanoparticles (i.e. without percolation),  $p_t$  would be equal to 0 and the simulations would revert to those in previous sections.
- Regarding the effective medium theory, we propose a rather simple approximation. In the studies of the linear response of structures considered here, it was concluded that the structures are percolated [27],[111]. In the VBD model of effective medium (3.3), the linear transient transmission  $\Delta E^{(1)}/E_T$  is then directly proportional to the product  $V\Delta\sigma_p^{(1)}(\omega) = V\Delta j_p^{(1)}(\omega)/E_p(\omega)$ . To make a simple estimate, we assume that the nonlinear response scales in the same way. The nonlinear transient transmissions (4.29) then read

$$\frac{\Delta E^T(\omega)}{E_T(\omega)} = -\frac{Z_0}{n_1(\omega) + n_2(\omega)} LV \frac{[j_p^{(1)}(\omega) + j_p^{\text{NL}}(\omega)]}{E_p(\omega)} \quad (7.5.1)$$

$$\frac{\Delta E^{(1)}(\omega)}{E_T(\omega)} = -\frac{Z_0}{n_1(\omega) + n_2(\omega)} LV \frac{j_p^{(1)}(\omega)}{E_p(\omega)} \quad (7.5.2)$$

$$\frac{\Delta E^{\text{NL}}(\omega)}{E_T(\omega)} = -\frac{Z_0}{n_1(\omega) + n_2(\omega)} LV \frac{j_p^{\text{NL}}(\omega)}{E_p(\omega)}. \quad (7.5.3)$$

We start with the response of ZnO nanoparticles under FELBE pulses ((7.1), Fig. 7.1(e),(f)) with field amplitude  $E_{\text{inc}} = 35 \text{ kV/cm}$  in the time-domain (corresponding to peak spectral amplitude  $A_{\text{inc}} \sim 9 \times 10^6 \text{ V/m/THz}$ ). The local field in the nanoparticles is then  $E_p = 20 \text{ kV/cm}$  (i.e. local peak spectral amplitude  $A_p \sim 5.1 \times 10^6 \text{ V/m/THz}$ ). The calculated electric current densities exhibit a distinct peak located at the fundamental frequency of the FELBE pulse  $f_0$  (Fig. 7.17(a),(c)): its amplitude is considerably lower than for the nanostructures of GaAs (Figs. 7.14 and 7.15) due to much lower carrier mobility in ZnO ( $\mu_{\text{GaAs}} \sim 7 \times 10^3 \text{ cm}^2 \text{V}^{-1} \text{s}^{-1}$ ;  $\mu_{\text{ZnO}} \sim 200 \text{ cm}^2 \text{V}^{-1} \text{s}^{-1}$ ). For 30 nm-sized nanoparticles, we can barely resolve the peaks emerging at the third harmonic frequency  $3f_0$  (Fig. 7.17(b)) with the electric current density 100 times lower than at the driving frequency  $f_0$ . For the nanoparticles

Material	$m$	$\tau_s$ (fs)	$p_t$	$T$ (K)	Statistics	$s$
ZnO	0.24	27	0.20	300	Boltzmann	0.7
CdS	0.20	16	0.34			0.8

Tab. 7.4. Summary of the parameters entering the calculations of nonlinear response of ZnO nanoparticles and CdS nanocrystals. The parameters were taken from the Refs. [27] and [111].

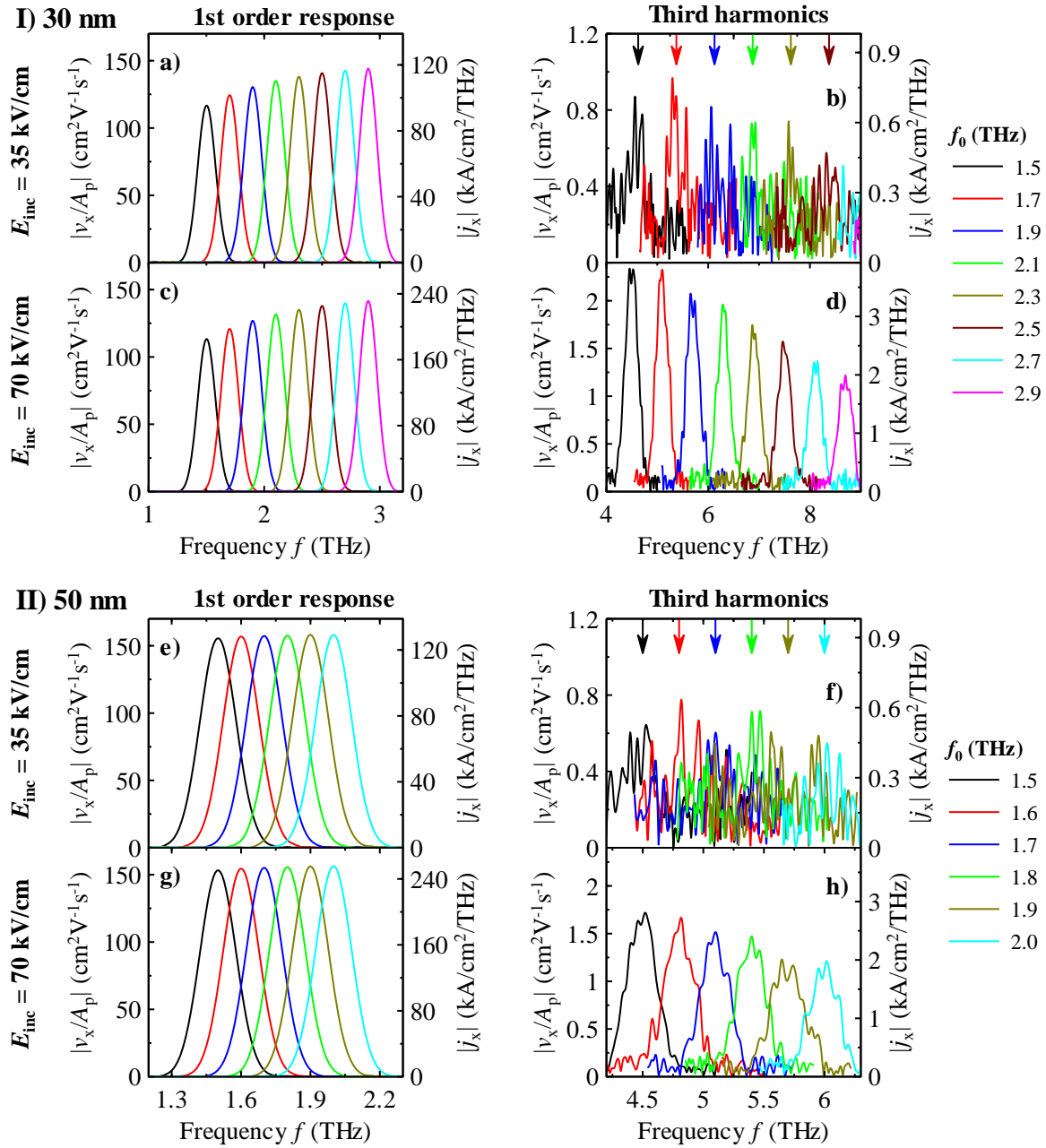


Fig. 7.17. Mean transverse velocity  $v_x$  of carriers inside ZnO nanoparticles with diameter 30 nm ((a)-(d)) and 50 nm ((e)-(h)) for several frequencies  $f_0$  of the driving FELBE pulses (Fig. 7.1(c),(d)) calculated by the non-perturbative Monte-Carlo approach. The incident fields had amplitudes 35 kV/cm and 70 kV/cm, respectively, in the time-domain. The velocity spectra are normalized by the peak spectral amplitude  $A_p$  ( $\sim 5.1 \times 10^6$  V/m/THz for 35 kV/cm, and  $\sim 10^7$  V/m/THz for 70 kV/cm) of the local electric field which gives a rough estimate of the mobility of carriers in the nanoparticles. The corresponding current density  $j_x$  (right axis) is illustrated for  $N = 10^{17} \text{ cm}^{-3}$ . The left column shows the response at the fundamental frequency while the right column shows the peaks emerging at the third harmonic frequencies.

with diameter 50 nm, the third harmonics generation is even weaker compared to the response at  $f_0$  (Fig. 7.17(e),(f)). This is due to the longer confinement length which enhances the amplitude of the linear response but at the same time it suppresses the nonlinearities due to the charge confinement. Even if we increase the incident field to e.g. 70 kV/cm (which correspond to the local field 40 kV/cm), the nonlinear response remains rather weak (compare Fig. 7.17 e.g. with the response of GaAs nanowires in Fig. 7.15); in this situation, intrinsic nonlinearities are expected to dominate the response.

Using (7.5), we provide upper estimates (i.e.  $sQ^2 = 1$ ) of measurable transient transmissions for carrier concentration  $N = 10^{17} \text{ cm}^{-3}$ . In the calculation, we identify a peak located at the fundamental frequency  $f_0$  with the linear component of the electric current density  $j_p^{(1)}$  and the peak at the third harmonic frequency  $3f_0$  with the nonlinear component  $j_p^{\text{NL}}$ . The estimated maximum linear transient transmissions are  $\Delta E^{(1)}/E_T \sim 0.03$  and the corresponding nonlinear signals  $\Delta E^{\text{NL}}/E_T$  are two orders of magnitude smaller (Tab. 7.4). The linear signals are thus rather high compared to the nanostructures of GaAs (Section 7.2.3) while the measurable nonlinear signals are comparable despite considerably weaker nonlinear conductivity of ZnO nanoparticles. The reason is the percolation between ZnO nanoparticles which leads to a stronger effective response (both the linear and nonlinear contributions scale in the same way (7.5)) than in the non-percolated nanostructures of GaAs. However, we cannot realistically expect to observe such signals experimentally due to the comparably strong "natural" third harmonics originating from nonlinear interactions in optical elements guiding the radiation (see discussion in Section 7.2.3). In addition, the real signals will be necessarily lower since  $V \leq 1$  (percolation strength  $V \sim 0.55$  for the sample investigated in [27]).

In principle, we could increase the nonlinear signals by increasing the concentration of carriers. However, this would break the assumed limit of small linear signal and the linear transient transmission will then follow the Tinkham formula (3.50) (where we consider  $\Delta\sigma_{\text{eff}} = Vj_p^{(1)}/E_p$ ). Obviously, this will compromise the nonlinear signals calculated by (7.5) and

<b>ZnO</b>	$E_{\text{inc}}$ (kV/cm)	$ \Delta E^{(1)}/E_T (\omega_0)$	$ \Delta E^{\text{NL}}/E_T (3\omega_0)$
30 nm	35	0.03	$2 \times 10^{-4}$
	70		$5 \times 10^{-4}$
50 nm	35	0.03	$2 \times 10^{-4}$
	70		$3 \times 10^{-4}$

Tab. 7.4. Upper estimates of the linear  $\Delta E^{(1)}/E_T$  and nonlinear  $\Delta E^{\text{NL}}/E_T$  transient transmissions for the ZnO nanoparticles (diameters 30 nm and 50 nm) placed on a quartz substrate probed by the FELBE pulses (Fig. 7.1(e),(f)). The linear and nonlinear transmissions correspond to the peaks in the electric current density located at the fundamental and third harmonic frequencies, respectively, and were calculated using (7.5). Carrier concentration:  $N = 10^{17} \text{ cm}^{-3}$ .

we would thus need to provide a more advanced theory. Development of such approach lies beyond the scope of this work.

We now briefly discuss why the broadband approaches are not expected to perform better high-field experiments. For the terahertz range (i.e.  $f \lesssim 3.0$  THz), we expect signals which are at best as high as those for the FELBE pulses (Tab. 7.4; calculations for GaAs nanowires indicated that the broadband THz signal is at least by a half order of magnitude lower than the narrowband signal (Section 7.2)). In the multi-THz range, the nonlinearity decreases considerably already for frequencies above  $\sim 5$  THz as a result of conductivity

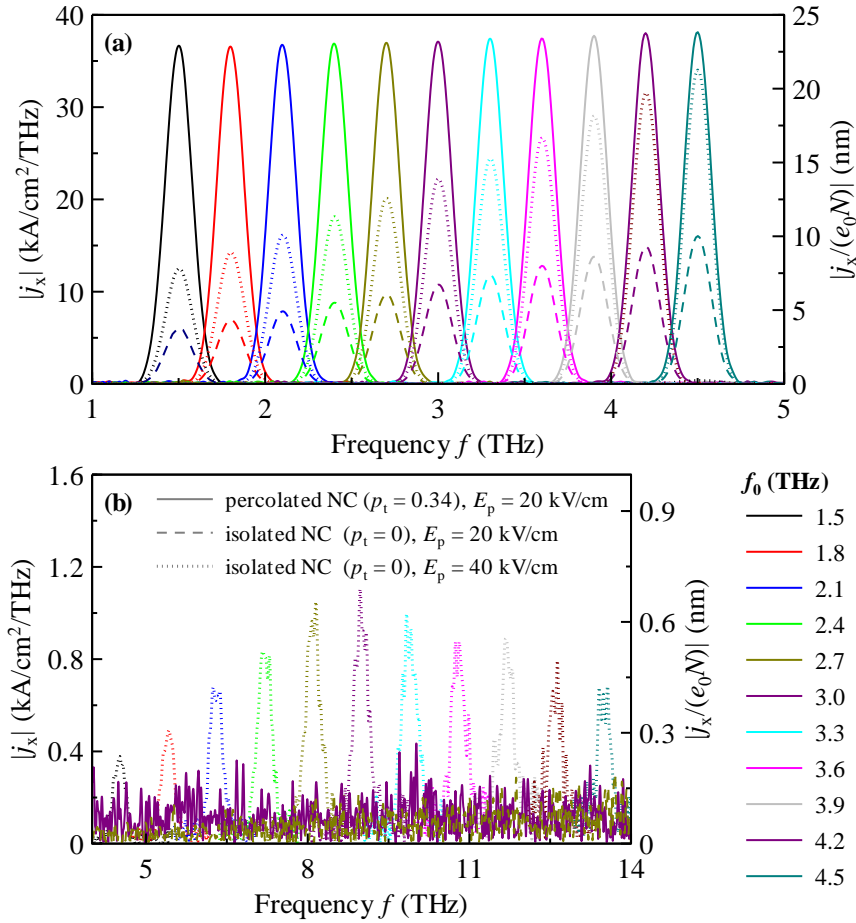


Fig. 7.18. Amplitudes of the local electric current density  $j_x$  induced in 6 nm-sized CdS nanocrystals (NC) induced by the FELBE (Fig. 7.1(c),(d)) with frequencies  $f_0$  calculated using the non-perturbative Monte-Carlo calculations. Several amplitudes of the local electric field  $E_p$  were considered. The calculations were provided both for the percolated (solid lines) and isolated (dashed and dotted lines) nanocrystals. Panel (a) shows the response at the driving frequency  $f_0$  while panel (b) shows the corresponding third harmonics generation (for 20 kV/cm, the response is below the noise floor of the calculations). Carrier concentration  $N = 10^{17}$  cm<sup>-3</sup> was considered.  $p_t$  is the probability of charge transfer into neighboring NC.

decrease due to inertia of carriers. This cannot be compensated by an enhancement due to plasmonic resonance as it does not develop in the percolated nanoparticles.

Using the modified non-perturbative Monte-carlo calculations, we also calculated the conductivity of 6 nm-sized CdS nanocrystals for the FELBE pulses. For the local field amplitude  $E_p = 20$  kV/cm, however, no third harmonics generation is observed and the response can be thus considered linear (Fig. 7.18). For further understanding of this negative result, we provide additional calculations for isolated nanocrystals (i.e.  $p_t = 0$  and  $p_{rel} = 1$  in the Monte-Carlo calculations). The long range transport is then prohibited and the conductivity spectrum is determined just by the charge confinement. In turn, the amplitude of the linear conductivity should decrease while the strongest nonlinearities are expected. The calculated response, however, remains linear (Fig. 7.18, although the linear conductivity indeed decreases) and we thus attribute the lack of strong nonlinear behavior to the combination of low carrier mobility in CdS ( $\mu_{CdS} \sim 140 \text{ cm}^2\text{V}^{-1}\text{s}^{-1}$ ), strong interparticle charge transport (i.e. high  $p_t$ ) inhibiting the role of the confinement and small nanocrystal diameter. To resolve the third harmonics generation in the conductivity spectra of the isolated nanocrystals, we would need to increase the local field at least up to 40 kV/cm (Fig. 7.18(b)).

We thus conclude that the investigated 30 nm and 50 nm-sized ZnO nanoparticles are not very promising for the considered experiments at the FELBE facility. While the percolation between individual nanoparticles substantially limits the local nonlinearities, at the same time it provides considerable enhancement of nonlinearities in the effective response. The corresponding transient transmissions, however, are at best comparable with the parasitic contributions (see the discussion in Section 7.2.3). The broad-band techniques are then even less suitable due to expected lower signals. The response of percolated CdS nanocrystals with diameter 6 nm remains linear even for rather high fields. The main reasons are the low carrier mobilities ( $\sim 140 \text{ cm}^2\text{V}^{-1}\text{s}^{-1}$ ) and the charge confinement weakened by the existing percolation.

## 7.4 The most promising structure – metallic nanoslits filled with GaAs nanobars

In previous sections, we studied nanostructures where the semiconducting parts were surrounded by a non-conducting material. In these systems, the local electric field  $E_p$  is typically considerably lower than the incident electric field  $E_{inc}$  due to the structure morphology (captured in the field-enhancement factors  $Q$  and  $Q_{exc}$ ) and Fresnel losses (4.16) which limits the strength of any nonlinearities. In a striking contrast, it is well known that metallic structures can concentrate the electric field into insulating gaps (enhancements in the order of several thousands with respect to the incident field were reported in [124]-[126]). This could be potentially exploited to observe much stronger nonlinear phenomena.

Here, we consider a periodic structure consisting of 250 nm wide GaAs nanobars placed between 2250 nm wide gold stripes (Fig. 7.19). The width of the nanobars is thus the same as in Section 7.2, but they fill only 10% of the entire structure (compared to 42% in Section 7.2). The structured layer is 1  $\mu\text{m}$  thick and lies on a GaAs substrate (this is dictated

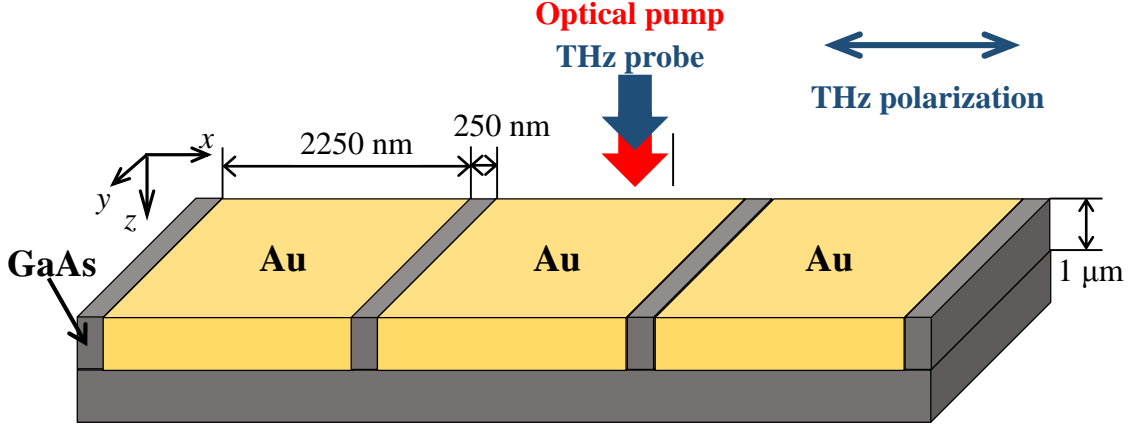


Fig. 7.19. Schematic illustration of GaAs (gray) nanobars filling the gold (yellow) nanoslits for the theoretical study of nonlinear THz photoconductivity. Filling factor of the nanobars is 10%. Both optical pump and THz probe beams propagate along the  $z$ -axis. The THz electric field is polarized in the  $x$ -direction.

by the fabrication requirements; we will discuss later that the photosignal possibly originating from the substrate is not very important for the considered system).

To assess the nonlinear response due to charge confinement of the slit-structure (Fig. 7.19), we employ the framework described in Section 7.1. The permittivity  $\epsilon_h$  of gold reads

$$\epsilon_h(\omega) = i \frac{\sigma_h}{\omega \epsilon_0}, \quad (7.6)$$

where  $\sigma_h = 4.5 \times 10^5$  S/cm is the dc conductivity of gold at room temperature [127]. Due to the low charge scattering time in gold ( $\tau_s \sim 27$  fs [127]), we can neglect the dispersion of conductivity and consider it constant in the investigated frequency range. Similarly as in previous sections, we consider  $\epsilon_p \sim 12.6$  without dispersion for non-photoexcited GaAs which is plausible outside the reststrahlen band between 8 THz and 8.7 THz [122]. In the Monte-Carlo calculations used in this part, we assume Boltzmann statistics and the following parameters:  $\tau_s = 270$  fs,  $m = 0.07m_e$ ,  $T = 300$  K.

#### 7.4.1 Linear response

The linear mobility  $\mu$  of carriers confined in the GaAs nanobars (Fig. 7.20(a)) was calculated using the Monte-Carlo calculations based on Kubo formalism (the spectrum is the same as in Fig. 7.5(a) in Section 7.2.1). Using the brick-wall model (3.10) (with permittivity  $\epsilon_h$  given by (7.6)), we further assess the effective response of the entire slit-structure.

In the limit of a weak photoexcitation (i. e. low  $N$ ), the conductivity of photoconductive parts  $\Delta\sigma_p = Ne_0\mu$  (e.g.  $\Delta\sigma_p \sim 0.5$  S/cm for  $N = 10^{15}$  cm $^{-3}$ ) is negligible compared to the conductivity of gold ( $\sigma_h = 4.5 \times 10^5$  S/cm [127]). The term  $\epsilon_p + i\Delta\sigma_p/(\omega\epsilon_0)$  in the denominator of (3.10) can be then neglected and the normalized effective photoconductivity  $\Delta\sigma_{\text{eff}}/(e_0N)$  of



the structure is thus directly proportional to the mobility of carriers confined in the GaAs nanobars

$$\frac{\Delta\sigma_{\text{eff}}(\omega)}{e_0 N} \approx \left(1 + \frac{d_h}{d_p}\right) \mu = \frac{\mu}{s}, \quad (7.7)$$

where the proportionality constant does not depend on  $N$  and it is equal to the reciprocal value of filling factor  $s$ . This can be understood in terms of electric circuits. Since gold is a very good conductor, the voltage drops are present just on the GaAs nanobars which directly implies the  $1/s$ -dependence. In our case,  $s = 0.1$  and the effective conductivity is thus ten times stronger than the local conductivity (Fig. 7.20(b)). We verified that this regime is attained for  $N$  up to  $\sim 10^{17} \text{ cm}^{-3}$ . We will further consider lower carrier concentrations and thus provide analysis within this limit.

We note that the considered metallic structure shows strikingly different behavior than the systems with non-conducting matrices studied in Section 7.2. For the latter, the effective photoconductivity  $\Delta\sigma_{\text{eff}}$  is usually approximately proportional to the filling factor  $s$  of the photoconductive material. In such case, the effective conductivity is always lower than the local conductivity since  $s < 1$ .

In experiments, the linear response is assessed by the transient transmission  $\Delta T/T$ . For the considered slit-structure, the thin-film limit is satisfied and  $\Delta T/T$  is thus directly proportional to the effective photoconductivity  $\Delta\sigma_{\text{eff}}$  (3.49). Since the normalized effective photoconductivity  $\Delta\sigma_{\text{eff}}/(Ne_0) \sim 3 \times 10^4 \text{ cm}^2 \text{ V}^{-1} \text{ s}^{-1}$  (Fig. 7.20(b)) is higher with the charge mobility in bulk GaAs ( $\mu \sim 7 \times 10^3 \text{ cm}^2 \text{ V}^{-1} \text{ s}^{-1}$ ), we expect the corresponding transient signal to

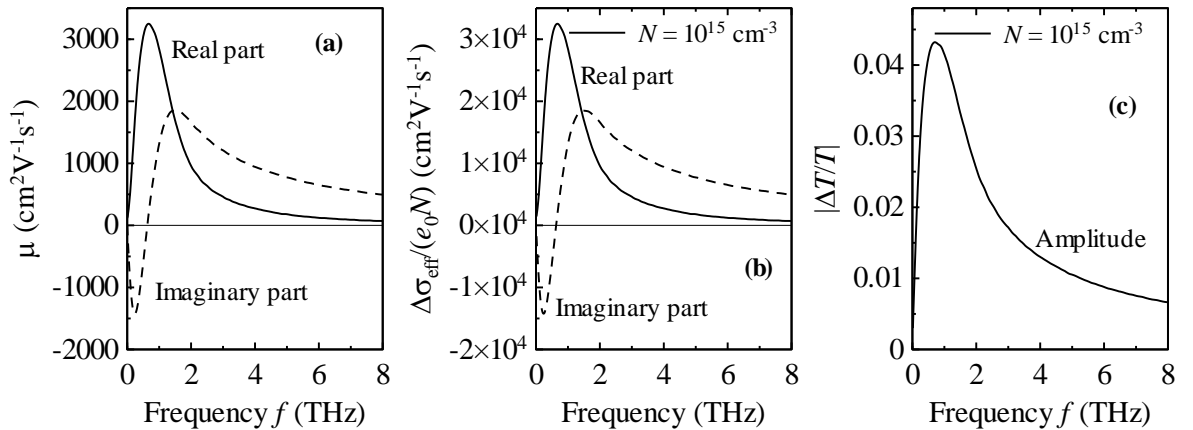


Fig. 7.20. Linear response of the GaAs nanobars filling the gold nanoslits (Fig. 7.19). (a) Linear mobility of carriers confined within the nanobars calculated using the Monte-Carlo calculations based on Kubo formalism. (b) Normalized effective photoconductivity spectra for carrier concentration  $N = 10^{15} \text{ cm}^{-3}$  calculated from panel (a) using (3.10). The spectrum of  $\Delta\sigma_{\text{eff}}/(Ne_0)$  does not change for  $N \lesssim 10^{17} \text{ cm}^{-3}$ . (c) Linear transient transmission spectrum calculated from panel (b) using (3.49).

be easily measurable. Indeed, for  $N = 10^{15} \text{ cm}^{-3}$ , the absolute value of the transient transmission is  $\sim 4 \times 10^{-2}$ , which is comfortably above the predefined detection sensitivity limit of  $10^{-5}$ .

One of the advantages of the considered metallic nanoslits is a good suppression of parasitic signals originating from substrate photoexcitation. The gold parts act as mirrors which reflect a large part of the pump beam. The rest of the pump beam is then attenuated in the nanobars before reaching the substrate and the concentration of photoexcited carriers is thus lower in substrate than in the nanobars. Also, the normalized effective photoconductivity of the metallic nanoslits  $\Delta\sigma_{\text{eff}}/(Ne_0)$  is roughly four times higher than the charge mobility in bulk material. At worst, we thus expect the parasitic signal to be a few percent of the transient transmission of the nanoslits. This could be further reduced if the optical pump beam were polarized along the slits (i.e. in the  $y$ -direction in Fig. 7.19) due to waveguiding effects.

The high value of  $\Delta T/T$  predicted above (i.e. for  $N = 10^{15} \text{ cm}^{-3}$ ), however, implies that we reached the limits of our theory on wave propagation which is valid just for weak transient changes ( $\Delta T/T \ll 1$ ). For higher concentrations, the measurable signal then follows the Tinkham formula (3.50). To evaluate the nonlinearities, we would then need to employ finite-difference time-domain calculations. For  $N \lesssim 10^{15} \text{ cm}^{-3}$ , (3.50) yields practically same results as our theory ( $\Delta T/T \sim 0.04$ ).

#### 7.4.2 Nonlinear response

Here, we focus on the nonlinear response of the gold nanoslits filled with GaAs nanobars from Fig. 7.19 under the incident low-frequency broadband THz pulses<sup>1</sup> (Fig. 7.1(a)). Using (3.14), we first evaluate the field-enhancement  $Q_{\text{exc}}$  and find that it is  $\sim 10$  with negligible dispersion for  $N \lesssim 10^{17} \text{ cm}^{-3}$ . The local field  $E_p$  thus has the same temporal profile and spectrum as the incident field  $E_{\text{inc}}$ . The combination of Fresnel losses and  $Q_{\text{exc}}$  then implies that  $E_p$  is enhanced four times compared to  $E_{\text{inc}}$ . This means that to guarantee e.g.  $E_p = 20 \text{ kV/cm}$  inside the nanobars requires only  $E_{\text{inc}} = 5 \text{ kV/cm}$ , which is achievable even in our existing setup utilizing ZnTe.

For  $E_{\text{inc}} = 5 \text{ kV/cm}$ , we employ the non-perturbative Monte-Carlo calculations to assess the nonlinear conductivity of carriers in the nanobars. The electric current density  $j_x$  clearly exhibits a strong nonlinear component: the nonlinearity decreases the signal by 2/3 compared to the original linear response (Fig. 7.21(a)) and a high-frequency tail extending up to  $\sim 6 \text{ THz}$  emerges. Since the incident pulse contains just the frequencies below  $\sim 1.3 \text{ THz}$ , generation of frequencies up to  $\sim 6 \text{ THz}$  implies that the nonlinearities of the third and the fifth order are involved in the response.

Since  $sQ_{\text{exc}} \sim 1$ , the total electric current density  $j_x$  and its linear and nonlinear components (Fig. 7.21(a)) are equal to their effective counterparts (4.27). In addition, the

---

<sup>1</sup> Here, we limit ourselves to the nonlinear response under the low-frequency THz pulses. In the multi-THz range, the nonlinearity decreases due to inertia of carriers. Since no plasmonic resonance develops in the studied metallic structure for low concentration  $N \sim 10^{15} \text{ cm}^{-3}$  considered here, an enhancement similar to that observed in Section 7.2.2.b) is not possible. Experiments at the FELBE facility are then less sensitive than the time-domain experiments with the low-frequency THz pulses.

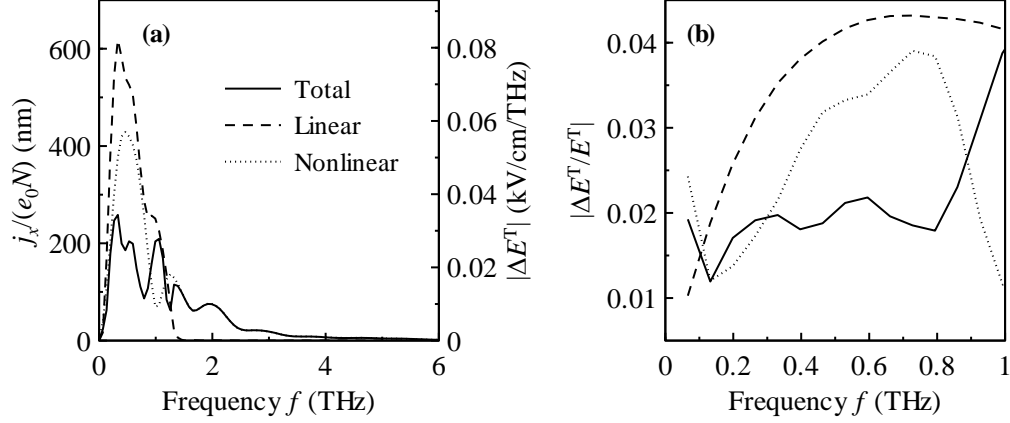


Fig. 7.21. Nonlinear response of the GaAs nanobars filling the gold nanoslits (Fig. 7.19) induced by the incident broadband low-frequency THz pulse with amplitude of 5 kV/cm. (a) The electric current density in the nanobars (left axis) calculated using the Monte-Carlo calculations exhibits a strong nonlinear component (dotted line). We note, that the normalized electric current density  $j_x/(e_0 N)$  represents the velocity of carriers. The Fourier transform then reduces the unit of velocity from meters per second just to meters. Since the field-enhancement factor  $Q_{\text{exc}}$  does not show any dispersion ( $N = 10^{15} \text{ cm}^{-3}$ ), the transient field  $\Delta E^T$  leaving the structure (right axis) is directly proportional to the electric current density ((4.27) and (4.28)). (b) The transient transmission spectra in the linear (dashed) and the nonlinear regime (solid) calculated from panel (a) using (4.29). Dotted line shows the nonlinear component of the total response.

spectrum of the transient field  $\Delta E^T$  leaving the sample (right axis in Fig. 7.21(a)) has the same shape as the spectrum of  $j_x$  (4.28).

We now judge the calculated results with respect to potential experiments. First, we focus on the field-dependence of the transient transmission signals  $\Delta E^T/E_T$ ,  $\Delta E^{(1)}/E_T$  and  $\Delta E^{\text{NL}}/E_T$  which we calculate directly using (4.29) (Fig. 7.21(b)). The estimated total signal  $|\Delta E^T/E_T| \sim 2 \times 10^{-2}$  is approximately twice lower than the signal corresponding to the purely linear response. The nonlinear transmission is then  $|\Delta E^{\text{NL}}/E_T| \sim 2 \times 10^{-2}$  which is easily detectable experimentally. Due to the significant enhancement of the local field, such measurements could be realized even in the setups optimized for low THz fields. Note that we would again need to perform measurements for various field intensities to be able to extract the nonlinear component.

The other option is the measurement of the high-frequency signal emerging in the total transient field  $\Delta E^T$  (Fig. 7.21(a); only noise would be present if the response were linear). Such type of experiment would be then potentially simpler since we could avoid the measurement of the linear transient response. As previously, we quantify the corresponding signal as  $\Delta E^T/E_{T,\text{peak}}$  where  $E_{T,\text{peak}}$  is the peak spectral amplitude of the field transmitted through the sample in equilibrium. The highest estimated signal is then  $\Delta E^T/E_{T,\text{peak}} \sim 7 \times 10^{-3}$  which is considerably above the detection limit and thus measurable.

The metallic stripes thus provide substantial enhancement of both the local electric field and the effective response. We thus predict a high enough nonlinear signals even for rather low incident electric fields. These signals could be measured even in the common amplifier-based setups utilizing ZnTe. This is in striking contrast with the dielectrics-based structures (Section 7.2) for which we essentially require high-field sources generating fields  $\gtrsim 100$  kV/cm.

## 7.5 Discussion of strength of nonlinearities

In previous sections, we investigated the nonlinear response due to charge confinement in selected nanostructures of various shapes and sizes. Here, we perform a more systematic study of the influence of the nanostructure size on the strength of the nonlinearities (the role of the shape is considered less important). In addition, we provide a comparison with the strength of nonlinearities in bulk GaAs. It is sufficient to provide the discussion at the local level as the effective medium will act in the same way on each nonlinearity.

For simplicity, we assume a non-degenerate electron gas confined in one-dimensional rectangular infinitely deep potential GaAs wells of various widths and subjected to a local monochromatic wave with amplitude  $E_{p,0}$  (6.1). To assess the nonlinear response, we employ our non-perturbative Monte-Carlo calculations. We then quantify the nonlinearities by a nonlinear mobility  $\mu^{\text{NL}}$  which describes the nonlinear response of a single carrier. Considering the linear relations (1.2) and (1.3), we express  $\mu^{\text{NL}}$  as

$$\mu^{\text{NL}} = \frac{j_p^{\text{NL}}}{Ne_0 E_{p,0}}, \quad (7.8)$$

where the nonlinear electric current density  $j_p^{\text{NL}}$  is a direct output of the calculations.

In Fig. 7.22, we show the dependencies of nonlinear mobility  $\mu^{\text{NL}}$  at the frequency 0.5 THz on the amplitude  $E_{p,0}$  of the monochromatic electric field in the time-domain for several well widths. For low enough electric fields, only the third-order nonlinearities contribute to the response and the nonlinear mobility  $\mu^{\text{NL}}$  thus initially follows a quadratic dependence on  $E_{p,0}$  (considering (1.15) and (7.8))

$$\mu^{\text{NL}} = gE_0^2. \quad (7.9)$$

The above relation indeed well matches the calculated data for a few lowest fields for each well width (dashed lines in Fig. 7.22, the three lowest fields were used to fit the value of  $g$ ). For higher field amplitudes  $E_{p,0}$ ,  $\mu^{\text{NL}}$  significantly deviates from the quadratic dependence and  $|\mu^{\text{NL}}|$  seems to saturate. In this regime, the response thus cannot be described by the perturbative approach common in nonlinear optics. The dependence of the nonlinearity strength on the well width (Fig. 7.22(c)) is non-monotonous; a maximum exists for  $l \sim 250$  nm. The real part of  $\mu^{\text{NL}}$  is negative (Fig. 7.22(b)) for narrow enough wells (i.e.  $l \lesssim 500$  nm). This implies the decrease of total charge mobility due to the nonlinearity (the driving electric field favors the interaction with boundary to bulk scattering). For wide enough potential wells and certain electric field

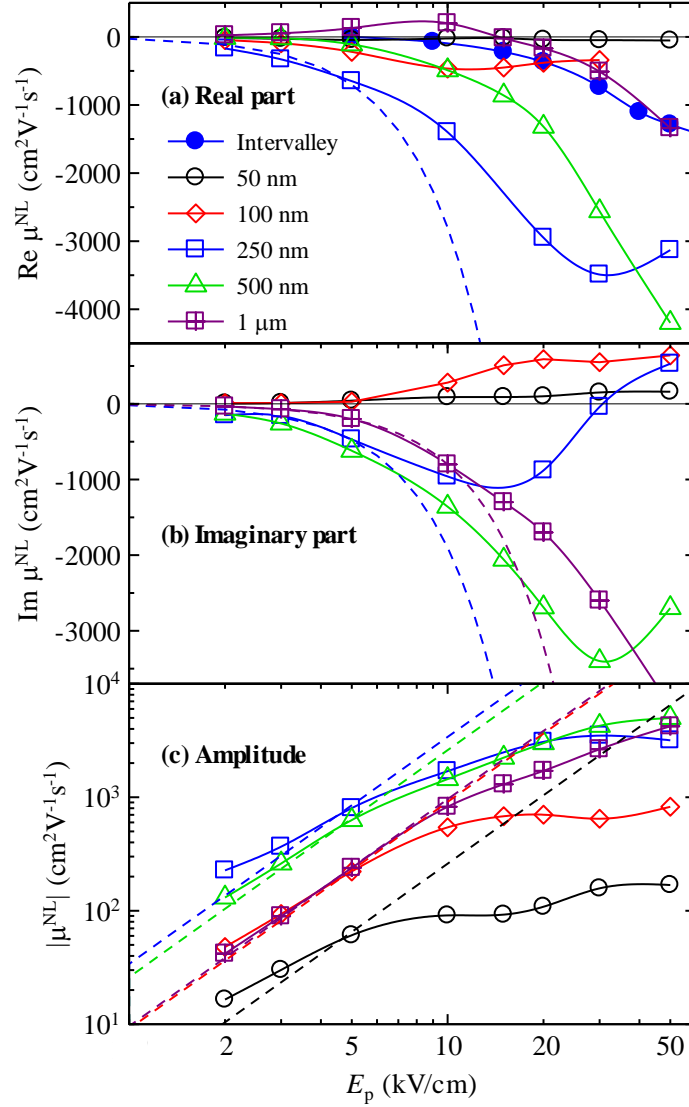


Fig. 7.22. The nonlinear mobility  $\mu^{\text{NL}}$  at the frequency 0.5 THz of non-degenerate electron gas confined in infinitely deep rectangular potential GaAs wells of various widths. The carriers were subjected to a local monochromatic wave with amplitude  $E_0$ . The mobilities were assessed by the non-perturbative Monte-Carlo calculations. Dashed lines: fits by quadratic function (7.9) (three lowest electric fields were considered). Solid line serves as guide for the eye only. Filled triangles are  $\mu^{\text{NL}}$  corresponding to the intervalley scattering in bulk GaAs (Fig. 7.24; Eq. (7.16)).

amplitudes (e.g.  $l = 1 \mu\text{m}$ ,  $E_{p,0} \lesssim 20 \text{ kV/cm}$ ), however, the real part of  $\mu^{\text{NL}}$  becomes slightly positive, i.e. the charge mobility increases. The origin of this increase is unclear and it is a subject of further studies.

The nonlinear coefficient  $g$  characterizes the third-harmonics generation and we can thus link it also with the third-order susceptibility  $\chi^{(3)}(3\omega_0; \omega_0, \omega_0, \omega_0)$ . The corresponding polarization  $P^{(3)}(3\omega_0)$  then reads

$$P^{(3)}(3\omega_0) = \varepsilon_0 \chi^{(3)}(3\omega_0; \omega_0, \omega_0, \omega_0) E_{p,0}^3(\omega_0). \quad (7.10)$$

Since electric current density  $j^{(3)}(3\omega_0)$  is a time-derivative of polarization  $P^{(3)}(3\omega_0)$ , we get in the frequency-domain

$$j^{(3)}(3\omega_0) = i3\omega_0 \varepsilon_0 \chi^{(3)}(3\omega_0; \omega_0, \omega_0, \omega_0) E_{p,0}^3(\omega_0). \quad (7.11)$$

Comparison with (7.8) and (7.9) then yields the third-order susceptibility  $\chi^{(3)}(3\omega_0; \omega_0, \omega_0, \omega_0)$  corresponding to the charge confinement

$$\chi^{(3)}(3\omega_0; \omega_0, \omega_0, \omega_0) = -i \frac{Ne_0}{3\omega_0 \varepsilon_0} g. \quad (7.12)$$

To compare the linear and nonlinear responses, we use the relation between the linear susceptibility  $\chi^{(1)}(\omega_0)$  and the linear mobility of carriers  $\mu(\omega_0)$

$$\chi^{(1)}(\omega_0) = i \frac{Ne_0}{\omega_0 \varepsilon_0} \mu(\omega_0). \quad (7.13)$$

In Fig. 7.23, we show the dependence of the amplitudes of linear mobility  $|\mu|$  and nonlinear coefficient  $|g|$  on the well width  $l$  ( $N = 10^{15} \text{ cm}^{-3}$  and  $f_0 = 0.5 \text{ THz}$ ). The amplitude of linear mobility  $|\mu|$  (Fig. 7.23(a)) initially sharply increases with  $l$  as the charges interact less with the well boundaries which reduces the effective scattering. For very large structures,  $|\mu|$  begins to saturate as it approaches the bulk value given by the Drude model (5.1). The amplitude of the nonlinear coefficient  $|g|$  also initially increases with confining length due to the reduced effective scattering (Fig. 7.23(b)). On the other hand, the nonlinearities are induced just by the charge confinement, therefore the nonlinear response must completely vanish for infinitely large structures. Between these two regimes, there is thus quite a broad region where the nonlinear response reaches its maximum ( $l \sim 250\text{-}300 \text{ nm}$  for  $f_0 = 0.5 \text{ THz}$ ). The relative strength of the nonlinearity with respect to the linear response  $|g|/|\mu|$  increases with decreasing confining length and saturates for lowest  $l$  (Fig. 7.23(c)).

As we already discussed in introduction to Section 7.2, a plethora of nonlinear phenomena was observed in bulk GaAs [18]-[22],[96],[97]. In real nanostructures, these effects are then expected to accompany any nonlinearities due to charge confinement. Any detected nonlinear signal will be then a mixture of signals of different origin. Therefore, it is important to mutually compare expected strengths of these effects.

For our work, we expect that the most important nonlinear effect originating from bulk GaAs is the acceleration of electrons in the conduction band which enables phonon-initiated scattering into low-mobility side valleys [18]-[20]. In Ref. [19], this effect was quantified as a decrease of THz absorption coefficient  $\alpha$  with increasing electric field (Fig. 7.24). We now estimate the nonlinear mobility  $\mu^{\text{NL}}$  corresponding to this effect. In an absorbing medium, the real part of conductivity  $\sigma$  is directly proportional to  $\alpha$  [128]

$$\sigma = n\varepsilon_0 c \alpha. \quad (7.14)$$

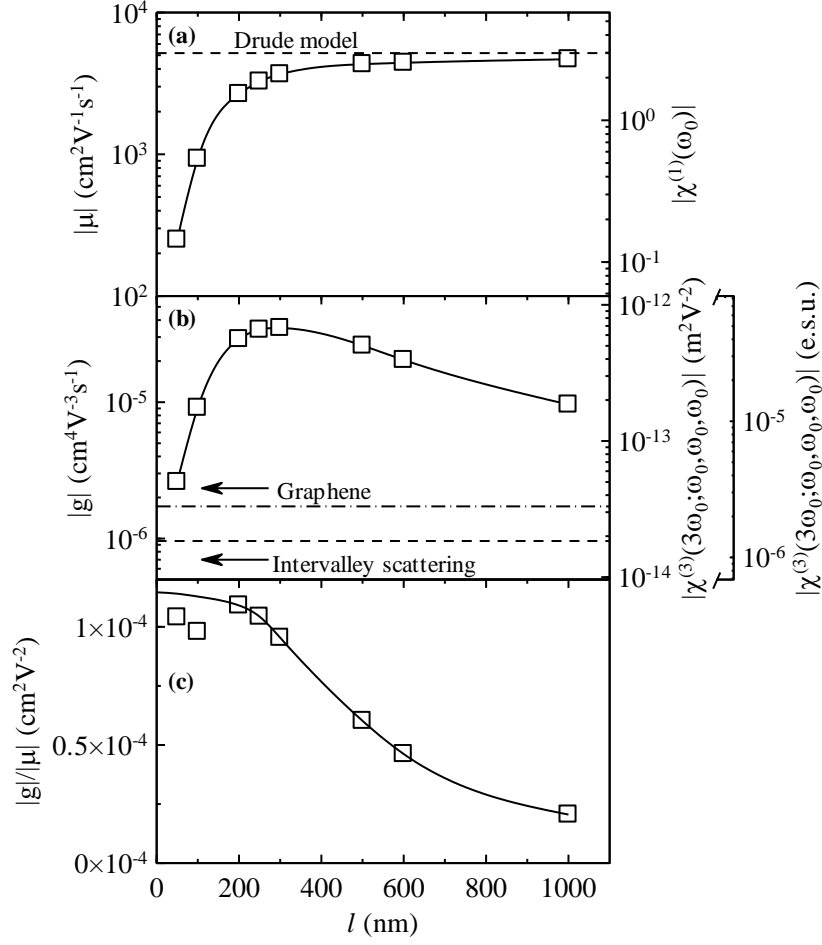


Fig. 7.23. Dependence of the strength of linear and nonlinear responses of a single carrier on the confining length  $l$ . (a) Amplitude of linear mobility of confined carriers. (b) Amplitude of the third-order nonlinear coefficient  $g$ . The dash-dot line shows  $g$  corresponding to graphene (7.17), the dashed line then corresponds to the intervalley scattering in bulk GaAs ( $g$  was found by combining Eqs. (7.16) and (7.9); the data from Fig. 7.22(a) were used). (c) Dependence of the relative strength of the nonlinearities due to charge confinement on the confining length  $l$ . The right axes show the corresponding susceptibilities (7.13) and (7.12), respectively, for  $N = 10^{15} \text{ cm}^{-3}$  and  $f_0 = 0.5 \text{ THz}$ . The susceptibilities are expressed in either SI or electrostatic units (e.s.u.) and characterize the response of entire ensemble of carriers. Solid lines serve as guide for the eye only.

We verified that the imaginary part of  $\sigma$  is negligible for frequencies above  $\sim 0.1 \text{ THz}$ . The nonlinear conductivity due to intervalley scattering  $\sigma^{\text{NL}}$  then reads

$$\sigma^{\text{NL}} = \sigma^{\text{L+NL}} - \sigma^{\text{L}} = n\varepsilon_0 c [\alpha(E) - \alpha_0], \quad (7.15)$$

where  $\alpha_0 \sim 250 \text{ cm}^{-1}$  (Fig. 7.22(a)). To describe the nonlinear response of a single carrier, we further determine the nonlinear component of charge mobility (in analogy to (1.3) and (1.20))

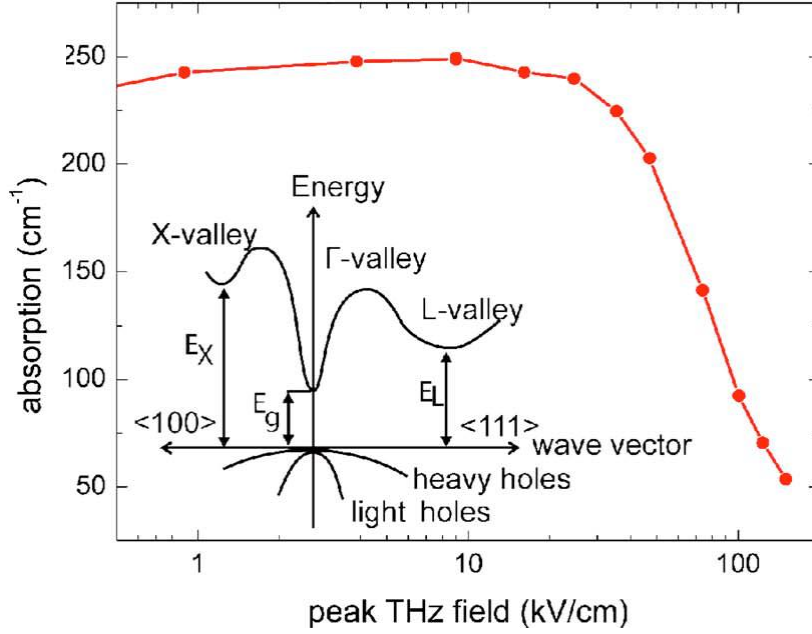


Fig. 7.24. Dependence of average THz absorption coefficient on peak incident electric field  $E_{\text{inc}}$  in n-type GaAs ( $N = 8 \times 10^{15} \text{ cm}^{-3}$ ). The graph was taken from Ref. [19]. Inset show a simplified band structure of GaAs.

$$\mu^{\text{NL}} = \frac{n\epsilon_0 c}{Ne_0} [\alpha(E) - \alpha_0], \quad (7.16)$$

which may be also viewed as a change of the linear mobility under the electric field  $E$ . The nonlinear component of mobility  $\mu^{\text{NL}}$  is the principal quantity which allows us to quantify and compare the strengths of various nonlinear phenomena.

In Fig. 7.22(a), we show  $\mu^{\text{NL}}$  corresponding to the intervalley scattering calculated using (7.16) (absorption coefficient  $\alpha(E)$  was taken from Fig. 7.24 and  $N = 8 \times 10^{15} \text{ cm}^{-3}$  according to [19]). The real part of nonlinear mobility  $\mu^{\text{NL}}$  is negative since the electron effective mass is considerably higher in the satellite X- and L-valleys than in the  $\Gamma$ -valley and the electron mobility thus decreases upon the intervalley scattering. As this effect originates from atomic properties, we do not expect it to depend on the confining volume in nanostructures, i.e.  $\mu^{\text{NL}}$  will be the same as in bulk material. For all considered nanostructure sizes and low enough fields (e.g.  $E_{p,0} \lesssim 5 \text{ kV/cm}$  for  $l = 50 \text{ nm}$ ,  $E_{p,0} \lesssim 20 \text{ kV/cm}$  for  $l = 100 \text{ nm}$ ), the intervalley scattering is weaker than the nonlinearities due to charge confinement (Figs. 7.22(a)), as confirmed by the values of the  $g$ -parameter (Fig. 7.23(b)). For nanostructures smaller than  $100 \text{ nm}$ , however, the intervalley scattering becomes stronger effect than the charge confinement for high enough electric fields. For nanostructures larger than  $\sim 200 \text{ nm}$ , the signal due to charge confinement remains considerably higher for realistic values of electric field.

Another bulk nonlinearities stem from optical nonlinear phenomena in GaAs. In [129] for example, it was found that the susceptibilities corresponding to four-wave mixing



( $f \sim 30$  THz) in n-doped GaAs ( $N \geq 10^{16} \text{ cm}^{-3}$ ) are  $\chi^{(3)} \sim 10^{-10}$  e.s.u. The considered nonlinearities due to charge confinement are then by at least several orders of magnitude stronger (Fig. 7.23(b) where  $\chi^{(3)}(3\omega_0; \omega_0, \omega_0, \omega_0)$  is for  $N = 10^{15} \text{ cm}^{-3}$ ).

We now discuss the results obtained for GaAs nanowires and nanobars in Sections 7.2 and 7.4 with respect to the above conclusions. In the GaAs nanowires (Section 7.2, diameter 50 nm), the strength of the nonlinearities due to charge confinement is strongly limited by their small diameter. To obtain a reasonably high nonlinear signals, we thus require local fields  $E_{p,0} \gtrsim 10$  kV/cm. For these fields, however, the nonlinear response is entirely dominated by the intervalley scattering which makes the nanowires unsuitable from our perspective. On the other hand, the charge confinement is considerably stronger effect for the investigated nanobars (width 250 nm). In addition, the nonlinear susceptibility is close to its maximum for this width. At the local level, the GaAs nanobars thus constitute almost the best possible system towards an experimental observation of the sought nonlinearities due to charge confinement.

We now show that the nonlinearities due to charge confinement are comparable even with the strongest known THz nonlinearity which was observed in graphene as an extremely efficient high harmonics generation [130]. To provide a comparison, we evaluate the  $g$ -coefficient (7.12) which characterizes the third-order response of a single carrier. Due to the nature of graphene, however, we have to consider the sheet third-order susceptibility  $L\chi_{\text{eff}}^{(3)}$  ( $L = 0.3$  nm is the thickness of the graphene layer indicated in [130]) and we thus obtain

$$|g|_{\text{graphene}} = \frac{3\omega_0 \epsilon_0}{N_c e_0} L\chi_{\text{eff}}^{(3)}. \quad (7.17)$$

The nonlinearity  $\chi_{\text{eff}}^{(3)} \sim 1.7 \times 10^{-9} \text{ m}^2 \text{V}^{-2}$  was observed for  $\omega_0 = 0.68$  THz and we thus find  $|g|_{\text{graphene}} \sim 1.7 \times 10^{-6} \text{ cm}^4 \text{V}^{-3} \text{s}^{-1}$  for doping carrier concentration  $N_c = 2.1 \times 10^{12} \text{ cm}^{-2}$ . The highest  $g$ -coefficients for the charge confinement are then by an order of magnitude higher (Fig. 7.23(b)). In other words, the single carrier nonlinearity due to charge confinement is thus considerably stronger than high harmonics generation in graphene. In this sense, the charge confinement is the source of the strongest known nonlinearities in solid state physics. The combination of the charge confinement with the strong "bulk" nonlinearities in doped graphene could then motivate a development of a material with ultimate nonlinear behavior.

## 7.6 Conclusions

In this part, we theoretically investigated the nonlinear THz photoconductivity originating from the charge confinement in several semiconductor nanostructures – GaAs nanobars and nanowires (Section 7.2), ZnO nanoparticles and CdS nanocrystals (Section 7.3) and gold nanoslits filled with GaAs nanobars (Section 7.4). We developed a framework (combining Monte-Carlo calculations of linear and nonlinear conductivity, both linear and nonlinear effective medium theories and solution of the wave equation) which allowed us to calculate the nonlinear signals which could be directly detected in optical pump-THz probe experiments with high-field THz pulses. We considered three different sources of intense THz

radiation – tilted-wavefront optical rectification in lithium niobate, air-based generation of multi-THz pulses (both generating ultrashort broadband pulses) and free electron lasers (i.e. longer narrowband pulses).

To obtain a high nonlinear conductivity, the nanostructures should be formed by a semiconducting material with high carrier mobility (i.e. low effective electron mass  $m$  and long scattering time  $\tau_s$ ). Indeed, the nonlinear conductivity is found to be significant in GaAs nanostructures ( $\mu_{\text{GaAs}} \sim 7 \times 10^3 \text{ cm}^2 \text{ V}^{-1} \text{ s}^{-1}$ ) while the nonlinearities in ZnO nanoparticles of comparable sizes ( $\mu_{\text{ZnO}} \sim 200 \text{ cm}^2 \text{ V}^{-1} \text{ s}^{-1}$ ) are very weak. We further demonstrated that the amplitude of the nonlinear mobility exhibits a maximum for certain dimensions of photoconductive constituents (e.g.  $\sim 250\text{-}300 \text{ nm}$  for the frequency  $0.5 \text{ THz}$ ; Figs. 7.22 and 7.23(b)). For much smaller dimensions, the confinement strongly limits the mobility amplitude. For too large dimensions, the confinement becomes suppressed and thus all corresponding nonlinearities vanish. These considerations imply that optimum frequencies are around  $\sim 1 \text{ THz}$  to match the spectra of nonlinear coefficients of structures with optimum dimensions.

Further requirements for a strong nonlinear signal stem from the layout of the nanostructures which controls the propagation of the incident field as well as of the generated harmonics (i.e. effective medium theory). We have to distinguish percolated and non-percolated systems and we also have to consider the character of the material (conducting or non-conducting) surrounding the photoconductive nanostructures:

#### **a) Metallic nanoslits**

- Metallic parts inherently act as short circuits concentrating the electric field into the nanostructures embedded in the slits. In nanostructures with suitable layout (i.e. Fig. 7.19), this considerably enhances the local field in the photoconductive constituents (the field-enhancement factor  $Q_{\text{exc}}$  follows  $1/s$  and thus  $|Q_{\text{exc}}| \gg 1$  can be easily achieved). This enhancement becomes stronger with decreasing filling factor  $s$  of the photoconducting material. The measurable transient transmission is directly proportional to  $1/s$  and thus can considerably exceed the detection limit (for low filling factors  $s$  of photoconductive material).

#### **b) Dielectric surroundings**

- In non-percolated structures, a plasmonic resonance develops for high enough carrier concentration and enhances not only the local field  $E_p$  within the nanostructure (compared to the local field in the unphotoexcited sample; Fig. 7.9) but also the nonlinearity in the transient waves  $\Delta E^T$  leaving the sample (Fig. 7.13). However, this implies that the photoconductive constituents should be as close as possible to the percolation (i.e. volume filling factor  $s \rightarrow 1$ ) and the gaps between them filled with a high-permittivity material (ideally  $|\epsilon| \rightarrow \infty$ , which would revert the structure to that of metallic nanoslits). These two requirements ensure that the plasmonic resonance begins to develop only at higher carrier concentrations and the measurable signals (scaling with

carrier density when below plasmonic resonance) are then adequately enhanced as in the case of metallic nanoslits.

- Above the percolation threshold, both the linear and the nonlinear effective responses are stronger than in the non-percolated case. The nonlinearities are then observable in the experiments as there is no mechanism suppressing their role. Note, however, that for strong enough interparticle charge transport (i.e. high interparticle transport probability  $p_t$  in the Monte-Carlo calculations) the charge confinement ceases to exist and in such case, no nonlinear conductivity due to charge confinement may appear.

From all the investigated nanostructures, the most promising for experiments are the gold nanoslits filled with GaAs nanobars (Fig. 7.19) for which we predicted the highest nonlinear signals in the THz range. The metallic stripes provide sufficient enhancement of the local electric field in the nanobars which even permits observation of these nonlinearities in common setups utilizing low THz fields (e.g. kHz amplifier-based setups utilizing optical rectification in ZnTe). Furthermore, the nonlinearities due to charge confinement are predicted to be considerably stronger than the intervalley scattering (Fig. 7.22(b)).

Promising for experiments are also the bare GaAs nanobars (Fig. 7.4 (a)), although the predicted nonlinearities due to charge confinement are considerably weaker. This was mostly due to the high permittivity contrast across the structure (resulting in low local fields  $E_p \sim 5$  kV/cm). We concluded, that the corresponding signals could be measured in very stable table-top setups using broadband THz pulses. The intervalley scattering should be also negligible (the size of nanobars is the same as in the preceding metallic structure).

For the GaAs nanowires embedded in PDMS (Fig. 7.4(b)), their small diameter limits the values of the nonlinear mobilities  $\mu^{NL}$  due to charge confinement. Since the intervalley scattering is considerably stronger effect, we cannot realistically expect to experimentally resolve the confinement-related nonlinearities.

For partly percolated ZnO nanoparticles (Section 7.3), we observed only a very weak local nonlinear response. Since the percolation preserves the nonlinearities in the effective response, the expected nonlinear signal exceeds the sensitivity of common experimental setups.

## 8. THz spectroscopy of TiO<sub>2</sub> nanotubes

Titanium dioxide (TiO<sub>2</sub>) is a wide band-gap semiconductor with many technologically and fundamentally intriguing properties. Its nanostructures are then very promising in a variety of applications (e.g. in photocatalysis or in photovoltaics) [1],[131]-[136]. The layers of self-organized TiO<sub>2</sub> nanotubes are then particularly attractive [137],[138]: their semiconductive nature, high surface area, anticipated uni-directional charge transport along their walls, and also the ability to be prepared on transparent conducting glasses makes them interesting as anode material in dye-sensitized solar cells [139]-[141] and perovskite solar cells [142]-[144]. Depending on the growth process, however, the geometry (e.g. nanotube diameter, wall thickness and nanotube lengths) and conductive properties of these layers may greatly differ. Therefore, it is essential to thoroughly understand the charge transport properties of a variety of nanotube structures.

In this section, we investigate linear THz photoconductivity of a series of TiO<sub>2</sub> nanotube layers of different properties, which were grown by Jan M. Macák from University of Pardubice [137],[145]-[150]. First, we overview the sample preparation and analysis by scanning electron microscope (SEM) which was also provided by our colleagues from University of Pardubice. Then, we briefly describe the experimental setup used for THz measurements. Using the Monte-Carlo calculations based on Kubo formalism introduced in Section 2 and linear effective medium theory and solution of linear wave equation from Section 3, we then develop a general model describing the linear THz response of the TiO<sub>2</sub> nanotube layers. Proper application of this model on the measured data then allows us to extract information on the intrinsic charge transport in the nanotube walls and also on the electrical connectivity between individual nanotubes. Finally, we provide a discussion and comparison with previous THz conductivity studies on TiO<sub>2</sub> nanotubes [57],[151]. Most of our results were published in [42] and [152].

### 8.1 Studied samples

In this work, we studied two pairs of TiO<sub>2</sub> nanotube layers of different thickness (equivalent to the nanotube length) and crystallinity. For simplicity, we therefore call them short (length  $\sim 1 \mu\text{m}$ ) and long (length  $\sim 30 \mu\text{m}$ ) nanotubes. The studied samples and their main characteristics are summarized in Tab. 8.1. Here, we first briefly describe the preparation of the samples [42],[150]. Then, we discuss their morphology based on the SEM images and their crystallinity.

#### 8.1.1 Sample preparation

The electrochemical setup consisted of a two electrode configuration: a platinum foil was used as the counter electrode, while the titanium substrates (working electrodes) were pressed against an O-ring of the electrochemical cell, leaving  $1 \text{ cm}^2$  open to the electrolyte. All electrochemical experiments were realized at room temperature using a high-voltage potentiostat (PGU-200V, IPS Elektroniklabor GmbH).

Sample		Phase	Layer thickness ( $\mu\text{m}$ )	Inner diameter (nm)	Wall thickness (nm)
Short nanotubes	H105	Anatase	$1.0 \pm 0.1$	$64 \pm 8$	3.5
	H141	Amorphous			
Long nanotubes	H172	Anatase	$30 \pm 2$	$120 \pm 10$	10
	H178	Amorphous			

Tab. 8.1. Summary of the studied  $\text{TiO}_2$  nanotubes samples and their morphologic properties. The nanotube layer thickness, inner diameter and wall thickness were determined from the SEM images (Figs. 8.1 and 8.2).

Prior to the anodization, the titanium substrates (Sigma-Aldrich 0.127 mm thick, 99.7% purity) were degreased by sonication in isopropanol and acetone, then rinsed with isopropanol and dried in air. The titanium substrates were then anodized in an ethylene glycol based electrolyte using the setup described above. To obtain nanotubes of different lengths and sizes, different conditions were applied during anodization:

- **Short nanotubes (H105, H141, Fig. 8.1):** The electrolyte contained 0.27M  $\text{NH}_4\text{F}$  and 10 vol.%  $\text{H}_2\text{O}$ . The titanium substrates were anodized at 20 V with a sweep rate of 1 V/s for 100 minutes.
- **Long nanotubes (H172, H178, Fig. 8.2):** The electrolyte containing 0.176M  $\text{NH}_4\text{F}$  and 1.5 vol.%  $\text{H}_2\text{O}$  was used. The anodization was carried out at 60 V (with a sweep rate 1 V/s) for 4 hours.

After anodization, the samples were rinsed and sonicated in isopropanol and dried.

The as-grown nanotubes are amorphous. Samples H105 and H172 were thus annealed at 400 °C for 1 h in air to convert them into a crystalline anatase phase (Fig. 8.2(f)). For THz

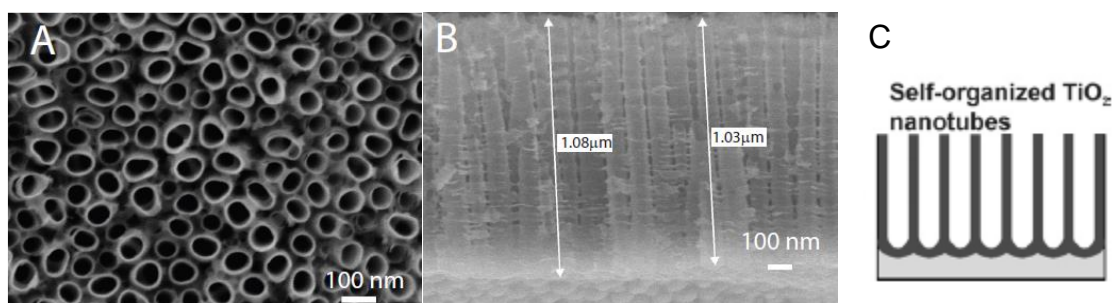


Fig. 8.1. SEM images of the short  $\text{TiO}_2$  nanotubes [152]: top-view (a) and cross-section with indicated layer thicknesses (b). The nanotubes form oriented layers: their tops are opened while their bottoms are closed (c). The nanotubes were originally grown on a Ti substrate which was dissolved prior to the THz measurements. Scheme in panel (c) was taken from Ref. [137].

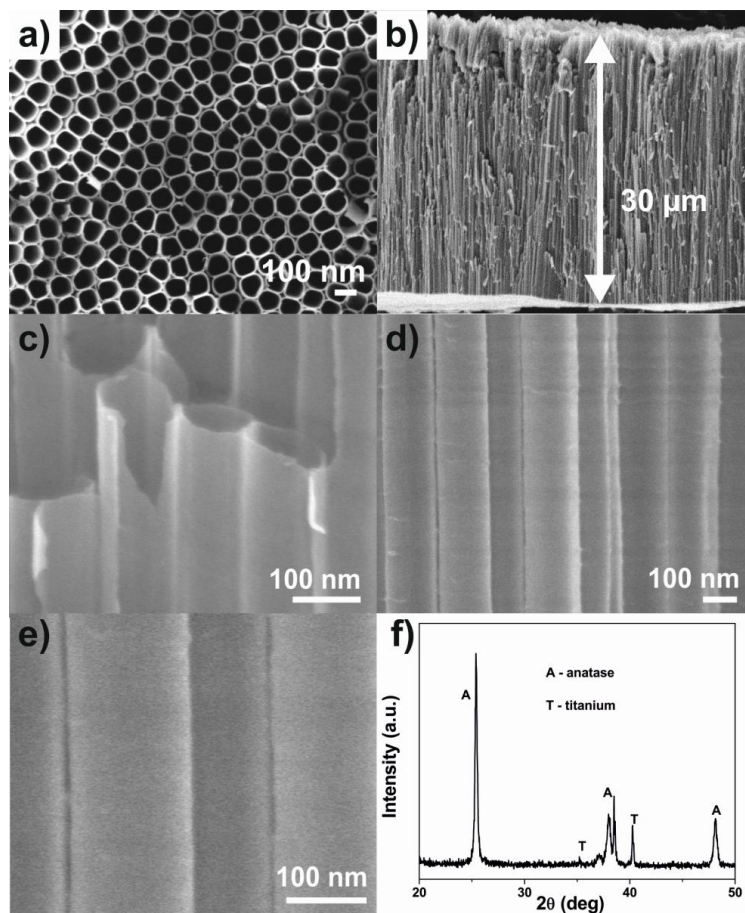


Fig. 8.2. SEM images of the free-standing layer of long  $\text{TiO}_2$  nanotubes [42]: top-view (a) and cross-sections (b)-(e). Images (c)-(e) are taken at high magnification. In image (b), the layer thickness is indicated. The x-ray diffraction pattern (f) confirms the anatase phase of the annealed samples (the titanium peaks come from the substrate underneath the layer).

spectroscopy measurements, the underlying titanium substrates were removed by dissolution in a  $\text{Br}_2$ /methanol mixture. The short nanotubes were then transferred onto fused silica substrates (the closed bottom parts of the nanotubes were in direct contact with these substrates (Fig. 8.1(c))). The long nanotubes formed an oriented free-standing layer.

### 8.1.2 Morphological characteristics

The morphology of the samples (including the length (i.e. layer thickness) and wall thickness of the nanotubes) was characterized using a field-emission scanning electron microscope (FE-SEM JEOL JSM 7500F). The precise knowledge of geometrical parameters is required to quantitatively interpret the measured THz spectra.

In Figs. 8.1 and 8.2, we show a few examples of SEM images of the short and long  $\text{TiO}_2$  nanotubes, respectively. The analyses of the images revealed that the short nanotubes were  $(1.0 \pm 0.1) \mu\text{m}$  long and had an average inner diameter  $(64 \pm 8) \text{ nm}$ . The layers of the long nanotubes then exhibited thickness  $(30 \pm 2) \mu\text{m}$  and inner diameter  $(120 \pm 10) \text{ nm}$ . The

nanotubes are also open at their top and closed at their bottom (i.e. where they were in contact with the titanium substrate prior to its dissolution; Figs. 8.1 and 8.2(a),(b)) which is in agreement with previous reports [137],[138].

## 8.2 Time-domain THz spectroscopy

The steady-state measurements were performed in a common experimental configuration for time-domain THz spectroscopy (Fig. 8.3) [71]. The setup was driven by an amplified femtosecond Ti:sapphire laser system (Spitfire Ace) delivering optical pulses at 800 nm with the repetition rate of 5 kHz. A part of the laser beam was used for the generation of THz pulses ( $\sim 0.1\text{--}2.5$  THz) by optical rectification in 1 mm thick (110) ZnTe crystal [153]. Using a sensor based on the Pockels effect (another 1 mm thick (110) ZnTe crystal), we then measure a polarization change of a synchronized optical gating pulse which allows us to determine the instantaneous THz electric field (Fig. 8.3) [153]. Varying the time delay between the THz and gating optical pulses (delay line D1) then enables the scanning of the entire waveform of the THz pulse. This detection is phase-sensitive: application of Fourier transform yields a complex spectrum of the THz pulse which in turn allows determination of complex effective permittivity of the sample.

For measurements of complex photoconductivity spectra, we modified the above setup by adding a branch for optical pumping (Fig. 8.3). Here, a part of the laser beam was frequency tripled using BBO crystals and the pulses at resulting wavelength 266 nm ( $\sim 4.66$  eV) were used for the optical excitation of the TiO<sub>2</sub> nanotubes. The photon energy of the pump beam is thus sufficient to ensure direct inter-band generation of photocarriers in the conduction band

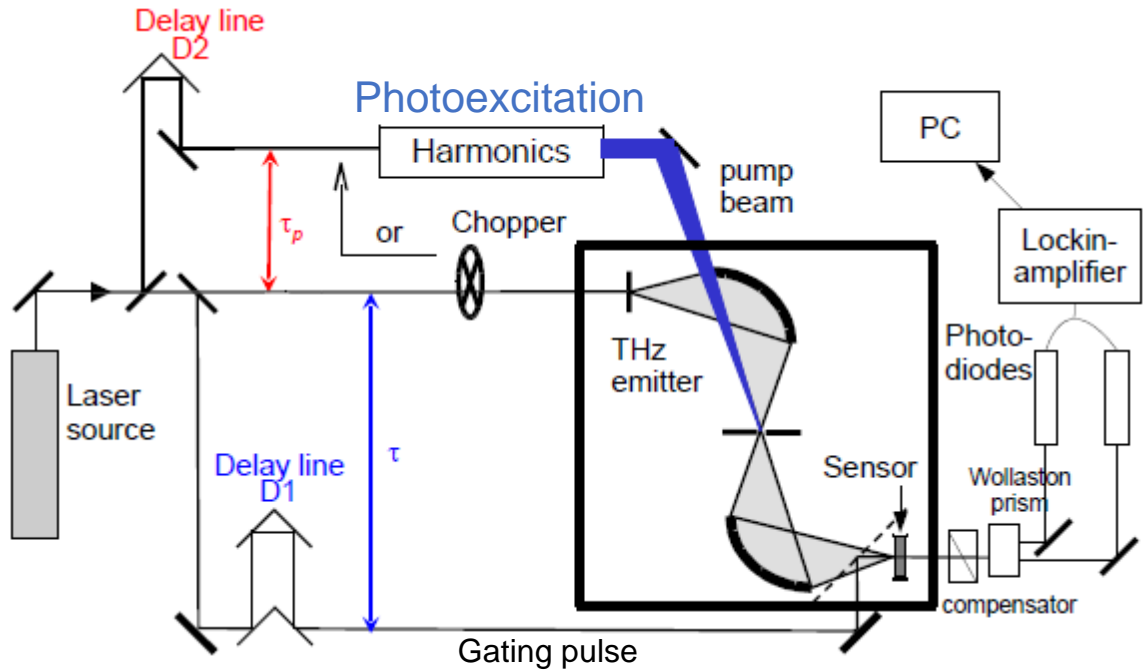


Fig. 8.3. The experimental setup used for the time-domain THz spectroscopy measurements. The scheme was taken from Ref. [71].

(the band gap of  $\text{TiO}_2$  in anatase phase is  $\sim 3.2$  eV [154]). To ensure a homogeneous concentration of photoexcited charges across the analyzed region of the samples (delimited by a metallic aperture with diameter 3 mm), the pump beam was defocused. Since electromagnetic radiation is transverse, the polarization of the THz is perpendicular to the nanotube axes, thus probing the lateral charge transport. In all measurements, the probed samples were placed in a primary vacuum chamber to eliminate the absorption of the THz beam by water vapours.

### 8.3 Theoretical calculations of the THz response

The main aim of this section is to establish the relation between the microscopic properties of the nanotubes (morphology of the nanotube layer, permittivity and photoconductivity of the nanotube walls) and the measurable THz signals: transmittance spectrum  $T$  of the unphotoexcited sample and transient transmission  $\Delta T/T$  of the sample upon photoexcitation (see Section 3.2). Due the inhomogeneity of the nanotube layer, three separate steps have to be considered (Fig. 8.4). First, we employ the Monte-Carlo calculations based on Kubo formalism to assess the local transient photoconductivity spectrum  $\Delta\sigma_p(\omega)$  (Section 8.3.1). Then, we use finite-element calculations to find the effective permittivity, effective absorption coefficient and morphologic parameters of the VBD model for several model structures emulating the real morphology of the nanotube layer (Section 8.3.2). Finally, we link these results to the measurable transmission functions  $T$  and  $\Delta T/T$  using the solution of the wave equation from Section 3.2 (Section 8.3.3).

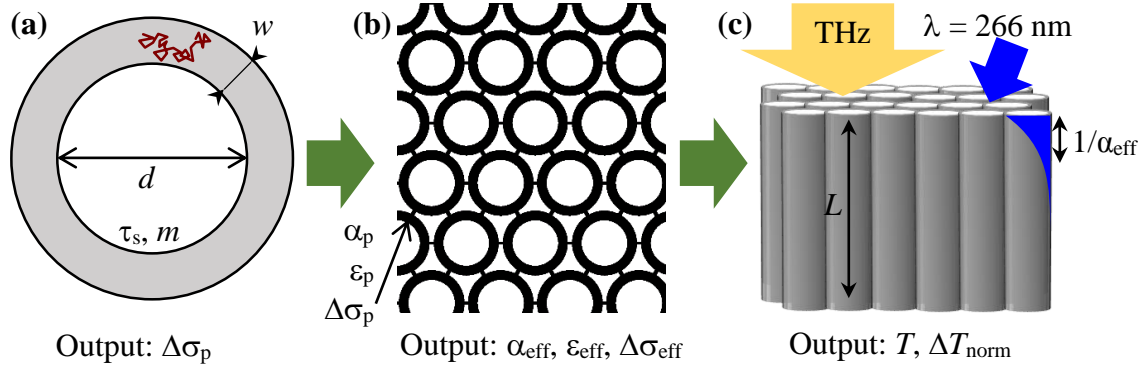


Fig. 8.4. Illustrations of the steps in theoretical calculations of the THz spectra. The outputs identify the quantities calculated in each step of the model while the rest indicates the most important input parameters for the given step. In the first step (a), we employ the Monte-Carlo calculations based on Kubo formalism (Section 2.1) to find the local transient photoconductivity spectrum  $\Delta\sigma_p$ . Effective medium theory (b) is then applied to transform the permittivity  $\epsilon_p$  and the transient photoconductivity  $\Delta\sigma_p$  of the nanotube walls into the effective permittivity  $\epsilon_{\text{eff}}$  and effective transient photoconductivity  $\Delta\sigma_{\text{eff}}$  of the nanotube layer. Finally, the complex steady-state and transient transmission functions  $T$  and  $\Delta T_{\text{norm}}$ , respectively, are calculated (c). For this, we use the solution of the wave equation with proper boundary conditions from Section 3.2 (i.e. considering internal Fabry-Pérot interferences of THz radiation inside the layer).



### 8.3.1 Microscopic properties of TiO<sub>2</sub> nanotube walls

We assume that the terahertz permittivity  $\epsilon_p$  and optical absorption coefficient  $\alpha_p$  of the unphotoexcited nanotubes are equal to those of bulk anatase, i.e.  $\epsilon_p \sim 30$  with negligible dispersion in the THz range [156] and  $\alpha_p \sim 7 \times 10^5 \text{ cm}^{-1}$  at the excitation wavelength of 266 nm [157]. The main parameters entering the calculations of mobility spectra  $\mu(\omega)$  are the nanotube geometry (inner nanotube diameter  $d$  and the wall thickness  $w$  which are read from SEM images), and the bulk scattering time  $\tau_s$  which is an adjustable parameter allowing us to match the spectra obtained from the experiments. There is an ongoing debate on the effective electron masses of electrons and holes in anatase; values in the range from  $\sim 0.4m_e$  to  $\sim 10m_e$  were reported [158]-[162]. It is also unclear whether electrons are lighter than holes or vice versa; the discussion is further complicated by the anisotropy of effective masses. THz spectra alone do not permit determination of the dominant carrier type. However, the THz conductivity is usually dominated by the carriers with lighter effective mass which is reported to be close to  $m_e$  or  $2m_e$  in anatase [158]-[162]. In our Monte-Carlo calculations, we thus consider carriers with effective mass  $m = m_e$ .

As we will show later, the mobility spectra of some samples can be explained just by the confinement of carriers by the physical nanotube boundaries (Fig. 8.5(a)). For other samples, however, a stronger confinement is required. We proposed and examined several different mechanisms (Fig. 8.5(b)-(d)):

- The nanotube walls may be formed by smaller grains; the grain boundaries then cause additional confinement of charges. To model this, we divided the nanotube wall into a set of cubes with the dimension  $a$  (Fig. 8.5(b)). Upon reaching a boundary of such cube, the carrier is scattered and either it enters the adjacent cube (with probability  $p_F$ ), or it remains in the original cube (with probability  $1 - p_F$ ). The nanoregion size  $a$  and the probability  $p_F$  are then additional adjustable parameters entering the calculations. We note that the case of  $p_F = 0.5$  is equivalent to the isotropic scattering. Therefore,  $p_F \ll 0.5$  is required to observe significant confining effect of the nanoregions.
- At the nanotube wall surfaces, a band bending occurs [78],[163]. This effect may be strong enough to confine carriers of one polarity in the central region of the nanotube walls and the charges with opposite polarity in the vicinity of the nanotube wall surfaces (Fig. 8.5(c)). The motion of the latter may be then also strongly influenced by possible surface defects (see the following paragraph). To approximate the band bending, we consider that the charges move in a potential with cylindrical symmetry and with harmonic cross-section (Fig. 8.5(c)). This potential involves just a single additional parameter: the harmonic resonance frequency  $f_0$

$$V(r) = 4\pi^2 m f_0^2 (r - r_0)^2, \quad (8.1)$$

where  $r$  is the distance from the nanotube center and  $r_0$  is the distance of the middle of the nanotube wall from the nanotube center. Since we do not know neither the polarity of mobile charges nor the character of band bending (the potential may increase or

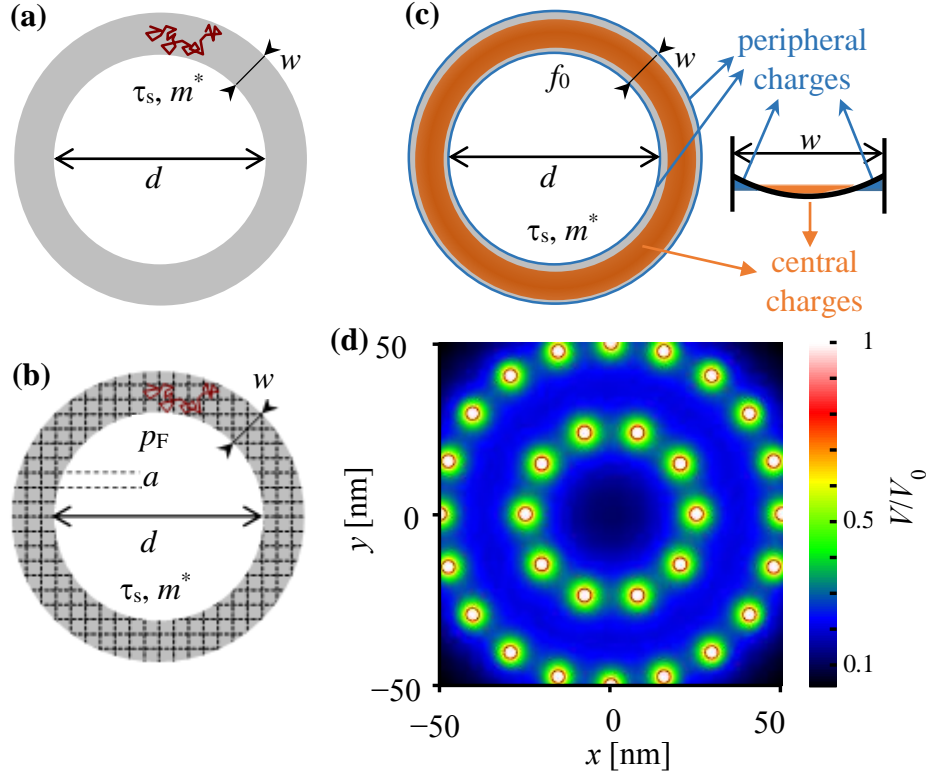


Fig. 8.5. Illustration of models considered for the Monte-Carlo calculations of mobility of carriers confined in  $\text{TiO}_2$  nanobars. In the simplest model, the charges are confined just by the nanotube walls (a). In other models (b)-(d), we consider additional mechanisms leading to stronger confinement. In model (b), we divide the nanotube wall into a set of cubes with dimension  $a$ , thus emulating a possible internal structure of the walls (e.g. grains). The carriers then scatter on the cube boundaries and with probability  $p_F$  enter the adjacent cube. In model (c), we simulate the role of the band bending close to the nanotube surfaces using an approximate potential (8.1). In model (d), we then study a role of charged surface defects which is described by potential (8.2). We also consider a combination of the above models to explain the shape of the mobility spectra.

decrease towards the nanotube wall surface), we introduce the following notation (Fig. 8.5(c)): *central* charges are those confined to the middle of the nanotube wall while *peripheral* charges are those confined to the vicinity of the nanotube surfaces.

- Charged surface defects repel mobile charges of the same polarity which may lead to the limitation of their motion. To account for this, we constructed a series of periodically spaced point charges distributed along the nanotube wall surfaces (Fig. 8.5(d)). We describe the influence of each defect by the screened Coulomb potential and the confined carriers thus move in the potential

$$V(r) = \frac{Q}{4\pi\epsilon_0} \sum_i \frac{1}{|r - r_i|} e^{-k_0|r-r_i|}, \quad (8.2)$$

where  $Q$  is the charge of the defects,  $r_i$  is the position vector of  $i$ -th defect,  $r$  is the position vector of mobile carrier and  $k_0$  is the screening parameter. For  $k_0 = 0$ , there is no screening and influence of each surface defect is thus described by the Coulomb potential. In such case, however, the application of Gauss's law of electrostatics implies that the potential inside the nanotube wall approaches zero for higher defect densities.

### 8.3.2 Effective properties of the TiO<sub>2</sub> nanotube layer

Here, we use the effective medium theory to account for the influence of the structure morphology. We thus transform the microscopic parameters of the nanotube walls (equilibrium permittivity  $\epsilon_p$ , absorption coefficient  $\alpha_p$ , photoconductivity  $\Delta\sigma_p$ ) and the surrounding air/vacuum into the effective parameters of the structure.

For a given model discretized structure, we employ the finite-element method described in [37]. First, the structure is approximated by unstructured triangular meshes. Then, the local electric field profile  $E(\vec{r})$  in the structure is calculated as the solution of quasi-static Maxwell equations with periodic boundary conditions. In the end, the effective permittivity  $\epsilon_{\text{eff}}$  is determined from the energy density

$$\frac{1}{2} \epsilon_{\text{eff}} \langle E \rangle^2 = \frac{1}{2V} \int_V \epsilon_{\text{loc}}(\vec{r}) E^2(\vec{r}) dV \quad (8.3)$$





$$\langle E \rangle = \frac{1}{V} \int_V E(\vec{r}) dV, \quad (8.4)$$

where  $\epsilon_{\text{loc}}$  is spatially dependent local permittivity (depending on  $\vec{r}$ , either  $\epsilon_{\text{loc}} = \epsilon_p$  or  $\epsilon_{\text{loc}} = 1$ ) and  $\langle E \rangle$  is the volume average of the electric field. The effective optical absorption coefficient  $\alpha_{\text{eff}}$  can be calculated in a similar way, we only need to express the permittivities ( $\epsilon_{\text{eff}}$  and  $\epsilon_p$ ) in terms of the corresponding absorption coefficients ( $\alpha_{\text{eff}}$  and  $\alpha_p$ )

$$\alpha_{\text{eff},p} = \frac{2\pi}{\lambda} \text{Im} \left\{ \sqrt{\epsilon_{\text{eff},p}} \right\}, \quad (8.5)$$

where  $\lambda$  is the wavelength of the radiation used for photoexcitation. As we mentioned in the previous section, the dispersion of anatase permittivity  $\epsilon_p$  is negligible in the THz spectral range. The effective steady-state THz response of the nanotube layer can be then characterized just by a single value of effective permittivity  $\epsilon_{\text{eff}}$ . The attenuation of the pump beam ( $\lambda = 266$  nm) in the structured layer is described by a single value of effective absorption coefficient  $\alpha_{\text{eff}}$ .

Upon photoexcitation, individual nanotubes exhibit a local photoconductivity  $\Delta\sigma_p$ . The effective photoconductivity  $\Delta\sigma_{\text{eff}}$  is then evaluated using the VBD model (3.3). Since the permittivity of anatase is real and practically non-dispersive, the pertinent morphology

Structure		$s$ (%)	$\epsilon_{\text{eff}}$	$\alpha_p/\alpha_{\text{eff}}$	$V$	$B$	$D$
N1		39	4.4	7.7	0	0.05	0.019
N2		43	5.6	6.1	0	0.09	0.015
P1		44	8.4	4.8	0.24	0.0028	0.027
P2		49	10.4	4.0	0.32	0.0005	0.032

Tab. 8.2. Calculated effective properties of model geometries of the long  $\text{TiO}_2$  nanotubes (black areas:  $\text{TiO}_2$  in anatase phase, white areas: air/vacuum). Several models with different connectivity between the nanotubes are considered: N1 and N2 are isolated nanotubes with different air gaps between them, P1 are percolated nanotubes connected by small contacts and P2 are percolated nanotubes directly touching each other.  $s$  is the filling factor of  $\text{TiO}_2$ . The effective permittivity  $\epsilon_{\text{eff}}$ , the effective absorption coefficient  $\alpha_{\text{eff}}$  and the morphologic parameters  $V$ ,  $B$  and  $D$  (defined by (3.3)) were assessed using the finite-element method from Section 7.2.2. Following parameters were considered:  $\epsilon_p = 30$  [156],  $n_p(266 \text{ nm}) = 3$  [157],  $\alpha_p(266 \text{ nm}) = 7 \times 10^5 \text{ cm}^{-1}$  [157].

parameters  $V$ ,  $B$  and  $D$  are real constants which were determined from fitting the calculated dependence of the photo-induced effective permittivity change  $\Delta\epsilon_{\text{eff}} = i\Delta\sigma_{\text{eff}}/(\omega\epsilon_0)$  on purely imaginary local permittivity change  $\Delta\epsilon_p = i\Delta\sigma_p/(\omega\epsilon_0)$  with VBD model (3.3).

The effective properties of the nanotube layer are expected to strongly depend on the level of percolation between individual nanotubes. We thus examined several model structures of the nanotube layers (in Tab. 8.2, we show the results for the long nanotubes) with varying percolation degrees, including two non-percolated structures consisting of isolated nanotubes separated by different air/vacuum gap widths (structures N1 and N2), a structure where the nanotubes are conductively connected by small contacts (structure P1), and finally a structure where the nanotubes touch each other (structure P2). The calculated steady-state effective permittivities  $\epsilon_{\text{eff}}$  significantly increase with enhanced percolation (Tab. 8.2). Comparison with the experimental results then allows us to discuss the morphology of the sample and estimate the  $V$ ,  $B$  and  $D$  coefficients required for the extraction of local photoconductivity  $\Delta\sigma_p$  from the transient transmission spectra.

### 8.3.3 THz wave propagation in the nanotube layer

For unphotoexcited free-standing layers (i.e. for long nanotubes), we directly measure the complex transmittance  $T$ . For the studied samples, the internal Fabry-Pérot reflections overlap and the transmittance  $T$  thus reads [58]

$$T = \frac{4n}{(n+1)^2} \frac{\exp[ik(n-1)L]}{1 - \left(\frac{n-1}{n+1}\right)^2 \exp(2iknL)}, \quad (8.6)$$

where  $n$  is the effective refractive index of the nanotube layer. The numerical solution of the above equation then yields the steady-state effective permittivity  $\epsilon_{\text{eff}}$  of the nanotubes ( $n^2 = \epsilon_{\text{eff}}$ ). We note, that analogous approach can be derived also for the short TiO<sub>2</sub> nanotubes which are placed on the fused silica substrate. However, precise evaluation of  $\epsilon_{\text{eff}}$  is not feasible in this case. This is mainly due to the uncertainty in the optical thickness which we can determine with the precision of  $\sim 1 \mu\text{m}$ . This is comparable with the real optical thickness of short TiO<sub>2</sub> nanotubes and the calculated effective permittivity would thus exhibit too large experimental errors.

In optical pump-THz probe experiments, a transient transmittance spectrum  $\Delta T/T$  is measured. To link  $\Delta T/T$  (or equivalently the normalized transient transmission  $\Delta T_{\text{norm}}$  (3.27)) to the local conductivity in the nanotube walls, we use the results from Section 3.2. There we discussed possible photoexcitation fluence-dependence of  $\Delta T_{\text{norm}}$ . If the shape of the measured  $\Delta T_{\text{norm}}$  spectra depends significantly on the fluence, the nanotube layers are non-percolated (i.e. plasmonic resonance builds up in the response). In such case,  $\Delta T_{\text{norm}}$  follows the general equation (3.40). If the measured  $\Delta T_{\text{norm}}$  does not depend on the fluence, two options are possible:

- Nanotubes are percolated. In such case,  $V \gg B$  (Tab. 8.2). The non-percolated term of the VBD model (3.3) can be then neglected and the response is dominated by the percolated parts. The normalized transient transmission  $\Delta T_{\text{norm}}$  then follows the relations from Section 3.2.1.
- Nanotubes are non-percolated, but the  $D$ -term in the VBD model is small (i.e.  $|D\Delta\sigma_p/(\omega\epsilon_0)| \ll 1$ ) which would be typically due to low local photoconductivity of the nanotubes  $\Delta\sigma_p$  (for a good-quality anatase crystal, the dc mobility of  $20 \text{ cm}^2\text{V}^{-1}\text{s}^{-1}$  was reported in [164]).  $\Delta T_{\text{norm}}$  is then described by the same equations as in the percolated case, we just replace the morphologic coefficient  $V$  with  $B$  (compare the wave equations (3.30) and (3.38)).

The properties of the nanotube layers (Tab. 8.1) then allow us to use appropriate simplified relations instead of the general ones. For the short nanotubes, the limits of thin sample and strong optical absorption are satisfied. For the long nanotubes, we can apply the temporal windowing.

## 8.4 Experimental results and discussion

### 8.4.1 Steady-state effective permittivity and percolation of samples

#### 8.4.1.a) Short nanotubes

As we already discussed, we cannot assess the morphology of the short TiO<sub>2</sub> nanotubes (sample identifiers H105 (anatase phase) and H141 (amorphous phase)) from the steady-state

measurements. The degree of electrical connectivity of the nanotubes is thus uncertain. To estimate the pertinent morphologic ( $V$ ,  $B$ ) and optical ( $\alpha_{\text{eff}}$ ) parameters, we employed the finite-element calculations for a model structures analogous to those from Tab. 8.2. Based on the SEM images (Fig. 8.1) and the photoconductivity measurements (Section 8.4.2), we assume that the nanotubes are interconnected by contacts of limited area. We then found the following values of morphologic parameters:  $V \sim 0.15\text{--}0.27$ ,  $B \sim 0.01$ ,  $D \sim 0.02$  and  $\alpha_p/\alpha_{\text{eff}} \sim 3$ .

#### 8.4.1.b) Long nanotubes

The measured steady-state effective permittivity of both anatase (sample identifier H172) and amorphous (H178) long  $\text{TiO}_2$  nanotubes layers is  $\sim 8\text{--}9$  (Fig. 8.6). These values are comparable to the calculated permittivity of model structure P1 and much higher than the values calculated for the non-percolated model structures N1 and N2 (Tab. 8.2). Indicating that the individual nanotubes are to some extent electrically interconnected. This is further supported by the fact that the layers do not disintegrate spontaneously during manipulation. At the same time, the measured steady-state permittivity is considerably lower than the calculated permittivity of the model structure P2 where the nanotubes overlap. Therefore, the contact area cannot be very large compared to the total outer surface of the nanotubes. We thus conclude that the nanotubes are on average weakly connected.

It is now necessary to elaborate on a comparison with the SEM images (Fig. 8.2), where the nanotubes seems to be closely packed. However, a detailed inspection of the top part

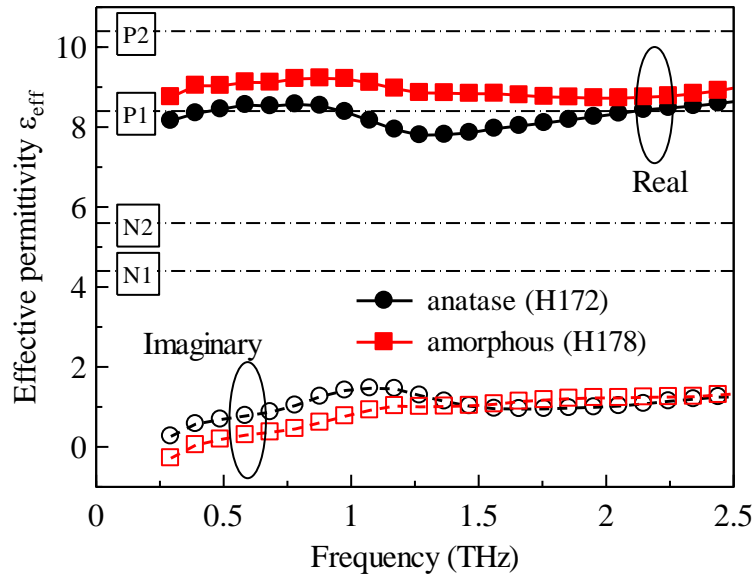


Fig. 8.6. Measured spectra of steady-state effective permittivity  $\epsilon_{\text{eff}}$  of the long  $\text{TiO}_2$  nanotubes in anatase and amorphous phases. Closed symbols: real part; open symbols: imaginary part. The horizontal dot-dashed lines indicate the real parts of the effective permittivities of the model structures from Tab. 8.2. Comparison of the measured and calculated data then implies that the nanotubes are conductively interconnected by small contact areas.

(Fig. 8.2(a)) reveals that there are narrow gaps between many of the nanotubes. A similar conclusion can be drawn also from the images of the cross-sections (Figs. 8.2(b)-(e)). To avoid difficult calculations accounting for the presence of both the isolated and interconnected nanotubes, we thus represent the layers of the long  $\text{TiO}_2$  nanotubes by the simplified model structure P1 (characterized by a weak average connectivity). In this sense, the morphology of long  $\text{TiO}_2$  nanotubes inferred from the THz measurements correlates with the limited contacting observed in the SEM images.

We note that a single value of the effective permittivity cannot completely describe the real morphology – it provides just an estimate of an average connectivity. Nevertheless, this knowledge is crucial for the analysis of the transient photoconductivity of the nanotube layers – it allows us to estimate the morphology parameters  $V$  and  $B$  and the effective optical absorption coefficient  $\alpha_{\text{eff}}$ . For the long  $\text{TiO}_2$  nanotubes, we thus consider  $V \sim 0.24$  and  $\alpha_p/\alpha_{\text{eff}} \sim 4.8$  (model structure P1 from Tab. 8.2). Since  $V \gg B$ , we neglect the  $B$ -term in our analysis of transient photoconductivity.

## 8.4.2 THz photoconductivity spectra and dynamics

### 8.4.2.a) Short nanotubes

In Fig. 8.7, we show the normalized transient transmission spectra  $\Delta T_{\text{norm}}$  measured for the short  $\text{TiO}_2$  nanotubes in anatase (Fig. 8.7(a)) and amorphous (Fig. 8.7(b)) phase. For both samples, the measured signal does not depend significantly on the photoexcitation fluence. Since the  $D$ -term is not negligible ( $|D\Delta\sigma_p/(\omega\epsilon_0)| \sim 0.34$  for the photoexcitation fluence  $1.7 \times 10^{14}$  photons/cm<sup>2</sup> and 1 THz), the nanotubes should then be percolated. In addition, the limits of a thin sample and strong optical absorption are satisfied and the normalized transient transmission  $\Delta T_{\text{norm}}$  (3.33) is thus directly proportional to the quantum yield-mobility product  $\xi\mu(\omega)$ . We further consider that each photon generates an electron-hole pair, i.e.  $\xi = 1$  shortly after photoexcitation. The mobility spectrum exhibits features typical for the response of confined carriers (Section 5.1): the real part is positive and slightly increases with frequency while the imaginary part is negative (at least for low frequencies).

In the Monte-Carlo calculations, it is sufficient to assume that the carrier movement is restricted just by the nanotube walls (Fig. 8.5(a); no further interactions are needed to reproduce shape of the spectra). Then, we use (3.33) to calculate the corresponding normalized transient transmission spectrum  $\Delta T_{\text{norm}}$ . A good match between the calculated and measured spectra is found for the scattering time  $\tau_s = 0.3$  fs (Fig. 8.7), which corresponds to the Drude mobility  $0.5 \text{ cm}^2\text{V}^{-1}\text{s}^{-1}$  (the accuracy of these values is limited by the uncertainties in the  $V$  factor (Section 8.4.1) and the carrier effective mass (Section 8.3.1)). Since the band bending and repelling charged surface defects would further confine the charges and thus change the shape of the THz spectra (see the response of the long nanotubes in Section 8.4.2b)), we conclude that these effects are marginal and the charges are confined just by the physical boundaries of nanotube walls.

The charge mobility in the short nanotubes is comparable to that in anatase nanoparticles [165] and in mesoporous anatase structures [37]. However, it is considerably

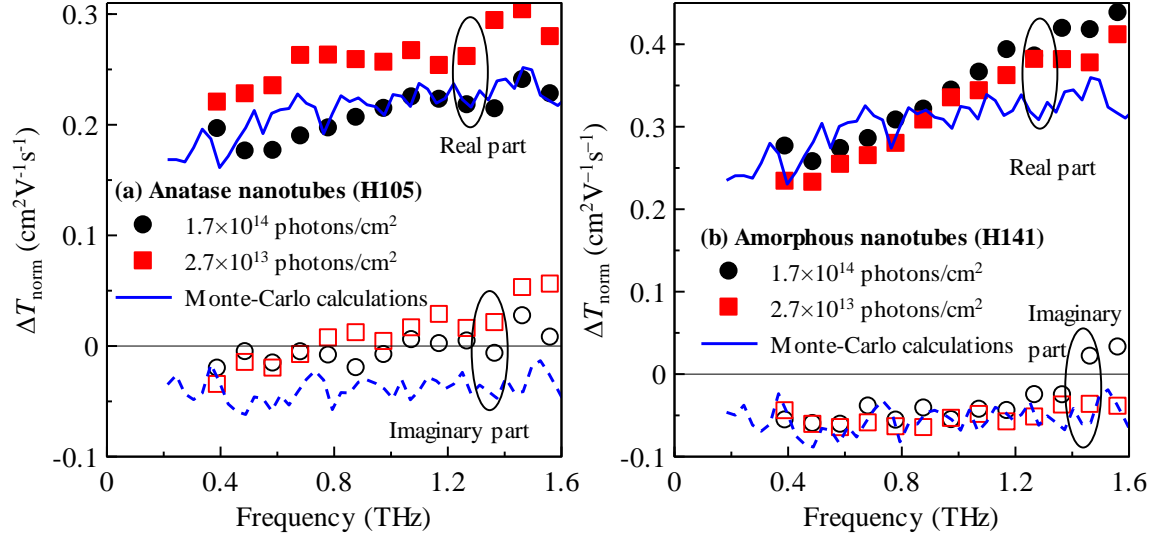


Fig. 8.7. Normalized transient transmission spectra  $\Delta T_{\text{norm}}$  of the short  $\text{TiO}_2$  nanotubes in anatase (a) and amorphous (b) phase (Tab. 8.1). Experimental data (points) were obtained for the pump-probe delay of 10 ps. Lines: results of Monte-Carlo calculations for charge mobility  $0.5 \text{ cm}^2\text{V}^{-1}\text{s}^{-1}$ . Only confinement by the nanotube walls was considered in the calculations (Fig. 8.5(a)). Solid lines and closed symbols: real part; dashed lines and open symbols: imaginary part.

lower than in high-quality intrinsic or niobium-doped bulk anatase [164],[166]. We thus conclude that the studied nanotubes contain a large density of defects which are responsible for strong scattering of carriers. Therefore, there is still a potential for improving the crystallinity and the charge transport properties of the nanotubes. We note that the estimated scattering time of 0.3 fs corresponds to a mean free path  $\sim 0.035 \text{ \AA}$ . Although this means that the charges interact too frequently to follow the Drude view of ballistic charge motion interrupted by scattering events, we still believe that the estimated mobility characterizes well the efficiency of the charge transport in the nanotubes.

Surprisingly, the normalized transient transmission  $\Delta T_{\text{norm}}$  is slightly higher for the amorphous nanotubes (Fig. 8.7). Even though we cannot say whether this is due to a better connectivity (higher value of  $V$ ) or a higher mobility, the presented results imply that the THz mobilities (i.e. the charge mobility on the nanoscale distances) in short anatase and amorphous nanotubes are comparable. Similar conclusion was also drawn for mesoporous  $\text{TiO}_2$  structures [37].

We now briefly address the charge dynamics in the short nanotubes (Fig. 8.8). Shortly after photoexcitation, the THz photoconductivities of both the anatase and amorphous samples are similar. Subsequently, trapping of charges occurs which reduces the THz photoconductivity. The estimated time-scale for trapping from Fig. 8.8 is then  $\sim 1 \text{ ns}$  in the amorphous nanotubes and somewhat longer in the anatase nanotubes. The anatase nanotubes are thus more suitable for photovoltaic applications where long-range charge transport is



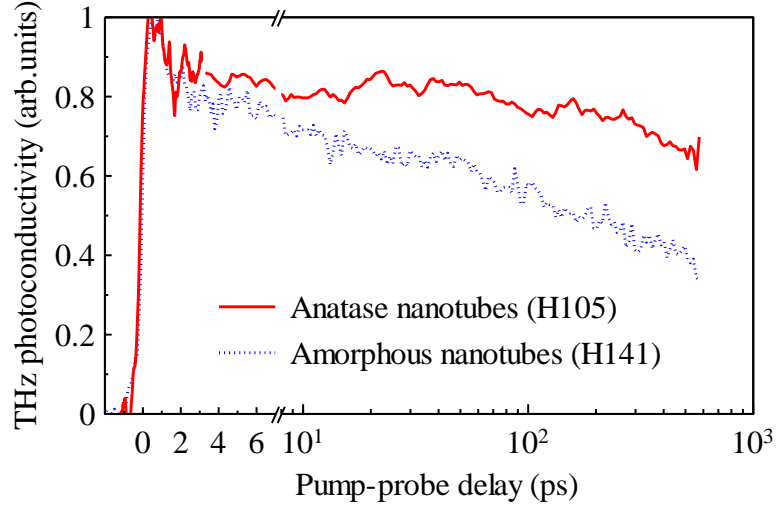


Fig. 8.8. Decay of the average THz photoconductivity in the short  $\text{TiO}_2$  nanotubes (photoexcitation fluence was  $2.7 \times 10^{13}$  photons/cm<sup>2</sup>). The curves are normalized to the peak value.

required (in correlation with the incident photon-to-electron conversion efficiency which was in detail discussed in [152]).

#### 8.4.2.b) Long nanotubes

Since the samples of long  $\text{TiO}_2$  nanotubes were free-standing layers, we could photoexcite them both from the open top part and the closed bottom part, respectively. The examples of the measured normalized transmission spectra  $\Delta T_{\text{norm}}$  are shown in Fig. 8.9(a). A significant response was observed just for the anatase nanotubes photoexcited from their open tops. The observed transient photoconductivity is long-lived: the initial decay rate is on the time scale of hundreds of picoseconds and it even seems to slow down after  $\sim 500$  ps (Fig. 8.9(c)). The response of the long anatase nanotubes photoexcited from the bottom part ( $|\Delta T_{\text{norm}}| \sim 0.05 \text{ cm}^2\text{V}^{-1}\text{s}^{-1}$ ) is close to the detection limit of our setup. The difference from the response of the photoexcited top part is not surprising: the bottom part of the nanotube lies in the area where the anodic oxidation of titanium substrates takes place. Therefore, it exhibits different properties than the top of the nanotube wall where the oxidation process is already completed. For the amorphous nanotubes, we observe no measurable signal even at the shortest pump-probe delay ( $\sim 1$  ps) which implies that  $|\Delta T_{\text{norm}}| \lesssim 0.02 \text{ cm}^2\text{V}^{-1}\text{s}^{-1}$ .

From now on, we discuss just the response of the long anatase nanotubes photoexcited from the top part. It is evident that the normalized transient transmission  $\Delta T_{\text{norm}}$  does not depend significantly on the photoexcitation fluence (Fig. 8.9(a)). Since the  $D$ -term in the VBD model is not negligible (for the photoexcitation fluence  $5.7 \times 10^{13}$  photons/cm<sup>2</sup> and 1 THz, we estimate  $|D\Delta\sigma_p/(\omega\epsilon_0)| \sim 0.34$ ), the nanotubes should be percolated (see the discussion in Section 8.3.3) which further supports our conclusion from the steady-state measurements (Section 8.4.1). Due to the optical thickness of the samples, we can also apply the temporal windowing and thus we use Eq. (3.35) to retrieve the mobility spectra of the nanotubes.

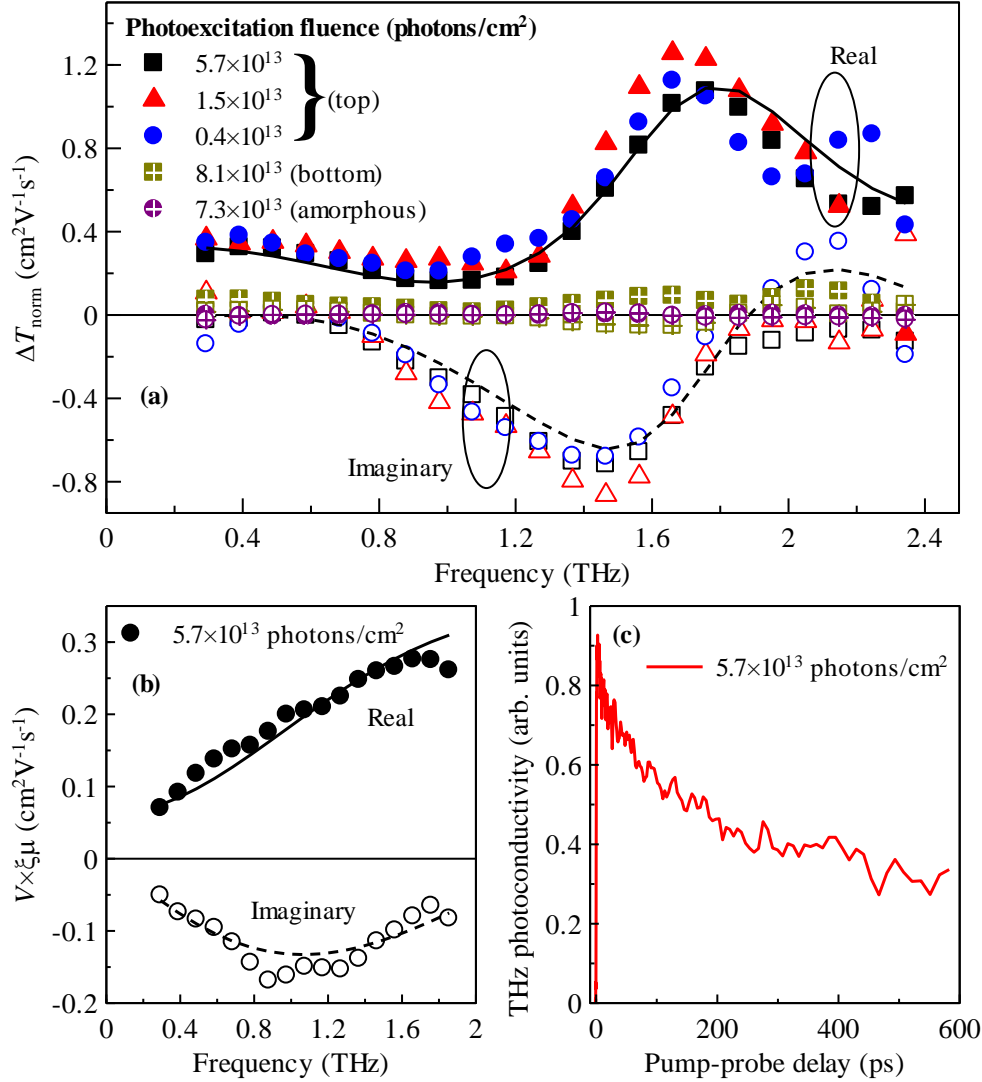


Fig. 8.9. (a) The measured normalized transient transmission spectra  $\Delta T_{\text{norm}}$  of the long  $\text{TiO}_2$  nanotube layers in anatase (sample H172) and amorphous (sample H178) phase (Tab. 8.1). The layers were photoexcited from top (i.e. open nanotubes) and from the bottom (i.e. closed nanotubes) parts, respectively. The spectra were measured 10 ps after photoexcitation. (b) Spectra of the product  $V \times \xi \mu$  calculated using Eq. (3.35) for the anatase nanotubes photoexcited from the top part. (c) Dynamics of the average THz photoconductivity in anatase nanotubes photoexcited from the top part. Lines in panels (a) and (b) serve as guides for the eye only. Closed symbols: real parts of the spectra, open symbols: imaginary parts.

The measured spectra of normalized transient transmission  $\Delta T_{\text{norm}}$  exhibit a resonant-like behavior (Fig. 8.9(a)). In [57], a similar feature was observed and attributed to the response of excitons. However, a precise analysis reveals that in our spectra it is an interference maximum in a 30- $\mu\text{m}$  thick nanotube layer. The spectrum of charge mobility retrieved from  $\Delta T_{\text{norm}}$  using (3.35) (this equation correctly accounts for the interferences) is indeed smooth and without any sharp resonances (Fig. 8.9(b)). Similar complicated

interference patterns were also observed and deconvoluted in nanocrystalline Si samples with thickness  $\sim 200 \mu\text{m}$  [56]. We note that the errors in the mobility spectra retrieved from  $\Delta T_{\text{norm}}$  are amplified in the vicinity of the interference maxima (these involve e.g. the noise in the measured spectra and the uncertainty in the sample thickness). The mobility spectra are thus reliably obtained in a narrower range of frequencies than the measured  $\Delta T_{\text{norm}}$  spectra (compare Figs. 8.9(a) and 8.9(b)).

The mobility spectra retrieved from the experiments (Fig. 8.9(b)) exhibit typical signatures of charge confinement (Section 5.1). In the simplest case when the charges are confined just by the nanotube walls, however, the calculated spectra are not compatible with those measured (case  $a = \infty$  in Fig. 8.10). The calculated real part increases too slowly with frequency and the calculated imaginary part has maximum at lower frequency than that observed experimentally. Since the peak frequency is inversely proportional to the confinement length ([27], Section 5), the charges must then be confined more strongly than just by the nanotube wall. To confirm this, we consider the models introduced in Section 8.3.1.

First, we investigate the role of possible internal structure of the nanotube wall (Fig. 8.5(b)). For this, we employed the Monte-Carlo calculations for several sizes  $a$  of the nanoregions forming the wall. A particularly good match is obtained for  $a = 10 \text{ nm}$  (Fig. 8.10). The probability of the charge transfer into an adjacent region is then  $p_F \sim 2.5\%$ . This implies that the nanotubes may be composed by such small anatase grains. The pronounced increase of the real part of the mobility spectrum can be achieved only for longer scattering times ( $\tau_s = 15 \text{ fs}$ ). This corresponds to a rather high Drude mobility  $\sim 30 \text{ cm}^2\text{V}^{-1}\text{s}^{-1}$  (this value is just an order of magnitude estimate mainly due to the ambiguity of the carrier effective mass entering the Monte-Carlo calculations, and, to some extent, also due to the uncertainty of the adjustable parameters  $\tau_s$  and  $a$ ) which is comparable with that in high-quality intrinsic or niobium-doped bulk anatase [164],[166]. The amplitude of the measured signal, however, is low compared to such high value of Drude mobility. This implies a low yield of mobile carriers (by amplitude fitting, we estimate  $\xi = 10\%$ ), which we attribute to a high density of deep traps at the nanotube wall surfaces. Furthermore, the used short-wavelength photoexcitation (for  $\lambda = 266 \text{ nm}$ , the penetration depth in anatase is  $\sim 15 \text{ nm}$ ) generates a considerable number of carriers close to the surface which may also reduce the overall yield of mobile carriers. Similarly low yield of mobile photoexcited charges was observed also in InP nanowires and ascribed to the photoabsorption in localized defect states [92].

We now try to explain the response of the long  $\text{TiO}_2$  nanotubes considering the two remaining proposed confining mechanisms introduced in Section 8.3.1 – band bending at the nanotube wall surface and the repelling potential of charged surface defects (Figs. 8.5(c),(d)). First, we investigate how these potentials individually influence the mobility spectrum (Fig. 8.11(a)). The band bending confines the motion of charges either into a central area of the nanotube wall (central charges), or to the vicinity of the nanotube wall surfaces (peripheral charges). Here, we consider  $f_0 = 3 \text{ THz}$  for which the bending energy reaches  $\sim 0.1 \text{ eV}$ . For central charges, the real part of the mobility spectrum exhibits more pronounced increase than for the confinement just by the nanotube walls (Fig. 8.11(a)). At the same time, the imaginary part remains negative in a broader frequency range. In contrast, the response of

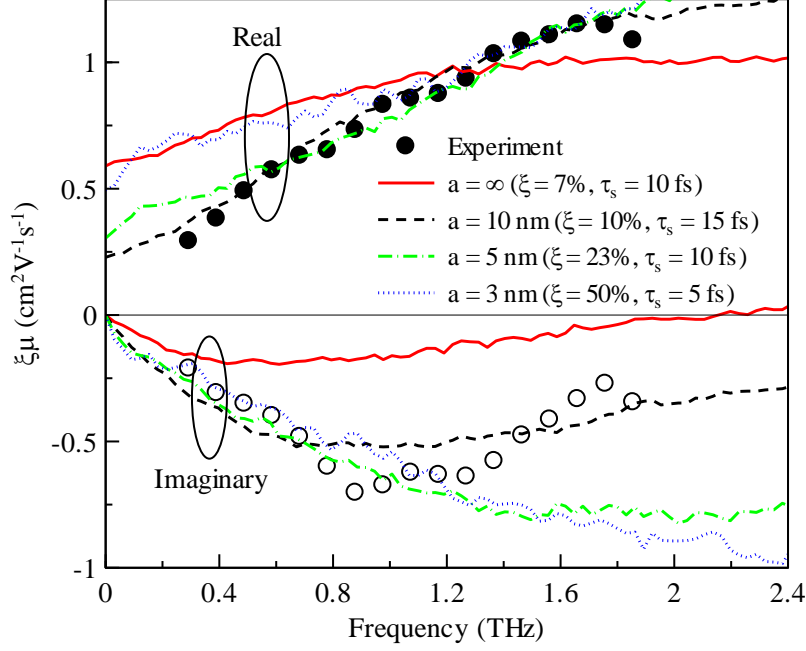


Fig. 8.10. Lines: charge mobility spectra in the model structure from Fig. 8.5(b) (a nanotube wall composed of cube nanoregions with dimension  $a$ ) obtained by the Monte-Carlo calculations (lines). Symbols show the mobility spectrum measured for long anatase nanotubes (photoexcitation fluence  $\phi = 5.7 \times 10^{13}$  photons/cm<sup>2</sup>). The values of the quantum yield  $\xi$ , scattering time  $\tau_s$  and the probability  $p_F$  of the charge transfer between adjacent nanoregions were optimized to find the best match between the calculated and measured data: values of  $\xi$  and  $\tau_s$  are summarized in the legend,  $p_F = 2.5\%$  for all the shown spectra. The spectrum for  $a = \infty$  corresponds to the homogeneous nanotube walls (i.e. without nanoregions).

peripheral charges is much weaker and completely flat. This stems from the highly non-parabolic potential shape in which the peripheral charges move: we can understand it as a motion in a potential well with a very broad distribution of eigenfrequencies, which sums up to a flat spectrum. The response of charges moving just in the repelling potential of surface defects (8.2) (there were 20 defects on the inner nanotube wall surface and 30 defects on the outer surface; screening parameter  $k_0 = 10^8$  m<sup>-1</sup>) is very weak (Fig. 8.11(a)), although it exhibits a dispersion comparable with that of electrons in the band bending potential (8.1).

Neither of the two models considered above, however, reproduces the shape of the mobility spectrum obtained from experiments (Fig. 8.11(b)). The comparison implies that the charges should be confined even more strongly. We thus examined a combined influence of band bending and of additional charged surface defects. However, no significant improvement of the match between the calculated and measured results was observed. We thus conclude that the charge confinement by nanoregions forming the nanotube wall is dominant effect in the studied long anatase TiO<sub>2</sub> nanotubes.

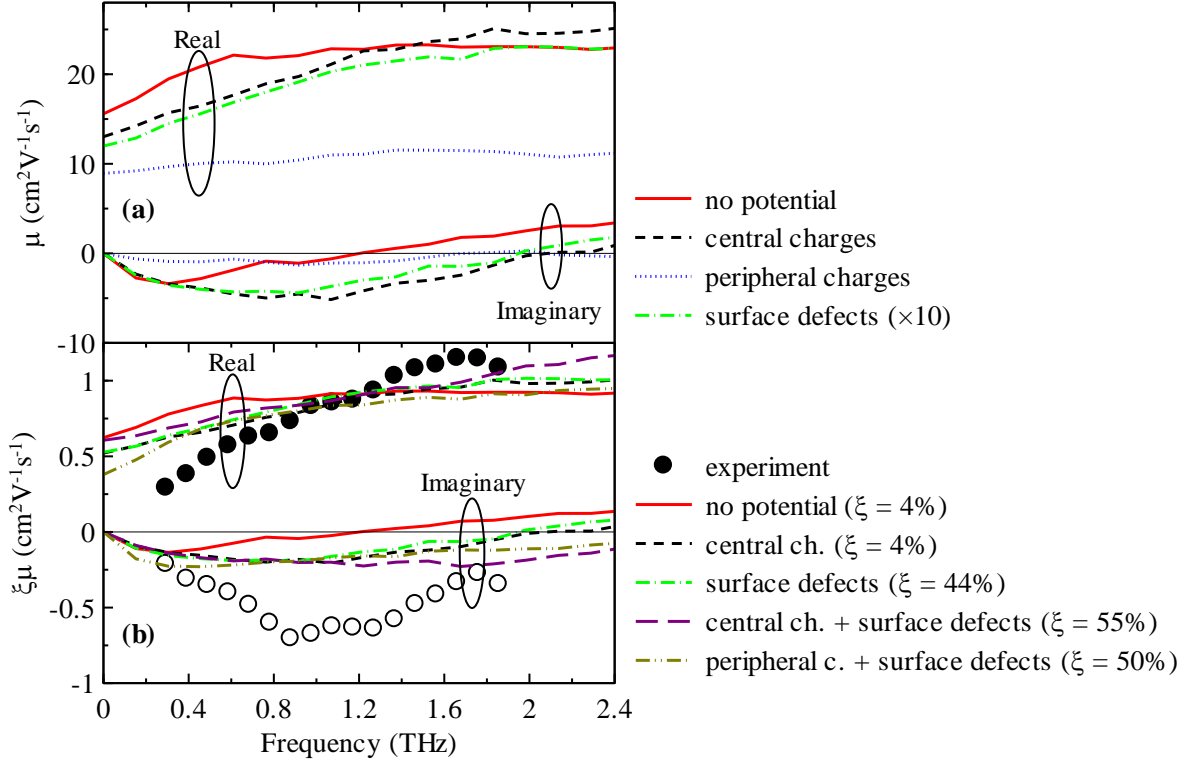


Fig. 8.11. (a) Influence of band bending and repelling potential of surface charges on THz mobility spectra of the long  $\text{TiO}_2$  nanotubes. The spectra were obtained using the Monte-Carlo calculations based on Kubo formalism (Section 2.1). Following parameters were assumed: scattering time  $\tau_s = 15$  fs, harmonic frequency of the band bending potential  $f_0 = 3$  THz, screening parameter  $k_0 = 10^8 \text{ m}^{-1}$ . There were 20 surface defects on the inner surface of the nanotube wall and 30 defects on the outer surface. (b) Comparison of the calculated (lines) and measured (symbols) data (long anatase nanotubes, photoexcitation fluence  $\phi = 5.7 \times 10^{13} \text{ photons/cm}^2$ ). In the calculations, we considered the potentials from panel (a) and also their combinations. The values of the quantum yield  $\xi$  (summarized in the legend) were optimized to find the best match between the calculated and measured data.

#### 8.4.2.c) Comparison with previous studies

The THz photoconductivity of the studied short and long  $\text{TiO}_2$  nanotubes strikingly differ. For the short nanotubes, we observed an extremely small mobility (Drude mobility  $\sim 0.5 \text{ cm}^2\text{V}^{-1}\text{s}^{-1}$ ) with the spectra characteristic for weakly localized charges. For the long nanotubes, much stronger confinement occurs and the mobility is also considerably higher (Drude mobility  $\sim 30 \text{ cm}^2\text{V}^{-1}\text{s}^{-1}$ ).

These results are also quite striking while compared with the previous studies of THz conductivity on  $\text{TiO}_2$  nanotubes. In nanotubes similar to ours, Wehrenfennig et al. reported a Drude-like mobility spectra with the dc mobility comparable to that in  $\text{TiO}_2$  nanoparticles [136]. In contrast, Richter and Schmittenmaier reported a power-law conductivity with an excitonic resonance for Ru-N3-sensitized nanotubes [57]. These strikingly different results

shows that the charge transport properties of TiO<sub>2</sub> nanotube layers depend strongly on the fabrication process.

## 8.5 Conclusions

Time-domain THz spectroscopy was employed to characterize various self-organized TiO<sub>2</sub> nanotube layers. A careful analysis of the measured spectra was required to reliably determine the effective THz permittivity and the effective THz photoconductivity of the nanotubes. In particular, we showed that the apparent resonance in the transient transmission spectra of the long TiO<sub>2</sub> nanotubes is caused by Fabry-Pérot interferences in the layer, and not by a low-energy excitation.

The analysis of the measured steady-state permittivity allowed us to assess the in-plane electrical connectivity of individual nanotubes. We found a good correlation with the geometrical connectivity of the nanotubes observed in SEM images. The THz photoconductivity strongly depends on the fabrication process:

- For short nanotubes, we observed very small conductivity (Drude mobility  $\sim 0.5 \text{ cm}^2\text{V}^{-1}\text{s}^{-1}$ ) with spectra characteristic for weakly localized charges. This implies that the carriers are confined just by the physical boundaries of the nanotube wall.
- For long nanotubes, the THz photoconductivity spectra show pronounced dispersion. This implies a confinement of charges on distances  $\sim 10 \text{ nm}$ , i.e. there are obstacles for charge motion along the circumference of the nanotube wall. The mobility of charges within these confinement areas is comparable to that in high-quality anatase crystals.

These results imply that the anodization process could be further optimized to provide a material with excellent long-distance charge mobility.

Transient photoconductivity of the nanotubes is long-lived. For short nanotubes, the estimated time-scale for trapping is  $\gtrsim 1 \text{ ns}$ . For long nanotubes, we observe a slowly decaying component with mean life-time of several hundreds of picosecond.

## Conclusions

THz conductivity spectra contain information on charge transport mechanisms on nanometer distances. In semiconductor nanostructures, a considerable departure from the bulk response can occur due to the charge confinement suppressing the long-range transport. The recent developments of high-field THz sources then open also a possibility for the investigation of charge transport in intense electric fields: additional nonlinearity due to the confinement in an anharmonic potential is anticipated. In this thesis, we focused on the investigation of three inter-related topics: theoretical studies of fundamental properties of linear conductivity of confined electron gas, combined theoretical and experimental analysis of TiO<sub>2</sub> nanotube layers, and development of a theoretical framework for calculations of the nonlinear response of semiconductor nanostructures.

### Linear conductivity of confined electron gas

Even though the linear THz conductivity of inhomogeneous media is thoroughly analyzed in the literature, we still provide new results of fundamental importance. We focused on a toy model where the carriers move (almost) ballistically with a uniform (Fermi) velocity (i.e. degenerate electron gas and long scattering times):

- For structures with a rectangular geometry, the conductivity spectra exhibit a series of geometrical resonances which are directly associated with the frequency of the bouncing of charges moving with the Fermi velocity and its higher harmonics. The presence of "higher harmonics" peaks reflects the anharmonic character of the charge motion despite the fact that we are in the linear regime. When the structure surface is round, the THz conductivity spectra exhibit complex patterns related to quasi-periodic trajectories.
- In mutually isolated nanoelements, a plasmonic resonance develops and couples with the observed geometrical resonances (their frequency depends on the Fermi velocity and thus also on the charge density). The character of this coupling differs with the dimensionality of the structure. In 3D nanostructures, the plasmonic mode dominates the response only at high carrier densities. Analogical behavior was already observed for non-degenerate electron gases in isolated nanostructures. In 1D systems, the plasmonic resonance then dominates in the spectra only at low enough carrier concentrations. The 2D nanostructures are then specific as the character of the resulting mixed mode does not depend on the charge density.

Our conclusions provide a link between the quantum mechanics and the commonly observed experimental results. In a quantum-mechanical view (expected for nanostructures), the conductivity spectrum consists of a series of peaks related to transitions between defined states of the system. For large enough structures containing degenerate electron gas, we showed that these peaks can be identified with a classical (quasi-)periodic motion of charges. Under common experimental conditions, the ensemble of mobile charges can be characterized as a non-degenerate electron gas: a broad distribution of charge velocities (and to a lesser extent also the bulk scattering and distribution of nanoelement sizes) then smears the sharp lines

corresponding to quantum transitions into a single broad resonance frequently associated with the phenomenological Drude-Smith model.

## **THz spectroscopy of TiO<sub>2</sub> nanotubes**

We used time-domain THz spectroscopy to study the dielectric, percolation and photoconductive properties of various self-organized TiO<sub>2</sub> nanotube layers prepared by the anodization of titanium. The SEM images reveal that the nanotubes do not fully overlap, but are rather connected by contacts of limited extent. The percolation properties inferred from steady-state THz measurements then confirm a limited (but existing) electrical connectivity between the nanotubes. The photoconductive properties of the nanotube walls then strongly depend on the fabrication process:

- For short nanotubes (length  $\sim 1\ \mu\text{m}$ ), the conductivity spectra show a very weak dispersion which is characteristic for weakly localized charges. Monte-Carlo calculations then revealed that the charges are confined just by the physical boundaries of the nanotube wall. The Drude mobility of charges  $\sim 0.5\ \text{cm}^2\text{V}^{-1}\text{s}^{-1}$  is then very small compared to a high-quality anatase crystals.
- For long nanotubes ( $\sim 30\ \mu\text{m}$ ), the THz photoconductivity spectra show pronounced dispersion. This implies that there are some obstacles for charge motion along the circumference of the nanotube wall. Using Monte-Carlo calculations, we estimated that the confinement of charges takes place on distances  $\sim 10\ \text{nm}$ . The Drude mobility of charges within these confinement areas ( $\sim 30\ \text{cm}^2\text{V}^{-1}\text{s}^{-1}$ ) is comparable to that in high-quality anatase crystals.

## **Nonlinear THz response of semiconductor nanostructures**

The nonlinear THz response of nanostructures has been a completely unexplored field. Therefore, we had to develop a pertinent theoretical framework (oriented on thin samples) from the scratch. Our theory covers the following issues:

- We introduced a phenomenological description of the nonlinear THz conductivity. This is not as straightforward as in nonlinear optics: the phase-matching condition is suppressed for thin samples in the THz range, therefore frequency mixing between all spectral components of the broadband THz pulses contributes to the transmitted spectrum. Additionally, the observed nonlinear THz response is often highly non-perturbative. The nonlinear THz conductivity describing the response to a monochromatic wave is thus more naturally expanded into a series of resulting harmonic frequencies in which we disregard the dependence on the exponent of electric field.
- To assess the THz nonlinear conductivity on the microscopic level, we developed non-perturbative Monte-Carlo calculations. These allow us to evaluate the response of confined carriers in the presence of a strong arbitrarily shaped electric field. The main output of these calculations is a field-dependent electric current density. If we employ



the calculations for several different electric field amplitudes, we can also determine the individual nonlinear (photo)conductivities of different orders.

- Semiconductor nanostructures are inherently inhomogeneous which causes complications for the evaluation of their response. Firstly, it is important to realize and account for the difference between the electric field incident on the sample and the local fields in the nonlinear constituents of the inhomogeneous structure. Then, we derived a nonlinear effective medium theory to homogenize the problem, i.e. to transform the complex spatial distribution of local nonlinear electric current densities or photoconductivities into a spatially homogeneous effective electric current density or photoconductivity, respectively.
- Finally, we analytically solved the nonlinear wave equation for a thin homogenized sample. This allows us to link the nonlinear electric current density (i.e. output of Monte-Carlo calculations) or nonlinear photoconductivity with the expected measurable signals. We pointed out that due to the inherent frequency mixing, it is generally impossible to get rid of the instrumental response functions in the measurable nonlinear signals. In this sense, the nonlinear experiments are expected to be much more complex than e.g. the linear transient transmission measurements where the instrumental response functions cancel out. In the THz range, the instrumental response functions are complex and frequency-dependent, therefore they severely influence the measurable broadband signals in a non-trivial way.

The nonlinear response of confined charges is highly non-perturbative even in moderate electric fields: we resolved an efficient high harmonics generation due to charge confinement already for fields  $\gtrsim 10$  kV/cm. The character of the nonlinearities then strikingly differs depending on the equilibrium distribution of thermal velocities:

- The nonlinear THz response of non-degenerate electron gas is qualitatively compatible with the response of an anharmonic oscillator. With increasing electric field, the charge mean velocity increases and nonlinear THz conductivity spectra thus blueshift.
- For degenerate electron gases, the nonlinear THz response is very complicated. For very low electric fields, the nonlinear spectra exhibit peaks located at the harmonic frequencies corresponding to the bouncing of charges moving with Fermi velocity. With increasing electric field, we observe a splitting of the peaks into multiplets and emergence of other features due to the resonant character of the carrier motion.

We theoretically evaluated the measurable nonlinear signals for various semiconductor nanostructures which can be fabricated by current nanotechnologies. To obtain a high nonlinear local conductivity, several issues have to be considered:

- The nanostructures should be formed by a semiconducting material with high carrier mobility (e.g. gallium arsenide) to enhance the interaction of charges with the THz radiation and the nanostructure boundaries.
- The strength of the nonlinearity non-trivially depends on the nanostructure dimensions and the target THz frequencies. Generally, the confinement strongly limits the mobility amplitude for small dimensions. For too large dimensions, the confinement is

suppressed and thus all corresponding nonlinearities vanish. For GaAs nanostructures and driving THz pulses with frequencies around  $\sim 1$  THz, the amplitude of nonlinear mobility exhibits a flat maximum for nanostructure size  $\sim 250$ - $300$  nm.

Per unit charge, the nonlinearities due to charge confinement are 20 times larger than the nonlinearities observed in doped unstructured graphene which has been believed to be the most nonlinear material in the THz range.

The strength of the measurable nonlinear signals is also strongly influenced by the nanostructure layout. In conventional semiconductor-air nanostructures, a large permittivity contrast limits the nonlinear signal (screening of the local electric field, weak effective response) and pushes the measurable signal close to the edge of detectability. We thus investigated also semiconductor-metal nanostructures where the metallic parts act as short circuit concentrating the electric field into the embedded semiconductor nanoelement. This provides sufficient enhancement of both the local field in the nanostructure and the resulting measurable nonlinear signal; the enhancement further scales with the reciprocal value of the semiconductor filling factor. Based on these findings, we identified a metallic nanoslits structure filled with GaAs nanobars as the most promising structure for experimental observation of nonlinearities due to charge confinement. Thanks to the enhancement of the effective nonlinear response, the nonlinearities should be easily observable in common low-field THz setups.

Our results achieved in the field of THz nonlinearities provide an inspiration for further research. The qualitative explanation of nonlinear response of confined degenerate electron gas is still an open problem. Development of a simple analytical model describing the response could bring more light on the physics of resonant systems. Further, we plan the fabrication of the metallic nanoslits filled with GaAs nanobars. Such structure should enable a straightforward experimental observation of nonlinear THz conductivity even in the low-field experimental setup employing optical rectification in ZnTe (delivering fields  $\sim 5$  kV/cm) which is well established in our lab. Finally, the reported nonlinearities due to charge confinement in GaAs nanostructures are among the strongest known THz nonlinearities in solid state physics. The combination of this mechanism with the strong "bulk" nonlinearities in doped graphene could then spark a development of an ultimately nonlinear material.

## Appendices

### A. Transient transmission of an inhomogeneous sample with background conductivity

In Section 3.2, we discussed the solution of wave equation for samples without free charges in the equilibrium state. Here, we provide generalized relations for a sample with a spatially homogeneous background local conductivity (this situation may occur e.g. in doped semiconductor nanoparticles). These formulas were derived to explain the THz response of TiO<sub>2</sub> nanotubes. However, a thorough analysis of the measured data (Section 8) did not confirm a presence of background conductivity.

In the ground state, we assume that each photoconductive part of the sample exhibits a conductivity  $\sigma_B$ . Upon photoexcitation, the local conductivity becomes depth-dependent and changes to

$$\Delta\sigma_p(z) = \sigma_B + \Delta\sigma_p \exp(-\alpha_{\text{eff}} z), \quad (\text{A.1})$$

where the factor  $\exp(-\alpha_{\text{eff}} z)$  accounts for the attenuation of the excitation beam. The effective conductivity  $\Delta\sigma_{\text{eff}}(z)$  is then given by the VBD model (3.3). We then use the general solution of the wave equation (3.20) for the transmission change  $\Delta E_T(\Delta\sigma_{\text{eff}}(z))$  of the sample for arbitrary depth-profile of effective conductivity [34]

$$\begin{aligned} \frac{\Delta E_T(\Delta\sigma_{\text{eff}}(z))}{E_T(0)} = & -\frac{Z_0}{2n_s} a \times \left[ (1 + r_1 r_2 \exp(2ikL)) \int_0^L \Delta\sigma_{\text{eff}}(z) dz + \right. \\ & \left. + r_1 \int_0^L \exp(2ikz) \Delta\sigma_{\text{eff}}(z) dz + r_2 \exp(2ikL) \int_0^L \exp(-2ikz) \Delta\sigma_{\text{eff}}(z) dz \right], \end{aligned} \quad (\text{A.2})$$

where  $E_T(0)$  is the field transmitted through unexcited sample without the background conductivity.

Similarly as for undoped samples, we wish to evaluate the transient transmission  $\Delta T/T$  defined as the transmission change normalized by the transmission in the unexcited sample:

$$\frac{\Delta T(\sigma_B, \Delta\sigma_p)}{T(\sigma_B)} = \frac{E_T(\sigma_B, \Delta\sigma_p) - E_T(\sigma_B)}{E_T(\sigma_B)}, \quad (\text{A.3})$$

where  $E_T(\sigma_B)$  is the THz field transmitted through the sample in equilibrium and  $E_T(\sigma_B + \Delta\sigma_p(z))$  is the wave transmitted through the photoexcited sample. The above relation can be equivalently expressed in terms of transient transmissions formally normalized by the field  $E_T(0)$

$$\frac{\Delta T(\sigma_B, \Delta\sigma_p)}{T(\sigma_B)} = \frac{\frac{\Delta E_T(\sigma_B, \Delta\sigma_p)}{E_T(0)} - \frac{\Delta E_T(\sigma_B)}{E_T(0)}}{1 + \frac{\Delta E_T(\sigma_B)}{E_T(0)}}, \quad (\text{A.4})$$

where  $\Delta E_T(\sigma) = E_T(\sigma) - E_T(0)$ . The above relation links the measured transient transmission  $\Delta T/T$  of a photoexcited doped sample with the material parameters since  $\Delta E_T(\sigma_B, \Delta\sigma_p)/E_T(0)$  and  $\Delta E_T(\sigma_B)/E_T(0)$  can be evaluated from (A.2). To find the unknown  $\Delta\sigma_p$  from optical pump-THz probe measurements, however, we additionally need to determine the background conductivity  $\sigma_B$ , e.g. from separate steady-state experiments (i.e. comparison with the propagation in free space). In the rest of this appendix, we will consider  $\sigma_B$  to be known without any further assumptions.

We now evaluate (A.4) for a two-component system described by VBD model (3.3). The character of considered equations allows us to treat the percolated and non-percolated terms separately.

We start with the percolated term for which the effective photoconductivity  $\Delta\sigma_{\text{eff}}(z)$  reads

$$\text{photoexcited: } \Delta\sigma_{\text{eff}}(z) = V[\Delta\sigma_p \exp(-\alpha_{\text{eff}} z) + \sigma_B] \quad (\text{A.5.1})$$

$$\text{equilibrium: } \Delta\sigma_{\text{eff}}(z) = V\sigma_B. \quad (\text{A.5.2})$$

The additivity of the integrals in (A.2) then ensures that the terms with  $\sigma_B$  cancel each other out in the numerator of (A.4) and we thus find

$$\frac{\Delta T(\sigma_B, \Delta\sigma_p)}{T(\sigma_B)} = \frac{\frac{\Delta E_T(\Delta\sigma_p)}{E_T(0)}}{1 + \frac{\Delta E_T(\sigma_B)}{E_T(0)}}, \quad (\text{A.6})$$

The numerator of the above relation is given by (3.31). Trivial integration then yields the term  $\Delta E_T(\sigma_B)/E_T(0)$  in the denominator:

$$\frac{\Delta E_T(\sigma_B)}{E_T(0)} = -\frac{Z_0}{2n_s} aL\sigma_B \times \left[ (1 + r_1 r_2 \exp(2ikL)) + \frac{r_1 - r_2}{2ikL} (\exp(2ikL) - 1) \right]. \quad (\text{A.7})$$

For non-percolated term, the situation becomes more complicated as the effective photoconductivity reads

$$\text{photoexcited: } \Delta\sigma_{\text{eff}}(z) = \frac{B[\sigma_p \exp(-\alpha_{\text{eff}} z) + \sigma_B]}{1 + i \frac{D}{\omega \epsilon_0} [\sigma_p \exp(-\alpha_{\text{eff}} z) + \sigma_B]} \quad (\text{A.8.1})$$

equilibrium: 
$$\Delta\sigma_{\text{eff}}(z) = \frac{B\sigma_B}{1 + i \frac{D}{\omega\epsilon_0} \sigma_B}. \quad (\text{A.8.2})$$

The evaluation of (A.2) and (A.4) requires the knowledge of the following integrals [56],[59]

$$\int \frac{\exp(-\alpha_{\text{eff}} z)}{1 + Y_0 \exp(-\alpha_{\text{eff}} z)} dz = -\frac{\text{Ln}[1 + Y(z)]}{\alpha_{\text{eff}} Y_0} \quad (\text{A.9})$$

$$\int \frac{\exp[-(2ik + \alpha_{\text{eff}})z]}{1 + Y_0 \exp(-\alpha_{\text{eff}} z)} dz = -\frac{\exp[-(2ik + \alpha_{\text{eff}})z]}{\alpha_{\text{eff}}} \times F\left(1 + 2i \frac{k}{\alpha_{\text{eff}}}, Y(z)\right), \quad (\text{A.10})$$

where we retain the notation introduced in Section 3.2.2. Upon integration, we find the following form of terms in (A.4):

$$\begin{aligned} \frac{\Delta E_T(\sigma_B, \Delta\sigma_p)}{E_T(0)} - \frac{\Delta E_T(\sigma_B)}{E_T(0)} = & -\frac{Z_0}{2n_s} a \times \left[ (1 + r_1 r_2 \exp(2ikL))(I_1 + I_2 - I_3) + \right. \\ & \left. + r_1(I_4 + I_5 - I_6) + r_2 \exp(2ikL)(I_7 + I_8 - I_9) \right] \end{aligned} \quad (\text{A.11.1})$$

$$\frac{\Delta E_T(\sigma_B)}{E_T(0)} = -\frac{Z_0}{2n_s} a \times \left[ (1 + r_1 r_2 \exp(2ikL))I_3 + r_1 I_6 + r_2 \exp(2ikL)I_9 \right]. \quad (\text{A.11.2})$$

The integrals  $I_j$  read

$$I_1 = \frac{B}{\alpha_{\text{eff}} X} \times \left\{ \text{Ln}[1 + X(\Delta\sigma_0 + \sigma_B)] - \text{Ln}[1 + X(\Delta\sigma_0 \exp(-\alpha_{\text{eff}} L) + \sigma_B)] \right\} \quad (\text{A.12.1})$$

$$I_2 = \frac{B\sigma_B}{\alpha_{\text{eff}}(1 + X\sigma_B)} \times \left\{ \text{Ln} \left[ \exp(\alpha_{\text{eff}} L) + \frac{X\Delta\sigma_0}{1 + X\sigma_B} \right] - \text{Ln} \left( 1 + \frac{X\Delta\sigma_0}{1 + X\sigma_B} \right) \right\} \quad (\text{A.12.2})$$

$$I_3 = \frac{B\sigma_B L}{1 + X\sigma_B} \quad (\text{A.12.3})$$

$$I_4 = \frac{B\Delta\sigma_0}{\alpha_{\text{eff}}(1 + X\sigma_B)} \times \left\{ F\left(1 - 2i \frac{k}{\alpha_{\text{eff}}}, -Y_0\right) - \exp[(2ik - \alpha_{\text{eff}})L] F\left(1 - 2i \frac{k}{\alpha_{\text{eff}}}, -Y_0 \exp(-\alpha_{\text{eff}} L)\right) \right\} \quad (\text{A.12.4})$$

$$I_5 = \frac{B\sigma_B}{\alpha_{\text{eff}} X\Delta\sigma_0} \times \left\{ \exp[(2ik + \alpha_{\text{eff}})L] F\left(1 + 2i \frac{k}{\alpha_{\text{eff}}}, -Y_0^{-1} \exp(\alpha_{\text{eff}} L)\right) - F\left(1 + 2i \frac{k}{\alpha_{\text{eff}}}, -Y_0^{-1}\right) \right\} \quad (\text{A.12.5})$$

$$I_6 = \frac{B\sigma_B}{1 + X\sigma_B} \frac{\exp(2ikL) - 1}{2ik} \quad (\text{A.12.6})$$

$$I_7 = \frac{B\Delta\sigma_0}{\alpha_{\text{eff}}(1 + X\sigma_B)} \times \left\{ F\left(1 + 2i\frac{k}{\alpha_{\text{eff}}}, -Y_0\right) - \exp[-(2ik + \alpha_{\text{eff}})L] F\left(1 + 2i\frac{k}{\alpha_{\text{eff}}}, -Y_0 \exp(-\alpha_{\text{eff}}L)\right) \right\} \quad (\text{A.12.7})$$

$$I_8 = \frac{B\sigma_B}{\alpha_{\text{eff}}X\Delta\sigma_0} \times \left\{ F\left(1 - 2i\frac{k}{\alpha_{\text{eff}}}, -Y_0^{-1} \exp(\alpha_{\text{eff}}L)\right) - \exp[-(2ik + \alpha_{\text{eff}})L] F\left(1 - 2i\frac{k}{\alpha_{\text{eff}}}, -Y_0^{-1}\right) \right\} \quad (\text{A.12.8})$$

$$I_9 = \frac{B\sigma_B}{1 + X\sigma_B} \frac{\exp(-2ikL) - 1}{2ik}, \quad (\text{A.12.9})$$

where  $X$  and  $Y_0$  are

$$X = i \frac{D}{\omega\epsilon_0} \quad (\text{A.13.1})$$

$$Y_0 = \frac{X\Delta\sigma_0}{1 + X\sigma_B}. \quad (\text{A.13.2})$$

## B. Derivation of mobility of classical anharmonic oscillator

Here, we derive formulae (6.7) for nonlinear mobilities  $\mu^{(a)}$ . These relations stem from nonlinear Lorentz model where electrons move classically in an anharmonic potential. This system can be treated in a perturbative way which was used in [28] to determine the first to third order susceptibilities. We will follow this derivation and we further expand it to the nonlinearities of the fifth order.

For our purpose, we focus on a 1D oscillator and centrosymmetric media where even order nonlinearities vanish. The restoring force acting on the electron then reads

$$F(x) = -m\Omega_{\text{osc}}^2 x + mbx^3 + mcx^5, \quad (\text{B.1})$$

where  $x$  is the electron displacement,  $\Omega_{\text{osc}}$  is the oscillator frequency and  $b$  and  $c$  are parameters characterizing the strength of the nonlinearity. This force is then associated with a binding potential

$$V(x) = \frac{1}{2} m\Omega_{\text{osc}}^2 x^2 - \frac{1}{4} mbx^4 - \frac{1}{6} mcx^6. \quad (\text{B.2})$$

where necessarily  $c < 0$  to ensure that the electron always remains bound.

The equation of motion of the bound electron is

$$\ddot{x} + 2\gamma\dot{x} + \Omega_0^2 x - bx^3 - cx^5 = -\frac{e_0 E(t)}{m}, \quad (\text{B.3})$$

where  $\gamma$  is a damping rate and the electric field  $E(t)$  is monochromatic and reads

$$E(t) = E_0 \cos(\omega_0 t) = \frac{1}{2} E_0 e^{-i\omega_0 t} + \text{c.c.} \quad (\text{B.4})$$

An analytical solution of equation (B.3) with electric field (B.4) in terms of elementary mathematical functions does not exist. However, a perturbative approach can be applied when the nonlinear displacement  $bx^3 + cx^5$  is much lower than the linear contribution  $\Omega_{\text{osc}}^2 x$  (i.e. for low enough electric fields). Under this assumption, we replace electric field  $E(t)$  with  $\lambda E(t)$ , where  $\lambda$  is a parameter ranging continuously between zero and one. The equation of motion (B.3) thus changes to

$$\ddot{x} + 2\gamma\dot{x} + \omega_0^2 x - bx^3 - cx^5 = -\lambda \frac{e_0}{m} E_0 \cos(\omega_0 t), \quad (\text{B.5})$$

and we assume its solution in the form of power series

$$x = \lambda x_1 + \lambda^3 x_3 + \lambda^5 x_5 + \dots, \quad (\text{B.6})$$

where we omitted the even order contributions as they necessarily vanish due to the symmetry reasons.

Expansion (B.6) is the solution of equation (B.5) if the terms proportional to the field strengths  $\lambda$ ,  $\lambda^3$ ,  $\lambda^5$ , etc., satisfy the equation separately. For the lowest-order contributions  $x_i$ , this leads to the equations

$$\ddot{x}_1 + 2\gamma\dot{x}_1 + \Omega_{\text{osc}}^2 x_1 = -\frac{e_0 E(t)}{m} \quad (\text{B.7.1})$$

$$\ddot{x}_3 + 2\gamma\dot{x}_3 + \Omega_{\text{osc}}^2 x_3 + bx_1^3 = 0 \quad (\text{B.7.2})$$

$$\ddot{x}_5 + 2\gamma\dot{x}_5 + \Omega_{\text{osc}}^2 x_5 + 3bx_1^2 x_3 + cx_1^5 = 0. \quad (\text{B.7.3})$$

The equation (B.7.1) for the linear electron displacement  $x_1$  is essentially the same as the one encountered in the linear Lorentz model. Its solution has the form of a harmonic wave

$$x_1(t) = \frac{1}{2} x_1(\omega_0) e^{-i\omega_0 t} + \text{c.c.} \quad (\text{B.8})$$

Its substitution into (B.7.1) then yields the amplitude  $x_1(\omega_0)$

$$x_1(\omega_0) = -\frac{e_0 E_0}{m} \frac{1}{\mathcal{N}(\omega_0)}, \quad (\text{B.9})$$

where we have introduced

$$\mathcal{N}(\omega_0) = \Omega_{\text{osc}}^2 - \omega_0^2 - 2i\gamma\omega_0. \quad (\text{B.10})$$

To solve the equation (B.7.2) for the third-order correction  $x_3$ , it is necessary to substitute for  $x_1$  raised to the third power which leads to two frequency components oscillating at the fundamental frequency  $\omega_0$  and its third harmonics  $3\omega_0$

$$x_1^3(t) = \frac{1}{8} x_1^3(\omega_0) e^{-i3\omega_0 t} + \frac{3}{8} x_1^2(\omega_0) x_1(-\omega_0) e^{-i\omega_0 t} + \text{c.c.} \quad (\text{B.11})$$

We thus assume  $x_3(t)$  in the form

$$x_3(t) = \frac{1}{2} x_{3,3}(3\omega_0) e^{-i3\omega_0 t} + \frac{1}{2} x_{3,1}(\omega_0) e^{-i\omega_0 t} + \text{c.c.}, \quad (\text{B.12})$$

where the amplitudes  $x_{3,3}(3\omega_0)$  and  $x_{3,1}(\omega_0)$  are related to the third harmonics generation and the nonlinear index of refraction, respectively. After the substitution into (B.7.2), we get

$$x_{3,1}(3\omega_0) = -\frac{e_0^3 E_0^3}{4m^3} \frac{b}{\mathcal{N}(3\omega_0)\mathcal{N}^3(\omega_0)} \quad (\text{B.13.1})$$

$$x_{3,2}(\omega_0) = -\frac{3e_0^3 E_0^3}{4m^3} \frac{b}{\mathcal{N}(\omega_0)\mathcal{N}^2(\omega_0)\mathcal{N}(-\omega_0)}. \quad (\text{B.13.2})$$

The denominators in the above expressions reflect the underlying nonlinear processes which result in the frequencies  $3\omega_0 = \omega_0 + \omega_0 + \omega_0$  and  $\omega_0 = \omega_0 - \omega_0 + \omega_0$ , respectively – the leftmost



$\mathcal{N}$ -term represents the resulting frequency while the other  $\mathcal{N}$ -terms represent the interacting frequency components. In Tab. B1, we introduce a schematical notation in which these processes read  $\omega_0 + \omega_0 + \omega_0 \rightarrow 3\omega_0$  and  $\omega_0 - \omega_0 + \omega_0 \rightarrow \omega_0$ , respectively.

Results (B.9) and (B.13) were already derived in [28]. Now, we provide the expansions for the fifth order nonlinearity. To do this, it is necessary to substitute for  $x_1$  and  $x_3$  in (B.7.3). The pertinent expressions then read

$$x_1^5(t) = \frac{1}{32} x_1^5(\omega_0) e^{-i5\omega_0 t} + \frac{5}{32} x_1^4(\omega_0) x_1(-\omega_0) e^{-i3\omega_0 t} + \frac{10}{32} x_1^3(\omega_0) x_1^2(-\omega_0) e^{-i\omega_0 t} + \text{c.c.} \quad (\text{B.14.1})$$

$$x_1^2(t) x_3(t) = \frac{1}{8} x_1^2(\omega_0) x_{3,3}(3\omega_0) e^{-i5\omega_0 t} + \frac{1}{8} \left[ x_1^2(\omega_0) x_{3,1}(\omega_0) + 2x_1(\omega_0) x_1(-\omega_0) x_{3,3}(3\omega_0) \right] e^{-i3\omega_0 t} + \frac{1}{8} \left[ x_1^2(-\omega_0) x_{3,3}(3\omega_0) + x_1^2(\omega_0) x_{3,1}(-\omega_0) + 2x_1(\omega_0) x_1(-\omega_0) x_{3,1}(\omega_0) \right] e^{-i\omega_0 t} + \text{c.c.} \quad (\text{B.14.2})$$

The fifth-order response thus contains three spectral components at frequencies  $\omega_0$ ,  $3\omega_0$  and  $5\omega_0$ . The solution of (B.7.3) thus takes the form

Order	Equation	Denominator	Interactions
1	(B.9)	$\mathcal{N}(\omega_0)$	$\omega_0 \rightarrow \omega_0$
3	(B.13.1)	$\mathcal{N}(3\omega_0) \mathcal{N}^3(3\omega_0)$	$\omega_0 + \omega_0 + \omega_0 \rightarrow 3\omega_0$
	(B.13.2)	$\mathcal{N}(\omega_0) \mathcal{N}^2(\omega_0) \mathcal{N}(-\omega_0)$	$\omega_0 - \omega_0 + \omega_0 \rightarrow \omega_0$
5	(B.16.1)	$\mathcal{N}(5\omega_0) \mathcal{N}^5(\omega_0)$	$\omega_0 + \omega_0 + \omega_0 + \omega_0 + \omega_0 \rightarrow 5\omega_0$
	(B.16.2)	$\mathcal{N}(3\omega_0) \mathcal{N}^4(\omega_0) \mathcal{N}(-\omega_0)$	$\omega_0 - \omega_0 + \omega_0 + \omega_0 + \omega_0 \rightarrow 3\omega_0$
	(B.16.3)	$\mathcal{N}(\omega_0) \mathcal{N}^3(\omega_0) \mathcal{N}^2(-\omega_0)$	$\omega_0 - \omega_0 + \omega_0 - \omega_0 + \omega_0 \rightarrow 5\omega_0$
	(B.16.1)	$\mathcal{N}(5\omega_0) \mathcal{N}^2(\omega_0) \mathcal{N}(5\omega_0) \mathcal{N}^3(\omega_0)$	$(\omega_0 + \omega_0 + \omega_0) + \omega_0 + \omega_0 \rightarrow 3\omega_0 + \omega_0 + \omega_0 \rightarrow 5\omega_0$
	(B.16.2)	$\mathcal{N}(3\omega_0) \mathcal{N}^2(\omega_0) \mathcal{N}(\omega_0) \mathcal{N}^2(\omega_0) \mathcal{N}(-\omega_0)$	$(\omega_0 - \omega_0 + \omega_0) + \omega_0 + \omega_0 \rightarrow \omega_0 + \omega_0 + \omega_0 \rightarrow 3\omega_0$
		$\mathcal{N}(3\omega_0) \mathcal{N}(\omega_0) \mathcal{N}(-\omega_0) \mathcal{N}(3\omega_0) \mathcal{N}^3(\omega_0)$	$(\omega_0 + \omega_0 + \omega_0) - \omega_0 + \omega_0 \rightarrow 3\omega_0 - \omega_0 + \omega_0 \rightarrow 3\omega_0$
	(B.16.3)	$\mathcal{N}(\omega_0) \mathcal{N}^2(-\omega_0) \mathcal{N}(3\omega_0) \mathcal{N}^3(\omega_0)$	$(\omega_0 + \omega_0 + \omega_0) - \omega_0 - \omega_0 \rightarrow 3\omega_0 - \omega_0 - \omega_0 \rightarrow \omega_0$
		$\mathcal{N}(\omega_0) \mathcal{N}^2(\omega_0) \mathcal{N}(-\omega_0) \mathcal{N}^2(\omega_0) \mathcal{N}(-\omega_0)$	$(\omega_0 - \omega_0 + \omega_0) - \omega_0 + \omega_0 \rightarrow \omega_0 - \omega_0 + \omega_0 \rightarrow \omega_0$

Tab. B1. Summary of the denominators in Eqs. (B.13) and (B.16). Their structure reflects the underlying nonlinear interactions (schematically captured in the rightmost column). In certain cases, two successive third-order interaction have to be considered (schematically represented by two arrows). Permutations of interacting spectral components are accounted for by the numerical coefficients in the pertinent equations.

$$x_5(t) = \frac{1}{2} x_{5,5}(5\omega_0) e^{-i5\omega_0 t} + \frac{1}{2} x_{5,3}(3\omega_0) e^{-i3\omega_0 t} + \frac{1}{2} x_{5,1}(\omega_0) e^{-i\omega_0 t} + \text{c.c.}, \quad (\text{B.15})$$

where the amplitudes  $x_{5,5}(5\omega_0)$ ,  $x_{5,3}(3\omega_0)$  and  $x_{5,1}(\omega_0)$  are

$$x_{5,1}(\omega_0) = -\frac{e_0^5 E_0^5}{16m^5} \left[ \frac{c}{\mathcal{N}(5\omega_0) \mathcal{N}^5(\omega_0)} + \frac{3b^2}{\mathcal{N}(5\omega_0) \mathcal{N}^2(\omega_0) \mathcal{N}(3\omega_0) \mathcal{N}^3(\omega_0)} \right] \quad (\text{B.16.1})$$

$$\begin{aligned} x_{5,2}(3\omega_0) = & -\frac{e_0^5 E_0^5}{16m^5} \left[ \frac{5c}{\mathcal{N}(3\omega_0) \mathcal{N}^4(\omega_0) \mathcal{N}(-\omega_0)} + \right. \\ & + \frac{3b^2}{\mathcal{N}(3\omega_0) \mathcal{N}^2(\omega_0) \mathcal{N}(\omega_0) \mathcal{N}^2(\omega_0) \mathcal{N}(-\omega_0)} + \\ & \left. + \frac{6b^2}{\mathcal{N}(3\omega_0) \mathcal{N}(\omega_0) \mathcal{N}(-\omega_0) \mathcal{N}(3\omega_0) \mathcal{N}^3(\omega_0)} \right] \end{aligned} \quad (\text{B.16.2})$$

$$\begin{aligned} x_{5,3}(\omega_0) = & -\frac{e_0^5 E_0^5}{16m^5} \left[ \frac{10c}{\mathcal{N}(\omega_0) \mathcal{N}^3(\omega_0) \mathcal{N}^2(-\omega_0)} + \right. \\ & + \frac{3b^2}{\mathcal{N}(\omega_0) \mathcal{N}^2(-\omega_0) \mathcal{N}(3\omega_0) \mathcal{N}^3(\omega_0)} + \\ & \left. + \frac{9b^2}{\mathcal{N}(\omega_0) \mathcal{N}^2(\omega_0) \mathcal{N}(-\omega_0) \mathcal{N}^2(\omega_0) \mathcal{N}(-\omega_0)} \right]. \end{aligned} \quad (\text{B.16.3})$$

The  $c$ -terms in the square brackets reflect nonlinear interactions of the fifth order between the spectral components at the fundamental frequency  $\omega_0$ . The  $b$ -terms then account for two successive third-order interactions which in the end result in the correct frequency. The underlying processes can be identified from the structure of the individual denominators and are summarized in Tab. B1.

Now, we link the displacement amplitudes  $x_\alpha$  with pertinent physical quantities. The linear polarization  $P^{(1)}(\omega_0)$  is directly proportional to the electric field

$$P^{(1)}(\omega_0) = \varepsilon_0 \chi^{(1)}(\omega_0) E_0(\omega_0), \quad (\text{B.17})$$

where  $\chi^{(1)}(\omega_0)$  is the linear susceptibility. At the same time, the linear polarization originates from the electron displacement  $x_1$  and thus reads

$$P^{(1)}(\omega_0) = -Ne_0 x_1(\omega_0), \quad (\text{B.18})$$

where  $N$  is the concentration of atoms. Comparison of (B.17) with (B.18) and subsequent substitution of (B.9) yield

$$\chi^{(1)}(\omega_0) = \frac{Ne_0^2}{\varepsilon_0 m} \frac{1}{\mathcal{N}(\omega_0)}. \quad (\text{B.19})$$

In the third-order nonlinearity, we have to carefully distinguish the processes resulting in frequencies  $3\omega_0$  (i.e. third harmonics generation) and  $\omega_0$ , respectively. We thus identify two contributions to the third-order polarization which satisfy

$$P^{(3)}(3\omega_0) = \varepsilon_0 \chi^{(3)}(\omega_0, \omega_0, \omega_0) E_0^3 = -Ne_0 x_{3,1}(3\omega_0) \quad (\text{B.20.1})$$

$$P^{(3)}(\omega_0) = \varepsilon_0 \chi^{(3)}(\omega_0, -\omega_0, \omega_0) E_0^3 = -Ne_0 x_{3,2}(\omega_0). \quad (\text{B.20.2})$$

The substitution for the displacements then yields the expressions for third-order susceptibilities  $\chi^{(3)}(\omega_0, \omega_0, \omega_0)$  and  $\chi^{(3)}(\omega_0, -\omega_0, \omega_0)$ , respectively

$$\chi^{(3)}(\omega_0, \omega_0, \omega_0) = \frac{Ne_0^4}{\varepsilon_0 m^3} \frac{b}{\mathcal{N}(3\omega_0) \mathcal{N}^3(\omega_0)} \quad (\text{B.21.1})$$

$$\chi^{(3)}(-\omega_0, \omega_0, \omega_0) = \frac{3Ne_0^4}{\varepsilon_0 m^3} \frac{b}{\mathcal{N}(\omega_0) \mathcal{N}^2(\omega_0) \mathcal{N}(-\omega_0)}. \quad (\text{B.21.2})$$

Analogically, the fifth-order polarization contains three spectral components

$$P^{(5)}(5\omega_0) = \varepsilon_0 \chi^{(5)}(\omega_0, \omega_0, \omega_0, \omega_0, \omega_0) E_0^5 = -Ne_0 x_{5,1}(5\omega_0) \quad (\text{B.22.1})$$

$$P^{(5)}(3\omega_0) = \varepsilon_0 \chi^{(5)}(-\omega_0, \omega_0, \omega_0, \omega_0, \omega_0) E_0^5 = -Ne_0 x_{5,2}(3\omega_0) \quad (\text{B.22.2})$$

$$P^{(5)}(\omega_0) = \varepsilon_0 \chi^{(5)}(-\omega_0, -\omega_0, \omega_0, \omega_0, \omega_0) E_0^5 = -Ne_0 x_{5,3}(\omega_0). \quad (\text{B.22.3})$$

The fifth-order susceptibilities then directly stem from the above relations and read

$$\begin{aligned} \chi^{(5)}(\omega_0, \omega_0, \omega_0, \omega_0, \omega_0) = \frac{Ne_0^6}{\varepsilon_0 m^5} & \left[ \frac{c}{\mathcal{N}(5\omega_0) \mathcal{N}^5(\omega_0)} + \right. \\ & \left. + \frac{3b^2}{\mathcal{N}(5\omega_0) \mathcal{N}^2(\omega_0) \mathcal{N}(3\omega_0) \mathcal{N}^3(\omega_0)} \right] \end{aligned} \quad (\text{B.23.1})$$

$$\begin{aligned} \chi^{(5)}(-\omega_0, \omega_0, \omega_0, \omega_0, \omega_0) = \frac{Ne_0^5}{\varepsilon_0 m^5} & \left[ \frac{5c}{\mathcal{N}(3\omega_0) \mathcal{N}^4(\omega_0) \mathcal{N}(-\omega_0)} + \right. \\ & + \frac{3b^2}{\mathcal{N}(3\omega_0) \mathcal{N}^2(\omega_0) \mathcal{N}(\omega_0) \mathcal{N}^2(\omega_0) \mathcal{N}(-\omega_0)} + \\ & \left. + \frac{6b^2}{\mathcal{N}(3\omega_0) \mathcal{N}(\omega_0) \mathcal{N}(-\omega_0) \mathcal{N}(3\omega_0) \mathcal{N}^3(\omega_0)} \right] \end{aligned} \quad (\text{B.23.2})$$

$$\begin{aligned} \chi^{(5)}(-\omega_0, -\omega_0, \omega_0, \omega_0, \omega_0) = & \frac{Ne_0^5}{\varepsilon_0 m^5} \left[ \frac{10c}{\mathcal{N}(\omega_0)\mathcal{N}^3(\omega_0)\mathcal{N}^2(-\omega_0)} + \right. \\ & + \frac{3b^2}{\mathcal{N}(\omega_0)\mathcal{N}^2(-\omega_0)\mathcal{N}(3\omega_0)\mathcal{N}^3(\omega_0)} + \\ & \left. + \frac{9b^2}{\mathcal{N}(\omega_0)\mathcal{N}^2(\omega_0)\mathcal{N}(-\omega_0)\mathcal{N}^2(\omega_0)\mathcal{N}(-\omega_0)} \right] . \end{aligned} \quad (\text{B.23.3})$$

Nonlinear susceptibilities (B.19), (B.21) and (B.23) are further linked with the nonlinear conductivities  $\sigma^{(\alpha)}$ . This relation stems from the equivalence of current density and the time-derivative of the polarization in the Maxwell's equation for the rotation of magnetic field (i.e. Ampère's circuital law) and it reads

$$\chi^{(\alpha)}(\dots) = i \frac{\sigma^{(\alpha)}(\dots)}{\omega_{\text{NL}} \varepsilon_0}, \quad (\text{B.24})$$

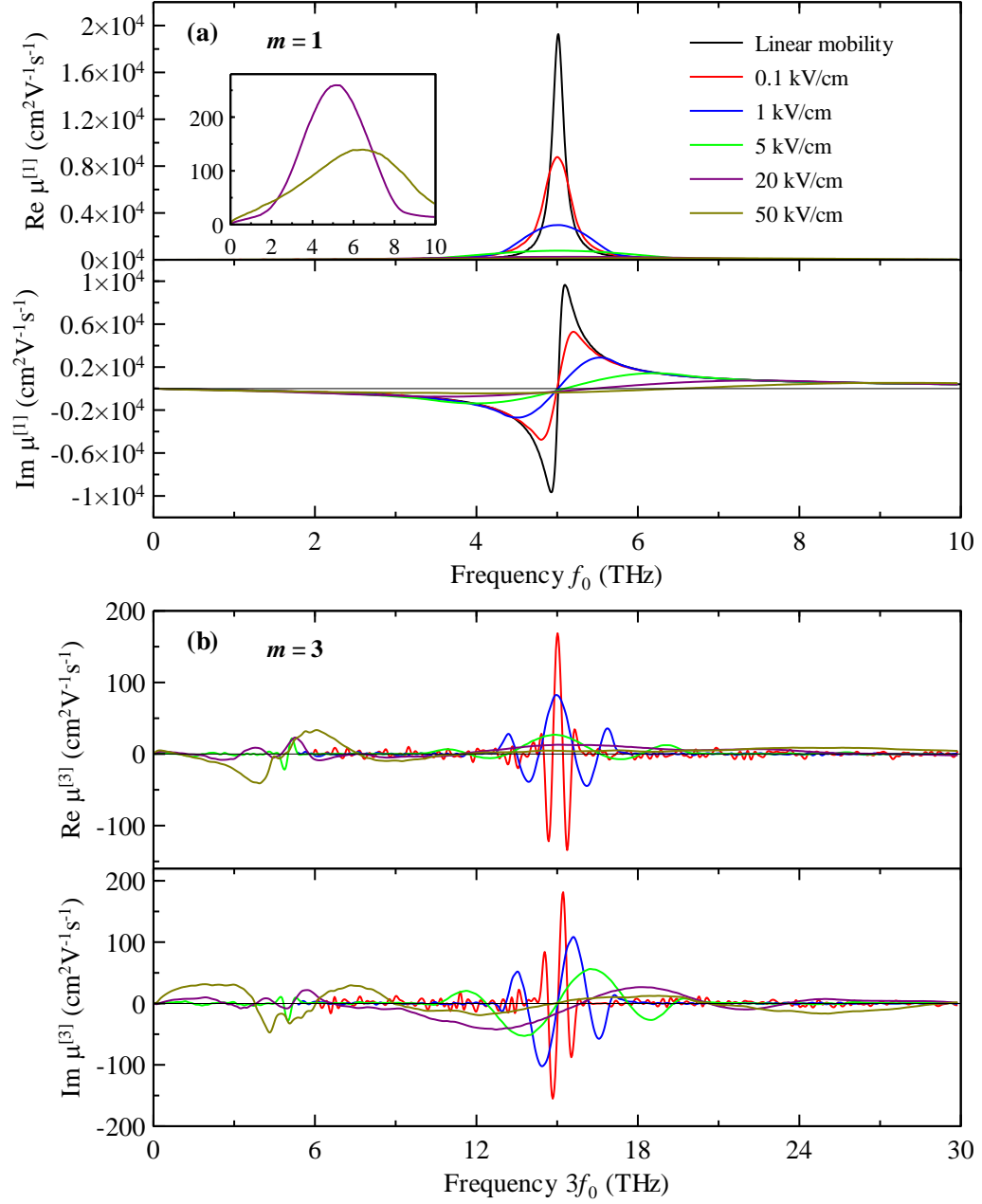
where  $\omega_{\text{NL}}$  is the resulting frequency of the underlying (nonlinear) process. Substitution of Eq. (1.20) from the main text into the above relation then links together the nonlinear susceptibility  $\chi^{(\alpha)}$  and the nonlinear mobility  $\mu^{(\alpha)}$

$$\mu^{(\alpha)}(\dots) = -i\omega_{\text{NL}} \frac{\chi^{(\alpha)}(\dots)}{e_0 N}. \quad (\text{B.25})$$

Substitution of (B.19), (B.21) and (B.23) into (B.25) then yields the relations (6.7) for the mobilities of classical anharmonic oscillator.

### C. Nonlinear response of 1D confined degenerate electron gas

Here, we show the real and imaginary parts of the harmonic mobility  $\mu^{[m]}$  corresponding to the amplitudes shown in Fig. 6.7 in the main text.



... continuation of the Figure is on the next page.

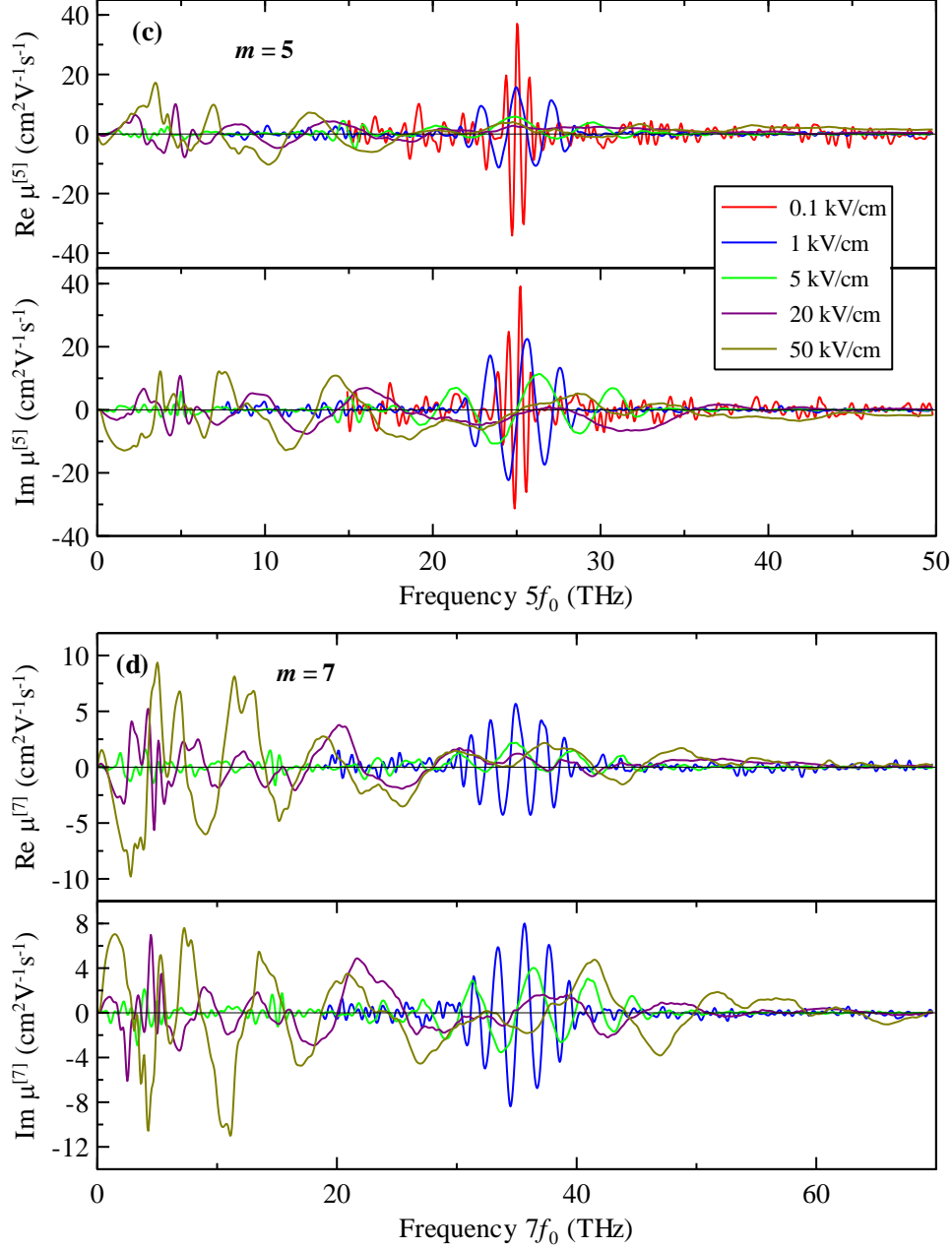


Fig. C1. Real and imaginary parts of the harmonic mobility  $\mu^{[m]}$  obtained by the non-perturbative Monte-Carlo calculations for 1D degenerate electron gas confined in an infinitely deep rectangular potential well and subjected to a monochromatic electric field. The spectra correspond to the amplitudes shown in Fig. 6.7 in the main text. Following parameters were considered in the calculations:  $v_F = 10^6$  m/s,  $E_F = 0.2$  eV,  $T = 4$  K,  $\tau_s = 1$  ps,  $m = 0.07m_e$ ,  $l = 100$  nm.

## D. Nonlinear response of GaAs nanobars under broadband THz pulses

In Fig. D1, we show the real and imaginary parts of the electric current density in GaAs nanobars induced by the broadband high-field THz pulses (Fig. 7.1(a)) with peak amplitude 100 kV/cm. These spectra correspond to the amplitudes shown in Fig. 7.7(a)-(c) in the main text.

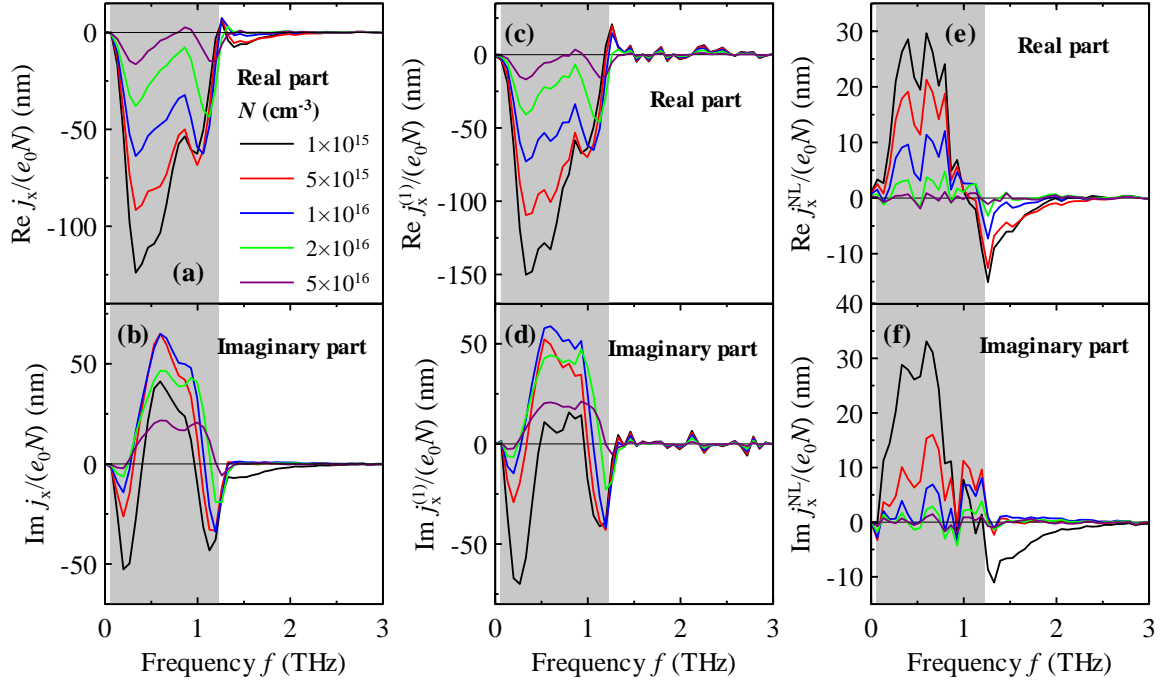


Fig. D1. Real and imaginary parts of the electric current density induced inside GaAs nanobars by the incident THz pulse from Fig. 7.1(a) with peak amplitude of 100 kV/cm for various carrier concentrations  $N$  calculated using the non-perturbative Monte-Carlo calculations. Clear departure from the linear response  $j_x^{(1)}$  and presence of tail in the nonlinear component  $j_x^{NL}$  above incident frequencies (gray areas) are observed for  $N \leq 10^{16} \text{ cm}^{-3}$ . For the linear component  $j_x^{(1)}$ , the data above the incident frequencies are just a noise originating from the calculations. The corresponding amplitudes are shown in Fig. 7.7 in the main text. We note, that the normalized electric current density  $j_x/(e_0 N)$  represents the velocity of carriers. The Fourier transform then reduces the unit of velocity from meters per second just to meters.

## E. Nonlinear response of GaAs nanowires under broadband THz pulses

In Fig. E1, we show the real and imaginary parts of the electric current density in GaAs nanowires induced by the high-field broadband THz pulses (Fig. 7.1(a)) with peak amplitude 100 kV/cm. These spectra correspond to the amplitudes shown in Fig. 7.7(d)-(f) in the main text.

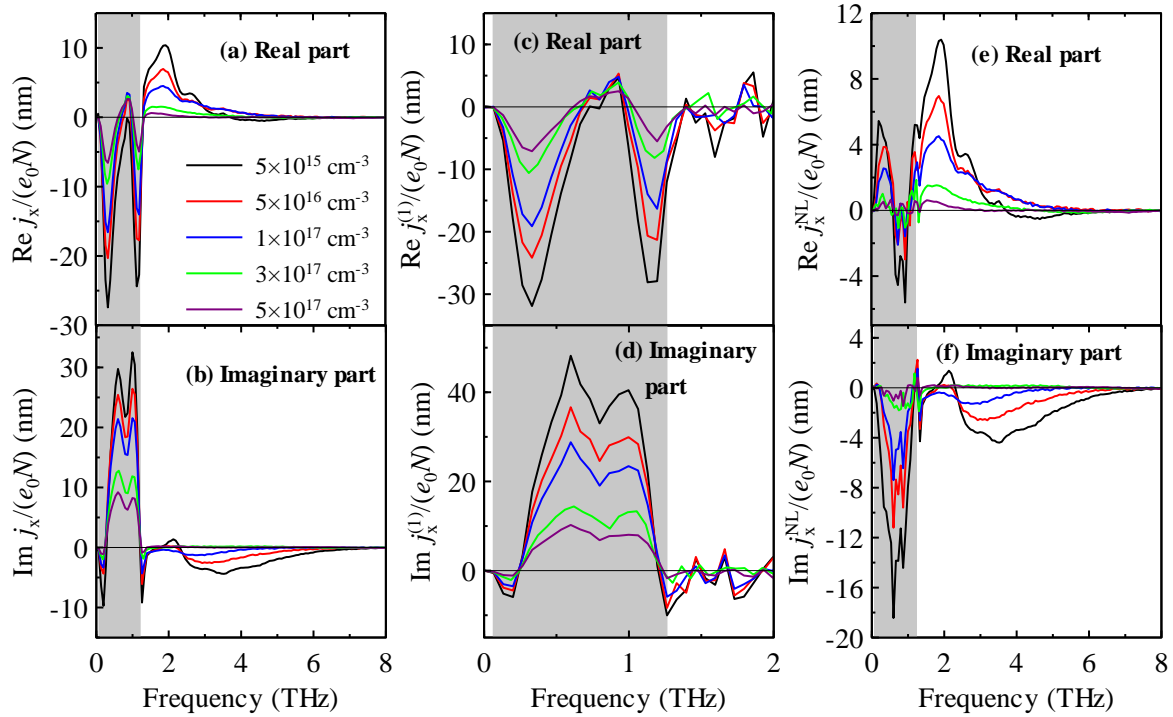


Fig. E1. Real and imaginary parts of the electric current density induced inside GaAs nanowires by the incident THz pulse from Fig. 7.1(a) with peak amplitude of 100 kV/cm for various carrier concentrations  $N$  calculated using the non-perturbative Monte-Carlo calculations. Clear departure from the linear response  $j_x^{(1)}$  and presence of tail in the nonlinear component  $j_x^{NL}$  above incident frequencies (gray areas) are observed for  $N \leq 3 \times 10^{17} \text{ cm}^{-3}$ . For the linear component  $j_x^{(1)}$ , the data above the incident frequencies are just a noise originating from the calculations. The corresponding amplitudes are shown in Fig. 7.7 in the main text. We note, that the normalized electric current density  $j_x/(e_0 N)$  represents the velocity of carriers. The Fourier transform then reduces the unit of velocity from meters per second just to meters.



## References

- [1] B. O'Regan and M. Grätzel, *Nature* **353**, 737 (1991).
- [2] P. Kužel and H. Němec, *Adv. Opt. Mater.* **7**, 1900623 (2019).
- [3] C. A. Schmuttenmaer, *Chem. Rev.* **104**, 1759 (2004).
- [4] P. U. Jepsen, D. G. Cooke, and M. Koch, *Laser Photonics Rev.* **5**, 1 (2011).
- [5] R. Ulbricht, E. Hendry, J. Shan, T. F. Heinz, and M. Bonn, *Rev. Mod. Phys.* **83**, 543 (2011).
- [6] J. Hebling, G. Almasi, I. Kozma, and J. Kuhl, *Opt. Express* **10**, 1161 (2002).
- [7] K.-L. Yeh, M. C. Hoffmann, J. Hebling, and K. A. Nelson, *Appl. Phys. Lett.* **90**, 171121 (2007).
- [8] J. Hebling, K.-L. Yeh, M. C. Hoffmann, B. Bartal, and K. A. Nelson, *J. Opt. Soc. Am. B* **25**, B6 (2008).
- [9] D. J. Cook, and R. M. Hochstrasser, *Opt. Lett.* **25**, 1210 (2000).
- [10] M. Kress, T. Löffler, S. Eden, M. Thomson, and H. G. Roskos, *Opt. Lett.* **29**, 1120 (2004).
- [11] T. Bartel, P. Gaal, K. Reimann, M. Woerner, and T. Elsaesser, *Opt. Lett.* **30**, 2805 (2005).
- [12] H. Zhong, N. Karpowicz, and X.-C. Zhang, *Appl. Phys. Lett.* **88**, 261103 (2006).
- [13] M. D. Thomson, M. Kress, T. Löffler, and H. G. Roskos, *Laser & Photon. Rev.* **1**, 349 (2007).
- [14] H. Hirori, A. Doi, F. Blanchard, and K. Tanaka, *Appl. Phys. Lett.* **98**, 091106 (2011).
- [15] S. Khan, *J. Mod. Opt.* **55**, 3469 (2008).
- [16] B. N. Murdin, *Contemp. Phys.* **50**, 391 (2009).
- [17] G. R. Neil, *J. Infrared Milli. Terahz. Waves* **35**, 5 (2014).
- [18] F. H. Su, F. Blanchard, G. Sharma, L. Razzari, A. Ayesheshim, T. L. Cocker, L. V. Titova, T. Ozaki, J.-C. Kieffer, R. Morandotti, M. Reid, and F. A. Hegmann, *Opt. Express* **17**, 9620 (2009).
- [19] M. C. Hoffmann, J. Hebling, H. Y. Kwang, K.-L. Yeh, and K. A. Nelson, *J. Opt. Soc. Am. B* **26**, 9 (2009).
- [20] J. Hebling, M. C. Hoffmann, H. Y. Hwang, K.-L. Yeh, and K. A. Nelson, *Phys. Rev. B* **81**, 035201 (2010).
- [21] W. Kuehn, P. Gaal, K. Reimann, M. Woerner, T. Elsaesser, and R. Hey, *Phys. Rev. Lett.* **104**, 146602 (2010).
- [22] P. Bownan, W. Kuehn, K. Reimann, M. Woerner, T. Elsaesser, R. Hey, and C. Flytzanis, *Phys. Rev. Lett.* **107**, 256602 (2011).
- [23] X. Chai, X. Ropagnol, S. M. Racis-Zadeh, M. Reid, S. Safavi-Nacini, and T. Ozaki, *Phys. Rev. Lett.* **121**, 143901 (2018).
- [24] O. Schubert, M. Hohenleutner, F. Langer, B. Urbanek, C. Lange, U. Huttner, D. Golde, T. Meier, M. Kira, S. W. Koch, and, R. Huber, *Nature Photonics* **8**, 119 (2014).
- [25] M. C. Hoffmann, B. S. Monozon, D. Livshits, E. U. Rafailov, and D. Turchinovich, *Appl. Phys. Lett.* **97**, 231108 (2010).

- [26] J. R. Danielson, Y.-S. Lee, J. P. Prineas, J. T. Steiner, M. Kira, and S. W. Koch, *Phys. Rev. Lett.* **99**, 237401 (2007).
- [27] H. Němec, P. Kužel, and V. Sundström, *Phys. Rev. B* **79**, 115309 (2009).
- [28] R. W. Boyd, *Nonlinear Optics*, Academic Press (2008).
- [29] T. L. Cocker, D. Baillie, M. Buruma, L. V. Titova, R. D. Sydora, F. Marsiglio, and F. A. Hegmann, *Phys. Rev. B* **96**, 205439 (2017).
- [30] R. Kubo, *J. Phys. Soc. Jpn.* **12**, 570 (1957).
- [31] R. P. Budoyo, *Conductance of Mesoscopic Rings*, Thesis, Wesleyan University, Middletown, USA (2008).
- [32] H.-K. Nienhuys and V. Sundström, *Appl. Phys. Lett.* **87**, 012101 (2005).
- [33] H. J. Joyce, C. J. Doherty, Q. Gao, H. H. Toe, C. Jagadish, J. Lloyd-Hughes, L. M. Herz, and M. B. Johnston, *Nanotechnology* **24**, 214006 (2013).
- [34] P. Kužel and H. Němec, *J. Phys. D: Appl. Phys.* **47**, 374005 (2014).
- [35] D. J. Bergman and D. Stroud, *Solid State Phys.* **46**, 147 (1992).
- [36] I. Rychetský and J. Petzelt, *Ferroelectrics* **303**, 5222 (2004).
- [37] H. Němec, V. Zajac, I. Rychetský, D. Fattakhova-Rohlfing, B. Mandlmeier, T. Bein, Z. Mics, and P. Kužel, *IEEE T. THz. Science Technol.* **3**, 302 (2013).
- [38] K. Ghosh and R. Fuchs, *Phys. Rev. B* **38**, 137 (1988).
- [39] J. Sturm, P. Grosse, and W. Theiss, *Z. Phys. B: Condens. Matter* **83**, 361 (1991).
- [40] R. Stognienko, T. Henning, and V. Ossenkopf, *Astron. Astrophys.* **296**, 797 (1995).
- [41] C. Pecharromán and F. J. Gordillo-Vázquez, *Phys. Rev. B* **74**, 035120 (2006).
- [42] J. Kuchařík, H. Sopha, M. Krbal, I. Rychetský, P. Kužel, J. M. Macák, and H. Němec, *J. Phys. D: Appl. Phys.* **51**, 014004 (2018).
- [43] J. C. M. Garnett, *Philos. Trans. R. Soc. London A* **203**, 385 (1904).
- [44] J. C. M. Garnett, *Philos. Trans. R. Soc. London* **205**, 237 (1906).
- [45] V. A. Markel, *J. Opt. Soc. Am. A* **33**, 1244 (2016).
- [46] C. Kadlec, F. Kadlec, P. Kužel, K. Blary and P. Mounaix, *Opt. Lett.* **33**, 2275 (2008).
- [47] V. Skoromets, H. Němec, V. Goian, S. Kamba, and P. Kužel, *J. Infrared Milli. Terahz. Waves* **39**, 1249 (2018).
- [48] P. Kužel, F. Kadlec, and H. Němec, *J. Chem. Phys.* **127**, 024506 (2007).
- [49] H. Němec, F. Kadlec, and P. Kužel, *J. Chem. Phys.* **117**, 8454 (2002).
- [50] D. You and P. H. Bucksbaum, *J. Opt. Soc. Am. B* **14**, 1651 (1997).
- [51] P. Kužel, M. A. Khazan, and J. Kroupa, *J. Opt. Soc. Am. B* **16**, 1795 (1999).
- [52] G. Gallot and D. Grischkowsky, *J. Opt. Soc. Am. B* **16**, 1204 (1999).
- [53] H. J. Bakker, G. C. Cho, H. Kurz, Q. Wu, and X.-C. Zhang, *J. Opt. Soc. Am. B* **15**, 1795 (1998).
- [54] P. Tiwana, P. Parkinson, M. B. Johnston, H. J. Snaith, and L. M. Herz, *J. Phys. Chem. C* **114**, 1365 (2010).
- [55] E. Hendry, M. Koeberg, J. Pijpers, and M. Bonn, *Phys. Rev. B* **75**, 233202 (2007).
- [56] V. Zajac, H. Němec, C. Kadlec, K. Kůsová, I. Pelant and P. Kužel, *New. J. Phys.* **16**, 093013 (2014).
- [57] C. Richter and C. A. Schmuttenmaer, *Nature Nanotechnology* **5**, 769 (2010).

- [58] L. Duvillaret, F. Garet, and J.-L. Coutaz, *IEEE J. Sel. Top. Quantum Electron.* **2**, 739 (1996).
- [59] M. Abramowitz and I. A. Stegun, *Handbook of Mathematical Functions: With Formulas, Graphs, and Mathematical Tables*, 10th edition, Dover Publications, New York (1964).
- [60] X. C. Zeng, D. J. Bergman, P. M. Hui, and D. Stroud, *Phys. Rev. B* **38**, 10970(R) (1988).
- [61] J. E. Sipe and R. W. Boyd, *Phys. Rev. A* **46**, 1614 (1992).
- [62] P. M. Hui and D. Stroud, *J. Appl. Phys.* **82**, 4740 (1997).
- [63] P. M. Hui, P. Cheung, and D. Stroud, *J. Appl. Phys.* **84**, 3451 (1998).
- [64] O. Levy and D. J. Bergman, *Phys. Rev. B* **46**, 7189 (1992).
- [65] H. Němec, F. Kadlec, C. Kadlec, P. Kužel, and P. Jungwirth, *J. Chem. Phys.* **122**, 104504 (2005).
- [66] Q. Wu and X.-C. Zhang, *Appl. Phys. Lett.* **70**, 1784 (1997).
- [67] J. C. Dyre, *J. Appl. Phys.* **64**, 2465 (1988).
- [68] P. Drude, *Ann. Phys.* **306**, 566 (1900).
- [69] P. Drude, *Ann. Phys.* **308**, 369 (1900).
- [70] N. V. Smith, *Phys. Rev. B* **64**, 155106 (2001).
- [71] Z. Mics, *Dynamics of delocalized states in molecular systems studied by time-resolved THz spectroscopy*, Doctoral thesis, Charles University in Prague (2012).
- [72] T. Ostatnický, V. Pushkarev, H. Němec, and P. Kužel, *Phys. Rev. B* **97**, 085426 (2018).
- [73] T. Ostatnický, *Opt. Express* **27**, 6083 (2019).
- [74] M. C. Beard, G. M. Turner, and C. A. Schmuttenmaer, *Nano Lett.* **2**, 543 (2002).
- [75] D. G. Cooke, A. Meldrum, and P. U. Jepsen, *Appl. Phys. Lett.* **101**, 211107 (2012).
- [76] F. A. Hegmann, O. Ostroverkhova, and D. G. Cooke, in *Photophysics of Molecular Materials*, edited by G. Lanzani, Wiley-VCH, Weinheim (2006).
- [77] P. Parkinson, J. Lloyd-Hughes, Q. Gao, H. H. Tan, C. Jagadish, M. B. Johnston, and L. M. Hertz., *Nano Lett.* **7**, 2162 (2007).
- [78] J. Lloyd-Hughes, S. K. E. Merchant, L. Sirbu, I. M. Tiginyanu, and M. B. Johnston, *Phys. Rev. B* **78**, 085320 (2008).
- [79] H. Němec, V. Zajac, P. Kužel, P. Malý, S. Gutsch, D. Hiller, and M. Zacharias, *Phys. Rev. B* **91**, 195443 (2015).
- [80] H. J. Joyce, J. L. Boland, C. L. Davies, S. A. Baig, and M. B. Johnston, *Semicond. Sci. Technol.* **31**, 103003 (2016).
- [81] V. Pushkarev, T. Ostatnický, H. Němec, T. Chlouba, F. Trojánek, P. Malý, M. Zacharias, S. Gutsch, D. Hiller, and P. Kužel, *Phys. Rev. B* **95**, 125424 (2017).
- [82] J. Lloyd-Hughes and T.-I. Jeon, *J. Infrared Milli. Terahz. Waves* **33**, 871 (2012).
- [83] J. Kuchařík, H. Němec, and T. Ostatnický, *Phys. Rev. B* **99**, 035407 (2019).
- [84] J. Kuchařík and H. Němec, *Proc. SPIE.* **10756**, 107560A (2018).
- [85] G. M. Turner, M. C. Beard, and C. Schmuttenmaer, *J. Phys. Chem. B* **106**, 11716 (2002).
- [86] X. Ai, M. C. Beard, K. P. Knutsen, S. E. Shaheen, G. Rumbles, and R. J. Ellingson, *J. Phys. Chem. B* **110**, 25462 (2006).

- [87] N. W. Ashcroft and N. D. Mermin, *Solid State Physics*, Holt, Rinehart and Winston, New York (1988).
- [88] C. M. Wolfe, G. E. Stillman, and T. L. Lindley, *J. Appl. Phys.* **41**, 3088 (1970).
- [89] M. Wilkinson and E. J. Austin, *J. Phys.: Condens. Matter.* **6**, 4153 (1994).
- [90] B. Mehlig and K. Richter, *Phys. Rev. Lett.* **80**, 1936 (1998).
- [91] L. Nádvorník, M. Orlita, N. A. Goncharuk, L. Smrčka, V. Novák, V. Jurka, K. Hruška, Z. Výborný, Z. R. Wasilewski, M. Potemski and K. Výborný, *New. J. Phys.* **14**, 053002 (2012).
- [92] C. S. Ponseca, Jr., H. Němec, J. Wallentin, N. Anttu, J. P. Beech, A. Iqbal, M. Borgström, M.-E. Pistol, and A. Yartsev, *Phys. Rev. B* **90**, 085405 (2014).
- [93] L. A. Bunimovich, *Sov. Phys. JETP* **62**, 842 (1985).
- [94] C. P. Dettmann, *Commun. Theor. Phys.* **62**, 521 (2014).
- [95] H. A. Lorentz, *The Motion of Electrons in Metallic Bodies*, in KNAW, Proceedings, Amsterdam **7**, 438 (1905).
- [96] P. Gaal, W. Kuehn, K. Reimann, M. Woerner, T. Elsaesser, and R. Hey, *Nature* **450**, 1120 (2007).
- [97] P. Gaal, K. Reimann, M. Woerner, T. Elsaesser, R. Hey, and K. H. Ploog, *Phys. Rev. Lett.* **96**, 187402 (2006).
- [98] W. Kuehn, P. Gaal, K. Reimann, M. Woerner, T. Elsaesser, and R. Hey, *Phys. Rev. B* **82**, 075204 (2010).
- [99] P. B. Corkum, *Phys. Rev. Lett.* **71**, 1994 (1993).
- [100] D. C. Hutchings, M. Sheik-Bahae, D. J. Hagan, and E. W. van Stryland, *Opt. Quant. Electron.* **24**, 1 (1992).
- [101] J. Hebling, A. G. Stepanov, G. Almási, B. Bartal, and, J. Kuhl, *Appl. Phys. B* **78**, 593 (2004).
- [102] M. C. Hoffmann, K.-L. Yeh, H. Y. Hwang, T. S. Sosnowski, B. S. Prall, J. Hebling, and K. A. Nelson, *Appl. Phys. Lett.* **93**, 141107 (2008).
- [103] M. C. Hoffmann, K.-L. Yeh, J. Hebling, and K. A. Nelson, *Opt. Express* **15**, 11706 (2007).
- [104] K.-L. Yeh, J. Hebling, M. C. Hoffmann, and K. A. Nelson, *Opt. Commun.* **281**, 3567 (2008).
- [105] Z. Mics, K.-J. Tielrooij, K. Parvez, S. A. Jensen, I. Ivanov, X. Feng, K. Müllen, M. Bonn, and D. Turchinovich, *Nat. Commun.* **6**, 7655 (2015).
- [106] P. Michel, F. Gabriel, E. Grosse, P. Evtushenko, T. Dekorsy, M. Krenz, M. Helm, U. Lehnert, W. Seidel, R. Wünsch, D. Wohlfarth, and A. Wolf, *Proceedings of the 26th International FEL conference*, 8 (Trieste, Italy, 2004).
- [107] W. Seidel, E. Cizmar, O. Drachenko, M. Helm, M. Justus, U. Lehnert, P. Michel, M. Ozerov, H. Schneider, R. Schurig, D. Stehr, M. Wagner, S. Winnerl, D. Wohlfarth, S. Zvyagin, S. C. Kehr, and L. M. Eng, *Proceedings of the 30th International FEL conference*, 382 (Gyeongju, Korea, 2008).
- [108] S. A. Zvyagin, M. Ozerov, E. Čížmář, D. Kamenskyi, S. Zherlitsyn, T. Herrmannsdörfer, J. Wosnitza, R. Wünsch, and W. Seidel, *Rev. Sci. Instrum* **80**, 073102 (2009).

- [109] *Laser power expected for the ELBE FELs*, retrieved December 12, 2018, from <https://www.hzdr.de/db/Cms?pOid=10502&pNid=205>.
- [110] O. Taratula, E. Galoppini, D. Wang, D. Chu, Z. Zhang, H. Chen, G. Saraf, and Y. Lu, *J. Phys. Chem. B* **110**, 6506 (2006).
- [111] Z. Mics, H. Němec, I. Rychetský, P. Kužel, P. Formánek, P. Malý, and P. Němec, *Phys. Rev. B* **83**, 155326 (2011).
- [112] P. Němec, I. Němec, P. Nahálková, K. Knížek, and P. Malý, *J. Cryst. Growth* **240**, 484 (2002).
- [113] H. Němec, I. Kratochvílová, P. Kužel, J. Šebera, A. Kochalska, J. Nožár, and S. Nešpůrek, *Phys. Chem. Chem. Phys.* **13**, 2850 (2011).
- [114] M. Tinkham, *Phys. Rev.* **104**, 845 (1956).
- [115] M. Walther, D. G. Cooke, C. Sherstan, H. Hajar, M. R. Freeman, and F. A. Hegmann, *Phys. Rev. B* **76**, 125408 (2007).
- [116] M. Wagner, H. Schneider, D. Stehr, S. Winnerl, A. M. Andrews, S. Schartner, G. Strasser, and M. Helm, *Phys. Rev. Lett.* **105**, 167401 (2010).
- [117] M. Beck, I. Rousseau, M. Klammer, P. Leiderer, M. Mittendorff, S. Winnerl, M. Helm, G. N. Gol'tsman, and J. Demsar, *Phys. Rev. Lett.* **110**, 267003 (2013).
- [118] J. C. König-Otto, M. Mittendorff, T. Winzer, F. Kadi, E. Malic, A. Knorr, C. Berger, W. A. de Heer, A. Pashkin, H. Schneider, M. Helm, and S. Winnerl, *Phys. Rev. Lett.* **117**, 087401 (2016).
- [119] N. Deßmann, S. G. Pavlov, V. V. Tsyplenkov, E. E. Orlova, A. Pohl, V. N. Shastin, R. Kh. Zhukavin, S. Winnerl, M. Mittendorff, J. M. Klopff, N. V. Abrosimov, H. Schneider, and H.-W. Hübers, *Phys. Status Solidi B* **254**, 1600803 (2017).
- [120] B. Piętka, N. Bobrovska, D. Stephan, M. Teich, M. Król, S. Winnerl, A. Pashkin, R. Mirek, K. Lekenta, F. Morier-Genoud, H. Schneider, B. Deveaud, M. Helm, M. Matuszewski, and J. Szczytko, *Phys. Rev. Lett.* **119**, 077403 (2017).
- [121] A. Podzorov and G. Gallot, *Chem. Phys. Lett.* **495**, 46 (2010).
- [122] F. D'Angelo, H. Němec, S. H. Parekh, P. Kužel, M. Bonn, and D. Turchinovich, *Opt. Exp.* **24**, 10157 (2016).
- [123] M. C. Beard, G. M. Turner, C. A. Schmuttenmaer, *Phys. Rev. B* **62**, 15764 (2000).
- [124] H. Merbold, A. Bitzer, and T. Feurer, *Opt. Express* **19**, 7262 (2011).
- [125] A. Novitsky, A. M. Ivinskaya, M. Zalkovskij, R. Malureanu, P. U. Jepsen, and A. V. Lavrinenko, *J. Appl. Phys.* **112**, 074318 (2012).
- [126] M. Shalaby, J. Fabiańska, M. Peccianti, Y. Ozturk, F. Vidal, H. Sigg, R. Morandotti, and T. Feurer, *Appl. Phys. Lett.* **104**, 171115 (2014).
- [127] D. Gall, *J. Appl. Phys.* **119**, 085101 (2016).
- [128] P. Malý, *Optika*, Univerzita Karlova v Praze, Nakladatelství Karolinum (2008).
- [129] J. J. Wynne, *Phys. Rev.* **178**, 1295 (1969).
- [130] H. A. Hafez, S. Kovalev, J.-C. Deinert, Z. Mics, B. Green, N. Awari, M. Chen, S. Germanskiy, U. Lehnert, J. Teichert, Z. Wang, K.-J. Tielrooij, Z. Liu, Z. Chen, A. Narita, K. Müllen, M. Bonn, M. Gensch, and D. Turchinovich, *Nature* **561**, 507 (2018).

- [131] X. Chen and A. Selloni (eds), *Special issue on titanium dioxide nanomaterials*, *Chem. Rev.* **114**, 9281 (2014).
- [132] A. L. Linsebigler, L. Guanguan, and T. J. Yates, *Chem. Rev.* **95**, 735 (1995).
- [133] A. Fujishima, T. N. Rao, and D. A. Tryk, *J. Photochem. Photobiol. C* **1**, 1 (2000).
- [134] K. Kalyanasundaram and M. Grätzel, *Coord. Chem. Rev.* **77**, 347 (1998).
- [135] B. E. Hardin, H. J. Snaith, and M. D. McGehee, *Nat. Photonics*. **6**, 162 (2012).
- [136] I. Robel, V. Subramanian, M. Kuno, and P. V. Kamat, *J. Am. Chem. Soc.* **128**, 2385 (2006).
- [137] J. M. Macák, H. Tsuchiya, A. Ghicov, K. Yasuda, R. Hahn, S. Bauer and P. Schmuki, *Curr. Opin. Solid State Mater. Sci.* **11**, 3 (2007).
- [138] K. Lee, A. Mazare, and P. Schmuki, *Chem. Rev.* **114**, 9385 (2014).
- [139] K. Zhu, N. Neale, A. Miedaner, and A. Frank, *Nano. Lett.* **7**, 69 (2007).
- [140] S. So, I. Hwang, and P. Schmuki, *Energy Environ. Sci.* **8**, 849 (2015).
- [141] F. Mohammadpour, M. Moradi, K. Lee, G. Cha, S. So, A. Kahnt, D. M. Guldi, M. Altomare, and P. Schmuki, *Chem. Commun.* **15**, 1631 (2015).
- [142] X. Gao, J. Li, J. Baker, Y. Hou, D. Guan, J. Chen, and C. Yuan, *Chem. Commun.* **50**, 6368 (2014).
- [143] X. Wang, Z. Li, W. Xu, S. A. Kulkarni, S. K. Batabyal, S. Zhang, A. Cao, and L. H. Wong, *Nano Energy* **11**, 728 (2015).
- [144] R. Salazar, M. Altomare, K. Lee, J. Tripathy, R. Kirchgeorg, N. T. Nguyen, M. Mokhtar, A. Alshehri, S. A. Al-Thabaiti, and P. Schmuki, *Chem. Electro. Chem.* **2**, 824 (2015).
- [145] J. M. Macák, H. Tsuchiya, and P. Schmuki, *Angew. Chem. Int. Ed.* **44**, 2100 (2005).
- [146] J. M. Macák and P. Schmuki, *Electrochim. Acta* **52**, 1258 (2006).
- [147] J. M. Macák, S. Aldabergerova, A. Ghicov, and P. Schmuki, *Phys. Status Solidi A* **203**, R67 (2006).
- [148] H. Sopha, A. Jäger, P. Knotek, K. Tesař, M. Jarošová, and J. M. Macák, *Electrochim. Acta* **190**, 744 (2016).
- [149] H. Sopha, M. Krbal, S. Ng, J. Přikryl, R. Zazpe, F. K. Yam, and J. M. Macák, *Appl. Mater. Today* **9**, 104 (2017).
- [150] H. Sopha, L. Hromadko, K. Nechvilova, and J. M. Macák, *J. Electroanal. Chem.* **759**, 122 (2015).
- [151] C. Wehrenfennig, C. M. Palumbiny, H. J. Snaith, M. B. Johnston, L. Schmidt-Mende, and L. M. Herz, *J. Phys. Chem. C* **119**, 9159 (2015).
- [152] M. Krbal, J. Kuchařík, H. Sopha, H. Němec, and J. M. Macák, *Phys. Status Solidi Rapid Res. Lett.* **10**, 691 (2016).
- [153] A. Nahata, A. S. Weling, and T. F. Heinz, *Appl. Phys. Lett.* **69**, 2321 (1996).
- [154] H. Němec, P. Kužel, and V. Sundström, *J. Photochem. Photobiol. A* **215**, 123 (2010).
- [155] H. Tang, H. Berger, P. E. Schmid, F. Lévy, and G. Burri, *Solid State Commun.* **87**, 847 (1993).
- [156] R. J. Gonzalez, R. Zallen, and H. Berger, *Phys. Rev. B* **55**, 7014 (1997).
- [157] G. E. Jellison, L. A. Boatner, J. D. Budai, B.-S. Jeong, and D. P. Norton, *J. Appl. Phys.* **93**, 9537 (2003).

- [158] T. Luttrell, S. Halpegamage, J. Tao, A. Kramer, E. Sutter, and M. Batzill, *Sci. Rep.* **4**, 4043 (2014).
- [159] Y. Furubayashi, N. Yamada, Y. Hirose, Y. Yamamoto, M. Otani, T. Hitosugi, T. Shimada, and T. Hasegawa, *J. Appl. Phys.* **101**, 093705 (2007).
- [160] M. Dou and C. Persson, *J. Appl. Phys.* **113**, 083703 (2013).
- [161] B. Enright and D. Fitzmaurice, *J. Phys. Chem.* **100**, 1027 (1996).
- [162] C. Kormann, D. W. Bahnemann, and M. R. Hoffmann, *J. Phys. Chem.* **92**, 5196 (1988).
- [163] M. Anpo, K. Chiba, M. Tomonari, S. Coluccia, M. Che, and M. A. Fox, *Bull. Chem. Soc. Japan* **64**, 543 (1991).
- [164] L. Forro, O. Chauvet, D. Emin, L. Zuppiroli, H. Berger, and F. Lévy, *J. Appl. Phys.* **75**, 633 (1994).
- [165] S. A. Jensen, K.-J. Tielrooij, E. Hendry, M. Bonn, I. Rychetský, and H. Němec, *J. Phys. Chem. C* **118**, 1191 (2014).
- [166] Y. Furubayashi, T. Hitosugi, Y. Yamamoto, K. Inaba, G. Kinoda, Y. Hirose, T. Shimada, and T. Hasegawa, *Appl. Phys. Lett.* **86**, 252101 (1994).

## List of publications

- 1) M. Krbal, J. Kuchařík, H. Sopha, H. Němec, and J. M. Macák, *Charge transport in anodic TiO<sub>2</sub> nanotubes studied by terahertz spectroscopy*, Phys. Status Solidi Rapid Res. Lett. **10**, 691 (2016).
- 2) J. Kuchařík, H. Sopha, M. Krbal, I. Rychetský, P. Kužel, J. M. Macák, and H. Němec, *Photoconductive, dielectric and percolation properties of anodic TiO<sub>2</sub> nanotubes studied by terahertz spectroscopy*, J. Phys. D: Appl. Phys. **51**, 014004 (2018).
- 3) J. Kuchařík and H. Němec, *Terahertz conductivity of degenerate electron gas confined in 2D model nanostructures*, Proc. SPIE. **10756**, 107560A (2018).
- 4) J. Kuchařík, H. Němec, and T. Ostatnický, *Terahertz conductivity and coupling between geometrical and plasmonic resonances in nanostructures*, Phys. Rev. B **99**, 035407 (2019).
- 5) J. Kuchařík and H. Němec, *Strong confinement-induced nonlinear terahertz response in semiconductor nanostructures revealed by Monte-Carlo calculations*, submitted to Phys. Rev. Lett.



# List of symbols

## A. Latin symbols

$a$	.....	in Section 3.2: coefficient describing multiple internal reflections of the THz wave in a sample, defined by Eq. (3.18)
	.....	in Section 5.4: period of a curvature for periodically perturbed boundaries
	.....	in Section 5.4: period of a hexagonal Lorentz gas potential
	.....	in Section 8: size of cubic nanoregions which form a nanotube wall
$A_{\text{inc}}$	.....	peak spectral amplitude of the FELBE pulses incident on a structure
$A_{\text{p}}, A_{\text{peak}}$	.....	peak spectral amplitude of the FELBE pulses
$b$	.....	parameter characterizing anharmonicity of binding potential
$B$	.....	weight of non-percolated parts in the VBD model of effective medium
	.....	for two-component systems
$c$	.....	in Section 5.1: parameter describing the localization of charges in Drude-Smith model
	.....	in Section 6.1.4 and Appendix B: parameter characterizing anharmonicity of binding potential
	.....	elsewhere: speed of light ( $c = 2.998 \times 10^8$ m/s)
$C, C_{\text{h}}, C_{\text{p}}$	.....	capacitances of capacitors used for the derivation of brick-wall effective medium model
$d$	.....	inner diameter of a nanotube wall
$d_{\text{h}}$	.....	width of the insulating block in two-component system consisting of periodically alternating conductive and insulating blocks
$d_{\text{p}}$	.....	width of the conducting block in two-component system consisting of periodically alternating conductive and insulating blocks
$D$	.....	in Sections 2 and 5: dimension
	.....	elsewhere: morphologic parameter of the VBD model of effective medium linked directly to a dominant depolarization factor
$\mathcal{D}(\omega)$	.....	instrumental function describing the detector response
$D_{\text{diff}}$	.....	diffusion constant
$\vec{e}$	.....	unit vector pointing in a direction of probing electric field
$e_0$	.....	elementary charge
$E$	.....	in Sections 2.1, 5.2: energy
	.....	elsewhere: THz electric field in a sample/slab
$E_{\text{i}}$	.....	in Section 5.2: energy of state $i$
$E_{\text{eff}}$	.....	effective THz electric field in an inhomogeneous sample
$E_{\text{F}}$	.....	Fermi energy
$E_{\text{h}}$	.....	local THz electric field in insulating parts (matrix) of a two-component system
$E_{\text{inc}}$	.....	THz electric field incident on a sample
$E_{\text{p}}$	.....	local electric field in photoconductive constituents of a two-component system

$E_{p,0}$	.....	local monochromatic electric field in photoconductive constituents of a two-component system
$E_R$	.....	THz electric field reflected from a sample in equilibrium
$E_s$	.....	THz electric field propagating through a sample/slab in equilibrium
$E_T$	.....	THz electric field transmitted through a sample in equilibrium
$E_T(\sigma)$	.....	THz electric field transmitted through a sample with conductivity $\sigma$
$E(t)$	.....	time-varying THz electric field
$E(\omega)$	.....	complex spectrum of the THz electric field
$E_{\text{peak}}$	.....	peak electric field of the FELBE pulses
$E_\alpha$	.....	in Section 2.1: energy of state $\alpha$
$E_0$	.....	in Section 7.1-7.4: peak electric field amplitude of of FELBE pulses
	.....	elsewhere: amplitude of a monochromatic THz electric field
$E_e^{\text{kin}}$	.....	kinetic energy of the electrons at the FELBE facility
$\Delta E$	.....	THz electric field induced in a photoexcited sample/slab
$\Delta E^{(1)}$	.....	linear component of the transient THz electric field leaving the output surface of a sample
$\Delta E^{\text{NL}}$	.....	nonlinear component of the transient THz electric field leaving the output surface of a sample
$\Delta E_m$	.....	THz electric field induced in a photoexcited sample/slab at the $m$ -th harmonic frequency $m\omega_0$
$\Delta E_R$	.....	transient THz electric field leaving the input surface of a sample
$\Delta E_T$	.....	(total) transient THz electric field leaving the output surface of a sample
$\Delta E_m^R$	.....	transient THz electric field at the $m$ -th harmonic frequency leaving the input surface of a sample
$\Delta E_m^T$	.....	transient THz electric field at the $m$ -th harmonic frequency leaving the output surface of a sample
$\Delta E_T/E_T$	.....	(total) transient transmission
$\Delta E^{(1)}/E_T$	.....	linear component of the total transient transmission $\Delta E_T/E_T$
$\Delta E^{\text{NL}}/E_T$	.....	nonlinear component of the total transient transmission $\Delta E_T/E_T$
$\Delta E^{\text{NL}}/E_{T,\text{peak}}$	.....	nonlinear transient transmission outside the bandwidth of the field $E_T$ transmitted through a sample in equilibrium
erf	.....	error function
erfcx	.....	scaled complementary error function
$f$	.....	linear frequency of the electromagnetic wave
$f_i$	.....	in Section 5.2.2: occupancy of quantum state $i$
$f_{ij}$	.....	linear frequency corresponding to a transition between quantum states $i$ and $j$
$f_{\text{peak}}$	.....	frequency of peak in linear response of confined charges
$f_{\text{peak}}^*$	.....	frequency of peak in nonlinear response of confined charges at the fundamental frequency $f_0$
$f_{\text{pl}}$	.....	plasma frequency
$f_r$	.....	linear frequency corresponding to the round-trip time $t_r$ ( $f_r = 1/t_r$ )
$f_{\text{rep}}$	.....	repetition rate of laser

$f_0$	..... in Sections 7.1-7.4: central frequency of the FELBE pulses
	..... in Section 8: harmonic resonance frequency of approximate band bending potential
	..... elsewhere: linear frequency of a monochromatic wave
$F$	..... in Sections 2, 5: statistical distribution function
	..... in Section 3: normalized Gaussian hypergeometric function ${}_2F_1$
	..... in Appendix B: restoring force acting on electrons
${}_2F_1$	..... Gaussian hypergeometric function [59]
$g$	..... third-order nonlinear coefficient of the nonlinearities due to charge confinement
$G(E)$	..... density of states
$G(z)$	..... particular solution of wave equation (3.20)
$h$	..... Planck constant ( $h = 6.626 \times 10^{-34}$ J/s)
$\hbar$	..... reduced Planck constant ( $\hbar = h/(2\pi)$ $1.054 \times 10^{-34}$ J/s)
$\Delta H$	..... THz magnetic field induced in a photoexcited sample/slab
$\Delta H_m$	..... THz magnetic field induced in a photoexcited sample/slab at the $m$ -th harmonic frequency $m\omega_0$
$\Delta H_m^R$	..... $m$ -th harmonic transient THz magnetic field leaving the input surface of a sample
$\Delta H_m^T$	..... $m$ -th harmonic transient THz magnetic field leaving the output surface of a sample
$j$	..... in Section 4.1: electric current density of free charges
$j[E]$	..... electric current density as a functional of an electric field $E$
$j^{[m]}, j^{[m]}(m\omega_0)$	..... harmonic electric current density of the $m$ -th order (i.e. response at the $m$ -th harmonic frequency $m\omega_0$ )
$j^{(\alpha)}, j^{(\alpha)}(t), j^{(\alpha)}(\omega)$	..... nonlinear electric current density of $\alpha$ -th order (i.e. directly proportional to $E^\alpha$ )
$j_{\text{eff}}$	..... effective electric current density in an inhomogeneous system
$j_{\text{eff}}^{(1)}$	..... linear component of the effective electric current density $j_{\text{eff}}$
$j_{\text{eff}}^{\text{NL}}$	..... nonlinear component of the effective electric current density $j_{\text{eff}}$
$j_{\text{exc}}[E]$	..... electric current density induced in a photoexcited slab
$j_p$	..... local electric current density (in the photoconductive parts of a two-component system)
$j(t)$	..... electric current density in the time-domain (both linear and nonlinear)
$j(\omega)$	..... complex spectrum of the electric current density (both linear and nonlinear)
$j(z)$	..... spatially dependent photoinduced electric current density
$j_p^{(1)}$	..... linear component of the local electric current density $j_p$
$j_p^{\text{NL}}$	..... nonlinear component of the local electric current density $j_p$
$k$	..... wave vector in a sample ( $k = n_s k_{\text{vac}}$ )
$k_B$	..... Boltzmann constant ( $k_B = 1.38 \times 10^{-23}$ J/K)
$k_m$	..... wave vector in a sample corresponding to the $m$ -th harmonic ( $k_m = m n_s k_{\text{vac}}$ )

$k_{\text{vac}}$	.....	wave vector in the vacuum
$k_0$	.....	screening parameter
$K$	.....	shape factor in the Maxwell-Garnett effective medium theory
$K_{\text{rms}}$	.....	undulator parameter
$l$	.....	several largely equivalent meanings depending on a context: size of a nanostructure confining, distance between two parallel planes, potential well width
$L$	.....	in Section 3.1: depolarization factor of non-percolated clusters
	.....	elsewhere: sample thickness
$L_0$	.....	depolarization factor dominant in the spectral function
$\text{Ln}$	.....	principal value of complex logarithm
$m$	.....	carrier effective mass
	.....	index denoting the order of generated harmonics
$m_e$	.....	electron rest mass ( $m_e = 9.109 \times 10^{-31}$ kg)
$n$	.....	in Section 5.2: charge density
	.....	in Section 5.3: number of charges per unit length, surface and volume
	.....	in Section 7.5: real part of complex refractive index
	.....	in Section 8: effective refractive index of the nanotube layer
$n_{\text{cross}}$	.....	crossover charge density where coupling between geometrical and plasmonic resonances occurs
$n_p$	.....	refractive index of the photoexcited material
$n_s$	.....	refractive index of a sample
$n_1$	.....	refractive index of substrate
$n_2$	.....	refractive index of superstrate
$N$	.....	concentration of (photoexcited) carriers
	.....	in Section 5.3: average number of charges per unit block
$N_C$	.....	doping carrier concentration in graphene
$\mathcal{N}(\omega_0)$	.....	symbol defined by the Eq. (B.10)
$\hat{p}$	.....	momentum operator
$p_F$	.....	probability that carrier is scattered on a nanoregion boundary and enters an adjacent within a nanotube wall in the Monte-Carlo calculations
$p_j$	.....	probabilities of the initial states considered for Monte-Carlo calculations
$p_{\text{rel}}$	.....	probability that carrier reflects elastically and specularly from a nanoparticle boundary in Monte-Carlo calculations
$p_t$	.....	probability that carrier passes through a nanoparticle boundary in Monte-Carlo calculations
$P$	.....	average power of the FELBE pulses
$\mathcal{P}(\omega)$	.....	instrumental function describing the propagation of THz pulses behind the sample
$P^{(1)}(\omega)$	.....	linear polarization
$P^{(\omega)}(\beta\omega)$	.....	nonlinear polarization of the $\alpha$ -th order at the resulting frequency $\beta\omega$ ( $\beta = 1, 3, 5, \dots$ )
$P_{\text{inc}}$	.....	average power of the FELBE pulses incident on a sample

$q$	.....	pitch of a motion between two periodically perturbed parallel planes
$Q$	.....	in Section 8: charge of the surface defects
	.....	elsewhere: field-enhancement factor for an unphotoexcited two-component structure
$Q_{\text{exc}}$	.....	field-enhancement factor for a photoexcited two-component structure
$r$	.....	in Section 5.4: radius of the cylinders forming hexagonal Lorentz gas potential
	.....	in Section 7: radius of a spot
	.....	in Section 8: distance from a nanotube center (equivalent to the position vector of mobile carriers)
$\vec{r}$	.....	charge position vector
$r_j$	.....	in Section 8: position vector the $j$ -th charge surface defect
	.....	reflection Fresnel coefficient at the sample input ( $j = 1$ ) or output ( $j = 2$ ) surface
$r_0$	.....	distance of the middle of a nanotube wall from the nanotube center
$\text{RSIPS}^{[m]}$	.....	relative spectrally integrated power signal of the $m$ -th harmonics
$s$	.....	volume filling factor of the photoconductive material in nanostructures
$S_m$	.....	particular solution of the nonlinear wave equation (4.6)
$S_T$	.....	THz signal measured for the sample in equilibrium
$\Delta S_T$	.....	transient THz signal measured for the photoexcited sample
$\Delta S_m^T$	.....	transient THz signal detected at the $m$ -th harmonic frequency
$t$	.....	time
$t_j$	.....	transmission Fresnel coefficient at the sample input ( $j = 1$ ) or output ( $j = 2$ ) surface
$t_r$	.....	in Section 5.2: round-trip time of carriers bouncing between two straight parallel planes
$t_{1,2}$	.....	times at which the carrier reaches wall of a potential well in model developed in Section 6.2
$T$	.....	in Section 8: complex transmittance for unphotoexcited nanotube layers
	.....	elsewhere: temperature
$\Delta T_{\text{norm}}$	.....	normalized transient transmission (used only for linear response in this work)
$\Delta T_{\text{norm}}^P$	.....	normalized transient transmission for percolated parts of a two-component system
$\Delta T_{\text{norm}}^N$	.....	normalized transient transmission for the non-percolated parts of a two-component system
$\Delta T/T$	.....	transient transmission in the linear regime
$v(t)$	.....	charge velocity in the time-domain
$v(\omega)$	.....	complex spectrum of the charge velocity
$v(L)$	.....	spectral functions weighting the influence of non-percolated clusters in Bergman spectral representation
$v_{\text{drift}}$	.....	drift charge velocity
$v_{x,y,z}$	.....	components of the velocity vector

$v_F$	.....	Fermi velocity
$v_{th}$	.....	thermal velocity
$v_0$	.....	initial correction to Fermi velocity considered in the model developed in Section 6.2
$v_{1,2}$	.....	components of the carrier velocity acquired during a half-period of movement in a potential well (in the model developed in Section 6.2)
$v^{[m]}(m\omega_0)$	.....	harmonic velocity characterizing the response at the $m$ -th harmonic frequency $m\omega_0$
$v^{(\alpha)}(\omega_1, \omega_2, \dots, \omega_\alpha)$	...	nonlinear velocity of the $\alpha$ -th order
$V$	.....	percolation strength of the photoconductive constituents in two-component systems (Bergman spectral representation, VBD model of effective medium)
$V(r)$	.....	in Section 2.2: local potential influencing movement of charges
	.....	in Section 8: approximate band bending and screened Coulomb potentials
$V(x)$	.....	anharmonic binding potential
$\mathcal{V}$	.....	volume of a nanocrystal
$V_h$	.....	percolation strength of the insulating constituents (matrix) in two-component systems (Bergman spectral representation, VBD model of effective medium)
$V_p$	.....	percolation strength of the photoconductive constituents in two-component systems (Bergman spectral representation, VBD model of effective medium)
$w$	.....	thickness of a nanotube wall
$x$	.....	in Section 6.1.4 and Appendix B: electron displacement
	.....	elsewhere: spatial coordinate
$x_1$	.....	linear electron displacement in nonlinear Lorentz model (i.e. anharmonic oscillator)
$x_3, x_5$	.....	third- and fifth-order corrections to electron displacement in the nonlinear Lorentz model (i.e. anharmonic oscillator)
$y$	.....	spatial coordinate
$Y, Y_0$	.....	in Section 3: symbols introduced by Eq. (3.41)
	.....	in Appendix A: symbols introduced by Eq. (A.13.2)
$z$	.....	spatial coordinate along the direction of THz wave propagation, i.e. perpendicular to the sample surface
$Z_0$	.....	vacuum impedance (376.73 $\Omega$ )

## B. Greek symbols

$\alpha$	.....	in Section 6: empirical factor related to shape of confining potential and distribution of thermal velocity
	.....	in Section 7.5: absorption coefficient
$\alpha_p$	.....	local absorption coefficient (i.e. absorption coefficient of the photoconducting material in inhomogeneous systems)
$\alpha_{\text{eff}}$	.....	effective absorption coefficient of an inhomogeneous system
$\alpha_0$	.....	absorption coefficient for low THz fields
$\alpha(E)$	.....	THz field-dependent absorption coefficient
$\beta$	.....	empirical factor related to nanoparticle geometry and exact shape distribution of thermal velocity
$\gamma$	.....	in Section 3.2: coefficient of the solution of homogeneous linear wave equation (3.20)
	.....	in Section 5: scattering rate ( $\gamma = 1/\tau_s$ )
	.....	in Section 6.1.4: oscillator damping rate
$\gamma_m$	.....	$m$ -th order coefficient of the solution of homogeneous nonlinear wave equation (4.6)
$\delta$	.....	in Section 3.2: coefficient of the solution of homogeneous linear wave equation (3.20)
	.....	elsewhere: delta function (Section 1.2, Section 5.2)
$\delta_m$	.....	$m$ -th order coefficient of the solution of homogeneous nonlinear wave equation (4.6)
$\varepsilon$	.....	linear permittivity of a homogeneous slab
$\varepsilon_{\text{loc}}$	.....	spatially dependent local permittivity
$\varepsilon_{\text{eff}}$	.....	effective linear permittivity of an inhomogeneous sample
$\varepsilon_h$	.....	linear permittivity of insulating material (matrix) in a two-component system
$\varepsilon_p$	.....	linear permittivity of photoconductive material in a two-component system
$\varepsilon_0$	.....	permittivity of vacuum ( $8.854 \times 10^{-12}$ F/m)
$\eta_1$	.....	density of the nanowires
$\eta_2$	.....	density of the nanosheets
$\theta$	.....	polar angle
$\lambda$	.....	in Section 8: wavelength of the radiation used for photoexcitation
	.....	in Appendix B: a parameter ranging continuously between zero and one
	.....	elsewhere: wavelength of the THz radiation
$\Lambda(x)$	.....	triangle function oscillating between +1 and -1 with period 1
$\mu(\omega)$	.....	complex spectrum of the (linear) charge mobility
$\mu^{[m]}(m\omega_0)$	.....	harmonic mobility characterizing the response at the $m$ -th harmonic frequency $m\omega_0$
$\mu^{\text{NL}}$	.....	nonlinear component of the charge mobility
$\mu^{(a)}(\omega_1, \omega_2, \dots, \omega_a)$	.....	nonlinear mobility of the $a$ -th order

$\mu^{(1)}$	.....	linear component of the charge mobility
$\mu_{\text{gen}}$	.....	generalized mobility of charges
$\mu_{jk}$	.....	linear mobility tensor
$\mu_0$	.....	permeability of vacuum ( $4\pi \times 10^{-7}$ H/m)
$\xi$	.....	quantum yield of photogenerated mobile carriers
$\sigma(t)$	.....	linear conductivity of the material in the time-domain
$\sigma(\omega)$	.....	complex spectrum of the linear conductivity
$\sigma^{\text{L}}$	.....	linear part of conductivity
$\sigma^{\text{NL}}$	.....	nonlinear part of conductivity
$\sigma_{\text{B}}$	.....	background conductivity of a doped photoconductive material
$\sigma_{\text{dc}}$	.....	dc conductivity
$\sigma_{\text{FWHM}}$	.....	full width at half maximum of the FELBE pulses
$\sigma_{\tau}$	.....	electron pulse lengths at the FELBE facility
$\sigma_{ij\dots kl}^{(\alpha)}(t_1, t_2, \dots, t_{\alpha})$	.....	$(\alpha + 1)$ -rank tensor of nonlinear conductivity of the $\alpha$ -th order in the time-domain
$\sigma^{(\alpha)}(\omega_1, \omega_2, \dots, \omega_{\alpha})$	.....	nonlinear conductivity of the $\alpha$ -th order in the frequency-domain
$\Delta\sigma(\omega)$	.....	complex spectrum of the linear photoconductivity
$\Delta\sigma_{\text{eff}}$	.....	effective linear photoconductivity of an inhomogeneous sample
$\Delta\sigma_{\text{eff}}^{(\alpha)}(\omega_1, \omega_2, \dots, \omega_{\alpha})$	.....	nonlinear effective photoconductivity of the $\alpha$ -th order in the frequency-domain
$\Delta\sigma_{\text{p}}$	.....	linear photoconductivity of the photoconductive material in a two-component system
$\Delta\sigma_{\text{p}}^{(\alpha)}(\omega_1, \omega_2, \dots, \omega_{\alpha})$	.....	nonlinear photoconductivity of the $\alpha$ -th order of the photoconductive material in a two-component system
$\Delta\Sigma_{\text{eff}}$	.....	transient sheet conductivity
$\tau'$	.....	effective scattering time in modified Drude-Smith model
$\tau_{\text{diff}}$	.....	diffusion time (i.e. how long does the carrier need to diffuse across the nanoparticle)
$\tau_{\text{DS}}$	.....	Drude-Smith scattering time
$\tau_{\text{s}}$	.....	mean bulk scattering time
$\varphi$	.....	azimuthal angle
$\varphi_0$	.....	initial phase shift between electric field and carrier motion in the model developed in Section 6.2
$\phi$	.....	photoexcitation fluence (expressed in photons per unit area)
$\chi, \chi^{(1)}(\omega_0)$	.....	linear susceptibility
$\chi^{(3)}$	.....	third-order susceptibility corresponding to general four-wave mixing
$\chi^{(\alpha)}(\omega_1, \omega_2, \dots, \omega_{\alpha})$	.....	nonlinear susceptibility of the $\alpha$ -th order
$\chi_{\text{eff}}^{(3)}$	.....	third-order susceptibility corresponding to the third harmonics generation in graphene
$\psi_i$	.....	wave function corresponding to state $i$



$\omega$	..... angular frequency ( $\omega = 2\pi f$ )
$\omega_{ij}$	..... angular frequency corresponding to a transition between quantum states $i$ and $j$
$\omega_{NL}$	..... resulting frequency of a nonlinear process
$\omega_0$	..... angular frequency of a monochromatic wave ( $\omega_0 = 2\pi f_0$ )
$\Omega_{osc}$	..... resonant oscillator angular frequency